ISSN (print) 0424-8570
ISSN (online) 3034-6185

Российская Академия Наук

Volume 61, No. 1

January 2025

ЭЛЕКТРОХИМИЯ

RUSSIAN JOURNAL OF ELECTROCHEMISTRY

NAUKA
1727

Russian Academy of Sciences

ЭЛЕКТРОХИМИЯ / RUSSIAN JOURNAL OF ELECTROCHEMISTRY

Volume 61 No. 1 2025 January

Founded in January 1965 at the initiative of A.N. Frumkin.
Published monthly.
ISSN (print) 0424-8570
ISSN (online) 3034-6185

The journal publication is guided by the Department of Chemistry and Material Sciences, RAS

Editorial office: 119071 Moscow, Leninsky prosp. 31/4
Frumkin Institute of Physical Chemistry and Electrochemistry Russian Academy of Sciences
E-mail address of the journal (Editorial Board): rjelectrochemistry@yandex.ru

Moscow
«Nauka» Publishers»

CONTENTS

Vol. 61, No. 1, 2025

Special issue based on the reports of the 17th International Meeting "Fundamental and applied problems of solid state ionics" (Chernogolovka, June 16–23, 2024)

Regular articles

RUSSIAN JOURNAL OF ELECTROCHEMISTRY, 2025, Vol. 61, No. 1, pp. 3–4

17TH INTERNATIONAL MEETING "FUNDAMENTAL AND APPLIED PROBLEMS OF SOLID STATE IONICS"

The 17th International Meeting "Fundamental and Applied Problems of Solid State Ionics", hereinafter referred to as FPSSI-2024, was held from 16 to 23 June, 2024 in Chernogolovka (Moscow region, Russia).

The FPSSI-2024 meeting was dedicated to the memory of Professor Evgeny Alexandrovich Ukshe and that year marked the 30th anniversary since the beginning of the event. E. A. Ukshe was the initiator of the organization of a series of regional seminars "Solid State Ionics" in the 1980s, which is currently continuing in the format of international conferences. The meeting brings together scientists in the fields of electrochemistry, crystal chemistry, physics and solid state chemistry and promotes the expansion of scientific research and contacts in many related fields, including in the field of applied electrochemistry.

The work of the FPSSI-2024 meeting was organized in four scientific areas:

Section 1. Ion conductors: synthesis, structure, properties and transport mechanisms;

Section 2. Electrode processes and electrocatalysis at phase boundaries;

Section 3. Experimental and theoretical methods for studying processes in solid-state ion and mixed conductors;

Section 4. Practical use of solid-state electrochemical devices: fuel cells, batteries, supercapacitors, sensors, electrochemical energy storage, etc.

More than 150 researchers, university teachers, undergraduates and postgraduates, engineers, technologists, representatives of industry and business took part in the work of the FPSSI-2024 meeting, including seven foreign participants from five countries. The meeting was held in face-to-face and virtual formats. About 110 people participated in the conference in person. 84 reports were heard, including 28 invited papers (three from foreign participants) and 56 oral presentations.

The 6th School for Young Scientists "Hydrogen and Electrochemical Power Engineering" was held as part of the FPSSI-2024 meeting. Six lectures were given by leading scientists and practitioners. Round tables were organized such as "Green energy, renewable energy, storage" in Chernogolovka with the participation of representatives of the Ministry of Industry and Trade of Russia, industry and business, and an offsite meeting of the international round table "Hydrogen Transport" in Moscow, organized by the Ministry of Energy of the Russian Federation, the Department of Transport of Moscow, the Department of Industrial Policy of the Eurasian Economic Commission (moderator: General Director of the AFK Sistema Hydrogen Energy Center Yu. A. Dobrovolsky).

The participants of FPSSI-2024 represented scientific and educational organizations from 21 cities of Russia such as Apatity, Voronezh, Gatchina, Dubna, Yekaterinburg, Kazan, Kirov, Krasnodar, Makhachkala, Moscow, Novosibirsk, Novocherkassk, Rostov-on-Don, Samara, St. Petersburg, Sterlitamak, Syktyvkar, Tomsk, Ufa, Chelyabinsk, Chernogolovka.

The international status of FPSSI-2024 was confirmed by the work of the international organizing committee, research materials presented at the meeting, prepared by foreign scientists and teams or in cooperation with Russian scientists from ten countries: Belarus, Germany, Israel, Kazakhstan, China, Russia, Slovenia, the USA, France, South Africa.

The materials of the reports presented at the meeting were published in the form of a collection of extended abstracts in the RSCI https://www.elibrary.ru/item.asp?id=69208560.

During the work of FPSSI-2024, a competition of works by young scientists (oral and poster presentations) was held. Ten reports were selected by an authoritative commission to participate in the final session. According to the results of the session, K. O. Paperzh (Southern Federal University, Rostov-on-Don) took the first place, G. S. Degtyarenko (Lomonosov Moscow State University, Moscow, FRC of Problems of Chemical Physics and Medical Chemistry of the Russian Academy of Sciences, Chernogolovka) took the second place, and A. A. Koshkina took the third place (Institute of Solid State Chemistry, Ural Branch of the Russian Academy of Sciences, Yekaterinburg). A special prize was awarded to S. V. Pavlov (Joint Institute for High Temperatures of the Russian Academy of Sciences, Moscow). The prizes are provided by the AFK Sistema Hydrogen Energy Center, Moscow and the SmartStat company, Chernogolovka.

Based on the materials of the reports, the participants of the FPSSI-2024 meeting prepared 12 articles for the special issue of the Russian Journal of Electrochemistry.

The Organizing Committee of FPSSI-2024 expresses its gratitude for the organization and management to the FRC PCF and MC, RAS, and the AFK Sistema Hydrogen Energy Center, for the information support to the Forum-SM scientific and consulting center, and for the financial support to the AFK Sistema Hydrogen Energy Center, the SmartStat Russian scientific and production company, Chernogolovka; Prometheus-RD LLC small innovative enterprise, Rostov-on-Don. The Organizing Committee expresses special gratitude to all participants of the conference and the authors of articles in the special issue of the Russian Journal of Electochemistry.

On behalf of the Organizing Committee of FPSSI–2024

N. G. Bukun, B. M. Grafov, Yu. A. Dobrovolsky, A. V. Pisareva

RUSSIAN JOURNAL OF ELECTROCHEMISTRY, 2025, Vol. 61, No. 1, pp. 5–36

APPLICATION OF GRAPHENES IN SUPERCAPACITORS (REVIEW)[1]

© 2025 Yu. M. Volfkovich*

Frumkin Institute of Physical Chemistry and Electrochemistry of the Russian Academy of Sciences, Moscow, Russia

**e-mail: yuvolf40@mail.ru*

Received May 08, 2024
Revised August 23, 2024
Accepted September 26, 2024

Abstract. This review examines the literature, mainly of recent years, on the current topic of using graphenes in supercapacitors. The influence of the porous structure, doping and irradiation of graphenes is considered. Methods for producing graphenes, composites of graphenes with metal oxides, sulfides and selenides, with metal particles, with electron-conducting polymers, with MXenes, as well as quantum dots are considered. Electrochemical characteristics are given for the types of graphene considered.

Keywords: *graphenes, oxides, sulfides, selenides, electron-conducting polymers, polyaniline MXenes, quantum dots*

DOI: 10.31857/S04248570250101e7

TABLE OF CONTENTS

LIST OF ABBREVIATIONS

AC – activated carbon
RGO – reduced graphene oxide
EDL – electrical double layer
SWCN – single-walled carbon nanotubes
PVA – polyvinyl alcohol
TEM – transmission electron microscopy
CNT – carbon nanotubes
SSA – specific surface area
CVA – cyclic voltammetry
EIS – electrochemical impedance spectroscopy
AC – activated carbon
CNT – carbon nanotubes
EDX – energy dispersive X-ray spectroscopy
EIS – electrochemical impedance spectroscopy
FESEM – Field emission scanning electron microscopy
FTIR – Raman infrared spectroscopy with Fourier transform
GCD – galvanostatic cycling
GO – graphene oxide
GQD – Graphene quantum dots
HRTEM – High-resolution transmission electron microscopy
PANi – polyaniline
PL – photoluminescence
PP – polyporphine
PPy – polypyrrole
PT – polythiophene
rGO – reduced graphene oxide
SEM – scanning electron microscopy
TEM – transmission electron microscopy
Uv-vis – ultraviolet visible spectroscopy
WSC – Wire supercapacitor
XRD – X-ray diffraction

INTRODUCTION

Recently, graphenes and their derivatives have been used as promising electrode materials for electrochemical supercapacitors [1, 2, 3–44]. Graphenes were discovered only about 15 years ago, for which their creators received the Nobel Prize, and almost immediately the remarkable properties of graphenes were discovered, which open up wide possibilities for their use in various sectors of the national economy, including chemical current

[1] Based on the materials of the report at the 17th International Meeting "Fundamental and applied problems of solid state ionics", Chernogolovka, June 16–23, 2024.

sources and electrochemical capacitors. A single layer of graphene sheet provides a specific external surface of up to 2,675 m^2/g available for liquid electrolyte, compared with an external specific surface of approximately 1,300 m^2/g for an individual single-walled carbon nanotube (SWNT). Graphene layers form plates of several single graphene layers, as a result of which the surface available for the electrolyte decreases. However, encouraging results have recently been obtained for ECSCs with graphene electrodes which often have the pseudo-capacity of Faraday redox reactions in addition to the capacity of the double electric layer (EDL).

Reduced graphene oxide (RGO) is usually obtained using a modified Hammers method. According to this technique, the initial graphite powder is added to a mixture of concentrated sulfuric acid and nitric acid during stirring and cooling, and after a while, three times the amount of potassium permanganate relative to graphite is added to the same mixture. Then a solution of hydrogen peroxide is added to it and after an hour it is diluted with three times the amount of distilled water. After settling for several hours, the upper transparent layer is decanted. The suspended sediment is filtered, washed with distilled water and dried at room temperature to a constant weight. As a result, a dry powdered graphite oxide is obtained, which is reduced by rapid heating to a temperature of 1000 °C. At the time of reduction, the material is stratified with a multiple increase in its volume (exfoliation). The final product is a powder of thin monolayers containing from 1 to 10 graphene monolayers in plates, which have a size range from 1 to 10 microns in the lateral direction. These monolayers, in turn, are grouped into agglomerates, between which pores with a wide (4–5 orders of magnitude) range of sizes are formed: micropores, mesopores, and macropores [8, 19–44].

It should be noted that the review analyzes many recent publications, from 2019 to 2024. In recent years, a number of reviews on the use of graphenes in supercapacitors have been published, for example [20, 21, 43]. However, they lacked the following important sections, which are systematically considered in this review: the effect of doping and irradiation, the effect of porous structure, quantum dots, graphene composites with metal oxides, with electron-conducting polymers, with MXenes.

An important place in the review is occupied by materials consisting of graphene composites with electron-conducting polymers (polyaniline, polypyrrole), with metal oxides and with MXenes. Supercapacitors with these materials have high electrochemical characteristics.

1. GRAPHENES AND THEIR COMBINATIONS WITH OTHER CARBON MATERIALS

Graphene electrodes are characterized by high reversibility of charge-discharge processes. This is clearly seen from Fig. 1, which shows the dependences of specific capacitance on specific current and on the number of galvanostatic charge/discharge cycles for two different electrodes with a specific surface area (SSA) of 450 and 520 m^2g^{-1}, made on the basis of RGO, which was applied to nickel felt. Electrochemical measurements were carried out at 30 wt.% KOH [45]. As you can see, when the specific current is changed by an order of magnitude, the capacity has hardly changed. It is also seen that for 500 cycles, the capacity remained practically constant.

In [18], it was found that graphene oxide has proton conductivity, and in [19], a supercapacitor consisting of a graphene oxide separator and two electrodes based on reduced graphene oxide was manufactured on this basis.

In [46], graphenes were obtained by three different methods and were investigated as electrode materials in electrochemical supercapacitors. The samples obtained by exfoliation of graphite oxide and nanodiamond transformation have a high specific capacity in H_2SO_4, the value reaches 117 F/g. When using an ionic liquid, the operating voltage was increased to 3.5 V (instead of 1 V in the case of an aqueous H_2SO_4 solution), the specific capacity and energy density are 75 F/g and 31.9 Wh/kg, respectively. The performance characteristics of graphenes, which are directly related to the number of layers and the size of the SSA, are superior to single-wall and multi-wall carbon nanotubes (CNTs).

Recently, many articles have been published on the use of graphenes in ECSCs. The study [47] is a summary of the latest developments in the use of graphene as a supercapacitor electrode in the form of foam (3D), thin layers (2D), nanofibers (1D) and nanodots (0D). This article provides a brief look at the discovery and advancement of graphene, followed by a study of the theoretical and experimental approaches used to produce top-quality graphene. In addition, the article focuses on the manufacture of electrodes while maintaining their basic characteristics. Their special effectiveness as an anode in supercapacitors is emphasized. The article concludes by identifying the main problems encountered and potential prospects.

Graphenic acid (GA) is a conductive graphene derivative dispersed in water that can be produced on a large scale from fluorographene. The paper [48] describes a study of synthesis with high reproducibility

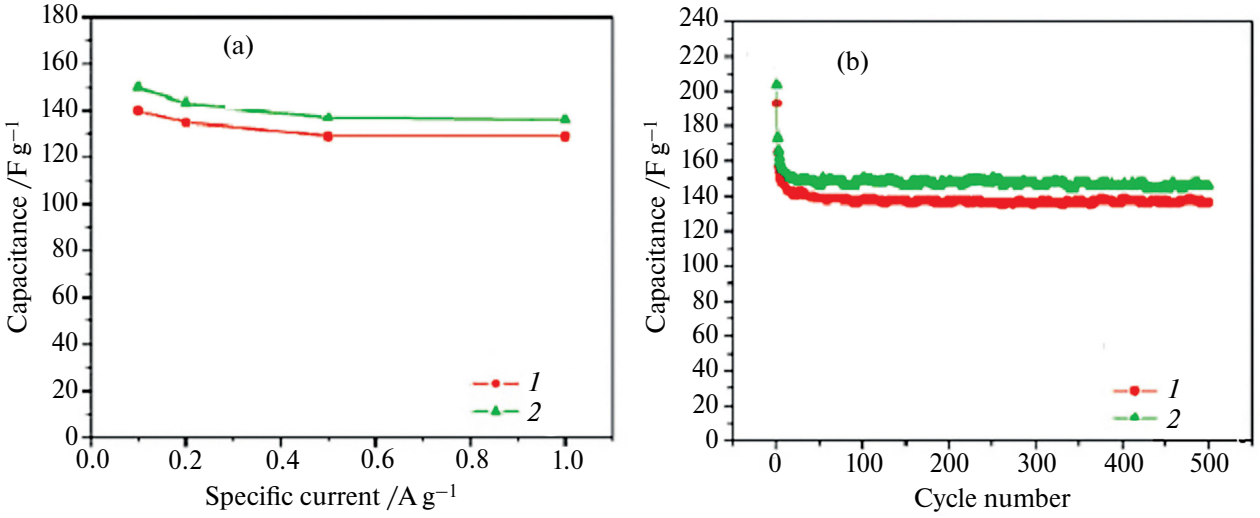

Fig. 1. Dependences of the specific capacitance on the specific current (a) and the dependences of the specific capacitance of 30 wt.% KOH on the number of galvanostatic charge/discharge cycles (b) at a specific current of 0.1 A/g for two RGO-based electrodes with different specific surface area values [45].

for the manufacture of GA. Charge/discharge cycling was performed. GA was tested in a two-electrode cell with a sulfuric acid electrolyte. The speed stability test showed that GA could be repeatedly cycled at a current density in the range from 1 to 20 A/g without loss of capacity. The cyclic stability experiment showed that even after 60,000 cycles, the material retained 95.3% of its specific capacity at a high current density of 3 A/g.

In [49], the concept of bipolar electrochemistry is used to develop a single-stage and controlled process for simultaneous exfoliation of a graphite source and for deposition of graphene oxide and reduced graphene oxide layers on conductive substrates. Electrochemical analysis performed on symmetrical cells showed a specific capacitance of 1.932 mF/cm^2 for high-quality reduced graphene oxide deposited on the negative electrode and 0.404 mF/cm^2 for graphene oxide deposited on the positive electrode at a scanning rate of 2 mV/s. The devices have also shown high stability to periodic and repetitive DC charge/discharge cycles, which is suitable for energy storage in supercapacitors. In the frequency domain, frequencies of 1820 and 1157 Hz were obtained with an impedance phase angle of –45° for devices based on positive and negative electrodes, respectively, which is a promising characteristic for AC filtration applications.

Recently, the rapid development of graphene-based supercapacitors has led to the need for devices with a certain adaptability, which will be a fundamental advantage in innovative electronic devices. Various materials are tested to ensure the appropriate properties. Graphene, which has unique properties such as high density and high conductivity, is considered as a potential candidate for use as a building material for superconductors. In [50], various aspects of graphene-based superconductors, their types, metal/nonmetal/polymer doping, as well as oxides and reduced oxides of superconductors incorporated into graphene were studied. To summarize, the processes followed by the researchers were compared to find out which of them is the most appropriate way to obtain the best electrochemical characteristics.

In [51], it was found that a supercapacitor with graphene-based electrodes has a specific energy density of **85.6 Wh/kg** at room temperature and **136 Wh/kg** at 80 °C at 1 A/g. These energy densities are comparable to those of a nickel-metal hydride battery, but the supercapacitor can be charged or discharged in seconds or minutes. The key to success was the ability to take full advantage of the high density of single-layer graphene by preparing curved graphene sheets, which makes it possible to form mesopores accessible and wetted with environmentally friendly ionic liquids capable of operating at a voltage of >4 V.

1.1. The effect of porous structure

The characteristics of the porous structure significantly affect the electrochemical characteristics of graphene electrodes and corresponding supercapacitors. The characteristics of the porous structure include the specific surface area (SSA), the volume ratio of micro (hierarchical type of porous nano) pores, mesopores and macropores, the total porosity and structures of the electrodes. The hierarchical type of porous structure means that the smallest particles stick together into agglomerates, which, in turn, agglomerate into larger agglomerates, etc.

It was established in [52] that zinc chloride is an ideal pore forming agent, and in combination with capillary drying can set the specific surface area of graphene from 370 to more than 1000 m^2/g. With a good balance of porosity and density, a granular graphene electrode with a thickness of up to 400 microns provides a capacity of 150 F/cm^3 in an ion-liquid electrolyte corresponding to a volumetric energy density of **~65 Wh/l**. This study presents the principle of designing electrode materials for next-generation energy storage devices.

Graphene-based supercapacitors are attracting more and more attention due to the possible high SSA, high electron mobility and many other excellent properties of graphene. Nevertheless, in some experiments, contemporary graphene electrodes are considered in [53] in order to solve the problems of combining graphene with other types (for example, with EPP, metal oxides, atomic clusters, nanostructured electrodes, etc. to overcome obstacles such as small surface area, low electrical conductivity, and low capacitance, which significantly limits their electrochemical characteristics for supercapacitors. This review discusses various principles of hybridization (conductor hybridization), and recommendations on hybridization approaches to address these issues. It provides high values of SSA to 960, 1330, and 1530 m2/g and very high values of specific capacity of 530, 780, and 990 F/g.

Fiber supercapacitors (FSC) can be used to power flexible devices such as wearable electronics and smart textiles. [54] describes highly porous activated graphene (AG), which is embedded in graphene fibers to improve the electrochemical characteristics of FSC based on the capacitance of a double electric layer (EDL). Wet spinning of AG in a mixture with graphene oxide (GO) and subsequent chemical reduction of GO to reduced graphene oxide (rGO) make it possible to produce continuous and conductive graphene fibers. AG powders with a very high concentration significantly improve the electrochemical characteristics of FSC. In particular, an rGO/AG fiber with an 80/20 rGO/AG mass ratio reaches a specific surface capacity of **145.1 mF/cm^2** at a current density of 0.8 mA/cm^2 with a PVA/LiCl gel electrolyte. This corresponds to a surface energy and power density of 5.04 $\mu Wh/cm^2$ and 0.50 mW/cm^2 for FSC, respectively. In addition, flexible FSCs using rGO/AG fibers demonstrate high cycling capacity with 91.5% capacity retention after 10,000 cycles. This work shows significant potential in the production of AG-based fibers for the development of highly efficient flexible FSCs.

In [55–57], it was described how the abundant bio-waste is efficiently converted into porous graphene sheets at a low temperature of 900 °C by using potassium hydroxide (KOH) as an activation agent to create porosity, as well as a catalyst to induce graphitization using a simple synthetic approach. The resulting carbon material has good textural properties, such as high SSA (2,308 m^2/g), large pore volume (1.3 cm/g), graphene sheet morphology with an interlayer d-distance of 0.345nm and highly ordered sp-carbon, which is confirmed by detailed textural analysis. Due to its numerous synergistic properties, the material was tested as an effective electrode material for use in supercapacitors and provided a high specific capacity of **240 F/g at 1 A/g**. In addition, the assembled symmetrical supercapacitor demonstrated fast rate capability to retain 87% of capacity at high current (50 A/g), exceptional cyclic stability (93% capacity retention after 25,000 cycles) and a high energy density of **21.37 Wh/kg at a high power density of 13,420 W/kg**.

Obtaining a carbon electrode with high gravimetric and volumetric capacity under heavy loads is crucial for supercapacitors. At the same time, defective graphene nanospheres (GNS) meet the above requirements well [56–62]. The morphology and structure of the GNS are controlled by the microwave heating time and the iron content. A typical GNS with an SSA of 2,794 m^2/g, a pore volume of 1.48 cm^3/g and a packing density of 0.74 g/ cm^3 sets high gravimetric and volumetric capacities of **529 F/g and 392 F/cm^3 at 1 A/g** with a retention of 62.5% of the capacity at 100 A/g in a three-electrode system of 6 mol/l KOH. In a two-electrode system, the GNS has an energy density of **18.6 Wh/kg** (13.8 Wh/l) with a high specific power of 504 W/kg.

Redox covalent organic frameworks (COFs) represent a new class of energy storage materials due to their significant number of active sites, well-defined channels, and high surface area. However, their low electrical conductivity and low electrochemical accessibility to active centers seriously limit their practical application. The article [57] describes the manufacture of an electrode based on anthraquinone COFs/ composite aerogel and graphene (DAAQ-COFs/GA) by electrostatic self-assembly between negatively charged graphene oxide (GO) nanolayers and modified positively charged DAAQ-COFs nanoflowers. Due to its hierarchical porous structure and fast reactions of redox centers, the electrode has a high specific capacity of **378 F/g at 1 A/g** and fast kinetics with a capacitive contribution of about 93.4% at 3 mV/s. In addition, the DAAQ-COFs /GA electrode, which does not contain a binder, and the pure graphene aerogel (GA) electrode were assembled into an asymmetric supercapacitor (ASC) with an energy density of up to 30.5 Wh/kg at a specific power of 700 W/kg. This work demonstrates the great potential for the development of high-performance energy storage devices based on COF.

[58] presents a simple method for obtaining graphene with a hierarchical porous structure by activating graphene oxide (GO) using a two-stage thermal annealing process. First, GO was processed at 600 °C by rapid thermal annealing in air, followed by thermal annealing in N_2. The prepared graphene powder contained a large number of slit nanopores with a high SSA of 653.2 m^2/g and a microporous surface area of 367.2 m^2/g. The porous structure could be easily adjusted by controlling the degree of oxidation of GO and the second annealing process. When graphene powder was used as a supercapacitor electrode, a specific capacity of **372.1 F/g** was achieved at **0.5 A/g** in electrolyte 1 M H_2SO_4. The performance of the supercapacitor was very stable, demonstrating a 103.8% retention of specific capacity after 10,000 cycles at 10 A/g. The effect of a porous structure on the performance of a supercapacitor has been systematically studied by varying the ratios between micro-, meso-, and macropores.

Activated reduced graphene oxide (a-rGO) is a material with a rigid 3D porous structure, high SSA, and a hierarchical type of porous structure. Using varying activation parameters and post-synthesis machining, in [59] two sets of materials with a wide range of SSA values of about 1000–3000 m^2/g were obtained, as well as significant differences in pore size distribution and surface oxygen content. The efficiency of activated graphene as an electrode in a supercapacitor with a KOH electrolyte correlated with the structural parameters of the materials and water absorption properties. It was found that a-rGO is a hydrophobic material, as evidenced by the negligible value of the BET concentration in H_2O, determined by analyzing the isotherms of water vapor sorption. However, the total pore volume determined by water vapor sorption and liquid water sorption practically did not differ from the volume obtained by analyzing nitrogen sorption isotherms. The best gravimetric and volumetric capacities in KOH electrolyte were not achieved for samples with the highest BET SSA (N_2) value for materials with 80–90% of the total pore volume in micropores and an increased BET SSA (H_2O). A comparison of the characteristics of electrodes made using rGO and a-rGO shows that a more hydrophilic surface is favorable for charge storage in supercapacitors with KOH electrolyte.

Fig. 2 shows the integral and differential curves of the pore size (width) distribution. As we can see, the differential curve has two obvious maxima and one weakly pronounced maximum. The SSA according to BET is equal to a very large value of **3,030 m^2/g**.

In [60], it is reported about the development of a seamless **mesoporous carbon sheet** consisting

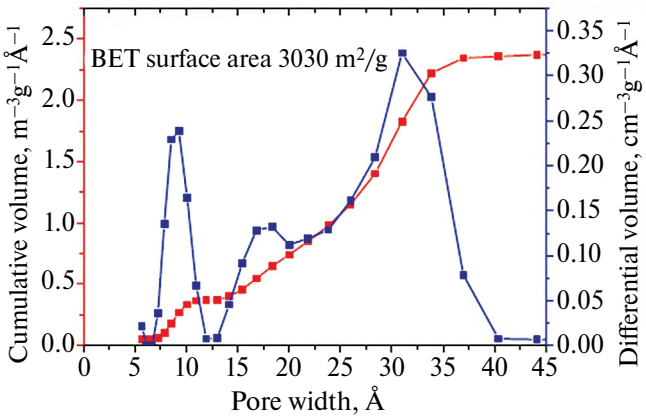

Fig. 2. Integral and differential curves of pore size (width) distribution [59].

of continuous graphene walls, which **exhibits** unusually high stability under high stress conditions. This material has a high SSA of 1,500 m^2/g and contains very few carbon edges (only 4% of the amount present in conventional activated carbons), and it can be used to assemble symmetrical supercapacitors with high stability for the electrolyte 1 MEt_3MeNBF_4/propylene carbonate. Operating at a high voltage of 4.4 V leads to a 2.7-fold increase in energy density compared to using conventional activated carbon.

The production of black liquor, lignin, carbon nanolayers, and multilayer graphene obtained by catalytic nickel graphitization was carried out in order to obtain electrode materials for supercapacitors (Ni@WE) in an environmentally friendly manner [61]. NaCO activation, nickel doping, and catalytic graphitization were performed synchronously; at the same time, the natural hierarchical porous structure of the wood was partially preserved. Cyclic voltammetry (**CV**), galvanostatic charge-discharge spectroscopy and electrochemical impedance spectroscopy (EIS) Ni@WE confirmed that the sample sintered at 1000 °C has a specific capacitance of 163.7 F/g at a scanning frequency of 0.2 V/s. In addition, a higher energy density of **26.2 Wh/kg** with a power density of 124.6 W/kg was obtained in the ECSC, and 89.37% of the capacity remains even after 2000 cycles.

Electrochemical properties and characteristics of high-density energy storage of a solid-state supercapacitor based on graphene nanolayers are described in [3]. The graphene electrode is made in an electrolyte containing 1-butyl-3-methylimidazolium tetrafluoroborate ($BMIMBF_4$) (ionic liquid) $LiClO_4$. The doping additive was enclosed in a polymer matrix in the form of a gel. The mesoporous graphene electrode was formed by dispersion in amorphous polyvinylidene fluoride, resulting in graphene with a minimum number

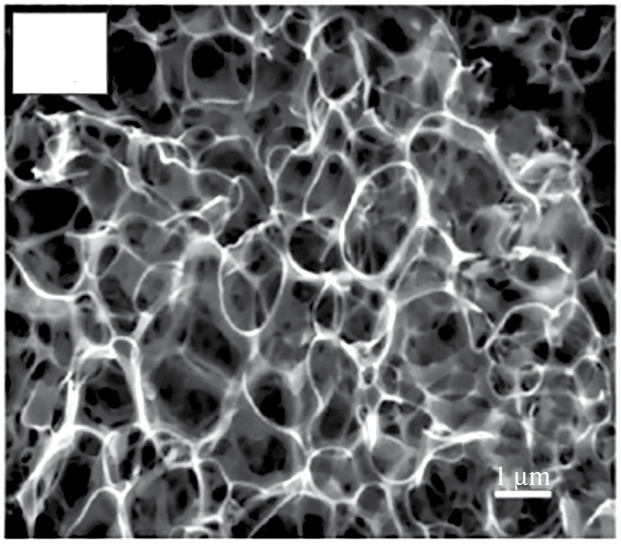

Fig. 3. SEM image of 3D graphene with macropores formed by removing the Na_2CO_3 pore forming agent [48].

of layers (<5 layers). Using the abundance of ions in an ion-liquid gel electrolyte and their efficient access to graphene layers through mesopores, a high specific capacity of **214 F/g** was obtained based on cyclic voltammetry data. Impedance studies show low charge transfer resistance and Warburg impedance, which indicates a high diffusion capacity for ion transport. The charge-discharge data show that the graphene supercapacitor, due to the presence of a wide (~ 2 V) potential window in the ion-liquid electrolyte gel, significantly increased the energy density to **33.3 Wh/kg at a power density of 3 kW/kg with a high ~ 3 A/g** discharge current density. It is reported about the integration of graphene supercapacitors with solar cells and the storage of electricity generated by light.

Three-dimensional (3D) porous graphene with planar nanopores and a hierarchical porous structure attracted great interest in [48] due to its use in supercapacitors because of its high SSA, very high conductivity, and unique porous structure. Combining the advantages of both porous materials and graphene, 3D porous graphene is considered as the embodiment of the idea to create a hierarchical hybrid with complex electrochemical characteristics in order to obtain high specific energy. In this review, the achievements of recent years in the field of manufacturing 3D porous graphene-based structures with micro-, meso- and macropores were summarized, as well as the relationship between structure and electrochemical properties was investigated, and their application in supercapacitors was discussed. Fig. 3 shows a SEM image of 3D graphene with macropores formed by removing the Na_2CO_3 pore forming agent.

In [48], porous particles with a hierarchical porous structure of activated carbon coated with graphene were obtained by spray drying of an aqueous suspension of GO/maltodextrin followed by carbonation and activation. The manufactured core-shell particles had a **high specific surface area (up to 2,457 m^2/g) and showed very high specific capacity (up to 405 F/g at 0.2 A/g**, 299 F/g at 1 A/g and 199 F/g at 50 A/g) along with excellent cycling stability, high energy density and high power density in KOH electrolyte. In addition, the spontaneous formation of the core-shell structure during spray drying was confirmed by calculations using the DFT method with XPS chemical analysis and the TEM method. This designed and controlled spray drying strategy can be implemented to develop new core-shell composite materials for potential applications in energy storage, catalysis, and adsorption.

Fig. 4 shows the differential pore size (width) distribution curves for various materials with a hierarchical porous structure described in [48].

1.2. The effects of doping and radiation

One of the effective ways to increase the electrochemical characteristics of graphenes is to dope them with various chemicals. According to [50], nitrogen-doped graphene is produced by the microwave method with EDA (ethylenediamine) as a nitrogen source. The experimental results show that nitrogen atoms from grafted EDA molecules on the graphene surface are effectively doped into graphene lattices. The NGS sample (nitrogen-doped graphene nanosheets) demonstrates high specific capacities of **197 and 151 F/g** at current densities of 0.5 and 5 A/g in an aqueous solution of 6.0 mol KOH, respectively. In addition, the supercapacitor demonstrates a high ability to operate at high currents: saving 77 and 70% at current densities of 5 and 40 A/g, respectively. In addition, this results in a capacity reduction below 2% after 5,000 charge and discharge cycles, which indicates long-term electrochemical stability.

In [51], N-doped graphenes based on graphene oxide and 3,3',4,4'-tetraaminodiphenylox (TADPO) were obtained using a single-stage hydrothermal method. The data obtained indicate that benzimidazole rings were formed during the reaction, and the nitrogen content by weight in the resulting material ranged from 12.3 to 14.7%, depending on the initial concentration of TADPO. Due to the redox activity of benzimidazole rings, the new N-doped graphene materials demonstrated a high specific capacity, reaching **340 F/g** at 0.1 A/g, which was significantly higher than that of a sample of reduced graphene oxide obtained under similar conditions without the use of TADPO

(169 F/g at 0.1 A/g). The resulting supercapacitor also demonstrated good cyclic stability after 5,000 cycles.

In [52], the two-stage sol-gel method was used to obtain graphene samples doped with nitrogen with a large surface area, differing in the values of the SSA and nitrogen content. In some electrolytes, the specific surface area and porosity had a higher effect on the capacitance characteristics of graphene than the nitrogen content. All samples had higher capacitance characteristics than graphene oxide and a sample without nitrogen, but with a higher acidic electrolyte content than an alkaline one, which gives a volumetric specific capacity of ~118 F/cm^3 with Coulomb efficiency >99% and capacity retention >80% after 10,000 consecutive cycles. Based on the weight of the active material, the maximum gravimetric energy density reached **39 Wh/kg** in an acidic electrolyte at 0.1 A/g, which is almost 2.6 times higher than that of graphene oxide without nitrogen used in this study.

In [63], single-chamber instantaneous Joule heating was developed for the synthesis of nitrogen-doped graphene, which does not use solvents and catalysts, and graphene flash-doped with nitrogen (FNG) was obtained. Precursors of amorphous carbon black and urea rapidly transform into high-quality graphene in less than 1 s under the action of a short electrical pulse with a bright flash of blackbody radiation. The finished FNG product is characterized by high graphitization and hierarchical porous structure. It provides a high surface area-normalized capacity of 152.8 μF/ cm^2 at 1 A/g, a high speed of charging and discharging processes with a high capacity retention of 86.1% even at a **very high current of 128 A/g, and a relaxation time of 30.2 ms.** In addition, the assembled symmetrical quasi-solid state supercapacitor has a **high energy density of 16.9 Wh/kg and a maximum specific power of 16.0 kW/kg**, as well as great cyclic stability (91.2% of the initial capacity is retained after 10,000 cycles). These high characteristics show that FNG is a promising candidate for the use of high-performance supercapacitors.

3D sponge graphene doped with nitrogen (NG) was economically prepared in [53] using a new one-step method from polyethylene terephthalate (PET) waste mixed with urea at various temperatures. The effect of temperature and the amount of urea on the formation of NG has been investigated. Measurements using cyclic voltammetry and impedance spectroscopy have shown that nitrogen fixation, which affects the structure and morphology of the prepared materials, improves charge propagation and ion diffusion. The obtained materials demonstrate high characteristics of supercapacitor electrodes with a specific capacity of up to **405 F/g at 1 A/g**. For an optimal sample, **high values of energy density of 68.1 Wh/kg and specific**

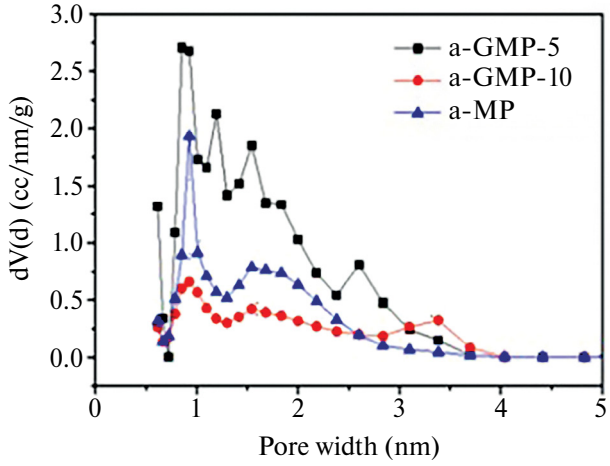

Fig. 4. Differential pore size (width) distribution curves for various materials with hierarchical porous structure described in [48].

power of 558.5 W/kg in 6 M KOH were recorded. The NG samples showed high cyclic stability with 87.7% capacity retention after 5,000 cycles at 4 A/g. Thus, the prepared NG is considered a promising, cheap material used in energy storage systems, and the method used is a cost-effective and environmentally friendly method of mass production of NG, and also opens up waste recycling opportunities for a wide range of applications. Fig. 5 shows the CVA curves, which show that they have a shape close to rectangular, which corresponds to the charge of the EDL. At low currents, the influence of Faraday reactions is also visible, which is expressed in the characteristic deviation of the shape of these curves from the rectangular one.

[64] describes a highly oriented graphene film electrode (NGF), efficiently doped with nitrogen, including its design. NGF has a unique structure that provides high packing density (up to 1.64 g/cm^3) and efficient ion transport at the same time. Symmetrical NGF-based supercapacitors (NGF-SC) showed a specific capacity of 370 F/cm3 **or 226 F/g** with a weight of 11.2 mg/cm^2 in an aqueous electrolyte. In this case, capacity retention was 90.1% after 100,000 cycles. In an ionic liquid, NGF-SC showed a high capacity of 352 F/cm3 or 215 F/g at 11.2 mg/cm2 and with a potential window of 0–3.5 V, providing an **ultra-high energy density of 138 Wh/l**. With a 3H design and high mass load, the energy density of the entire NGF-SC ECSC reaches 65 Wh/L, which is much higher than that of commercial supercapacitors. Notably, this NGF-SC has demonstrated a **long service life of up to 50,000 cycles with 84.8% retention, which is a record**.

Porous graphene fibers doped with nitrogen and sulfur (NS-GFs) were synthesized by hydrothermal self-assembly followed by thermal annealing,

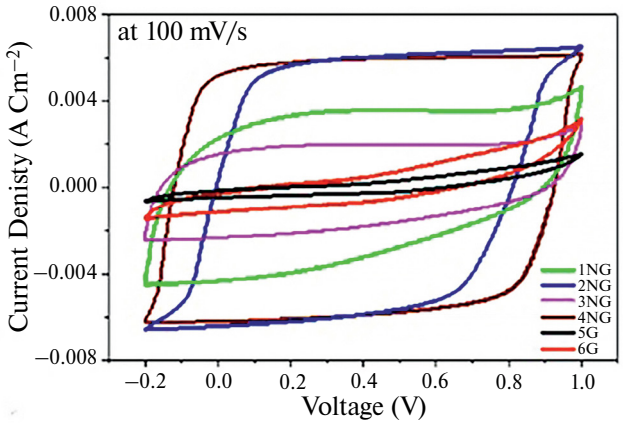

Fig. 5. CVA curves for a supercapacitor based on electrodes developed in [53].

demonstrating high capacitance characteristics of **401 F/cm^3 at 400 mA/cm^3** due to the synergistic effect of double doping by heteroatoms [65]. The manufactured symmetrical fully solid-state supercapacitor with polyvinyl alcohol/H_2SO_4 gel electrolyte and graphene oxide had a high capacity of 221 F/cm^3 and a high energy density of 7.7 MWh/cm^3 at 80 mA/cm^3. Interestingly, the conversion of solar-thermal energy from 0.1 wt.% graphene oxide extends the operating temperature range of the supercapacitor to 0 °C. In addition, the effect of photocatalysis of heteroatoms with double doping increases the capacity of NS-GFs. At an ambient temperature of 0 °C, the capacity increases to 182 F/cm^3 under solar radiation due to the excellent absorption of sunlight and the efficient conversion of solar-thermal energy by graphene oxide, preventing the freezing of the aqueous electrolyte.

[20] presents a porous carbon/graphene composite (PCG) obtained from pollen doped with nitrogen and sulfur with an interconnected "sphere in a layer" structure, in which carbon microspheres with a hierarchical structure can serve as "porous pads" preventing agglomeration of graphene nanolayers. Optimized PCG composite, manufactured with 0.5 wt.% graphene oxide (PCG-0/5), demonstrated **high specific capacity (420 F/g at 1 A/g), speed characteristics (280 F/g at 20 A/g) and excellent cyclic stability with 94% capacity retention after 10,000 cycles**. The symmetrical ECSC **provides a high energy density of 31.3 Wh/kg** in a neutral environment.

In [66], supercapacitor characteristics with phosphorus-doped graphene electrodes were studied, which were synthesized in one stage using Yucel's method. The formation of graphene layers in the mesopore structure was observed by scanning electron microscopy. X-ray photoelectron spectroscopy has been used to identify ordinary phosphorus and phosphorus included in the functional groups -[(−P O)] and -(PO) formed on the inner surface of the electrode. Cyclic voltammetry and electrochemical impedance spectroscopy were used for electrochemical characterization of the electrodes. Cyclic charge-discharge tests were also performed for 1000 cycles to determine the cyclic stability of the electrode materials. As the number of cycles in the electrode synthesis process increased, the number of different molecular functional groups on the surface increased. The largest capacity is 301.3 mF/cm^2 at a current density of 10 mA/cm^2 in a sulfuric acid solution.

A simple approach to obtaining phosphate-functionalized carbon composites based on graphene is presented in [67]. Homogeneous deposition of a thin layer of phenolic resin onto the surface of graphene oxide (GO) layers was achieved using orthophosphoric acid as a polymerization catalyst and functionalization agent. As a result of subsequent pyrolysis of the composite, homogeneous lamellar microstructured porous carbon-graphene composites were obtained, combining accelerated molecular diffusion and accelerated electron transfer. To determine the effect of GO and porosity on the operation of the supercapacitor, a graphene-free sample and a KOH-activated composite using aqueous and organic electrolytes were also obtained and tested. It was found that the presence of GO and KOH activation leads to an increase in specific surface area in combination with progressive pore expansion. As a result, the KOH-activated composite reached specific capacities of 211 and 105 F/g when using 1 M H_2SO_4 and 1.5 M Et_4NBF_4 electrolytes, respectively. It has also been found that phosphorous functionalization of the electrodes makes it possible to achieve an operating voltage of 1.3 V in an aqueous electrolyte, which leads to a significant increase in the energy density of the cell. Finally, both non-activated and activated graphene-based composites provide very good conservation of capacitance, energy density and power, as well as cycling stability.

[68] describes the use of graphene aerogels doped with boron (B-GA), which were produced by a simple hydrothermal method. These B-GA are characterized by high SSA and high mesoporosity. B-GA supercapacitors have a **high specific capacity of 308.3 F/g at 1 A/g**. Moreover, B-GA provides high stability during cycling, namely 92% of capacity retention after 5000 cycles at 1 A/g, which is higher than that of undoped graphene aerogels (86%). The performance improvement is due to a combination of a mesoporous structure, high SSA, and an abundance of B-GA defects. This study demonstrates the significant potential of B-GA electrodes for high-performance

supercapacitors. Fig. 6 shows a schematic representation of the molecular structure of graphene aerogel doped with boron (B-GA).

In [69], boron-doped diamond (BG/BDD) was synthesized by chemical deposition from the gas phase using electron filaments (EA-HFCVD). Boron atoms efficiently dope graphene and diamond, and boron graphene (BG) sheets are grown vertically on boron diamond (BDD). The boron content in BG affects the characteristics of the BG/BDD electrode, and the electrode has a high specific capacity. The electrochemical behavior of the BG/BDD electrode was analyzed at both positive and negative potential windows in three-electrode electrochemical cells using saturated aqueous NaCl as an electrolyte. A symmetrical supercapacitor (SSC) was then manufactured to evaluate the practical application of the BG/BDD electrode. The BG/BDD-based device operates at a high voltage of 3.2 V. The SSC provides a **high energy density of 79.5 Wh/kg** with a specific power of 221 W/kg and a **high specific power of 18.1 kW/kg** with an energy density of 30.7 Wh/kg. It also retains 99.6% of its specific capacity in the range of 0–2.5 V. Therefore, this ECSC has a significant advantage in stability at high operating voltages.

Thus, it has been shown that supercapacitors using boron doping of graphenes have high electrochemical characteristics.

In the study [70], a one-step method was implemented for manufacturing various electrodes from graphene oxide doped with S, N, and Cl heteroatoms as electrode materials for high-capacity supercapacitors. X-ray photoelectron spectroscopy has revealed the formation of $-ClO_2$, $-ClO_3$, $-SO_x$ (x:2, 3) and $-NO_2$ groups in graphene oxide-based electrodes. The detailed mechanisms of formation of these groups are investigated. Graphene oxide electrodes doped with sulfur, nitrogen, and chlorine were used as electrode materials for supercapacitors. The capacitances of graphene oxide electrodes doped with -S, -N, and -Cl were determined to be 206.4, 533.2, and 1098 mF/cm^2, respectively, at a current density of 10 mA/cm^2.

In [71], the stability and electrochemical properties of graphene doped with B, N, P, and S atoms were investigated. The B, N, P, and S atoms bind strongly to graphene, and all the studied systems exhibit metallic behavior. While graphene with large SSA can increase the capacity of EDL, its low quantum capacity limits its use in supercapacitors. This is a direct result of the limited density of states near the Dirac point in the original graphene. It has been established that the doping of N and S with one vacancy has a relatively stable structure and a high

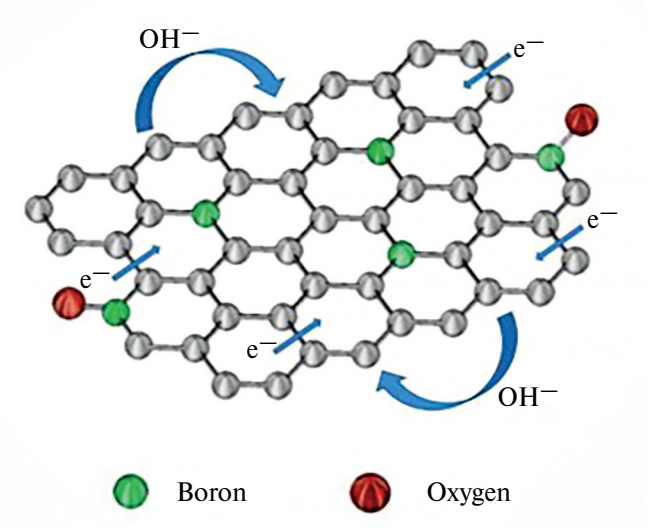

Fig. 6. Schematic representation of the molecular structure of graphene aerogel doped with boron (B-GA) [68].

quantum capacity. It is assumed that such electrodes can be used as ideal electrodes for symmetrical supercapacitors. The advantages of some codoped graphene systems have been demonstrated by calculating the quantum capacity. It was found that graphene doped with N/S and N/P with one vacancy is suitable for asymmetric supercapacitors. The increased quantum capacity contributes to the formation of localized states near the Dirac point and/or shifts in the Fermi level due to the introduction of a doping and vacant complex. Fig. 7 shows a Ragone diagram for symmetrical BG/BDD-based ECSCs and other graphene-based ECSCs studied. As we can see, high characteristics were obtained in [71].

1.3. Methods for obtaining reduced graphene oxide

Obtaining high-quality graphene-like structures and materials in an environmentally friendly way is still difficult to achieve. Recent studies have shown that laser irradiation of the corresponding precursors represents great potential and versatility for the realization of high-quality graphene-like materials at low cost. [72] presents a detailed study of the laser transformation of homogenized dried Corinthian raisins (Vitisvinifera L., var. Apyrena) into graphene-like material. This is a one-step process, as the conversion of raw materials from biomass takes place in the environment. Diffraction, Raman scattering, and electron microscopy have shown that the structure of the laser-irradiated product differs significantly from that of graphite carbon. XPS analysis shows a very high C/O ratio of 19 after decomposition of the crude biomass. The combination of the turbostratic structure and the almost complete removal of oxygen forms leads to an ultra-low resistance,

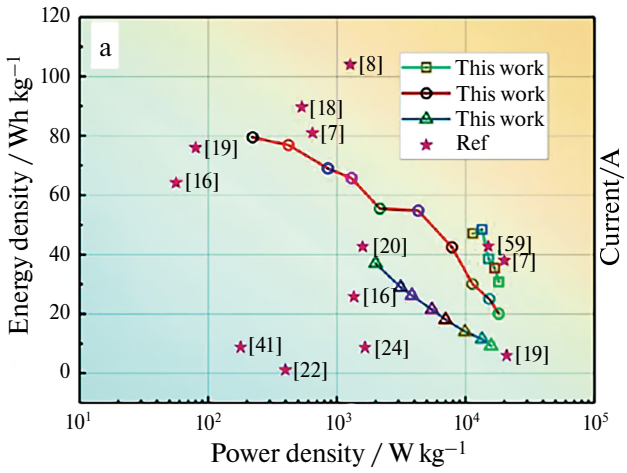

Fig. 7. Ragone diagram for symmetrical BG/BDD-based ECSCs and other graphene-based ECSCs studied [71].

which confirms the successful modification of the raw material to a graphene-like structure with a high degree of sp hybridization. An additional advantage of this approach is that this process can induce both the growth of graphene-like structures on the irradiated target and produce high-quality graphene-like powders. The latter were used to prepare electrodes for symmetrical supercapacitors, which demonstrate higher performance compared to graphene-based supercapacitors prepared by other laser methods.

[73] reports on the simultaneous exfoliation and reduction of graphene oxide (GO) and graphene nanolayers (GNPs) by rapid microwave irradiation in order to overcome the obstacles associated with low electrical conductivity and a tendency to re-aggregation, as well as realize their full potential as materials for supercapacitor electrodes. Morphological studies revealed the porous structure of microwave graphene oxide (MW-GO) and microwave graphene nanolayers (MW-GNPs), which showed the exfoliation of graphene-based materials. The supercapacitor was manufactured using a mixture of MW-GO, MW-GNP and polypyrrole and showed a specific capacity of 137.2 F/g during cycling, stability of 89.8% after 1000 charge/discharge cycles.

In [74], graphene was obtained by irradiating graphite oxide dissolved in an aqueous electrolyte with an excimer laser at various laser energies and irradiation times. The morphology and structure of laser-reduced graphene were characterized using scanning electron microscopy, small-angle X-ray diffraction (XRD), and X-ray photoelectron spectroscopy. The results of X-ray diffraction confirm that deoxygenation of graphite oxide layers occurred almost completely for all laser irradiation conditions used. Graphene obtained by this method is a chaotically aggregated, crumpled, disordered and fine sheet-like solid material. Graphene recovered by a laser was used as the electrode active material for supercapacitors, and its specific capacity was evaluated in a two-electrode cell with an aqueous solution of 0.5 M Na_2SO_4 or in 1 M electrolyte based on tetraethylammonium tetrafluoroborate acetonitrile. It has been established that the specific capacity of graphene produced using a laser depends on the energy and time of laser irradiation. The highest specific capacitance was determined to be 141 F/g at 1.04 A/g and 84 F/g at 1.46 A/g in aqueous electrolytes and electrolytes with ACN (acetonitrile), respectively. Comparing the characteristics of graphene-based supercapacitors is difficult due to the variety of methods for obtaining materials.

Graphenes obtained by several methods are compared in [75]. These include anodic and cathodic electrochemically expanded graphene, liquid-phase expanded graphene, graphene oxide, reduced graphene oxide, and graphene nanoribbons. The reduced graphene oxide showed the highest capacity of about **154 F/g in 6 M KOH at 0.5 A/g**, which was explained by the influence of functional oxygen-containing groups providing additional pseudo-capacity. However, the storage capacity was poor due to low conductivity. In comparison, anodic electrochemically expanded graphene showed a capacity of about 44 F/g and demonstrated excellent capacity retention due to its higher conductivity. These results highlight the importance of matching the graphene production method to a specific application. For example, graphene oxide and anodic electrochemically expanded graphene are best suited for high-energy and high-power ECSC applications, respectively.

Graphene synthesis often involves the use of toxic chemicals that threaten the environment. Due to the recent shift due to the recent shift in focus to to the synthesis of nanomaterials from agricultural waste due to their easy accessibility, cost-effectiveness, and, most importantly, environmental friendliness, [76] presented for the first time a new and "green" synthesis of multilayer graphene layers using pomegranate peel as a precursor at a low temperature of 80 °C. Surface morphology and microstructural properties were determined using transmission electron microscopy (TEM), energy dispersive X-ray spectroscopy (EDX), X-ray diffraction (XRD), Fourier Transform Infrared spectroscopy (FTIR), UV-visible spectroscopy (UV-Vis), and electrical properties were determined by Hall effect measurements. The supercapacitor was also investigated using cyclic voltammetry (CV), galvanostatic charge-discharge cycling (GCD) and electrochemical impedance spectroscopy (EIS). The resulting

supercapacitor provided a capacity of 3.39 mF/cm^2 at a current density of 15.6 μA/cm^2, which makes such graphene a good material for electrochemical storage devices.

In [77], a simple and economical method of manufacturing water-soluble graphene layers using coal is reported. The synthesized carbon graphene (CDG) layers were characterized by X–ray diffraction (XRD), high-resolution transmission electron microscopy (HRTEM), field emission scanning electron microscopy (FESEM), Raman infrared (FTIR) with Fourier transform (FTIR), ultraviolet visible (UV-vis) spectroscopy, and photoluminescence (PL). The presence of marginal oxygen functions in CDG sheets leads to the induction of fluorescent properties. To determine the electrochemical properties of CDG, measurements of cyclic voltammetry (CV), charge-discharge, and electrochemical impedance spectroscopy (EIS) in various electrolytes were performed. The value of the CDG specific capacitance in 1 M Na_2SO_4 turned out to be **277 F/g** at a scan rate of 5 mV/s. CDGs demonstrate stability over long cycles, i.e. the value of the specific capacitance remains at ~91% after 2000 cycles at a current density of 10 mA/g.

Given the non-biodegradable nature of plastic, its recycling is crucial to ensure effective waste management and resource conservation. [78] reports on a low-cost and environmentally friendly method of recycling plastic waste to produce a large number of graphene nanolayers (GN) using a two-stage pyrolysis process. To analyze the usefulness of GNs synthesized by this method, their capacitive behavior with various current sinks was studied, such as copper tape (CuT), indium tin oxide (ITO) glass, graphite sheet (GS) and aluminum sheet (AlS) in PVA (polyvinyl alcohol)-H_3PO_4 in a gel electrolyte. The results obtained confirm that the AlS current collector provided the highest specific capacity of 38.78 F/g. Thus, the present study shows a cost-effective option for achieving a closed-loop economy by recycling plastic waste using energy storage systems.

[79] reports on processing plastic waste into graphene nanolayers (GN) and their subsequent use in dye-sensitized solar cells (DSSC) and supercapacitors. Bentonite nanoclay was used as an agent for the decomposition of plastic waste using two-stage pyrolysis methods at 450 and 945 °C in an inert N_2 atmosphere to produce GN. The presence of GN with a small number of layers was confirmed by Raman spectroscopy, XRD and HRTEM. In addition, IR Fourier and EDX analyses were also performed to identify and quantify functional groups in GN. The use of GN as the material of the active layer of the supercapacitor electrodes provided a **high specific capacity of 398 F/g** at a sweep rate of 0.005 V/s. The supercapacitor also showed **significant energy and power densities of 38 Wh/kg and 1009.74 W/kg**, respectively. Thus, this method has shown the benefits of recycling plastic waste to preserve the environment and high electrochemical characteristics.

Many types of agricultural waste can be considered as an abundant and inexpensive carbon source for large-scale production of graphene-type materials. It was shown in [80] that widely available coconut waste can be efficiently converted to reduced graphene oxide by a simple catalytic process using ferrocene as an efficient and inexpensive catalyst. The structure and morphology of the manufactured materials were characterized by XRD, SEM, and TEM methods. The results obtained confirmed the formation of high-quality reduced graphene oxide. It was found that this material showed high ECSC performance and excellent cyclic stability. Thus, reduced graphene oxide, obtained in a simple, environmentally friendly way from this type of agricultural waste, may be a good candidate for the role of supercapacitor electrodes.

Wood, as a type of biomass materials, has potential application value in many aspects. In [81], a composite material made of carbonized graphene oxide@PVA (CWCC-rGO@PVA) with a high specific capacity, high flexibility, deformability, and the ability to generate electricity from the environment using carbonized wood cell chamber (CWCC) as a base was designed and manufactured. GO, as an intermediate, binds to CWCC in the form of C–C bonds, and the resulting CWCC-rGO intermediate combines with PVA (polyvinyl alcohol) to form hydrogen bonds. The resulting final hybrid is CWCC-rGO@PVA demonstrates high electrochemical characteristics, including a high specific capacity of **288 F/g**, a capacity retention of 91%, an energy density of **36 Wh/kg** and a power density of **3600 W/kg**.

In [82], the design and assembly method of nanocellulose-graphene composite materials used for flexible supercapacitors are considered. Mechanical flexibility, specific capacity, electrochemical characteristics, cyclic stability, renewability and biodegradability are taken into account in order to evaluate the characteristics of composite materials and better evaluate the advantages of this material.

The article [83] describes a new technique for producing high-density graphene flakes (HDGF) for high-performance supercapacitors. HDGF are produced by crushing into small pieces of a thermally reduced graphene oxide film. The high packing density, as well as the rapid transfer of electrons and ions, were achieved simultaneously by disrupting the continuity of the graphene film while maintaining

its dense structure. The manufactured HDGF had a high gravimetric capacity **(237 F/g)** and a volumetric capacity of **261 F/cm**^{3}, as well as excellent cycle stability with 98% of the initial capacity after 10,000 cycles. In addition, a symmetrical supercapacitor using HDGF as electrode materials can obtain a volumetric capacity of up to 16 Wh/l with a power density of 88 W/l in an aqueous system. This strategy provides a new way to develop high-volume supercapacitors for energy storage in the future.

Miniaturization of energy storage is crucial for the development of next-generation portable electronic devices. Microsupercapacitors (MSCs) have great potential to work as embedded micro-power sources and energy storage devices that complement batteries and energy harvesting systems. Scalable production of materials for supercapacitors using cost-effective and high-performance processing methods is crucial for the widespread use of MSCs. It was reported in [84] that wet-jet milling of graphite makes it possible to increase the production of graphene as a material for supercapacitors. The formulation of water-based/alcohol-based graphene ink makes it possible to screen print flexible MSCs that do not contain metals. These MSCs have a surface capacity of up to 5,296 mF/cm^2 for one electrode, which corresponds to a very high volumetric capacity of 1,961 F/cm^3. Screen-printed MSCs can operate at a power density of more than 20 MW/cm^2. The devices demonstrate excellent resistance to charge-discharge cycles (10,000 cycles), bending cycles (100 cycles with a bending radius of 1 cm) and folding (up to 180° angles).

Recently, printing technologies have become promising methods for manufacturing electrochemical energy storage devices (ECSD), while newly developed printers have significantly improved printed electrodes due to lower cost, easier preparation, higher productivity, and improved electrochemical and mechanical properties. In [85], an overview of printing technologies for the production of ECSD is presented and the main attention is paid to graphene-based materials. Inkjet, aerosol, screen, roll and 3D printing were considered, the latest literature was reviewed, illustrative examples of the technical application of printing technologies for energy storage and electrochemical characteristics were presented.

2. COMPOSITES WITH GRAPHENES

2.1. Composites with metal oxides

Graphene composites with transition metal oxides, as a rule, have high electrochemical characteristics due to both the effective characteristics of graphene and the pseudo-capacitance properties of transition metal oxides [41, 86–137]. Metal oxides are common materials for supercapacitor electrodes, demonstrating high energy and power density, as well as long service life. In composites, graphene and metal oxides have demonstrated a combination of high cyclic stability of graphene and high capacity of metal oxides, which significantly improve the complex properties of nanocomposites. In [41], modern developments of graphene composites with metal oxides (MGr) (and nitrogen doping) in the field of electrochemical capacitors are highlighted, taking into account their synergetic properties. It is shown that MGr composites, in comparison with individual materials, have achieved a significant increase in the speed, capacity and stability of cycling. An overview of the characteristics, approaches to the preparation and application of graphene (Gr) is presented. The mechanism of implementation of various types of electrochemical capacitance is described in detail. Finally, the future prospects and problems of MGr composites for energy storage were discussed.

In the study [86], a metal current-removing film was deposited on a flexible substrate in the form of a microgrid by selective laser sintering of silver nanoparticles. The specific capacity was 5.8 mF/cm^2 at 1.5 mA/cm^2 with the electrolyte PVA-H_3PO_4. Then, electrodeposition of manganese dioxide (MnO_2) nanoparticles was carried out, which further increased the capacity to 49.1 mF/cm$_2$ at 1 mA/cm$_2$ in 0.5 M Na_2SO_4. As a result, the capacity reduction remained below 10% for 10,000 charge/discharge cycles.

In [87], a new approach was presented to the creation of electrodes with a hierarchical structure that allows supercapacitors to maintain their capacity under mechanical deformation. The electrodes are manufactured first by growing vertical graphene nanolayers (VGN), and then by depositing manganese dioxide (MnO_2) on plastic nickel wires. Two such electrodes are used to make a symmetrical supercapacitor using a solid-state electrolyte containing carboxymethylcellulose and sodium sulfate. This supercapacitor achieves a high capacity of up to 56 mF/cm^2, a high energy density of 7.7 MWh/cm^2 and a high power density of 5 MWh/cm^2. These exceptional properties are due to the synergy between the VGN and MnO_2, where the highly porous VGNs fulfill the important function of a mechanically robust platform with a large surface area that allows the application of a pseudo-high-capacity MnO_2 material. Supercapacitors made from these electrodes can be shaped into different forms by bending and twisting with little loss of performance. The promising results presented in this study open up

a new path for manufacturing high-performance energy storage devices for wearable electronics and wireless communications.

In [88], electrodes were created from carbon fiber (CF) modified with vertically oriented graphenes (VG) and manganese dioxide (MnO_2), as well as with nitrogen doping. The results show that the hybridization of VG and MnO_2 creates a significant synergistic effect, leading to an increase in the surface capacity of the electrode. This synergistic effect is explained by the double effect on VG increase in effective surface area and electrical conductivity, which provide a better distribution of MnO_2, as well as a highly conductive network. A supercapacitor based on a CF/VG/MnO_2 hybrid electrode and a polymer electrolyte has a specific capacity per surface area of 30.7 mF/cm_2, an energy density of 12.2 MW/kg, and a power density of 2210.3 MW/kg. In addition, the mechanical characteristics demonstrate a tensile strength of 86 MPa and a bending strength of 32 MPa for this supercapacitor design.

Work [89] is devoted to the production of composite thin films of manganese dioxide (MnO_2)/graphene oxide (GO) doped with silver (Ag) and nitrogen. A BET study showed that MnO_2–Ag_3/GO nanosheets have a specific surface area of 192 m_2/g. A specially defined morphology in the form of a flower and interconnected nanolayers of MnO_2–Ag_3/GO electrodes made it possible to achieve high electrochemical characteristics. The maximum specific capacity of **877 F/g** at a scanning speed of 5 mV/s was obtained for the MnO_2–Ag_3/GO electrode tested in 1 M Na_2SO_4 with 94.57% capacity retention after 5000 cycles. A flexible solid-state symmetrical supercapacitor based on MnO_2Ag_3/GO composite produced a specific energy of **57 Wh/kg** with a specific power of **1.6 kW/kg** and maintaining 94% capacity after 10,000 cycles.

In [39], CuMnO nanocrystals and a composite CuMnO/graphene quantum dot (GQD) (with phosphorus doping) were synthesized by the hydrothermal method, and they were used to create a new type of supercapacitor. GQDs have been applied to increase the specific capacity and increase the efficiency of the supercapacitor. As you know, a quantum dot is a fragment of a conductor or semiconductor whose charge carriers are limited in space in all three dimensions. The size of a quantum dot is so small that the quantum effects are significant. Various methods were used to identify the synthesized nanocomposite and study its morphology, structure, and surface area. Cyclic voltammetry (CV) and electrochemical impedance spectroscopy (EIS) were used to record and track the electrochemical behavior of the synthesized nanocomposite used as an electrode material. A study of changes in the capacitance of CuMnO/GQD and $CuMnO_2$ electrodes during 5,000 consecutive charge/discharge cycles showed that the stability of the nanocomposite electrode is higher and its capacity after this number of cycles reaches 83.3%, while the capacity of the electrode made of CuMnO nanoparticles reaches 65.4% of the initial one. The specific capacity of the CuMnO/GQD nanocomposite and CuMnO nanoparticles at a current density of 1 A/g was 520.2 and 381.5 C/g, respectively. The maximum specific energy of the asymmetric supercapacitor SIMPO/GQD/AC, obtained with a specific power of 1108.1 W/kg, is equal to a large value of **47.9 Wh/kg**. The capacity of the asymmetric supercapacitor decreased by only 13.3% after 5,000 charge and discharge cycles, which is a very good service life compared to similar materials. All these results indicate that the CuMnO/GQD nanocomposite can be considered as a possible option for a high-speed and stable supercapacitor.

Miniature graphene-based supercapacitors obtained by laser conversion of suitable precursors have recently attracted attention for the production of small-sized energy storage devices. In [90], LightScribe technology was used to perform single-chamber synthesis of TiO nanoparticles embedded in porous graphene-based electrodes by converting precursor materials by absorbing infrared laser irradiation. Improved electrochemical characteristics of supercapacitors have been achieved by combining Faraday reactions occurring with metal oxide nanoparticles with conventional EDL charging occurring in porous graphene. Microsuperapacitors consisting of TiO-graphene electrodes were tested using two hydrogel polymer electrolytes based on polyvinyl alcohol/HPO and polyvinyl alcohol/HSO, respectively. In devices based on TiO-graphene, a specific capacity of up to 9.9 mF/cm^2 has been obtained, which corresponds to a volumetric capacity of 13 F/cm3 and doubles the characteristics of graphene-based supercapacitors. The microsupercapacitors have achieved specific surface energy and specific surface power of 0.22 and 39 μW/cm^2, as well as a cycle capacity of more than 3,000 cycles. These high results suggest that laser-produced TiO graphene nanostructures are excellent candidates for microsupercondensors for environmentally friendly, large-scale, and low-cost applications. Fig. 8 shows a change in capacitance over 3,000 charge-discharge cycles at a current of 5 mA/cm^2 for microsupercondensors developed in [90].

[91] demonstrates a simple method for obtaining a functionalized spongy graphene nanocomposite/titanium dioxide (FG-$HTiO_2$) hydrogenated from nanotubes, doped with boron (in the form

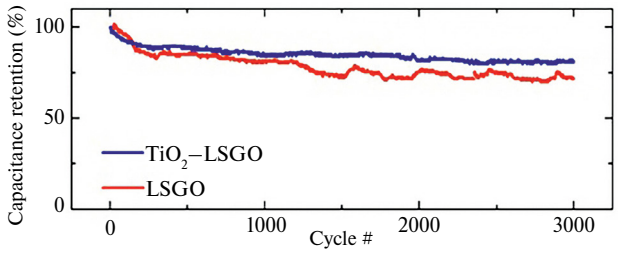

Fig. 8. Capacitance change over 3000 charge-discharge cycles at a current of 5 mA/cm^2 for microsupercondensors developed in [90].

of interconnected, porous 3-dimensional (3D) network layers. This 3D network structure provides better contact at the electrode/electrolyte interface and accelerates the kinetics of charge transfer. The manufactured FG-TiO_2 composite was characterized by X-ray diffraction (XRD), IR Fourier, scanning electron microscopy (FESEM), Raman spectroscopy, thermogravimetric analysis (TGA), absorption spectroscopy, and transmission electron microscopy (TEM). The synthesized materials were evaluated in relation to their use in 0.5 MH_2SO_4 supercapacitors using cyclic voltammetry (CV) at various potential scanning speeds and galvanostatic charge/discharge tests at various current densities. The FG-$HTiO_2$ electrodes showed a maximum specific capacity of **401 F/g** at 1 mV/s. The energy density was **78.66 Wh/kg** at a power density of 466.9 W/kg at 0.8 A/g.

[92] describes a simple and binder-free technique for obtaining layered double hydroxides of β-$Ni(OH)_2$/Nickel-cobalt (β-$Ni(OH)_2$/NiCo) in combination with graphene modified with fluorine (FG) as a supercapacitor electrode. Electrodes (β-$Ni(OH)_2$/NiCo) were obtained by the hydrothermal method by synchronous electrochemical stratification of graphite into fluor-modified graphene and the use of a composite (β-$Ni(OH)_2$/NiCo). This hybrid structure (β-$Ni(OH)_2$/NiCo) of modified graphene as a supercapacitor electrode demonstrates high conductivity, rapid ion diffusion, and high mechanical strength. As a result, the β-$Ni(OH)_2$/NiCo@FG electrode has a very high capacity (3996 mF/cm^2 at 1 mA/cm^2), high speed capability and extended service life. β-$Ni(OH)_2$/NiCo in combination with undoped electrochemically stratified graphene demonstrates significantly improved cyclic stability (79% capacity retention after 1000 cycles at a current of 5 mA/cm^2), surpassing that of β-Ni(OH). Thus, this technique has great potential to improve the performance of electrodes.

[93] reports on the simple synthesis of porous graphene-NiO (PGNO) nanocomposites using a unique system of mixed solvents using a solvothermal approach. Microscopic characterization of porous graphene (PG) shows the presence of pores in graphene sheets; NiO (NO) shows a scaly structure, and the PGNO composite shows the fixation of NO nanocapsules on PG sheets. A series of electrode materials were obtained by varying the percentage of PG (and the materials were designated as 5–30 PGNO, respectively). An electrochemical study showed **a high capacitance value of 511 F/g** at a scan rate of 5 mV/s for a 10 PGNO composite in the 3-electrode method and 80% retention of the initial capacitance after 10,000 cycles at a current density of 8 A/g. The manufactured symmetrical hybrid supercapacitor using PGNO electrodes also showed a good capacity value of 86.0 F/g at a sweep speed of 5 mV/s. The manufactured device retained 84% of the initial capacity at the end of 10,000 cycles at a current density of 8 A/g, demonstrating good electrochemical stability and high-speed ability of the material. The percentage contribution of the EDL capacity and pseudo-capacity to the total specific capacity of the PGNO supercapacitor was also estimated.

Graphene oxide (GO) nanosheets, as well as two-dimensional $Ni(OH)_2$ with very good uniformity were obtained by the Hammers method and the hydrothermal method, respectively [94]. $Ni(OH)_2$ nanosheets treated with cationic surfactants and graphene oxide with negative charges were mixed with each other by electrostatic self-assembly. After annealing, hybrid two-dimensional nanosheets of reduced graphene oxide NiO-(NiO-rGO) were obtained. Due to the synergistic effects, the NiO-rGO electrode has optimized electrochemical characteristics, unlike pure NiO or rGO. The results show that NiO nanosheets are uniformly dispersed on the surface of rGO nanosheets, and a hybrid electrode with NiO-rGO nanosheets can provide a **high capacity of 343 C/g (at 1 A/g)**. In addition, electrodes consisting of NiO-rGO nanosheets were used to assemble a symmetrical supercapacitor. The energy density of the manufactured supercapacitor device can reach 5.4 Wh/kg at a power density of 0.43 kW/kg when operating in the voltage range 0–1.4 V. In addition, the symmetrical supercapacitor also demonstrates excellent capacity retention at 90% after 10,000 cycles (10 A/g).

In [95, 96], composite structures made of nickel-cobaltite/graphene (NiCo O/GQD) were studied, which exhibit increased electrical conductivity and function as electrode materials with a higher energy density compared to GQD (graphene quantum dots) and NiCoO. The electrochemical characteristics of the NiCoO/GQD composite were obtained by galvanostatic charge-discharge method for three-electrode systems with 0.1 M potassium hydroxide electrolyte. It was found that

the observed specific capacitance for the composite is a large value of **481.4 F/g** at 0.35 A/g. This is higher than that of graphene quantum dots (GQD) (45.6 F/g) and is associated with increased electrical conductivity and diffusion of ions, which move faster between the electrodes and the electrolyte. These results demonstrate the unique characteristics of the manufactured composites as promising electrode materials for use in supercapacitors.

The $W_{18}O_{49}$ nanocomposite with reduced graphene oxide (rGO) from nanowires (NW) is considered in [97] as a new active material for supercapacitor electrodes. It demonstrates high specific capacity and excellent speed characteristics in $AlCl_3$ aqueous electrolyte. Electrochemical studies show that the presence of rGO accelerates the diffusion of Al^{3+} ions in the nanocomposite, thereby providing more ions for the intercalation pseudo-capacity. The manufactured asymmetric supercapacitor $W_{18}O_{49}$NWs-rGO//rGO demonstrates a **high specific capacity of 365.5 F/g at 1 A/g** and excellent cyclic stability while maintaining 96.7% capacity at 12,000 cycles. It is important to note that it provides a **high energy density of 28.5 Wh/kg at a power density of 751 Wh/kg**, which is the highest energy density value for all known devices based on the $W_{18}O_{49}$ supercapacitor.

In [98], multilayer graphene films uniformly coated with a thin layer of V_2O_5 (graphene/V_2O_5 composite) were obtained by combining laser reduction and low-temperature atomic layer deposition. To test the effect of crystallinity on the electrochemical characteristics of the graphene/V_2O_5 composite, high-temperature annealing was first performed, followed by a detailed comparative study of the amorphous and crystalline coating of the composite. It has been shown that graphene coated with amorphous V_2O_5 can provide higher performance of a supercapacitor electrode (i.e., specific capacity, energy density, and cyclic stability) than its crystalline counterpart.

In [30], vanadium pentoxide (V_2O_5) was grown on graphene using the microwave method, which is simple, fast, energy-saving, and efficient. Thanks to this method of microwave synthesis, homogeneous V_2O_5 nanoparticles with a size of about 20 nm are evenly distributed over graphene. The resulting V_2O_5/graphene composite was used in symmetrical supercapacitors, showing specific capacitance of **673.2 and 474.6 F/g at 1 and 10 A/g**, respectively, and retention of 96.8% capacity after 10,000 cycles at 1 A/g. In addition, supercapacitors have demonstrated high energy and power density characteristics (**46.8 Wh/kg at 499.4 W/kg and 32.9 Wh/kg at 4746.0 W/kg**), which outperform many similar devices.

Metal oxide nanoparticle (MONP)-graphene composites are highly valuable candidates as electrode materials for electrochemical supercapacitors (ECCS). In [99], the development of a universal approach to the manufacture of ECSC electrodes by impregnating MONP (M = Ti, Ni, Sn) synthesized by laser ablation in liquid on laser-induced graphene (LIG) was described. A typical SnO_2/LIG microsupercapacitor (MSC) provides a specific capacity of 18.58 mF/cm^2 at a scanning speed of 10 mV/s, which is 5.2 times higher than that of an unmodified LIG. In addition, the microsupercapacitor (MSC) demonstrates long-term cyclic stability (retains 82.15% of specific capacity after 5,000 cycles) and good mechanical flexibility (specific capacity decreases by 5% at a bending angle of 150°). MONP and LIG are manufactured using the same laser processing system, without the use of chemical ligands or reducing agents in the synthesis process, which is a cost-effective and environmentally friendly method. This simple and straightforward method provides a highly efficient solution for large-scale MSCs manufacturing.

In [100], nanocomposites of reduced graphene oxide/lanthanum oxide were obtained. The reduced graphene oxide with a large specific surface area was successfully doped with lanthanum oxide. The reduced graphene oxide/lanthanum oxide composites were manufactured as an electrode material for a supercapacitor, which demonstrated a significant specific capacity of 156.25 F/g at a current density of 0.1 A/g and high cycling stability. The material retains 78% of its original charge-discharge efficiency after 500 cycles. The high electrochemical characteristics of the composite material may be associated with the deposition of lanthanum oxide nanoparticles on the surface of the reduced graphene oxide, which increase the effective conductive area of the reduced graphene oxide and the contact area between the electrolyte and graphene. Graphene and lanthanum oxide composites can significantly improve the stability and electrical characteristics of supercapacitors and have great potential for chemical sensors, microelectronics, energy storage and conversion.

In [101], a hybrid type of energy storage device is presented, consisting of electrodes based on a composite of graphene and zinc oxide plates. This composite exhibits both the electrochemical characteristics of a supercapacitor with a high power density and a battery with a sufficiently high energy density compared to each individual material. The improved characteristics of the hybrid correlated with the structure of the electrodes. To improve the electrochemical characteristics of supercapacitors,

it is necessary to have a well-defined mass, shape and surface area of the electrode materials. In this work, the original design of the mounting device was presented, which makes it possible to accurately determine all the critical parameters of the electrode materials: specific mass and surface area. With the initial installation, a supercapacitor device was created that could also act as a battery due to its high energy density values, which is why it was named *superbat*. In this work, 3D graphene foam was used as the first electrode due to its large surface, while ZnO nanocrystals were used for the second electrode due to their defective structure. A high specific capacitance value of **448 F/g** was obtained, which was associated not only with the quality of synthesis, but also with the choice of electrode and electrolyte materials. Moreover, each component used in the design of the hybrid supercapacitor also played a key role in achieving a high capacity value. The results demonstrated the high performance and stability of the device.

In [102], $Ni3Si_2$/NiOOH composites/graphene nanostructures were synthesized by chemical deposition from the gas phase at low pressure. In a carbon-rich atmosphere, high-energy atoms bombarded the surface of Ni and Si and reduced free energy during thermodynamic equilibrium of Ni-Si solids, significantly catalyzing the growth of Ni-Si nanocrystals. Electrochemical measurements have shown that these nanostructures have an **ultrahigh**

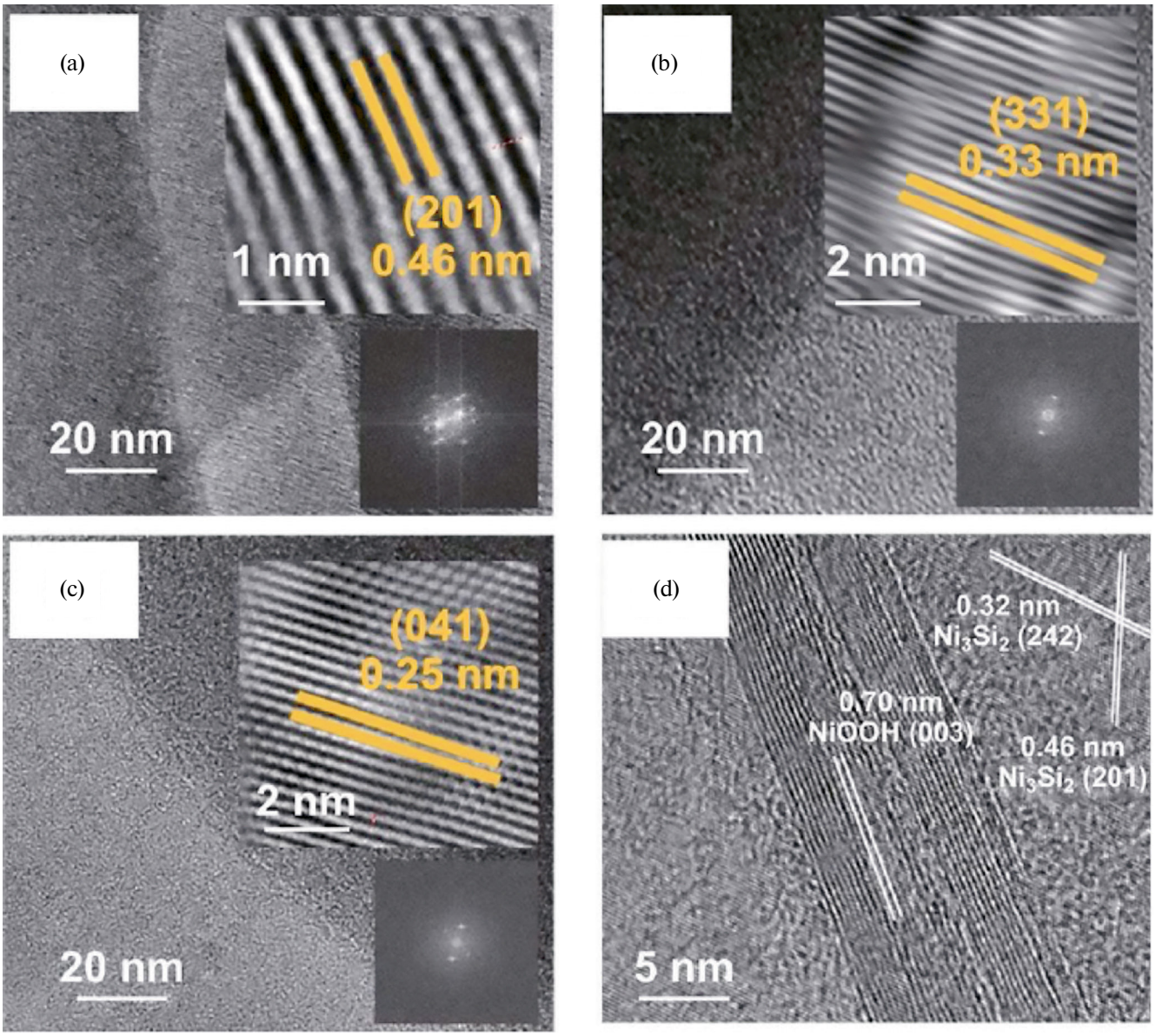

Fig. 9. TEM images of Ni_3Si_2/NiOOH/graphene nanostructures obtained in [102].

specific capacity of 1193.28 F/g at 1 A/g. When integrated into a solid-state supercapacitor, it provides a high energy density of up to **25.9 Wh/kg at a power density of 750 W/kg**, which can be attributed separately to the Ni3Si2/graphene skeleton, which provides high power, as well as to NiOOH in an alkaline solution. Fig. 9 shows TEM images of Ni_3Si_2/NiOOH/graphene nanostructures obtained in [102].

In [113], positive electrodes without a binder were produced by electrochemical deposition, in which nanorods (CuONRs) grown directly on copper foam (CF) are decorated with bimetallic cobalt-zinc-sulfide (Co-Zn-S NAs) nanomatrices. The manufactured Co-Zn-S@CuO-CF composites have a very high specific capacity of **317.03 mAh/g at 1.76 A/g**, as well as very good cyclic stability (retention of 113% after 4,500 cycles). The negative electrodes were additionally manufactured by direct deposition of iron sulfide (Fe-S NSs) nanosheets graphene oxide (GO), showing a remarkable specific capacity of **543.9 F/g at 0.79 A/g**. Having the advantages of obtaining high values of specific energy and specific power (**25.71 Wh/kg and 8.73 kW/kg**) along with acceptable stability, the manufactured asymmetric supercapacitor is very promising.

[104] describes the manufacture of flexible microsupercondensators (MSCs) based on hybrid materials from single-walled carbon nanotubes (SWCNs) with laser-induced graphene fibers (LIGF) decorated with manganese dioxide (MnO_2) nanoparticles. SWCNs are applied to the surface of LIGF and the space between them, which can bind LIGF to form more conductive pathways and provide more active areas for the growth of MnO_2 nanoparticles. Due to the synergistic effect between the LIGF conductive network of single-walled nanocarbon nanoparticles and MnO_2 nanoparticles with high theoretical capacity, the obtained flexible MSCs based on LIGF-C4/MnO_2 hybrid electrodes provide a high capacity of 156.94 mF/cm^2, which is about 8 times higher than that of MSCs based on LIGF-MnO_2 (20 mF/cm_2). In addition, LIGF-C4/MnO_2 also exhibit significant specific energy of 21.8 MWh/cm_2, long-term cycling stability, significant modular integration, and very high mechanical flexibility (with 90.5% capacity retention after 1,200 bending cycles). Thus, the design of hybrid electrode materials proposed in this paper provides a simple and novel method for the development of flexible energy storage devices with high performance characteristics, which opens up great prospects for use in wearable electronics. Thus, it has been shown that supercapacitors using graphene composites with metal oxides have high electrochemical characteristics.

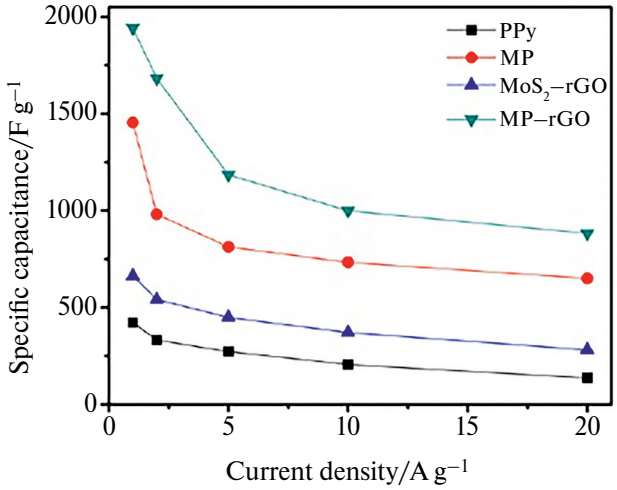

Fig. 10. Dependences of the specific capacitance on the specific current for the samples developed in [106].

2.2. Composites with metal sulfides and selenides

Other types of graphene composites that have been intensively developed recently are composites with transition metal sulfides and selenides. In [105–135], a system of co-dissolution in a deep eutectic solvent (DES) was developed by mixing water and acetonitrile with a typical DES electrolyte consisting of acetamide and lithium perchlorate. The addition of co-solvents not only solves the problems of high viscosity and low conductivity of DES, but also creates some unique properties. For example, the presence of water improves the fire-retardant properties of DES electrolyte. In contrast, the addition of acetonitrile further improves ionic conductivity without compromising the wide window of electrochemical stability (ESW). The effect of the amount of co-solvent in DES and the optimal molar ratio between the co-solvents was investigated. When the molar ratio of acetonitrile to water is 4.4:1, hybrid DES exhibits the best physical properties, including a wide ESW potential window (2.55 V), high conductivity (15.6 mS/cm) and low viscosity (5.82 MPa s). In addition, a series of spectroscopic measurements were performed to understand the interaction between the electrolyte components. On the other hand, the use of a hydrogel consisting of MoS_2 and reduced graphene oxide (rGO) as electrode materials for supercapacitors has been demonstrated. This hydrogel inherited the porous structure of the rGO hydrogel and the high conductivity of MoS_2. Finally, high-voltage symmetrical supercapacitors were manufactured using hybrid DES and hydrogel as the electrolyte and electrode, respectively. The optimized supercapacitor operates at a wide operating voltage range of 2.3 V and reaches a maximum energy density

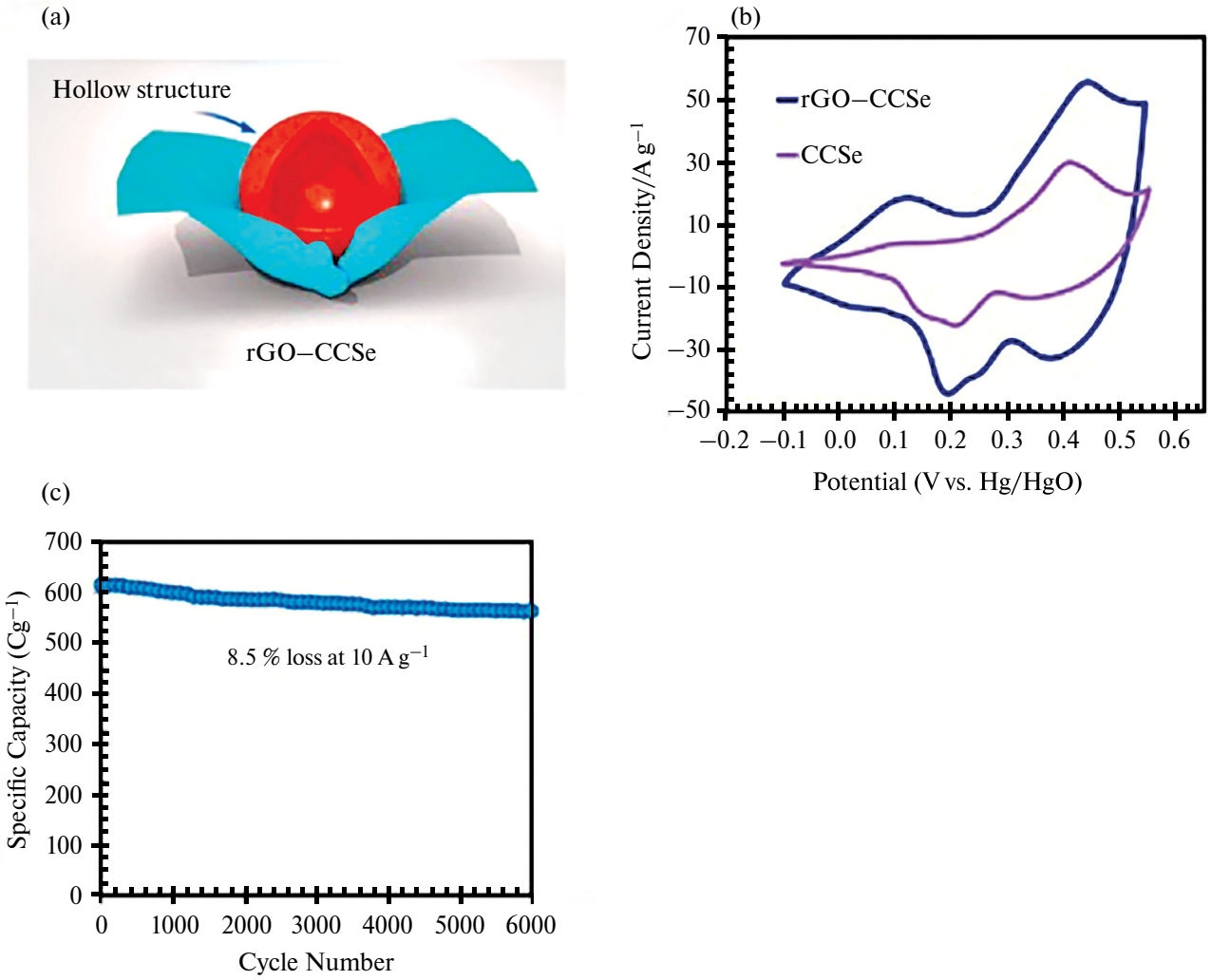

Fig. 11. (a) Schematic formation of hollow structures of cobalt and copper selenide (rGO-CCSe) wrapped in graphene; (b) CVA curves for rGO-CCSe and CCSe; (c) capacity change during rGO-CCSe cycling [109].

of **31.2 Wh/kg at a power density of 1164 W/kg**. In addition, this ECSC has demonstrated the retention of 91% capacity after **20,000 cycles**.

A composite of polypyrrole (PPy) on reduced graphene (rGO) with vertically oriented MoS_2 sulfide was produced in [106] using a single-stage hydrothermal method (MP-rGO). Ultrathin MoS_2 nanosheets mixed with PPy lamellae are well coated with rGO, forming a triple nanostructure. PPy lamellae are formed on rGO using MoS_2 nanosheets as a result of the redox reaction between ammonium tetrathiomolybdate and pyrrole. The conductivity of MoS_2 was effectively increased by using PPy and rGO, and MoS_2/PPy (MP) nanohybride gives MoS_2 low crystallinity, and PPy amorphousness. The MP-rGO electrode has a **high specific capacity of 1942 F/g** (215.8 mAh/g) at a current density of 1 A/g and satisfactory cycling stability. An asymmetric MP-rGO/AC supercapacitor was assembled, which has a **high energy density of 39.1 Wh/kg** with a specific power of 0.70 kW/kg, which confirms its potential use in energy storage. Fig. 10 shows the dependences of the specific capacitance on the specific current for the samples developed in [106].

Cobalt pentlandite (CoS) has lately become a promising electrode material for energy storage devices. A hybrid of CoS and graphene was synthesized by the hydrothermal method [107]. Small-sized CoS flakes are thinly deposited on the surface of the graphene sheet, and an interconnected CoS/graphene structure is obtained. The results of electrochemical tests showed that the CoS/graphene electrode provides a high charging capacity of **540 C/g** for 1 minute and retains 74.5% of the capacity for 14 seconds. The hybrid supercapacitor assembly with an electrode including CoS provides a high energy density of **37 Wh/kg** at a power density of 170 W/kg, and 15.3 Wh/kg can be

maintained even at a high power density of **12 kW/kg**. The very high electrochemical characteristics should be explained by the large number of active centers, improved charge transfer characteristics, and the maximum capacitive contribution of the CoS/graphene electrode.

Nickel selenide and its nanocomposites (nickel graphene selenide; NiSe/G, graphene doped with nitrogen and boron, designated as NiSe/NG and NiSe/BG, respectively) were obtained using the hydrothermal method, and these materials were used for energy storage [108]. These materials were examined using various analytical and morphological methods such as X-ray diffractometry and FESEM analysis. Further, the prepared materials were examined by electrochemical methods such as voltammetry and a controlled potentiostatic test to calculate the capacitance, energy and power density of the manufactured electrode. The electrochemical behavior of graphene nanocomposites of nickel selenide was studied in KOH electrolyte. It was found that NiSe/NG showed a specific capacity of 99.03 F/g at a power density of 0.55 W/kg. The results proved that graphene doping has a synergistic effect.

In [109], a lightweight template method was developed for producing porous hollow copper-cobalt selenide microspheres wrapped in conductive networks of reduced graphene oxide (rGO-CCSe). The synthesized electrode is able to provide significant capacity retention at 91.5% after 6,000 charge cycles due to a well-thought-out structural design and the use of advantages of bimetallic synergy at the atomic level, with a very high specific capacity of **724 C/g at 2 A/g**. In addition, an asymmetric cell was manufactured using an rGO-CCSe hollow microspherical electrode to achieve very high energy densities (**57.8 Wh/kg**). Graphene conductive carrier together with CCSe cubes of battery type create a synergistic effect, which explains such high electrochemical characteristics (Fig. 11*a*). Fig. 11*b* shows that pseudo-capacity makes a significant contribution to the capacity of rGO-CCSe and CCSe. Fig. 11*c* shows that there is a slight decrease in capacitance during cycling of the rGO-CCSe electrode for 6000 cycles [109].

[110] reports on the production of $NiSe_2$ nanoparticles by nitrogen doping of reduced graphene oxide (N-rGO/$NiSe_2$) using a simple two-stage method that includes hydrothermal production of $Ni(OH)_2$ precursor and then solvothermal synthesis of N-rGO/$NiSe_2$ composites with different N-rGO content. The newly prepared N-rGO/$NiSe_2$ composites have been characterized by X-ray diffraction, Raman spectroscopy, high-resolution X-ray photoelectron spectroscopy, autoemission scanning electron microscopy,

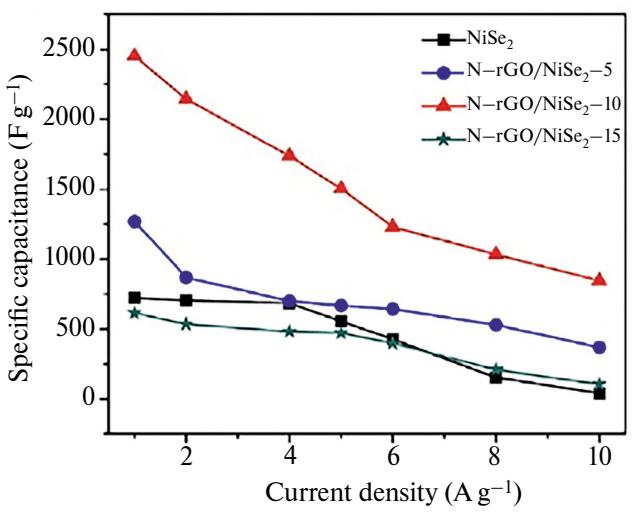

Fig. 12. Dependences of the specific capacitance of the N-rGO/NiSe2 EHSC on the specific current [121].

transmission electron microscopy, energy dispersive X-ray spectroscopy, and BET. The results show that N-rGO acts as a protector of $NiSe_2$ nanoparticles, preventing their aggregation, which leads to an increase in the specific surface area and electrical conductivity of the material. The optimized N-rGO/$NiSe_2$ composite can provide a **very high specific capacitance of 2451.4 F/g at a current density of 1 A/g** (Fig. 12). Using activated carbon (AC) as the negative electrode and an optimized N-rGO/$NiSe_2$ composite as the positive electrode, an asymmetric supercapacitor was created. It operated stably in a potential window of 0–1.6 V and provided a high maximum energy density of **40.5 Wh/kg** at a power density of 841.5 W/kg. In addition, the asymmetric N-rGO/$NiSe_2$//AC supercapacitor demonstrated good cyclic stability (Fig. 12).

Thus, it has been shown that supercapacitors using graphene-selenide composites have high electrochemical characteristics.

2.3. Composites with metal particles

High efficiency in supercapacitors was demonstrated by electrodes based on composites doped with metal particles. In [122], in order to increase the stored energy, defective graphene was doped with Ni nanoparticles. During the first charge cycle in an aqueous electrolyte (3.5 M KOH), it was found that Ni attached to graphene is easily converted into Ni(OH) at the nanoscale. Such a reversible Faraday mechanism led to an increase in the specific capacitance of the electrodes by an order of magnitude, reaching a very high value of **1900 F/g** at 2 mV/s in 3.5 M KOH. An asymmetric supercapacitor was manufactured by coupling a negative electrode made of pure graphene

with a positive graphene electrode decorated with nickel. Such a supercapacitor was successfully cycled in the voltage range 0–1.5 V, reaching a maximum specific energy of **37 Wh/kg and a maximum specific power of 5 kW/kg**. The supercapacitor has shown good reversibility and conservation of 72% of specific energy over 10,000 cycles.

In [123], an electrode was made by producing paper with silver-modified fibers and graphene oxide-modified (GO) fibers, followed by GO reduction. Ag- and GO-modified fibers were obtained by *in situ* growing Ag nanoparticles and self-assembling GO sheets on cellulose fibers, respectively. The Ag-modified fibers act as a flexible current receiver with numerous three-dimensional interconnected electron transport pathways, allowing the recovered GO-modified fibers to be used as electrode materials to achieve high conductivity and high performance. Simple drying can reduce the weight of the supercapacitor by 40% to facilitate transportation and storage, and capacity efficiency can be restored by wetting if necessary.

In [124], an efficient textile-based electrode was successfully obtained by introducing silver nanoparticles (AgNPs) onto the surface of cotton fabric (CF) with reduced graphene oxide (rGO). The CF electrode with Ag/rGO coating showed a high specific capacity of **426±10 F/g** in 0.5M NaOH. Symmetrical supercapacitor cells based on the Ag/rGO/CF composite had a very long service life (126% retention of the initial specific capacity after 1000 charge-discharge cycles) and good speed characteristics. The rGO coating layer gives the electrode excellent electrical conductivity, high power consumption and high DES capacity. At the same time, the chemical coating with silver improves the capacitive properties by increasing conductivity and induces pseudo-capacitance effects. Thus, the favorable synergistic effects of rGO, AgNPs, and the 3D hierarchical CF structure lead to high electrochemical performance. A fully solid-state flexible symmetrical supercapacitor was assembled using this composite fabric. It demonstrated high electrochemical stability under mechanical bending (89% of the initial capacity is retained after 1000 bending cycles) and provided a **high energy density of up to 34.6 Wh/kg** (at a power density of 125 W/kg).

3. COMPOSITES WITH CONDUCTIVE POLYMERS (CPS)

One of the achievements of electrochemistry in the last 25–30 years has been the development of the (CPs). The electronic conductivity of the (CPs) is displayed in the process of its doping with counterions due to the formation of delocalized π-electrons or holes and their transfer under the influence of an electric field through a system of polyconjugated double bonds, which any CP possesses. CP includes: polyacetylene (PAc), polyaniline (PANi), poly- (p-phenylene) (PPh), polythiophene (PT), polypyrrole (PPy), polyporphine (PP) and their derivatives. Since quasi-reversible electrochemical charge-discharge processes can occur in many electronic devices, they are widely used in ECSC [125–150]. CP adds a pseudo-high Faraday capacitance to the total capacity of the composites.

The growing development of flexible and wearable supercapacitors has stimulated the smart electronics industry. Conductive polymer hydrogels are considered the most promising and viable sources for manufacturing flexible supercapacitors, as well as for powering flexible miniature electronic devices. As reported in [127], conductive polymer hydrogels can be synthesized using numerous physical and chemical bonding methods. Conductive polymer hydrogels as electrodes have a combination of high electrical conductivity, outstanding electrochemical characteristics, and unique three-dimensional porous morphology with swelling characteristics, ideal electrolyte interaction, environmental friendliness, strength, and mechanical flexibility. These features make them ideal options for flexible supercapacitors. Conductive polymers such as polypyrrole, polyaniline, and poly (3,4-ethylenedioxythiophene): polystyrene sulfate (PEDOT: PSS) are effective electrode materials for supercapacitors with the aforementioned important properties. These conductive polymers in a composite hybrid with graphene hydrogel are used as electrode materials in highly efficient and stable flexible supercapacitors. Subsequently, these highly efficient flexible supercapacitors will contribute to the development of wearable electronics, as well as environmentally friendly transportation.

Conductive polymers (CPs) have the potential to become next-generation ECSC electrodes due to their low cost, easy synthesis methods, and high pseudo-capacity. Graphene/CP-based composites demonstrate sufficiently high electrochemical characteristics when used as electrode materials for ECSC. Synthesis methods and electrochemical characteristics of graphene/CP composites for ECSC are summarized in [128]. In addition, a method for synthesizing electrode materials to improve electrochemical characteristics is discussed.

In [129], a durable, highly efficient graphene electrode modified with polyaniline was successfully used to assemble the supercapacitor. Graphene is covalently bonded to doped polyaniline (SPANi) and is therefore used in supercapacitors. Layered

graphene modified with 4-aminobenzoic acid (ABF-G) was first attached to aniline functional groups. Aniline, the monomer of o-aminobenzenesulfonic acid, and an oxidizer were then added to the aqueous dispersion of ABF-G to achieve polymerization on the surface of ABF-G. This covalently bonded thin-film electrode material ABF-G (SPANi-ABF-G), modified by SPANi, was then used to manufacture supercapacitors. The supercapacitor with the proposed SPANi-ABF-G electrodes has a **high specific capacity of 642.6 F/g at a current density of 1 A/g**. After testing for a service life of 5,000 cycles, this supercapacitor demonstrated the retention of charging and discharging capacity of 100% and 98.13% at current densities of 1 and 2 A/g, respectively. These capacity retention rates are higher than those of supercapacitors with conductive polymer electrodes. The results obtained prove that electrode materials prepared using covalently bonded graphene and PANi can significantly improve the performance of supercapacitors.

In [130], a graphene-based film (CNT@PANi/rGO/TA) was made from biomass using electroactive tannin (TA), which serves as an adhesive bonding carbon nanotubes to a composite (CNT@PANi) and for bonding with reduced graphene oxide (rGO). Thanks to the thin PANi layer on CNT@PANi, the nanowires intercalate into the intermediate layers of rGO, thereby binding the nanolayers and forming a well-defined porous multilayer structure. The resulting CNT@PANi/rGO/TA film has high mechanical strength (174.6 MPa) and impact strength (9.17 MJ m^3). Meanwhile, the fully solid-state flexible supercapacitor assembly with CNT@PANi/rGO/TA demonstrates a **high capacity of 548.6 F/cm^3** and a very high performance of 70.5% from 1 to 50 A/g. Even at –40 °C, the specific capacity of the supercapacitor is up to 454.9 F cm^{-3}, i.e. approximately 83% of the capacity produced at room temperature.

The review article [131] presents the latest achievements in the field of synthesis, fabrication, and characterization of PANi@r-GO hybrid nanocomposites for supercapacitors. Market data for such ECSCs is also presented.

For the development of highly efficient supercapacitors in [132], the initial PANi and PANi nanocomposites with highly conductive two-dimensional graphene were successfully produced by chemical method. The electrochemical properties of ready-made solid-state supercapacitors, established for initial polyaniline composites (PANi/PVA/PANi) and nanocomposites based on polyaniline/graphene (PANi-graphene/PVA/PANi-graphene), were studied using CVA, galvanostatics, and electrochemical impedance spectroscopy. The electrochemical device based on PANi electrodes has a capacity of ~160F/g while retaining ~64% of the capacity. This capacity of polyaniline electrodes was significantly increased to **~1,412 F/g** with ~89% of the capacity remaining after 10,000 charge-discharge cycles, at a content of 8 wt.% of graphene nanolayers in PANi electrodes. A supercapacitor based on a polyaniline nanocomposite with a content of 8 wt.% graphene also had **very high values of energy density (~1382 Wh/kg) and power (~49786 W/kg)**.

Nanocomposites of graphene materials and conductive polymers have been widely studied as promising materials for supercapacitor electrodes. In [133], the heterostructure of the graphene/PANi composite, consisting of a monolayer of graphene and polyaniline, and its electrochemical operation in a supercapacitor were investigated. The synthesis is based on the functionalization of graphene by phenylene sulfone groups and the oxidative polymerization of aniline by ammonium persulfate under reaction conditions that do not produce bulk polyaniline. Scanning electron microscopy, atomic force microscopy, and Raman spectroscopy have shown the selective formation of polyaniline on graphene. *In situ* Raman spectroscopy and cyclic voltammetry (both in a microdroplet setup) confirmed the reversibility of polyaniline redox transitions and electrochemical doping of graphene. After an increase during the initial 200 cycles due to the formation of benzoquinone-hydroquinone defects in polyaniline, the specific surface capacity was maintained for 2400 cycles with a retention of ±1% at 21.2 μF cm^{-2}; this is an order of magnitude higher than the capacity of the original graphene.

[134] demonstrates a simple synthetic method for covalent grafting of aniline tetramer (TANI), the main building block of PANi, to 3D graphene networks with perfluorophenylazide to create a hybrid electrode material for supercapacitors with an ultra-long service life. The design, which replaces long-chain PANi with short-chain TANI and introduces covalent bonds between TANI and 3D graphene, significantly increases the cyclic charge-discharge stability of PANi-based supercapacitors. The electrode material, as well as the symmetrical fully solid-state supercapacitors manufactured, demonstrate an unusually long service life (retaining a capacity of >85% after 30,000 charge-discharge cycles). The capacity can be further increased by rapid and reversible redox reactions on the electrode surface using a redox electrolyte while maintaining excellent cycle stability (retaining 82% capacity after **100,000 cycles** for a symmetrical fully solid-state device). Despite the fact that conductive polymers

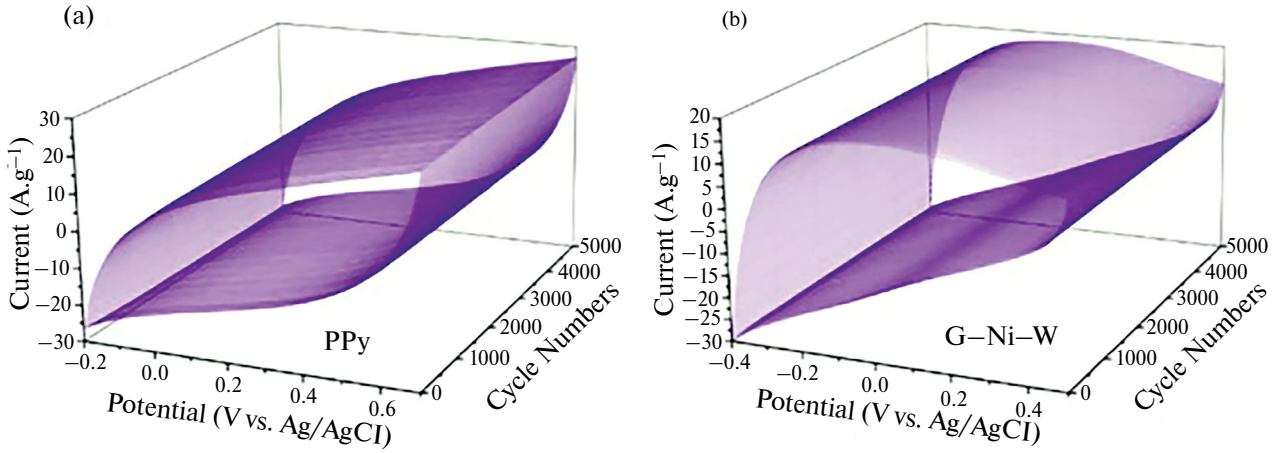

Fig. 13. Three-dimensional demonstration of cyclic stability of a three-electrode supercapacitor system based on (a) PPy, (b) G-Ni–W [138].

are known to be limited by their low cyclic stability, this work offers an effective strategy to achieve an extended service life of supercapacitors.

The paper [135] presents the production of hydrophilic graphene oxide nanolayers by liquid-shear peeling. Graphene oxide nanolayers were used to synthesize three-dimensional graphene/polyaniline composites, which were used directly as supercapacitor electrodes. Composites have better electrochemical properties (gravimetric capacity **483 F/g at 1 A g**) compared to materials made from a mixture of graphene, graphene oxide and polyaniline as precursors. In addition, a symmetrical supercapacitor made of composites demonstrated a high energy density of **17.9 Wh/kg** at a power density of 500 W/kg.

In [9], during polymerization to obtain PANi, the time of electrochemical polymerization was controlled, which led to the formation of graphene-coated paper (PANi-Graphene). The newly prepared electrode showed a high surface capacity of 176 mF/cm^2 in a three-electrode cell at a current density of 0.2 mA/cm^2, which is about 10 times higher than that of pure graphene paper due to the pseudo-capacitance behavior of PANi. More importantly, a fully solid-state symmetrical capacitor assembled with two PANi-Graphene electrodes with a polymer electrolyte had a surface capacity of 123 mF/cm^2, which corresponds to a surface energy density of 17.1 MWh/cm^2 and a surface power density of 0.25 MW/cm^2. The symmetrical capacitor retained 74.8% of its capacity after 500 bending tests from 0 to 120°, indicating good flexibility and mechanical stability.

In [136], the synthesis of stable, conductive, and highly active polythiophene enriched in graphene nanoplatelets (GNPL) by chemical polymerization *in situ* was investigated. X-ray diffraction studies have confirmed the formation of finished nanomaterials. Morphological studies have shown that polythiophene is successfully fixed on the surface of GNPL during polymerization. Elemental mapping has shown the presence of carbon, oxygen, and sulfur in the GNPLs/PTh electrode. Cyclic voltammetry (CV) measurements have shown that the GNPLs/PTh electrode has a maximum specific capacity of **960.71 F/g** at a scanning speed of 10 mV/s. The gravimetric capacity of the manufactured electrodes reached 673 F/g at a current density of 0.25 A/g, which corresponds to an energy density of 2.25 Wh/kg. A cyclic stability study has shown that a GNPLs/PTh-based supercapacitor can retain 84.9% of its initial capacity after 1,500 consecutive CV cycles, indicating excellent cyclic stability of the material.

In the study [137], composite films of reduced graphene oxide (rGO) and poly (3,4-ethylenedioxythiophene) polystyrene sulfate (PEDOT: PSS) were prepared by solvent evaporation using PEDOT: PSS as a binder for fixing oriented graphene in order to ensure its good conductivity and strong π-π-packing interactions with graphene layers. Analyses using scanning electron microscopy (SEM), nitrogen adsorption-desorption, and small-angle X-ray scattering showed that graphene layers were well aligned when a magnetic field was applied, although they were randomly oriented without a magnetic field. As a capacitor electrode material, the composite oriented RGO and (PEDOT: PSS) demonstrated a specific capacitance of 169/g while maintaining about 70% of the capacitance at a current density of 50 A/g, and its CV curves retain a rectangular shape at a voltage scanning rate of 2 V/s.

In [138], a highly active 2D nanostructure consisting of reinforced conductive polypyrrole (PPy) with decorated rGO and a hybrid complex of Ni/W metal oxides (PPy-G-Ni-W) was developed for use in supercapacitors. The hybrid 2D platform showed remarkable specific capacitance of **597 and 557 F/g** when measuring CV and galvanostatic analysis, respectively, using a three-electrode system. The developed supercapacitor has demonstrated very high stability, retaining 98.2% of its overall performance after 5,000 charge-discharge cycles. Similarly, studies in a two-electrode electrochemical cell consisting of PPy-G-Ni-W//PPy-G-Ni-W showed specific capacitances of 361 and 342 F/g at a scanning speed and current density of 2 mV/s and 0.5 A/g using CV and galvanostatic methods, respectively. At the same time, a high energy density of 14.4 Wh/kg was obtained with a power density of 275 W/kg. More importantly, the device retained 96.4% of its total specific capacity after 5,000 charge-discharge cycles (Fig. 13), which highlights the high capacity, mobility, and superstability of the developed ECSC in relation to real-world energy applications.

4. COMPOSITES WITH MXENES

MXenes are a class of two-dimensional inorganic compounds that consist of atomically thin layers of carbides, nitrides, or carbonitrides of transition metals. MXenes have various hydrophilic surface groups. MXenes was first reported in 2012, and their research is undergoing exponential growth. Since 2020, the number of patents on MXenes has exceeded the number of journal articles on MXenes, indicating that they are potentially commercially successful materials. In recent years, MXenes have been used in supercapacitors [5, 139–146].

The great popularity of portable smart electronics has intensively stimulated the development of energy storage devices and other advanced products such as displays and touchpads. Interactive devices such as smartphones, tablets, and other touchscreen devices require mechanically strong transparent conductive electrodes (TCE). The development of a transparent supercapacitor as a power source is essential for next-generation transparent electronics. Recently, graphene and MXene, two representatives of a large two-dimensional family, have shown excellent electronic conductivity and attracted a lot of attention from researchers in the field of energy storage. It is important to note that high-performance TCEs are necessary conditions for creating transparent supercapacitors. The reviews [139, 140] provide a comprehensive analysis of flexible TCEs based on graphene and MXene, covering detailed methods for manufacturing thin films, estimates, performance limitations, as well as approaches to overcome these limitations. Special attention is paid to the fundamental aspects of TCE, such as percolation and conduction.

The new 2D $Ti_3C_2T_x$MXene material (T_x – surface functional groups) is widely studied in the field of supercapacitors. However, the electrochemical characteristics of supercapacitors are reduced due to the presence of $Ti_3C_2T_x$. However, the $Ti_3C_2T_x$ flexible composite/composite membrane/graphene synthesized in [140] effectively eliminates this disadvantage. In contrast to the use of traditional reduced graphene oxide, the structural integrity and large flakes of graphene were synthesized in this work using anhydrous ferric chloride $FeCl_3$. The assembled symmetrical supercapacitor without binder showed a high energy density of 13.1 Wh/kg with a specific power of 75 W/kg. The article presents new perspectives on the analysis of the mechanism of inhibition of MXene self-storage.

Despite the fact that large capacities have been obtained using MXene electrodes in supercapacitors, the relatively high resistance limits the scope of application of these materials. [141] reports on an innovative simple method for manufacturing MXene wrapped in graphene in combination with plasma exfoliation. This method includes two key aspects: 1) incorporation of graphene oxide (GO) into MXene and 2) plasma exfoliation of GO-modified MXene. The resulting materials, referred to as MXene@rGO, have a layered structure with reduced graphene oxide on the surface of MXene. Fully solid-state flexible supercapacitors were manufactured from MXene@rGO materials. Compared to conventional MXenes, MXene@rGO supercapacitors have shown twice the specific capacity, as well as excellent cycling and mechanical stability.

In [142], an ultrahigh-capacity supercapacitor was manufactured using nanolayer MXene as an active electrode material, and nickel foil was used as a current collector. High-quality titanium for $Ti_3C_2T_x$, obtained from the filler fluid, significantly increases the specific capacity in the etching and washing processes. As another technique, graphene grown by chemical deposition from the gas phase was applied to the surface of nickel foil. Graphene grown directly on nickel foil is used as a current collector, forming the $Ti_3C_2T_x$/graphene/Ni electrode structure. It has been found that the capacity of graphene-based supercapacitors is more than 1/5 times higher than the capacity without graphene. A high specific capacity of **~542 F/g** is achieved at a scanning speed of 5 mV/s. In addition, the graphene-based supercapacitor exhibits

a quasi-rectangular shape on cyclic voltammetric curves and symmetrical behavior on galvanostatic charge/discharge curves. Cyclic stability of up to 5000 cycles is confirmed by maintaining high capacity at a high scanning speed of 1000 mV/s.

It follows from the well-known formula for energy density [2] that expanding the voltage window and increasing the capacitance are effective ways to increase the energy density of supercapacitors. However, aqueous electrolyte-based devices usually have a voltage window of less than 1.2 V, taking into account water electrolysis, and chemically converted graphene provides mediocre capacity. According to [143], multielectron redox, structurally stable π-frameworks of indanthrone (IDT:(6,15-dihydrodinaphtho[2,3-a;2',3'-h] phenazine-5,9,14,18-tetraone) were effectively bound to reduced graphene oxide (rGO) to form the IDT@rGO molecular heterojunction. Such electrodes, which do not contain conductive agents and binders, provided a maximum capacity of up to 345 F/g in the potential range from –0.2 to 1.0 V. The $Ti_3C_2T_x$ MXene film partner electrode, operating in the negative potential range from –0.1 to –0.6 V, provided a capacity of up to 769 F/g. Thanks to the realized potentials of the IDT@rGO heterojunction positive electrode Ti3C2Tx MXene and the negative electrode polyvinyl alcohol/H2SO4, the flexible asymmetric supercapacitor based on hydrogel electrolyte provided an increased voltage window of 1.6 V and an impressive energy density of **17 Wh/kg** with a high specific power of **8 kW/kg**, as well as efficient high-speed capability and long service life (maintaining 90% capacity after 10,000 cycles), as well as exceptional flexibility.

As demand for wearable electronic devices grows, so does interest in small, lightweight, and deformable energy storage devices. Among these devices, wire supercapacitors (WSC) are considered key components of wearable devices due to their geometric similarity to woven fiber. One of the potential methods for creating WSC devices is the layer-by-layer assembly (LbL) method, which is a bottom-up electrode manufacturing method. WSC stands for the conformal and adhesive coating of a functional material on a wire substrate, which is difficult to obtain using other processing methods such as vacuum filtration or spray coating. The LbL assembly technology allows for convenient and durable coatings that can be applied to various substrates and shapes, including wire. A study [144] reports on WSCs made using LbL assembly of alternating layers of positively charged reduced graphene oxide functionalized with poly(diallyldimethylammonium chloride) and negatively charged $Ti_3C_2T_x$ MXene nanolayers effectively deposited on activated carbon filaments. In this design, the added LbL film increases capacity, energy density, and power density by 240, 227, and 109%, respectively, compared to uncoated activated carbon yarn, providing high specific and volumetric capacity (**237 F/g**, 2193 F/cm^3). In addition, the WSC has good mechanical stability, maintaining 90% of its original performance after 200 bending cycles. This study demonstrates that LbL coatings based on carbon filaments are promising as energy storage devices for fiber electronics.

2D-MXene materials have attracted close attention in the field of energy storage. However, MXenes usually undergo major re-engineering to increase stability, which significantly hinders their continued commercial use. The article [145] demonstrates an effective and fast self-assembly method for obtaining a 3D porous MXene/graphene (PMG) composite resistant to oxidation to suppress oxidation and self-assembly of MXene. The self-organizing 3D porous architecture can effectively prevent oxidation of MXene layers without visible changes in electrical conductivity in air at room temperature, ensuring high electrical conductivity and a large number of electrochemical active sites accessible to electrolyte ions. The PMG electrode has a high specific capacity of **393 F/g** at 10V/s, excellent performance and outstanding cycling stability. In addition, the assembled asymmetric supercapacitor had a high energy density of 50.8 Wh/kg and remarkable cycle stability with a decrease in specific capacity of only 4.3% after 10,000 cycles. This work paves a new path for solving important issues with MXene in the future.

Two-dimensional (2D) materials are expected to be among the most efficient compounds for use in the energy industry. The ability to store energy in two two-dimensional materials, reduced graphene oxide (rGO) and NbCMXene due to the creation of hetero-assembly, was first realized in [146] by double doping with nitrogen on both lattices using the method of supercritical fluid treatment. As is well known, supercritical fluid synthesis of hetero-assembly based on 2D/2D MXene is unique and distinctive. The high charge storage capacity of N-(NbC/rGO) composites and the typical reaction kinetics contribute to very high electrochemical performance due to this unique synthetic technique. Thus, N-(NbC/rGO) exhibits exceptional electrochemical characteristics **with a high specific capacity of 816 F/g at a current density of 1 A/g and a remarkable energy density of 29 Wh/kg in an aqueous H_2SO_4 electrolyte and 33 Wh/kg in a non-aqueous $TEABF_4$/acetonitrile electrolyte**. In addition, after **100,000 cycles**, 100% of the initial capacity is retained in a quasi-solid electrolyte based on PVA/HSO_4.

5. QUANTUM DOTS

The Nobel Prize in Chemistry in 2023 was awarded to three scientists for one discovery. Moungi Bawendi, Louis Brus and Alexey Ekimov were awarded the highest scientific award for the discovery and synthesis of quantum dots, semiconductor nanocrystals with unique optical and electronic properties.

A quantum dot is a fragment of a conductor or semiconductor whose charge carriers are limited in space in all three dimensions. The size of a quantum dot should be so small that the quantum effects are significant.

The inclusion of new functional components in a three-dimensional graphene (3DG) framework improves the performance of 3DG-based supercapacitors in electrodes by adapting the structure and properties of the framework. Recently, quantum dot materials have been used in supercapacitors [7, 32, 94, 113, 147–150]. In [147] graphene quantum dots (GQD) were incorporated into 3DG by single-stage hydrothermal treatment of GQD and graphene oxide (GO). By simply adjusting the GQDs/GO ratio by weight, various GQD/3DG composites were formed. The maximum ratio was 80%, while composites obtained with a GQDs/GO ratio of 40% for electrodes showed a maximum specific capacity of **242 F/g** for supercapacitors, which means an increase of 22% compared to pure 3DG electrodes (198F/g). This improvement in performance was mainly due to the higher electrical conductivity and larger surface area of GQD/3DG composites. The manufactured GQD/3DG composites as electrodes for supercapacitors have shown high electrochemical stability. Their capacity remained 93% of its original value after 10,000 charge-discharge cycles.

Despite the fact that activated carbons (AC) with a large surface area are widely used in supercapacitors, they usually have limited capacity and speed characteristics, primarily due to their low conductivity and slow electrochemical kinetics caused by their amorphous microporous structure. The article [148] suggests a simple strategy for improving the electrochemical characteristics of AC by embedding highly crystallized graphene quantum dots. Due to the formation of common conductive networks, the kinetics of charge transfer and ion migration in the battery is significantly improved, facilitating the transportation and storage of electrolyte ions in deep and branched micropores. As a result, graphene quantum dots are embedded in activated carbon, which has a microporous structure with a specific surface area of **2829 m^2/g**. This results in a high double-layer capacity of **388 F/g at 1 A/g**, as well as excellent speed characteristics while maintaining 60% of the capacity at 100 A/g in a two-electrode system. The capacitance and velocity characteristics are much higher than those of AC without graphene quantum dots, as well as most porous carbons reported in the literature. This strategy opens up new opportunities for the development of advanced porous carbon materials for high-performance energy storage.

The paper [149] reports on mathematical modeling to study the contribution of quantum dots to the total differential capacitance of functionalized graphene as a material for electrodes of water-based supercapacitors. The effects of nitrogen and oxygen inclusion in the quantum and double-layer capacitance of graphene in four different models of supercapacitors with Li_2SO_4 and LiTFSI aqueous electrolytes are considered. It was found that the total differential capacitance is limited by the double-layer capacitance. The best model of the electrode/electrolyte system was obtained for a symmetrical supercapacitor assembled from epoxy/hydroxyl-functionalized graphene electrodes impregnated with 1 M Li_2SO_4 aqueous electrolyte.

In [150], a simple hydrothermal method for the synthesis of CeO_2/Ce_2O_3 quantum dots fixed on layers of reduced graphene oxide (rGO) of various weight fractions is reported for use as a supercapacitor electrode. Of all the tested samples, a sample containing 7 wt.% rGO ($CrGO_3$), measured by thermogravimetry, demonstrated the highest specific capacity of **1027 F/g at 1 A/g** along with good cyclic stability. At a current density of 4 A/g, the $CrGO_3$ sample showed charge retention of 79% after 5,000 cycles, whereas at 20 A/g it showed charge retention of 85% after 3,000 cycles. The values obtained for the $CrGO_3$ electrode are higher than for all previous cerium and rGO-based electrodes, which suggests its potential use in supercapacitors. High-resolution transmission electron microscopy (HRTEM) clearly revealed crystalline CeO_2 nanoparticles (~5 nm) evenly distributed on the rGO layers, as well as several lattice planes indicating the presence of some amount of Ce_2O_3 mixed with CeO_2. X-ray photoelectron spectroscopy (XPS) revealed the presence of mixed oxides containing mainly CeO_2 with some phase Ce_2O_3 on the surface.

CONCLUSION

This review examines the literature, mainly for recent years, on the relevant subject of graphene applications in supercapacitors. The influence of the porous structure of graphenes, the effect of doping and irradiation of graphenes is considered. Methods for obtaining

graphenes, graphene composites with metal oxides, sulfides and selenides, composites with metal particles, with electron-conducting polymers, with MXenes, as well as quantum dots are considered. Electrochemical characteristics are given for various types of graphenes and their composites.

Particularly high electrochemical characteristics were obtained for composites of graphene with polyaniline, with metal oxides, with selenides, with MXenes and with doping of graphene with boron.

The following maximum values of specific energy were obtained: 40.5 Wh/kg (for $NiSe_2$), 78.66 Wh/kg (for TiO_2), 79.5 Wh/kg (for boron doping), 1382 Wh/kg (polyaniline).

ACKNOWLEDGMENTS

The work was carried out with the financial support of the Ministry of Science and Higher Education of the Russian Federation.

CONFLICT OF INTEREST

The author declares that he has no conflict of interest.

REFERENCES

1. Pandolfo, A.G. and Hollenkamp, A.F., Carbon properties and their role in supercapacitors, *J. Power Sources,* 2006, vol. 157, p. 11.
2. Dhaka, T.P., Chapter 8 – Simple Parallel-Plate Capacitors to High–Energy Density Future Supercapacitors: A Materials Review (Carbide-Derived Carbon – an overview), *Emerging Mater. for Energy Conversion and Storage,* 2018, p. 247.
3. Chee, W.K., Lim, W.K., Zainal, H.N, Huang, Z., Harrison, N.M., and Andou, Y., Flexible Graphene-Based Supercapacitors: A Review, *J. Phys. Chem. C,* 2016, vol. 120, p. 4153.
4. Hussain, N., Abbas, Z., and Nabeela, K., Free-standing metal–organic frameworks on electrospun core–shell graphene nanofibers for flexible hybrid supercapacitors, **J.** *Mater. Chem. A,* 2024. https://doi.org/10.1039/D4TA02221A
5. Karim, G.M., Dutta, P., Majumdar, A., Patra, A., and Deb, S.K., Ultra-fast electro-reduction and activation of graphene for high energy density wearable supercapacitor asymmetrically designed with MXene, *Carbon*, 2023, vol.23, p.191.
6. Liu, L., Xie, Z., Du, X., Yu, D., Yang, B., Li, and Liu, X., Large-scale mechanical preparation of graphene containing nickel, nitrogen and oxygen dopants as supercapacitor electrode materia, *Chem. Engineering J.,* 2022, vol. 430, 132815.
7. Xiaoshan, L., Ruiyi, L., Zaijun, L., and Yongqiang, Y., Construction of advanced Nb_9VO_{25} electrode material by introducing graphene quantum dot for high energy supercapacitors with exceptionally high diffusive, *J. Industrial and Engineering Chem.,* 2024. https://doi.org/10.1016/j.jiec.2024.06.036
8. Haridas, H., Kader, A.K., and Sellathurai, A., Non-covalent functionalization of graphene nanoplatelets and their applications in supercapacitors, *ACS Appl. Mater. Interfaces,* 2024, vol. 16, p. 16630. https://doi.org/10.1021/acsami.3c18174
9. Morenghi, A., Scaravonati, S., Magnani, G., and Sidoli, M., Asymmetric supercapacitors based on nickel decorated graphene and porous graphene electrodes, *Electrochim. Acta*, 2022, vol. 424, p. 140626.
10. Liu, B., Zhang, Q., Zhang, L., Xu, C., and Pan, Z., Electrochemically exfoliated chlorine doped graphene for flexible all solid state microsupercapacitors with high volumetric energy density, *Advanced Mater.*, 2022, vol. 34, p. 2106309.
11. Mohanty, G.C., Gowda, C.C., and Gakhad, P., Enhanced energy density of high entropy alloy (Fe-Co-Ni-Cu-Mn) and green graphene hybrid supercapacitor, *Energy Storage*, 2024, vol. 6, p. e668. https://doi.org/10.1002/est2.668
12. Tyagaraj, H.B., Mahamiya, V., and Marje, S.J., Waste-to-Energy Material: Winery-Waste Derived Heteroatoms Containing Graphene-like Porous Carbon for High-Voltage Supercapacitor, *Mater. Today Sustainability*, 2024, p. 100901. https://doi.org/10.1016/j.mtsust.2024.100901
13. Mohamed, N.B. and El Kady, M.F., Macroporous graphene frameworks for sensing and supercapacitor applications, *Advanced Functional Mater.*, 2022, vol. 32, p. 2203101.
14. Najafi, M.D., Ehsani, A., Nabatian, M., and Hamza, Z., Advanced Supercapacitor Electrodes: Synthesis and Electrochemical Characterization of Graphene Oxide-Bismuth Metal-Organic Framework Composites for Superior Performance, *Electrochim. Acta*, 2024, p. 144636. https://doi.org/10.1016/j.electacta.2024.144636
15. Subrahmanian, S.K. and Palliyal, K.V., In-situ green gram scale synthesis of carbon sphere/graphene for high-performance supercapacitors, *Nano-Structures & Nano-Objects*, 2024, vol. 37, p. 101107. https://doi.org/10.1016/j.nanoso.2024.101107
16. Shi, Z. Sun, G., Yuan, R., Chen, W., Wang, Z., and Zhang, L., Scalable fabrication of $NiCo_2O_4$/reduced graphene oxide composites by ultrasonic spray as binder-free electrodes for supercapacitors with ultralong lifetime, *J. Mater. Sci. & Technol.*, 2022, vol. 99, p. 260
17. Mupit, M., Islam, M.R., Azam, M.A., and Yunus, R., Magnetic particle-filled polyaniline-doped graphene oxide nanocomposite-based electrode in application of supercapacitor, *Energy & Fuels*, 2024, vol. 35. https://doi.org/10.1177/0958305X221145

18. Hoque, M.I., Donne, S.W., and Holze, R., Graphene Nanocomposite Materials for Supercapacitor Electrodes, *Encyclopedia*, 2024, vol. 4, p. 101. https://doi.org/10.3390/encyclopedia4010009
19. Kalicharan, A., Pitchaimani, J., and Kanna, C.B., Green Chemistry Approach for One Step Synthesis of Iodinated Graphene Material for Supercapacitor Applications, *Chem. Europe*, 2024, vol. 9, e202400820.
20. Ahmad, F., Zahid, M., Jamil, H., Khan, M.A., and Atiq, S., Advances in graphene-based electrode materials for high-performance supercapacitors: a review, *J. Energy Storage,* 2023, vol. 72, p. 108731.
21. Smaisim, G.F., Abed, A.M., Al-Madhhachi, H., and Hadrawi, S.K., Graphene-Based Important Carbon Structures and Nanomaterials for Energy Storage Applications as Chemical Capacitors and Supercapacitor Electrodes: A Review, *BioNanoSci.*, 2023, vol. 13, p. 219.
22. Kumar, R., Sahoo, S., Joanni, E., Singh, R.K., and Yadav, R.M., Graphene-metal oxide hybrid materials with 2D and 3D morphologies for advanced supercapacitor electrodes: status, challenges and prospects, *Mater. Today Nano*, 2023, vol. 24, 100399.
23. Mousavi, S.M., Hashemi, S.A., and Kalashgrani, M.Y., Recent advances in energy storage with graphene oxide – for supercapacitor technology, Sustainable Energy Fuels, 2023, vol. **7**, p. 5176.
24. Xia, C., Ren, T., Darabi, R., and Shabani-Nooshabadi, M., Spotlighting the boosted energy storage capacity of $CoFe_2O_4$/Graphene nanoribbons: A promising positive electrode material for high-energy-density asymmetric supercapacitor, *Energy*, 2023, vol. 270, p. 126914.
25. Ran, J., Liu, Y., Feng, H., Shi, H., and Ma, Q., A review on graphene-based electrode materials for supercapacitor, *J. Industrial and Engineering Chem.,* 2024. https://doi.org/10.1016/j.jiec.2024.03.043
26. Li, Z., Xiong, Z., Pan, H., and Shang, N., Graphene Oxide-Based Aluminum Complex Ion Supercapacitor, *ACS Appl. Energy Mater.,* 2023, vol. 6, p. 10554.
27. Youssry, S.M., Abd Elkodous, M., Kumar, R., and Kawamura, G., Thermal-assisted synthesis of reduced graphene oxide-embedded Ni nanoparticles as high-performance electrode material for supercapacitor, *Electrochim. Acta,* 2023, vol. 463, p. 142814.
28. Sayahi, H., Mehrvar, Z., Mohsenzadeh, F., and Darabi, H.R., Room-temperature defect-controlled fabrication of graphene via sustainable electrochemical exfoliation: An ultra-performance supercapacitor, *J. Energy Storage*, 2023, vol. 68, p. 107646.
29. Anagbonu, P., Ghali, M., and Allam, A., Low-temperature green synthesis of few-layered graphene sheets from pomegranate peels for supercapacitor applications, *Sci. Rep.,* 2023, vol. 13, p. 15627.
30. Méndez-Reséndiz, A., and Méndez-Romero, U.A., Highly crystalline selectively oxidized graphene for supercapacitors, *FlatChem*, 2023, vol. 38, vol. 201, p. 100483.
31. Peng, Q., Tan, X., Venkataraman, M., and Militký, J., Application of Graphene in Supercapacitor and Wearable Sensor, *Advanced Structured Mater.*, 2023, vol. 201. https://doi.org/10.1007/978–981–99–6002–6_3
32. Zhou, Q., Wang, L., Ju, W., Su, D., Zhu, J., Yong, Y., and Wu, S., Quantum capacitance of graphene-like/graphene heterostructures for supercapacitor electrodes, *Electrochim. Acta,* 2023, vol. 461, p. 142655.
33. Wu, C., Zhu, J., Zhang, B., Shi, H., Zhang, H., and Yuan, S., Efficient pH-universal aqueous supercapacitors enabled by an azure C-decorated N-doped graphene aerogel, *J. Colloid and Interface Sci.*, 2023, vol. 650, p. 1871.
34. He, M., Wu, L., Yu, A., Li, X., Guan, S., Han, Q., and Wang, H., Surface functionalization of vertical graphene significantly enhances the energy storage capability for symmetric supercapacitors, *Carbon,* 2024, vol. 216, p. 118511. https://doi.org/10.1016/j.carbon.2023.118511
35. Bo, W., Zhang, H., Yin, G., Zhang, L., and Qin, J., Recent advances in graphene-based mesoporous nanosheets for supercapacitors, *J. Carbon Res.,* 2023, vol. 9, p. 91. https://doi.org/10.3390/c9040091
36. Madhushani, K.A., and Gupta, R.K., 3D Graphene for High-Performance, Supercapacitors, Graphene: Fundamentals, Synthesis, *Carbon Nanostructures*. Springer, Cham., 2023. https://doi.org/10.1007/978–3–031–36249–1_16
37. Kumar, R., Sahoo, S., Joanni, E., and Singh, R.K., A review on the current research on microwave processing techniques applied to graphene-based supercapacitor electrodes: An emerging approach beyond, *J. Energy Chem.*, 2022, vol. 74, p. 252.
38. Arvas, M.B., Gürsu, H, Gencten, M., and Sahin, Y., Supercapacitor applications of novel phosphorus doped graphene-based electrodes, *J. Energy Storage*, 2022, vol. 55, p. 105766.
39. Saad, A.G., Emad-Eldeen, A., and Tawfik, W.Z., Data-driven machine learning approach for predicting the capacitance of graphene-based supercapacitor electrodes, *J. Energy Storage*, 2022, vol. 55, p. 105411.
40. Zhu, S., Zhang, F., Lu, H.G., Sheng, J., and Wang, L., Flash nitrogen-doped graphene for high-rate supercapacitors, *ACS Mater. Lett.,* 2022, vol. 4, p. 1863.
41. Li, X., Li, Y., Zhao, X., Kang, F., and Dong, L., Elucidating the charge storage mechanism of high-performance vertical graphene cathodes for zinc-ion hybrid supercapacitors, *Energy Storage Mater.*, 2022, vol. 53, p. 505.
42. Ibrahim, M., Abdelhamid, H.N., and Abuelftooh, A.M., Covalent organic frameworks (COFs)-derived nitrogen-doped carbon/reduced graphene oxide nanocomposite

as electrodes materials for supercapacitors, *J. Energy Storage*, 2022, vol. 55, p. 105375.

43. Athanasiou, M., Yannopoulos, S.N., and Ioannides, T., Biomass-derived graphene-like materials as active electrodes for supercapacitor applications: A critical review, *Chem. Engineering J.*, 2022, vol. 446, p.137191.
44. Sawant, S.A., Patil, A.V., Waikar, M.R., and Rasal, A.S., Advances in chemical and biomass-derived graphene/graphene-like nanomaterials for supercapacitors, *J. Energy Storage*, 2022, vol. 51, p. 104445.
45. Shulga, Yu.M., Baskakova, S.A., Baskakova, Yu.V., Lobach, A.S., Kabachkov, Volfkovich, Yu.M., Sosenkin, V.E., Shulga, N. Yu., Nefedkin, S.I., Kumar, Y., and Michtchenko, A., Preparation of graphene oxide-humic acid composite-based ink for printing thin film electrodes for micro-supercapacitors, *J. Alloys and Compounds*, 2018, vol. 730, p. 88.
46. Shulga, Yu.M., Baskakov, S.A., Baskakova, Y.V., Lobach, A.S., Volfkovich, Yu.M., Sosenkin, N.Y., Shulga, Parkhomenko, Y.N., Michtchenko, A., and Kumar, Y., Hybrid porous carbon materials derived from composite of humic acid, *Microporous and Mesoporous Mater.,* 2017, vol. 245, p. 24.
47. Kryazhev, Yu.G., Volfkovich, Yu.M., Mel'nikov, V.P., Rychagov, A. Yu., Trenikhin, M.V., Solodovnichenko, V.S., and Likholobov, V.A., Synthesis and study of electrochemical properties of nanocomposites with graphene-like particles integrated into a high-porosity carbon matrix, *Protection Metals and Phys. Chem. Surfaces,* 2017, vol. 53, p. 422.
48. Shulga, Yu.M., Baskakov, S.A.,.Baskakova, Yu.V., Volfkovich, Yu.M., Shulga, N. Yu., Skryleva, E.A., Parkhomenko, Y.N., Belay, K.G., Gutsev, G.L., Rychagov, A.Y., Sosenkin, V.E., and Kovalev, I.D., Supercapacitors with graphene oxide separators and reduced graphite oxide electrodes, *J. Power Sources*, 2015, vol. 279, p. 722.
49. Ke, Q., and Wang, J., Graphene-based materials for supercapacitor electrodes. A review, *J. Materiomics*, 2016, vol. 2, p. 37.
50. Lee, H., and Lee, K.S., Interlayer distance controlled graphene, supercapacitor and method of producing the same, *US Patent* 10, 214, 422 B2, 2019.
51. Yang, X., Cheng, C., Wang, Y., Qiu, L., and Li, D., Liquid-Mediated Dense Integration of Graphene Materials for Compact Capacitive Energy Storage, *Science,* 2013, vol. 341, p. 534.
52. Aboutalebi, H., Chidembo, A.T., Salari, M., Konstantinov, K., Wexler, D., Liu, H.K., and Dou, S.X., Comparison of GO, GO/MWCNTs composite and MWCNTs as potential electrode materials for supercapacitors, *Energy Environ. Sci.*, 2011, vol. 4, p. 1855.
53. Zhong, M., Song, Y., Li, Y., Ma, C., Zhai, X., Shi, J., Guo, Q., and Liu, L., Effect of reduced graphene oxide on the properties of an activated carbon cloth/polyaniline flexible electrode for supercapacitor application, *J. Power Sources,* 2012, vol. 217, p. 6.
54. Sun, D., Yan, X., Lang, J., and Xue, Q., High performance supercapacitor electrode based on graphene paper via flame-induced reduction of graphene oxide paper, *J. Power Sources,* 2013, vol. 222, p. 52.
55. Zhou, Z. and Wu, X.F., Graphene-beaded carbon nanofibers for use in supercapacitor electrodes: Synthesis and electrochemical characterization, *J. Power Sources,* 2013, vol. 222, p. 410.
56. Mohammadi, A., Arsalani, N., Tabrizi, A.G., Moosavifard, S.E., Naqshbandi, Z., and Ghadimi L. S., Engineering rGO-CNT wrapped Co3S4 nanocomposites for high-performance asymmetric supercapacitors, *Chem. Engineering J.,* 2018, vol. 334, p. 66.
57. Smirnov, V.A., Denisov, N.N., Dremova, N N., Volfkovich, Yu.M., Rychagov, A. Yu., Sosenkin, V.E., Belay, K.G., Gutsev, G.L., Shulga, N. Yu., and Shulga, Yu.M., A comparative analysis of graphene oxide films as proton conductors, *Appl. Phys. A,* 2014, vol. 117, p. 1859.
58. Volfkovich, Yu.M., Lobach, A.S., Spitsyna, N.G., Baskakov, S.A., Sosenkin, V.E., Rychagov, A. Yu., Kabachkov, E.N., Sakars, A., Michtchenko, A., and Shulga, Yu.M., Hydrophilic and Hydrophobic Pores in Reduced Graphene Oxide Aerogel, *J. Porous Mater.,* 2019, vol. 26, p. 1111.
59. Rychagov, A. Yu., Volfkovich, Yu.M., Vorotyntzev, M.A., vacheva, L.D., Konev, D.V., Krestinin, A.V., Kryazhev, Yu.G., Kuznetzov, V.L., Kukushkina, Yu.A., Mukhin, V.M., Sokolov, V.V., and Chervonobrodov, S.P., Promising Electrode Materials for Supercapacitors, *Electrochemical Energetiks.*
60. Yang, Z., Tian, J., Yin, Z., Cui, C., Qian, W., and Wei, F., Carbon nanotube and graphene-based nanomaterials and applications in high-voltage supercapacitor: A review, *Carbon,* 2019, vol. 141, p. 467.
61. Volfkovich, Yu.M., Rychagov, A. Yu., Sosenkin, V.E., Efimov, O.N., Os'makov, M.I., and Seliverstov, A.F., Measuring the Specific Surface Area of Carbon Nanomaterials by Different Methods, *Russ. J. Electrochem.,* 2014, vol. 50, p. 1099.
62. Eftekhari, A., Shulga, Y.M., Baskakov, S.A., and Gutsev, G.L., Graphene oxide membranes for electrochemical energy storage and conversion. *Intern. J. Hydrogen Energy,* 2018, vol. 43, p. 2307.
63. Liu, H., Wang, Y., Gou, X., Qi, T., Yang, J., and Ding, Y., Three-dimensional graphene/polyaniline composite material forhigh-performance supercapacitor applications, *Mater. Sci. and Engineering B,* 2013, vol. 178, p. 293.
64. Inagaki, M., Konno, H., and Tanaike, O., Carbon materials for electrochemical capacitors, *J. Power Sources,* 2010, vol. 195, p. 7880.

65. Vivekchand, S.R., Rout, C.S., and Subrahmanyam, K.S., Graphene-based electrochemical supercapacitors, *J. Chem. Sci.*, 2008, vol. 120, p. 9.
66. Šedajová, V., Jakubec, P., Bakandritsos, A., and Ranc, V., New limits for stability of supercapacitor electrode material based on graphene derivative, *Nanomaterials,* 2020, vol. *10*, p. 1731.
67. Khakpour, I., Rabiei, and Baboukani, A., Bipolar exfoliation and in situ deposition of high-quality graphene for supercapacitor application, *ACS Appl. Energy Mater.,* 2019, vol. 2, p. 4813.
68. Malik, M.T., Sarker, A., and Rahat, S.M., Performance enhancement of graphene/GO/rGO based supercapacitors: A comparative review, *Mater. Today*, 2021, vol. 28, p. 102685.
69. Liu, C., Yu, Z., Neff, D., Zhamu, A., and Jang, B.Z., Graphene-based supercapacitor with an ultrahigh energy density, *Nano Lett.,* 2010, vol. 10, p. 4863.
70. Li, H., Tao, Y., Zheng, X., Luo, J., and Kang, F., Ultra-thick graphene bulk supercapacitor electrodes for compact energy storage, Energy Environ. Sci., 2016, vol. 9, p. 3135.
71. Zhang, H., Yang, D., Lau, A., Ma, T., Lin, H., and Jia, B., Hybridized graphene for supercapacitors: Beyond the limitation of pure graphene, *Small*, 2021, vol. 17, p. 2007311.
72. Ho, B.T., Lim, T.G., Jeong, M.H., and Suk, J.W., Graphene fibers containing activated graphene for high-performance solid-state flexible supercapacitors, *ACS Appl. Energy Mater.,* 2021, vol. 4, p. 8883.
73. Sarada, K.B.V., Varadaraju, U.V., and Rao, T.N., A novel approach to synthesize porous graphene sheets by exploring KOH as pore inducing agent as well as a catalyst for supercapacitors with ultra-fast rate capability, *Renewable Energy*, 2021, vol. 172, p. 502.
74. An, N., Guo, Z., Xin, J., He, Y., Xie, K., and Sun, D., Hierarchical porous covalent organic framework/graphene aerogel electrode for high-performance supercapacitors, *J. Mater. Chem.* **A**, 2021, vol. 9, p. 16824.
75. Yan, Z., Gao, Z., Zhang, Z., Dai, C., Wei, W., and Shen, P.K., Graphene nanosphere as advanced electrode material to promote high performance symmetrical supercapacitor, *Small*, 2021, vol. 17, p. 2007915.
76. Kim, J., Eum, J.H., Kang, J., Kwon, O., Kim, H., and Kim, D.W., Tuning the hierarchical pore structure of graphene oxide through dual thermal activation for high-performance supercapacitor, *Sci. Rep.,* 2021, vol. 11, p. 2063.
77. Iakunkov, A., Skrypnychuk, V., and Nordenström, A., Activated graphene as a material for supercapacitor electrodes: Effects of surface area, pore size distribution and hydrophilicity, *Phys. Chem.Chem. Phys.*, 2019, vol. 21, p. 17901.
78. Nomura, K., Nishihara, H., and Kobayashi, N., V supercapacitors based on super-stable mesoporous carbon sheet made of edge-free graphene walls, *Energy Environ. Sci.*, 2019, vol. 12, p. 1542.
79. Sun, D., Yu, X., Ji, X., Sun, Z., and Sun, D., Nickel/woodceramics assembled with lignin-based carbon nanosheets and multilayer graphene as supercapacitor electrode, *J. Alloys and Compounds*, 2019, vol. 805, p. 327.
80. Obeidat, A.M., Luthra, V., and Rastogi, A.C., Solid-state graphene-based supercapacitor with high-density energy storage using ionic liquid gel electrolyte: electrochemical properties and performance in storing solar electricity, *J. Solid State Electrochem.*, 2019, vol. 23, p. 1667.
81. Xiong, C., Li, B., Lin, X., Liu, H., Xu, Y., Mao, J., and Duan, C., The recent progress on three-dimensional porous graphene-based hybrid structure for supercapacitor, *Composites Part B: Engineering,* 2019, vol. 165, p. 10.
82. Huang, Y., Shi, Y., Gong, Q., Weng, M., Li, Y., and Gan, J., Scalable preparation of hierarchical porous activated carbon/graphene composites for high-performance supercapacitors, *J. Mater. Chem. A*, 2019, vol. 7, p. 10058.
83. Wang, K., Li, L., Zhang, T., and Liu, Z., Nitrogen-doped graphene for supercapacitor with long-term electrochemical stability, *Energy*, 2014, vol. 70, p. 612.
84. Gorenskaia, E.N., and Kholkhoev, B.C., Hydrothermal synthesis of N-doped graphene for supercapacitor electrodes, *J. Nanosci. and Nanotechnol.*, 2020, vol. 20, p. 3258.
85. Karaman, K., Bayram, E., and Aktash, O., Preparation of high surface area graphene doped with nitrogen to evaluate the influence of morphological properties and nitrogen content on supercapacitors, *J. Electroanal. Chem.,* 2020, vol. 868, p. 114197.
86. Elessawy, N.A., Nady, J.E., Wazeer, W., and Kashyout, A.B., Development of high-performance supercapacitor based on a novel controllable green synthesis for 3D nitrogen doped graphene, *Sci. Rep.,* 2019, vol. 9, p. 1129.
87. Huang, T., Chu, X., Cai, S., Yang, Q., Chen, H., and Liu, Y., Tri-high designed graphene electrodes for long cycle-life supercapacitors with high mass loading, *Energy Storage Mater.*, 2019, vol. 17, p. 349.
88. Zhao, T., Yang, D., Xu, T., and Zhang, M., Cold Resistant Nitrogen/Sulfur Dual Doped Graphene Fiber Supercapacitors with Solar–Thermal Energy Conversion Effect, *Chemistry A Europ. J.*, 2021, vol. 27, p. 3473.
89. Cao, L., Li, H., Liu, X., Liu, S., Zhang, L., Xu, W., and Yang, H., Nitrogen, sulfur co-doped hierarchical carbon encapsulated in graphene with "sphere-in-layer" interconnection for high-performance supercapacitor, *J. Colloid and Interface Sci.,* 2021, vol. 599, p. 443.
90. Moreno-Fernández, G. and Gómez-Urbano, J.L., Flat-shaped carbon–raphene microcomposites as

electrodes for high energy supercapacitors, *J. Mater. Chem. A*, 2019, vol. 7, p. 14646.

91. Li, J., Li, X., Xiong, D., Wang, L., and Li, D., Enhanced capacitance of boron-doped graphene aerogels for aqueous symmetric supercapacitors, *Appl. Surface Sci.*, 2019, vol. 475, p. 285.
92. Cui, D., Li, H., Li, M., Li, C., Qian, L., and Zhou, B., Boron-doped graphene directly grown on boron-doped diamond for high-voltage aqueous supercapacitors, *ACS Appl. Energy Mater.* 2019, vol. 2, p. 1526.
93. Arvas, M.B., Gürsu, H., Gencten, M., and Sahin, Y., Preparation of different heteroatom doped graphene oxide based electrodes by electrochemical method and their supercapacitor applications, *J. Energy Storage*, 2021, vol. 35, 102328.
94. Xu, Q., Yang, G., Fan, X., and Zheng, W., Improving the quantum capacitance of graphene-based supercapacitors by the doping and co-doping: first-principles calculations, *ACS Omega,* 2019, vol. 4, p. 13209.
95. Athanasiou, M., Samartzis, N., Sygellou, L., and Dracopoulos, V., High-quality laser-assisted biomass-based turbostratic graphene for high-performance supercapacitors, *Carbon*, 2021, vol. 172, p. 750.
96. Hamra, A.A., Lim, H.N., and Huang, H.N., Microwave exfoliated graphene-based materials for flexible solid-state supercapacitor, *J. Molec. Structure*, 2020, vol. 1220, p. 128710.
97. Yang, D. and Bock, C., Laser reduced graphene for supercapacitor applications, *J. Power Sources,* 2017, vol. 337, p. 73.
98. Le Fevre, L.W., Cao, J., Kinloch, I.A., and Forsyth, A.J., Systematic comparison of graphene materials for supercapacitor electrodes, *Chem. Open*, 2019, vol. 8, p. 418.
99. Singh, A. and Ojha, A.K., Coal derived graphene as an efficient supercapacitor electrode material, *Chem. Physics*, 2020, vol. 530, p. 110607.
100. Karakoti, M., Pandey, S., and Jangra, R., Waste plastics derived graphene nanosheets for supercapacitor application, *Materials and Manufacturing Proc. Mater.*, 2021, vol. 36, p. 171.
101. Pandey, S., Karakoti, M., Surana, K., and Dhapola, P.S., Graphene nanosheets derived from plastic waste for the application of DSSCs and supercapacitors, 2021, *Sci. Rep.,* vol. 11, p. 3916.
102. Tamilselvi, R., Ramesh, M., Lekshmi, G.S., and Bazaka, O., Graphene oxide-based supercapacitors from agricultural wastes: A step to mass production of highly efficient electrodes for electrical transportation systems, *Renewable Energy*, 2020, vol. 151, p. 731.
103. Xiong, C., and Li, B., Carbonized wood cell chamber-reduced graphene oxide@PVA flexible conductive material for supercapacitor, strain sensing and moisture-electric generation applications, Chem. Engineering J., 2021, vol. 15, 129518.
104. Xing, J., Tao, P., Wu, Z., Xing, C., Liao, X., and Nie, S., Nanocellulose-graphene composites: A promising nanomaterial for flexible supercapacitors, *Carbohydrate Polymers*, 2019, vol. 207, p. 447.
105. Peng, X., Cao, H., Qin, Z., Zheng, C., Zhao, M., Liu, P.Z., and Xu, B., A simple and scalable strategy for preparation of high density graphene for high volumetric performance supercapacitors, *Electrochim. Acta*, 2019, vol. 305, p. 56.
106. Bellani, S., Petroni, E., and Del Rio Castillo, A.E., Scalable production of graphene inks via wet-jet milling exfoliation for screen-printed microsupercapacitors, *Advanced Functional Mater.,* 2019, vol. 29, p. 1807659.
107. Mensing, J.P., Lomas, T., and Tuantranont, A., 2D and 3D printing for graphene based supercapacitors and batteries: A review, *Sustainable Mater. and Technol.,* 2020, vol. 25, p. 190.
108. Nandi, D., Mohan, V.B., and Bhowmick, A.K., Metal/metal oxide decorated graphene synthesis and application as supercapacitor: a review, *J. Mater. Sci.*, 2020, vol. 55, p. 63752020.
109. Choi, H., Nguyen, P.T., Van Tran, P.T., and In, J.B., Micro-patterned metal current collectors for high aspect ratio flexible graphene supercapacitors, *Appl. Surface Sci.*, 2020, vol. 510, 145432
110. Zhou, Y., Cheng, X., Huang, F., Sha, Z., Han, Z, and Chen, J., Hierarchically structured electrodes for moldable supercapacitors by synergistically hybridizing vertical graphene nanosheets and MnO_2, *Carbon,* 2021, vol. 172, p. 272.
111. Sha, Z., Huang, F., Zhou, Y., Zhang, J., Wu, S., and Chen, J., Synergies of vertical graphene and manganese dioxide in enhancing the energy density of carbon fibre-based structural supercapacitors, *Composites Sci. and Technol.*, 2021, vol. 201, p. 108568.
112. Mane, V.J., Kale, S.B., Ubale, S.B., and Lokhande, V.C., Enhanced specific energy of silver-doped MnO_2/graphene oxide electrodes as facile fabrication symmetric supercapacitor device, *Mater. Today Chem.*, 2021, 20, p. 100473.
113. Ashourdan, M., Semnani, A., and Hasanpour, F., Synthesis of $CuMnO_2$/graphene quantum dot nanocomposites as novel electrode materials for high performance supercapacitors, *J. Energy Storage,* 2021, vol. 36, p. 102449.
114. Fornasini, L., Scaravonati, S., Magnani, G., and Morenghi, A., *In situ* decoration of laser-scribed graphene with TiO_2 nanoparticles for scalable high-performance micro-.supercapacitors, *Carbon*, 2021, vol. 176, p. 296.
115. El-Gendy, D.M., Ghany, N.A., and Allam, N.K., Black titania nanotubes/spongy graphene nanocomposites for high-performance supercapacitors, *RSC advances*, 2019, vol. 9, 12555.
116. Jiang, D., Zheng, M., You, Y., Li, F., Yuan, H., and Zhang, W., β-Ni $(OH)_2$/nickel-cobalt layered

double hydroxides coupled with fluorine-modified graphene as high-capacitance supercapacitor electrodes with improved cycle life, *J. Alloys and Compounds*, 2021, vol. 875, p. 159929.

117. Sethi, M., Shenoy, U.S., and Bhat, D.K., Simple solvothermal synthesis of porous graphene-NiO nanocomposites with high cyclic stability for supercapacitor application, *J. Alloys and Compounds*, 2021, vol. 854, p. 157190.
118. Gao, X., Zhang, H., Guo, E., Yao, F., Wang, Z., and Yue, H., Hybrid two-dimensional nickel oxide-reduced graphene oxide nanosheets for supercapacitor electrodes, *Microchem. J.*, 2021, vol. 164, p. 105979.
119. Le, K., Wang, Z., Wang, F., Wang, Q., and Shao, Q., Sandwich-like NiCo layered double hydroxide/reduced graphene oxide nanocomposite cathodes for high energy density asymmetric supercapacitors, Dalton Trans., 2019, vol. 48, p. 5193.
120. Kharangarh, P.R., Ravindra, N.M., and Rawal, R., Graphene quantum dots decorated on spinel nickel cobaltite nanocomposites for boosting supercapacitor electrode material performance, *J. Alloys and Compounds,* 2021, vol. 876, 159990.
121. Thalji, M.R., Ali, G.A., Liu, P., and Zhong, Y.L., $W_{18}O_{49}$ nanowires-graphene nanocomposite for asymmetric supercapacitors employing $AlCl_3$ aqueous electrolyte, *Chem. Engineering J.*, 2021, vol. 409, p. 128216.
122. Lee, S.M., Park, Y.J., Kim, J.H., and Lee, K., Effects of annealing on electrochemical performance in graphene/V_2O_5 supercapacitor, *Appl. Surface Sci.*, 2020, vol. 512, p. 145626.
123. Fu, M., Zhuang, Q., Zhu, Z., Zhang, Z., Chen, W., and Liu, Q., Facile synthesis of V_2O_5/graphene composites as advanced electrode materials in supercapacitors, *J. Alloys and Compounds*, 2021, vol. 862, p. 158006.
124. Zhu, C., Dong, X., Mei, X., Gao, M., Wang, K., and Zhao, D., General fabrication of metal oxide nanoparticles modified graphene for supercapacitors by laser ablation, *Appl. Surface Sci.*, 2021, vol. 568, p. 150978.
125. Zhang, J., Zhang, Z., Jiao, Y., Yang, H., Li, Y., and Zhang, J., The graphene/lanthanum oxide nanocomposites as electrode materials of supercapacitors, *J. Power Sources*, 2019, vol. 419, p. 99.
126. Kasap, S., Kaya, I.I., Repp, S., and Erdem, E., Superbat: battery-like supercapacitor utilized by graphene foam and zinc oxide (ZnO) electrodes induced by structural defects, *Nanoscale Advances*, 2019, vol. 1, p. 2586.
127. Ning, J., Xia, M., Wang, D., Feng, X., Zhou, H., and Zhang, J., Ni_3Si_2/NiOOH/Graphene Nanostructure for an All-Solid-State Supercapacitor, *Nano-Micro Letters*, 2021, vol. 13, p. 2.
128. Shahi, M., Hekmat, F., and Shahrokhian, S., Hybrid supercapacitors constructed from double-shelled cobalt-zinc sulfide/copper oxide nanoarrays and ferrous sulfide/graphene oxide nanostructures, *J. colloid and interface*, 2021, vol. 585, p. 750.
129. Yuan, M., Luo, F., Rao, Y., Yu, J., Wang, Z., Li, H., and Chen, X., SWCNT-bridged laser-induced graphene fibers decorated with MnO_2 nanoparticles for high-performance flexible micro-supercapacitors, *Carbon*, 2021, vol. 183, p. 128.
130. Lien, C.W., Vedhanarayanan, B., Chen, J.H., and Lin, J.Y., Optimization of acetonitrile/water content in hybrid deep eutectic solvent for graphene/MoS_2 hydrogel-based supercapacitors, *Chem. Engineering J.*, 2021, vol. 405, p. 126706.
131. Hao, J., Liu, H., Han, S., and Lian, J., MoS_2 Nanosheet-Polypyrrole Composites Deposited on Reduced Graphene Oxide for Supercapacitor Applications, *ACS Appl. Nano Mater.*, 2021, vol. 4, p. 2339.
132. Xie, B., Yu, M., Lu, L., Feng, H., Yang, Y., Chen, Y., and Cui, H., Pseudocapacitive Co_9S_8/graphene electrode for high-rate hybrid supercapacitors, *Carbon*, 2019, vol. 141, p. 134.
133. Sitaaraman, S.R., Santhosh, R., Kollu, P., and Jeong, S.K., *Diamond and Related Mater.*, 2020, vol. 108, p. 107983.
134. Moosavifard, S.E., Mohammadi, A., and Darzi, M.E., A facile strategy to synthesis graphene-wrapped nanoporous copper-cobalt-selenide hollow spheres as an efficient electrode for hybrid supercapacitors, *Chem. Engineering J.*, 2021, vol. 415, p. 128662.
135. Gu, Y., Fan, L.Q., Huang, J.L., Geng, C.L., and Lin, J.M., N-doped reduced graphene oxide decorated $NiSe_2$ nanoparticles for high-performance asymmetric supercapacitors, *J. Power Sources*, 2019, vol. 425, p. 60.
136. Huang, Q., Yang, Y., Chen, R., and Wang, X., High performance fully paper-based all-solid-state supercapacitor fabricated by a papermaking process with silver nanoparticles and reduced graphene oxide-modified pulp fibers, *EcoMat*, 2021, vol. 3, p. 12076.
137. Karami, Z., Youssefi, M., Raeissi, K., and Zhiani, M., An efficient textile-based electrode utilizing silver nanoparticles/reduced graphene oxide/cotton fabric composite for high-performance wearable supercapacitors, *Electrochim. Acta*, 2021, vol. 368, p. 137647.
138. Conway, B., *Electrochemical Supercapacitors: Scientific Fundamentals and Technological Applications*, Berlin: Springer Science &Business Media, Germany, 2013.
139. Bagotsky, V.S., Skundin, A.M., and Volfkovich, Yu.M., *Electrochemical Power Sources. Batteries, Fuel Cells, Supercapacitors*. N.J.: Jhon Wiely&Sons Inc. Publisher, 2015.
140. Snook, G.A., Kao, P., and Best, A.S., Conducting-polymer-based supercapacitor devices and electrodes, *J. Power Sources,* 2011, vol. 196, p. 1.
141. Peng, C., Zhang, S., Jewell, D., and Chen, G.Z., Carbon nanotube and conducting polymer composites

for supercapacitors, *Progress in Natural Sci.,* 2008, vol. 8, p. 777.

142. Huang, Z., Li, L., Wang, Y., Zhang, C., and Liu, T., Polyaniline/graphene nanocomposites towards high-performance supercapacitors: A review, *Composites Commun.,* 2018, vol. 8, p. 83.
143. Wang, J., Xu, Y., Chen, X., and Sun, X., Capacitance properties of single wall carbonnanotube/polypyrrole composite films, *Composites Sci. and Technol.,* 2007, vol. 67, p. 2981.
144. Kim, B.C., Kwon, J.S., Ko, J.M., Park, J.H., Too, C.O., and Wallace, G.G., Preparation and enhanced stability of flexible supercapacitor prepared from Nafion/polyaniline nanofiber, *Synthetic Metals,* 2010, vol. 160, p. 94.
145. Cong, H.P., Ren, X.C., Wang, P., and Yu, S.H., Flexible graphene–polyaniline composite paper for high-performance supercapacitor, *Energy Environ. Sci.*, 2013, vol. 6. p. 1185.
146. Qin, W., Jian-ling, L., Fei, G., Wen-sheng, L., Ke-zhong, W., and Xin-dong, W., Poly (ethylenedioxythiophene) (PEDOT) as polymer electrode in redox supercapacitor, *New Carbon Mater.,* 2008, vol. 1, p. 275.
147. Cai, J.J., Kong, L.B., Zhang, J., Luo, Y.C., and Kang, L., A novel polyaniline/mesoporous carbon nano-composite electrode for asymmetric supercapacitor, *Chinese Chem. Letters,* 2010, vol. 21, p. 1509.
148. Yang, M., Cheng, B., Song, H., and Chen, X., Preparation and electrochemical performance of polyaniline-based carbon nanotubes as electrode material for supercapacitor, *Electrochim. Acta,* 2010, vol. 55, p. 7021.
149. Fang, Y., Liu, J., Yu, D.J., Wicksted, J.P., Kalkan, K., Topal, C.Q., Flanders, B.N., Wu, J., and Li, J., Self-supported supercapacitor membranes: Polypyrrole-coated carbon nanotube networks enabled by pulsed electrodeposition, *J. Power Sources,* 2010, vol. 195, p. 674.
150. Vorotyntsev, M.A., Konev, D.V., Devillers, Ch.H., Bezverkhyy, I., and Heintz, O. Electroactive polymeric material with condensed structure on the basis of magnesium (II) polyporphine, *Electrochim. Acta,* 2011, vol. 56, p. 3436.

RUSSIAN JOURNAL OF ELECTROCHEMISTRY, 2025, Vol. 61, No. 1, pp. 37–51

ALL SOLID STATE THIN-FILM LITHIUM-ION BATTERIES (REVIEW)[1]

© 2025 A. M. Skundin*, T. L. Kulova

Frumkin Institute of Physical Chemistry and Electrochemistry, Russian Academy of Sciences, Moscow, Russia

**e-mail: askundin@mail.ru*

Received: June 25, 2024

Revised: September 05, 2024

Accepted: September 25, 2024

Abstract. The main features of all-solid-state lithium-ion batteries and similar batteries with a lithium metal electrode are considered. The main areas of application of such batteries are noted. Solid inorganic electrolytes and electrode materials are considered in detail. The main manufacturers are briefly listed.

Keywords: *li-ion battery, lithium electrode, solid electrolyte, electrode materials*

DOI: 10.31857/S04248570250102e3

INTRODUCTION

All-solid-state thin-film lithium-ion batteries [1] represent a special, relatively small, but very important category of such devices. All-solid-state batteries have certain advantages over traditional batteries with liquid electrolytes. Firstly, the absence of organic solvents increases the safety of the battery by eliminating the risk of possible leakage of liquid and vapors and, consequently, reducing the risk of fire and explosion. Secondly, liquid electrolyte solvents are often involved in the degradation of lithium-ion batteries, so it is assumed that the service life of solid-state batteries will be much longer. Thirdly, the use of liquid electrolyte leads to a number of limitations on the design and size of the battery. (The typical thickness of conventional separators in lithium-ion batteries is about 20 μm, while the thickness of solid electrolytes is 1 μm). Thus, the concept of all-solid-state devices opens the way to the creation of thin-film (including flexible and transparent) and microbatteries.

The need for all-solid-state thin-film lithium-ion batteries arises due to the rapidly developing microelectronics, especially with the advent of battery-powered smart cards, radio frequency identification (RFID) tags, smart watches, implantable medical devices, remote micro sensors and transmitters, Internet of Things (IoT) systems and various other wireless devices, including intelligent building management and so on. Often, these batteries need to be placed on the same chip as the microelectronics device itself, creating a so-called embedded system. The manufacturing technology of solid-state thin-film lithium-ion batteries must be compatible with the manufacturing technology of integrated circuits, microelectromechanical systems (MEMS devices), semiconductor sensors, etc., i.e., in general, it must be VLSI-compatible (VLSI: "very large scale integration"). Flexible and transparent devices are quite important types of thin-film batteries. It should be noted that significant progress in the field of solid-state lithium-ion batteries has recently been achieved through the experimental development and optimization of solid electrolytes and functional electrode materials.

Interest in all-solid-state lithium-ion batteries is steadily increasing. The number of publications on this topic in 2010 was about 500, and in 2021 it exceeded 2,500 [2]. Fairly detailed review papers can be mentioned [3–16].

GENERAL PROVISIONS

A schematic diagram of an all-solid-state thin-film lithium-ion battery is shown in Fig. 1.

The negligible thickness of a thin-film battery forces it to be placed on a more or less large structural element (substrate), which may be part of a device powered by this battery. And this is perhaps the main difference between thin-film batteries and conventional commercial lithium-ion batteries. The second fundamental difference is the possibility of using lithium metal as a negative electrode in all-solid-state batteries. It is known that the main feature of lithium-ion batteries is the use of intercalation electrodes instead of lithium metal.

The structural base of a thin-film battery can in principle be made of any material, including metals, ceramics, glass, polymers, and even paper. If this material is an electronic conductor, then the structural

[1] Based on the materials of the report at the 17th International Meeting "Fundamental and applied problems of solid state ionics", Chernogolovka, June 16–23, 2024.

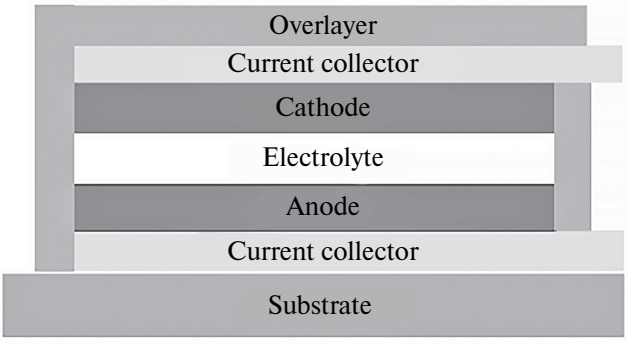

Fig. 1. Diagram of an all-solid-state thin-film lithium-ion battery.

base (substrate) can play the role of a current collector of one electrode (usually lithium). In any case, the substrate material must comply with the conditions of application and operation of the functional layers. The substrate material should not interact with other layers of the battery. The substrate material should also prevent lithium from diffusing from the battery. The battery, in fact, consists of two electrodes, between which there is an electrolyte. The outside of each electrode is in contact with the corresponding current collector. The battery as a whole is enclosed in an appropriate housing. The housing is a very important structural element. It must protect the internal contents of the battery from external physical and chemical influences, in particular, prevent the interaction of active battery materials with air and moisture. Ideally, the battery and the electronic device powered by it should be functionally integrated with maximum efficiency and voltage control.

Although the first attempts to create fully solid-state thin–film batteries were made back in the 1950s, real success was achieved only 40 years later and was due to the development of a successful solid electrolyte, LiPON – lithium phosphorus oxynitride [17–20] which is obtained by magnetron radiofrequency sputtering of a Li_3PO_4 target in a nitrogen medium. Its average composition can be expressed as $Li_{3.3}PO_{3.8}N_{0.22}$ with some uncertainty of nitrogen content. It was assumed that the introduction of nitrogen into the glass structure would increase its chemical and thermal stability. LiPON is stable in contact with lithium metal, has very low electronic conductivity and adequate ionic conductivity of about 2.3 μS/cm at room temperature, and most importantly, has a lithium transfer number equal to unity. The decomposition voltage of LiPON exceeds 5.5 V. Using this very electrolyte, thin-film batteries with various active materials of the positive electrode, including $Li_xMn_2O_4$, TiS_2, $LiCoO_2$ и V_2O_5, have been manufactured.

In the first decade of the 21st century, several companies launched the production of all-solid-state thin-film batteries with capacities from 0.1 to 5 mAh. These batteries used negative electrodes made of both lithium and conventional intercalation materials (Sn, Si, Ge, and C). Total thickness of the active part (current sinks, electrodes and electrolyte) ranged from 20 to 50 μm. The first LiPON electrolyte batteries could withstand hundreds and even thousands of cycles with low degradation. Such excellent cyclicity was explained by a combination of several factors. Firstly, the high stability of LiPON, secondly, the ability of thin-film materials to withstand volumetric changes caused by lithiation and delithiation, and thirdly, the uniform distribution of current in the thin-film structure.

The diagram in Fig. 1 shows a "plate-like" (one-dimensional) structure. Various 3D constructions are more rational [4, 21–27]. 3D designs can significantly increase the specific energy of the battery, as the total surface area of the electrodes per unit area of the substrate increases. In fact, the energy needs of micro- and nanoelectromechanical systems, including implantable medical devices, drug delivery systems, microsensors, etc., have opened up a niche for 3D batteries with a characteristic size from 1 to 10 mm^3 and a capacity from 10 nW to 1 mW.

Various designs of 3D batteries with regular or chaotic geometry are described. It can be a periodic grid or an aperiodic ensemble of electrodes. For example, it can be an array of cylindrical (columnar) electrodes of both signs grown on substrates. Two arrays of different electrodes are inserted into each other. The space between the electrodes must be filled with electrolyte (Fig. 2). The main disadvantages of this design are a rather large volume of electrolyte, a large and variable interelectrode distance.

A more effective design is one consisting of an array of column electrodes of the same sign placed on a substrate and coated with a thin layer of electrolyte. In this case, the remaining space is filled with the active material of the counter-electrode.

An interesting 3D battery design is described in [21]. Here, a number of grooves are made in a massive silicon substrate by anisotropic etching. The substrate itself plays the role of a single current collector. The active electrode layers are deposited inside this highly structured substrate, starting with an effective barrier layer, preferably TiN or TaN, to protect the substrate from lithium penetration, followed by a thin-film silicon negative electrode with a thickness of about 50 nm, a solid-state LiPON-like electrolyte and a thin-film material of the positive electrode, in this example $LiCoO_2$ with a thickness of 1 μm. The second current collector is applied last.

The chaotic analogue of the regular structure shown in Fig. 2 is a kind of "sponge" design (Fig. 3). In this case, the solid mesh of the sponge ("web"), which is the cathode, is covered with a very thin layer of solid electrolyte. The remaining voids are filled with anode material.

Probably the most advanced technology for the production of 3D batteries is 3D printing (in the English-language literature, additive manufacturing (AM)) [28–30]. This technology makes it possible to produce objects with well-controlled and very complex geometries through layer-by-layer deposition directly on computerized equipment without using any templates. Recently, 3D printing of lithium-ion batteries of various geometries has been developed in order to increase their specific energy, specific power and mechanical characteristics. In fact, 3D printing is not a single method, but a group of methods that includes: (i) material extrusion (for example, direct ink writing, DIW, and fused deposition modeling, FDM); (ii) inkjet processing of materials (for example, inkjet printing); (iii) binder jet cleaning; (iv) powder layer melting (e.g., selective laser sintering and selective laser melting); (v) directed energy release; (vi) photopolymerization (e.g., stereolithography (SLA)); (vii) sheet lamination. The most popular 3D printing method used in the manufacture of lithium-ion batteries is direct ink writing. The DIW equipment is not complicated (and therefore inexpensive) and includes a simple desktop 3D printer, a heated table, a pneumatic dispenser, and a micronozzle.

A kind of 3D version of an all-solid-state lithium-ion battery is a transparent (or translucent) flexible battery. The concept of a translucent battery with opaque active electrode materials was proposed in 2011 [31] and developed later [32]. The concept is based on the principle of electrodes with a mesh structure. A distinctive feature of this mesh design is the fact that the size of the electrodes is lower than the resolution of the human eye, and thus the entire battery appears transparent. [31] described a thin-film battery of the $LiMn_2O_4/Li_4Ti_5O_{12}$ electrochemical system with a gel polymer electrolyte, whereas [32] described a $LiCoO_2$/Si battery with LiPON electrolyte. The transparency of both batteries is close to 60%.

FUNCTIONAL MATERIALS FOR SOLID-STATE THIN-FILM LITHIUM–ION BATTERIES

Materials for electrolytes. The electrolytes of solid-state thin-film batteries are fundamentally different from those of traditional lithium-ion batteries, and quite a lot of research has been devoted to the development

Fig. 2. 3D design with interdigital arrays of electrodes.

and improvement of such electrolytes (see, for example, reviews [33–42]).

Electrolytes for solid-state thin-film batteries must have high ionic and low electronic conductivity at operating temperature (preferably room temperature), a wide electrochemical stability window, adaptability, and compatibility with electrodes. The latter feature suggests that the electrolyte must be resistant to interaction with electrodes, especially with lithium and lithium alloy electrodes, and have the same coefficients of thermal expansion with both electrodes. Both crystalline and amorphous materials are used as solid electrolytes. A typical representative of an amorphous (glass-like) electrolyte for solid-state thin-film batteries is the already mentioned LiPON. Other examples of amorphous solid electrolytes are oxide and sulfide glass. Crystalline solid electrolytes are represented by solid solutions with a perovskite structure, lithium-ion conductors such as NASICON, LISICON and thio-LISICON, as well as lithium-ion conductors of the garnet type.

An interesting example of a LiPON-like glassy electrolyte is the so-called LiSON with a typical composition of $Li_{0,29}S_{0,28}O_{0,35}N_{0,09}$ and an ionic conductivity of about 2×10^{-5} S/cm [43]. This material was produced by RF magnetron sputtering using a Li_2SO_4 target in an atmosphere of pure nitrogen. Another similar glassy electrolyte, known as LiPOS ($6LiI\text{-}4Li_3PO_4–P_2S_5$), has the same conductivity [44].

Sulfide glassy solid electrolytes, especially those with a high concentration of Li+ ions, have generally higher conductivity than LiPON-like electrolytes. In the $Li_2S–P_2S_5$ system, when the Li_2S content is more than 70 mol.%, the electrolytes have a conductivity of more than 10^{-4} S/cm, which is one and a half orders of magnitude higher than the conductivity of LiPON-like analogues. However, the synthesis of sulfide glass with a sufficiently high concentration of Li+ ions is difficult due to easy crystallization during cooling, so such glass is made by double-roll rapid quenching or mechanical milling. The addition of halides, borohydride, or lithium

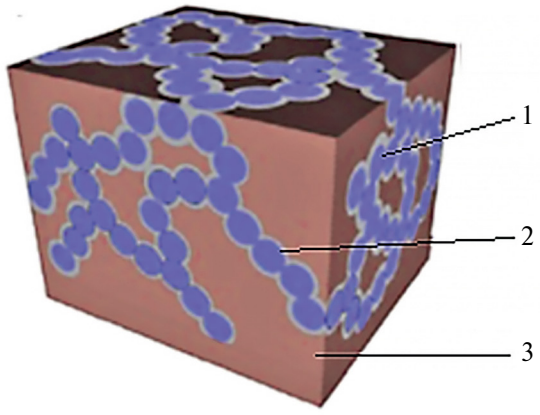

Fig. 3. The "spongy" design of the 3D battery. 1 is the active material of the positive electrode, 2 is the electrolyte, 3 is the active material of the negative electrode (from [24], open access).

orthophosphate increases the conductivity of the glass to 10^{-3} S/cm at room temperature. For example, an electrolyte of composition $95(80Li_2S\text{-}20P_2S_5) + 5LiI$ has a conductivity of 2.7 mS/cm [45], an electrolyte of composition $Li_{5.5}PS_{4.5}Cl_{1.5}$ with an argyrodite structure is 10.2 mS/cm [46], and an electrolyte of composition $Li_{5.4}PS_{4.4}Cl_{1.6}$ is 8.4 mS/cm [47].

Intermediate forms, the so-called glass-ceramic electrolytes, represent a kind of palliative. Their conductivity is higher than that of amorphous electrolytes, but lower than that of crystalline electrolytes. Such glass-ceramic electrolytes can be obtained by crystallization of real glass electrolytes. The separation of thermodynamically stable crystalline phases from the initial glass leads to a decrease in intercrystalline resistance. For example, glass–ceramic electrolytes obtained by heat treatment of $Li_2O–Al_2O_3–TiO_2–P_2O_5$ glasses are described in [48]. The maximum conductivity of 1.3 mS/cm was achieved in a system heat-treated at a temperature of 950 °C.

Glass ceramics of the compositions $70Li_2S–30P_2S_5$ [49], $80Li_2S\text{-}20P_2S_5$ [50], $Li_{3,25}P_{0,95}S_4$ [51] и $Li_7P_3S_{11}$ [51] have even higher conductivity. Glass ceramics $70Li_2S\text{-}30P_2S_5$ were synthesized by heat treatment of the corresponding glass at a temperature of about 240 °C (slightly higher than the crystallization temperature). This treatment resulted in an increase in conductivity at room temperature to 3.2 mS/cm. The conductivity of glass ceramics $80Li_2S\text{-}20P_2S_5$ is 0.74 ms/cm. Glass ceramics $Li_{3.25}P_{0.95}S_4$ and $Li_7P_3S_{11}$ demonstrate conductivity at room temperature of 1.3 and 17 mS/cm (!) The glass-ceramic electrolyte $Li_7P_3S_{11}$ ($70Li_2S\text{-}30P_2S_5$) is characterized not only by the highest conductivity, but also by the lowest activation energy of 17 kJ/mol at room temperature (and, consequently, the weakest temperature dependence of conductivity).

The most popular crystalline electrolytes of the (ABO_3) type peroxite family with A = Li, La, and B = Ti are solid solutions with the general formula $Li_{3x}La_{2/3\text{-}x\text{-}1/3–2x}TiO_3$ (where the square indicates the lattice vacancy) [52]. Usually $0.04<x<0.17$, in this case the abbreviation LLTO is used. Such electrolytes have a conductivity at room temperature of about 1 mS/cm. Lithium-enriched oxyhalides with an anti-perovskite structure have an even higher conductivity. For example, the compound $Li_3OCl_{0.5}Br_{0.5}$ exhibits a specific conductivity of about 2 mS/cm at room temperature and about 5 mS/cm at 230 °C [53].

A classic example of an electrolyte with the NASICON structure is $NaA^{IV}_2(PO_4)_3$, where A^{IV}=Ge, Ti, and Zr. Such a structure can be represented as a $[A_2P_3O_{12}]–$ framework consisting of AO_6 octahedra and PO_4 tetrahedra. The most popular Li^+ conducting electrolyte with a NASICON-like structure is $Li_{1.3}Al_{0.3}Ti_{1.7}(PO_4)_3$ (LATP), belonging to the family with the general formula $Li_{1+x}Ti_{2\text{-}x}M_x(PO_4)_3$ (M=Al, Ga, B, Sc). Among Li^+-conducting electrolytes with a NASICON-like structure, $Li_{1+x}Al_xGe_{2\text{-}x}(PO_4)_3$ (LAGP) has the highest conductivity at room temperature of 3 mS/cm^3. Of particular interest is a silicon-substituted electrolyte in which part of the phosphorus is replaced by silicon $Li_{1+x+y}Ti_{2\text{-}x}Al_xSi_y(PO_4)_{3\text{-}y}$.

The electrolyte analogue with the NASICON – LISICON structure with the formula $Li_{2+2x}Zn_{1\text{-}x}GeO_4$ has too low conductivity and is of no practical interest. At the same time, thio-LISICON is very attractive [54]. The highest conductivity, 2.2 mS/cm, is shown by an electrolyte of the composition $Li_{3.25}Ge_{0.25}P_{0.75}S_4$ (which can be considered as $Li_{4\text{-}x}Ge_{1\text{-}x}P_xS$ with x=0.75). At the same time, the $Li_2S–GeS_2–P_2S_5$ electrolytes proved to be incompatible with the graphite negative electrode. To solve this problem, the authors of [55] proposed a battery design with a two-layer solid electrolyte. The layer facing the negative (graphite) electrode is $LiI–Li_2S–P_2S_5$ glass, and the layer facing the positive ($LiCoO_2$) electrode is $Li_2S–GeS_2–P_2S_5$ crystalline material. It is known that the first electrolyte is resistant to electrochemical reduction, and the second to oxidation.

An even higher conductivity, 12 ms/cm, is provided by a similar superionic conductor of the composition $Li_{10}GeP_2S_{12}$ with a special crystal structure [56].

Special attention has recently been paid to solid electrolytes with structures similar to garnet. Ideal garnets can be represented by the general formula $A_3B_2(XO_4)_3$, where A = Ca, Mg, Y, La or rare earth elements; B = Al, Fe, Ga, Ge, Mn, Ni or V; X = Si, Ge or Al. The most important feature of the garnet

structure is the ability to introduce Li^+ ions into the structure. Garnets usually contain from five to seven Li atoms per formula unit. An increase in the number of lithium atoms in the formula unit to five, as, for example, in $Li_5La_3B'_2O_{12}$ (B' = Bi, Sb, Na, Ta), leads to an increase in ionic conductivity by three orders of magnitude to 2×10^{-5} S/cm [57]. Partial replacement of Zr in lithium-enriched garnet $Li_7La_3Zr_2O_{12}$ with Nb makes it possible to obtain a material with lithium-ion conductivity up to 0.8 mS/cm [58]. $Li_7La_3Zr_2O_{12}$ doped with Ga has an ionic conductivity of 0.54 mS/cm [59]. For substituted garnet $Li_{6.75}La_3Zr_{1.75}Ta_{0.25}O_{12}$, room temperature conductivity of 0.9 mS/cm was reported [60]. Doping of an electrolyte with a garnet structure by a bromide anion leads to a two-three-fold increase in the conductivity of Li^+ ions.

Fig. 4 summarizes the temperature dependence of the conductivity of various solid electrolytes. As a rule, these dependences are well described by the Arrhenius equation (unlike many liquid electrolytes). Fig. 4 also clearly shows how the conductivity of the new electrolytes has increased compared to LiPON.

Materials for negative electrodes. As already mentioned, a significant advantage of solid-state thin-film batteries is the possibility of using lithium metal as a negative electrode. Lithium has the maximum theoretical specific capacity and the most negative equilibrium potential, therefore, the use of lithium metal, all other things being equal, provides the highest discharge voltage. However, the use of lithium metal as a rechargeable negative electrode in batteries with liquid aprotic electrolyte encounters well-known fundamental problems of dendrite formation and encapsulation. Both problems lead to a drastic reduction in service life.

When lithium metal comes into contact with a solid electrolyte, the problems of dendrite formation do not play such a decisive role as in the case of liquid electrolytes. This statement is clearly confirmed by the successful commercialization of fully solid-state batteries with a lithium metal negative electrode, implemented at Oak Ridge National Laboratory (USA) at the beginning of the current millennium, as well as in companies such as STMicroelectronics, CymbetTM Corp., Front Edge Technology, Inc., Exxellatron, etc. For example, STMicroelectronics claimed that its thin-film batteries last up to 4,000 cycles. To combat dendrite formation at the interface with solid electrolytes, the same techniques are used that have been developed in systems with liquid electrolyte, primarily the creation of a lithium-ion current-carrying substrate and the application of artificial SEI (solid electrolyte interface, passive film) [61].

As a rule, lithium electrodes are applied by thermal evaporation or magnetron sputtering directly onto a solid electrolyte [62]. The typical thickness of a lithium thin–film electrode is 2–5 μm, which corresponds to a capacity of 0.4–1.0 mAh/cm^2.

A serious disadvantage of lithium metal negative electrode batteries is the limited operating temperature, determined by the melting point of lithium (180.54 °C). Since thin-film solid-state batteries are designed primarily for microelectronic devices, these batteries are used in modern semiconductor technology, i.e. they should be suitable for soldering at higher temperatures. A rather ingenious option to solve this problem is the so-called "lithium-free construction" [63]. Such a lithium-free battery is assembled without lithium metal (and, therefore, can withstand high-temperature solder melting procedures), but with some excess of the active material of the positive electrode. During the first charge, the required amount of lithium is deposited on the current collector. (In this respect, "lithium-free" batteries are similar to the recently popular so-called "anode-free" batteries.) For a lithium-free battery to function properly, it is very important that the negative electrode current collector material does not form intermetallic compounds with lithium. The most suitable material in this regard is copper, which is used as current receivers in conventional lithium-ion batteries, although some alternative materials such as Ti, Co and TiN are also being discussed.

Another approach to increase the operating temperature of thin-film solid-state batteries is to replace pure lithium with a lithium alloy, such as an alloy with magnesium. The melting point of such an alloy, depending on the magnesium content, ranges from 200 °C with a magnesium content of 4 at.% up to 400 °C with a magnesium content of 40 at.%.

However, a more fundamental solution to the problem is to replace the lithium electrode with an electrode typical of lithium-ion batteries, that is, an electrode in which lithium ions are reversibly embedded in a matrix. Elements of the 4th group of the Periodic Table (carbon, silicon, germanium, tin), oxides and some other compounds can be used as such matrices (as in traditional lithium-ion batteries).

Silicon is known to have a record capacity for the reversible incorporation of lithium. When lithium is introduced into silicon, intermetallic alloys are formed, and the most lithium-rich intermetallic compound is $Li_{4.4}Si$ ($Li_{22}Si_5$), which corresponds to a specific capacity of 4200 mAh/g. Such an alloy is formed only at elevated temperatures. At room temperature, the most lithium-rich intermetallic compound is $Li_{3.75}Si$ ($Li_{15}Si_4$), which corresponds to a specific capacity of 3590 mAh/g. It should be emphasized that these specific capacity values relate to the process of introducing lithium into silicon,

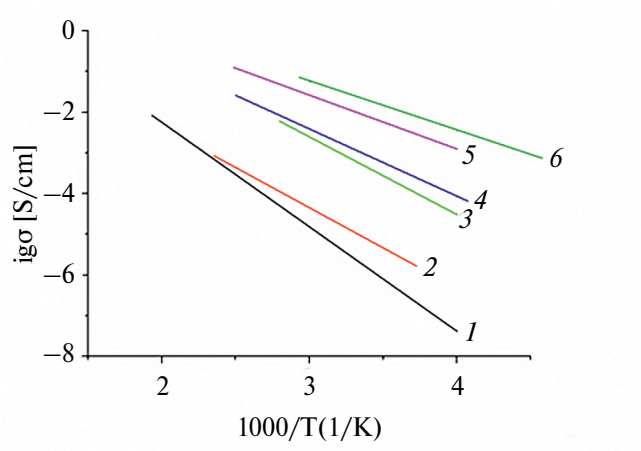

Fig. 4. Temperature dependence of the specific conductivity of solid electrolytes. *1* – LiPON, *2* – $Li_{3.6}Si_{0.6}P_{0.4}O_4$, *3* – $Li_{0.5}La_{0.5}TiO_3$, *4* – glass-ceramic $Li_7P_3S_{11}$, *5* – $Li_{10}GeP_2S_{12}$, *6* – $Li_{9.54}Si_{1.74}P_{1.44}S_{11.7}Cl_{0.3}$.

i.e. to the charge of the negative electrode. During discharge, i.e., when lithium is extracted from $Li_{3.75}Si$ intermetallide, the specific capacity is 1852 mAh/g (recall that the specific capacity of pure lithium is 3828 mAh/g). The introduction of lithium into silicon proceeds at potentials close to the potential of lithium, and its anode extraction is mainly in the range of 0.3–0.5 V (Li^+/Li).

The fundamental possibility of long-term operation of a silicon electrode in contact with a solid electrolyte (LiPON) was experimentally confirmed in [64]. In [65], a boron-doped LiPON electrolyte was used. In a later work [66], the compatibility of porous silicon with a glassy electrolyte of the composition $80Li_2S{\cdot}20P_2S_5$ was shown. In this work, for 100 cycles, the capacity of the silicon electrode was almost 3000 mAh/g. In [67, 68], the operability of amorphous silicon electrodes in contact with a glass-ceramic electrolyte of the composition $70Li_2S{\cdot}30P_2S_5$ was shown. [69] describes the characteristics of a monolithic silicon electrode with a thickness of 1 μm in contact with an electrolyte with a garnet structure ($Li7La_3Zr_2O_{12}$ doped with 3 wt.% Al_2O_3). A specific capacity of 2685 mAh/g has been achieved here. An increase in the thickness of the electrode to 2 and 3 μm led to an expected decrease in capacity to 1700 and 830 mAh/g. Stable cycling of silicon electrodes with a columnar structure in contact with an argyrodite-like electrolyte of the composition Li_6PS_5Cl was reported in [70]. Similar results for electrodes made of silicon microparticles are given in [71–73]. The latest work also showed that the introduction of a small amount of LiI into the sulfide electrolyte leads to an increase in the elasticity of the electrolyte and protects silicon particles from destruction during lithiation-delithiation.

Electrodes in the form of films from a silicon-FeS mixture with a thickness of up to 1 μm in contact with the aforementioned sulfide glass-ceramic electrolyte demonstrated specific capacitance of 3000 and 2200 mAh/g when discharged in C/10 and 10 C modes [74].

It is known that when a sufficiently large amount of lithium is introduced into silicon, a significant increase in the specific volume occurs, leading to internal stresses and destruction of the material. To prevent this destruction, nanomaterials based on silicon and its alloys are widely used in traditional lithium-ion batteries with liquid electrolyte. A variety of nanoforms (nanopowders, nanofibers, thin films, etc.) are generally used. Multilayer structures in which thin layers of silicon are interspersed with layers of other materials are of particular interest [75–81]. Si-O-Al layered structures, which have proven themselves well in contact with the LiPON solid electrolyte, are described in [82–87]. Among other silicon-based composite materials used as negative electrodes in contact with solid electrolytes, composites with carbon [88], tin [89], and even such exotic materials as $Li_xTi_4Ni_4Si_7$ [90, 91] should be mentioned.

When using silicon in the form of micro- and nanopowders, a solid electrolyte is introduced into the active mass of the electrode [92, 93]. Amorphous silicon films also show a good ability to cycle in contact with a solid electrolyte [94, 95].

If silicon has the maximum specific capacity for the introduction of lithium, then lithium titanate $Li_4Ti_5O_{12}$ has the best cyclability. A distinctive feature of this material is the practical constancy of its specific volume during full lithiation (and reverse delithiation) and, as a result, the absence of internal stresses during cycling of the electrodes [96]. The process of reversible lithiation/delithiation is described by the equation

$$Li_4Ti_5O_{12} + 3\,e^- + 3\,Li^+ \leftrightarrow Li_7Ti_5O_{12}, \qquad (1)$$

therefore, the theoretical specific capacity of this process is 175 mAh/g. Lithium titanate, as such and in the form of various doped derivatives, is widely used in liquid electrolyte batteries. Examples of its use in contact with solid electrolytes are quite rare. In [97, 98], the characteristics of a model battery with a negative electrode made of lithium-indium alloy and a positive electrode made of $Li_4Ti_5O_{12}$ composite, a glass-ceramic electrolyte ($70Li_2S{\cdot}29P_2S_5{\cdot}1P_2S_3$) and an electrically conductive carbon fiber additive are given. The charging and discharging characteristics of such a model showed almost horizontal lines (which is typical for $Li_4Ti_5O_{12}$). The models withstood 700 cycles at a current density of 10 mA/cm^2 without noticeable degradation. The specific capacity of $Li_4Ti_5O_{12}$ in this case was 140 mAh/g. Models

of batteries with sulfide electrolytes of the compositions $Li_{9.54}Si_{1.74}P_{1.44}S_{11.7}Cl_{0.3}$ and $Li_{9.6}P_3S_{12}$ are described in [99]. In these models, a mixture of $LiCoO_4$ with an electrolyte and an electrically conductive additive (acetylene black) was used as the positive electrode, and a mixture of $Li_4Ti_5O_{12}$ composite with graphite, an electrolyte and an electrically conductive additive was used as the negative electrodes. It is reported that phenomenal results have been achieved: stable cycling of up to 1000 cycles in modes up to 0.9 C at a temperature of –30 °C and in modes up to 150 C and 1500 C at temperatures of 25 and 100 °C, respectively.

Materials for positive electrodes. The most popular active material for the positive electrodes of fully solid-state lithium-ion batteries remains lithium cobalt oxide $LiCoO_2$ (already mentioned in the references [20, 32, 40, 56, 63, 79, 99]. Unfortunately, deep cycling (dividing at potentials above 4.2 V, which means the extraction of approximately 50% or more of Li) leads to irreversible distortions of the $LiCoO_2$ crystal lattice from hexagonal to monoclinic symmetry, and this change worsens the cycling characteristics. In reality, only about 50% of lithium is extracted during cycling, that is, the electrode process is described by the equation

$$LiCoO_2 \leftrightarrow x\,Li^+ + x\,e + Li_{1-x}CoO_2, \qquad (2)$$

where $0<_x<0.5$.

The theoretical specific capacity of $LiCoO_2$ is 273 mAh/g, while the actual values do not exceed 140 mAh/g. Despite this, $LiCoO_2$ is still used in thin-film batteries with various solid electrolytes [100–114]. It was with such positive electrodes that flexible translucent batteries were created [100, 102]. However, the interaction of $LiCoO_2$ with sulfide electrolytes caused a certain problem [104–106]. Upon contact of these materials, mutual diffusion occurs and the formation of a kind of intermediate layer, which complicates interphase transport. One of the ways to combat this unpleasant phenomenon is to apply the thinnest (several monolayers) coating of various materials to the surface of the $LiCoO_2$ electrode, including Al_2O_3 [107], $LiNbO_3$ [108], $Li_4Ti_5O_{12}$ [109] and even Nb [110].

A radical method of increasing the specific capacity (i.e., the depth of cycling) of $LiCoO_2$-based electrodes, as well as reducing their cost, is the use of mixed lithium-containing oxides, i.e., lithium-cobalt oxides, in which some of the cobalt ions are replaced by ions of one or two other metals. Quite a lot of different multicomponent lithium oxides have been studied, of which the most popular are the $LiNi_xCo_yMn_zO_2$ (NMC) and $LiNi_xCo_yAl_zO_2$ (NCA) systems, including $LiNi_{1/3}Co_{1/3}Mn_{1/3}O_2$ and $LiNi_{0,8}Co_{0,15}Al_{0,05}O_2$ systems. Both materials are currently considered environmentally friendly, fairly cheap products with high specific capacity and good cyclability. NMC and NCA are very widely used in lithium-ion batteries with a liquid electrolyte, and examples of their use in fully solid-state batteries are limited (for instance, [115–119].

The theoretical specific capacity of NMC is 278 mAh/g, in practice it reaches up to 230 mAh/g. NMC has the same structure as $LiCoO_2$, i.e. it belongs to the type α-$NaFeO_2$ layered structure of rock salt. From a formal point of view, NMC can be considered as a solid solution of $LiCoO_2$-$LiNiO_2$-$LiMnO_2$ (1:1:1). In the initial state, nickel, cobalt, and manganese in NMC are in the 2+, 3+, and 4+ states, respectively, and Ni (2+/4+) and Co (3+/4+) transitions occur during cycling, and during the dilithiation, the Ni^{2+}/Ni^{3+} transition occurs first (with increasing $_x$ in the formula $Li_{1-x}[Co_{1/3}Ni_{1/3}Mn_{1/3}]O_2$ from 0 to 1/3), then the transition Ni^{3+}/Ni^{4+} (with x in the range $1/3 <x <2/3$) and finally Co^{3+}/Co^{4+} (with an increase in x from 2/3 to 1). It is this scheme of redox processes that provides the above value of the theoretical specific capacity.

The stable cycling of NMC is due to a slight change in the crystal lattice. When extracting 60% of the total amount of lithium contained in $LiNi_{1/3}Mn_{1/3}Co_{1/3}O_2$, the volume of the crystal cell does not change and amounts to 0.1 nm^3, and when it is almost completely removed, it decreases to only 0.095 nm^3.

The practical specific capacity of NCA also exceeds 200 mAh/g, and the cycling capacity of such electrodes is not inferior to traditional $LiCoO_2$-based electrodes.

Upon contact of both NMC and NCA with sulfide solid electrolytes, as in the case of $LiCoO_2$, a transition layer with increased resistance is also formed. Thin protective layers of various materials, including diamond-like carbon [115], $Li_4Ti_5O_{12}$ [116], and HfO_2 [118], are also applied to the surface of NMC and NCA.

In the initial period of the development of traditional lithium-ion batteries, lithium-manganese spinels of a composition close to $LiMn_2O_4$, as well as lithium-mixed nickel-manganese oxides, were widely used as the active material of the positive electrode. An important advantage of lithium-manganese spinels over other materials is their relatively low cost. Manganese compounds are much less toxic than cobalt compounds, and the manganese content in the earth's crust is also much higher than that of cobalt. In all-solid-state lithium-ion batteries, lithium manganese oxides are used much less [19, 62, 114, 120, 121], but with different types of electrolytes (LiPON [19, 62, 120], garnet type [114], phosphate [121]).

Electrodes made of lithium ferrophosphate ($LiFePO_4$), which belongs to the class of polyanionic compounds, are very widely used in batteries with liquid electrolyte. The theoretical specific capacity of $LiFePO_4$ is 170 mAh/g. The most important advantages of lithium ferrophosphate are relatively low cost, accessibility, non-toxicity, safety in operation, and most importantly, good cyclability. The main disadvantage is the extremely low electronic conductivity and low diffusion coefficient of lithium, which forces it to be used as a nanomaterial with a thin (about 3 nm) carbon coating, as well as to resort to doping with other cations, or fluoride and chloride anions.

The reversible process of lithium extraction and incorporation (during charging and discharging of the electrode) is described by a simple equation:

$$LiFePO_4 \leftrightarrow FePO_4 + Li^+ + e. \quad (3)$$

$LiFePO_4$ and $FePO_4$ are isostructural, so the course of reaction (3) is not accompanied by any structural changes, which ensures very good cycling of lithium ferrophosphate-based electrodes and the possibility of accelerated charges and discharges. The mutual solubility of $LiFePO_4$ and $FePO_4$ is insignificant, therefore, the process (3) proceeds according to a two-phase mechanism. In this respect, the $LiFePO_4/FePO_4$ system is very similar to the $Li_4Ti_5O_{12}/Li_7Ti_5O_{12}$ system described above. The galvanostatic curves obtained on lithium ferrophosphate electrodes also show almost horizontal sections (sections with constant potential) corresponding to the existence of two contacting phases $Li_\delta FePO_4$ and $Li_{1-\delta}FePO_4$. An example of using $LiFePO_4$-based electrodes in a solid electrolyte system is [122], which describes the design of a 3D battery with negative electrodes made of silicon nanorods, LiPON as an electrolyte, and a positive electrode made of a $LiFePO_4$ composite with carbon. Other examples of using $LiFePO_4$ are the works [123, 124]. The latter work is notable for the fact that it describes a mock-up of a lithium-ion battery in which a positive electrode from $LiFePO_4$ is combined with a negative electrode from $Li_3V_2(PO_4)_3$. Lithium vanadophosphate $Li_3V_2(PO_4)_3$ can function both as a negative electrode (then the V^{3+}/V^{2+} redox system with an operating potential of about 1.8 V (Li/Li^+) is implemented in it) and as a positive electrode (in this case, the V^{4+}/V^{3+} redox system with an operating potential is implemented, close to 4 V). The article [125] describes a symmetrical solid-state battery in which in the discharged state both electrodes have $Li_3V_2(PO_4)_3$. The electrolyte here is phosphate $Li_{1.5}Al_{0.5}Ge_{1.5}(PO_4)_3$ with the NASICON structure. When charged, one electrode is oxidized to $LiV_2(PO_4)_3$, and the other is reduced to $Li_5V_2(PO_4)_3$ with the transfer of two electrons and two Li^+ ions.

In general, the ability of vanadium to change its valence in oxide compounds in the range from +2 to +5 makes it tempting to use vanadium oxides as positive electrodes of lithium-ion batteries. Theoretically, the specific capacity of vanadium pentoxide can reach 883.5 mAh/g, which is much higher than the specific capacity of other compounds. Indeed, V_2O_5 was used in the first samples of fully solid-state lithium-ion batteries [18, 19, 126–128]. Unfortunately, the introduction of lithium into the crystal lattice of vanadium oxide is associated with significant structural changes. Even with the introduction of 2 moles of lithium per mole of V_2O_5, the γ-$Li_2V_2O_5$ phase appears with an irreversible change in structure. Unlike lithium ferrophosphate, vanadium oxide-based materials operate in a fairly wide range of potentials, which is a definite disadvantage.

Sulfides, including nickel sulfides [129, 130], titanium sulfides [131], and molybdenum sulfides [132], have become significantly less widespread as the active materials of the positive electrode of all-solid-state lithium-ion batteries.

PRODUCTION OF SOLID-STATE LITHIUM-ION BATTERIES

The scale of commercial production of fully solid-state lithium-ion batteries is still quite modest. In some cases, such production facilities existed for several years and then closed.

Cymbet Corp. (USA) produced miniature batteries (with overall dimensions of 1.7x2.25x 0.2 mm and 5.7x6.1.x0.2 mm) with a nominal capacity of 5 and 50 mAh. Front Edge Technology Inc. (USA) produced $LiCoO_2$|LiPON|Li batteries with dimensions of 25x20x0.1 mm and 25x20x0.3 mm with a capacity of 100 and 1000 mAh. Similar batteries with a capacity of 1000 mAh were manufactured by Infinity Power Solutions (USA), STMicroelectronics (France) and Excellatron (USA) [82].

It was reported [7] that Fujifilm Co. and Samsung produced batteries with sulfide electrolyte in a laminate case. Samsung batteries had a specific energy of 175 Wh/kg, they used positive electrodes based on NMC and negative electrodes based on graphite.

In 2016, Sony released batteries with LiPON electrolyte [7]. ProLogium Corporation (China) has announced the launch of ceramic electrolyte batteries with a specific energy of 810 Wh/l.

CONCLUSION

Despite the fact that all-solid-state thin-film lithium-ion batteries represent a special, relatively small category of batteries in terms of production

volume, the need for them has been increasing, especially in recent decades. This need is due to both the rapid development of microelectronics and high technologies in general, and the fundamental advantages of all-solid-state batteries in comparison with traditional batteries with liquid electrolytes (increased fire and explosion safety, the possibility of using lithium metal electrodes, the possibility of using technologies compatible with the manufacturing technology of integrated circuits and other semiconductor devices).

It would seem that such indisputable advantages would stimulate the development of large-scale production of all-solid-state lithium-ion batteries, however, as noted in the section "Production of solid-state lithium-ion batteries", only relatively small-sized products with a capacity of no more than 1 mAh have actually become production items. The reasons for this lag in industrial manufacturing, both from consumer demands and from the results of basic research, have been repeatedly discussed in the literature (see, for example, [2, 13, 133]). Along with the mentioned advantages of fully solid-state batteries, they also have certain disadvantages, in particular technological problems, and scaling, i.e. the transition to increasingly energy-intensive single products, is accompanied by increasing technological problems [134]. For example, the relatively low electronic conductivity of solid inorganic electrolytes dictates the need to minimize their thickness; at the same time, as the area of a single product increases, the risk of uneven thickness and other indicators increases markedly, as well as the risk of defects, in particular the appearance of through pores.

With an increase in the area of the electrodes in a single battery, the probability of local excess of the interfacial resistance at the interface of the electrode with a solid electrolyte increases markedly (which is impossible in systems with a liquid electrolyte) [135]. An increase in the size (and capacity) of individual products also encounters certain economic problems [136, 137].

Progress in the development of solid-state thin-film lithium-ion batteries is determined primarily by improvements in solid electrolytes, as well as improvements in functional electrode materials. In the future, we can expect the appearance of solid electrolytes with increased conductivity and a lithium transfer number close to unity. Of particular fundamental interest is the study of processes at the interface between an electrode and a solid electrolyte. Technologically, the development of 3D structures and the use of 3D printing is of particular interest.

FUNDING

The work was carried out with the financial support of the Ministry of Science and Higher Education of the Russian Federation.

CONFLICT OF INTEREST

The authors declare that there is no conflict of interest.

REFERENCES

1. Kulova, T., Mironenko, A., Rudy, A., and Skundin, A. *All Solid State Thin-Film Lithium-Ion Batteries: Materials, Technology, and Diagnostics,* CRC Press. Taylor & Francis Group. 2021. 214 p. ISBN 9780367086824
2. Guo, Y., Wu, S., He, Y., Kang, F., Chen, L., Li, H., and Yang, Q., Solid-state lithium batteries: Safety and prospects, *eScience*, 2022, vol. 2, p. 138. https://doi.org/10.1016/j.esci.2022.02.008
3. Patil, A., Patil, V., Shin, D.W., Choi, J., Paik, D., and Yoon, S., Issue and challenges facing rechargeable thin film lithium batteries, *Mat. Res. Bull.*, 2008, vol. 43, p. 1913. doi:10.1016/j.materresbull.2007.08.031
4. Oudenhoven, J.F.M., Baggetto, L., and Notten, P.H.L., All-Solid-State Lithium-Ion Microbatteries: A Review of Various Three-Dimensional Concepts, *Adv. Energy Mater.*, 2011, vol. 1, p. 10. https://doi.org/10.1002/aenm.201000002
5. Zhou, Y., Xue, M., and Fu, Z., Nanostructured thin film electrodes for lithium storage and all-solid-state thin-film lithium batteries, *J. Power Sources*, 2013, vol. 234, p. 310. http://dx.doi.org/10.1016/j.jpowsour.2013.01.183
6. Ko, J., and Yoon, Y.S., Lithium phosphorus oxynitride thin films for rechargeable lithium batteries: Applications from thin-film batteries as micro batteries to surface modification for large-scale batteries, *Ceram. Int.*, 2022, vol. 48, p. 10372. https://doi.org/10.1016/j.ceramint.2022.02.173
7. Sun, C., Liu, J., Gong, Y., Wilkinsone, D.P., and Zhang, J., Recent advances in all-solid-state rechargeable lithium batteries, *Nano Energy*, 2017, vol. 33, p. 363. http://dx.doi.org/10.1016/j.nanoen.2017.01.028
8. Patil, A., Patil, V., Choi, J., Kim, J., and Yoon, S., Solid Electrolytes for Rechargeable Thin Film Lithium Batteries: A Review, *J. Nanosci. Nanotechnol.*, 2017, vol. 17, p. 29. DOI:10.1166/jnn.2017.12699
9. Xu, R.C., Xia, X.H., Zhang, S.Z., Xie, D., Wang, X.L., and Tu, J.P., Interfacial challenges and progress for inorganic all-solid-state lithium batteries, *Electrochim. Acta,* 2018, vol. 284, p. 177. https://doi.org/10.1016/j.electacta.2018.07.191
10. Moitzheim, S., Put, B., and Vereecken, P.M., Advances in 3D Thin-Film Li-Ion Batteries, *Adv. Mater. Interfaces,* 2019, vol. 6, article # 1900805. DOI: 10.1002/admi.201900805

11. Clement, B., Lyu, M., Kulkarni, E.S., Lin, T., Hua, Y., Lockett, V., Greig, C., and Wanga, L., Recent Advances in Printed Thin-Film Batteries, *Engineering,* 2022, vol. 13, article # 238. https://doi.org/10.1016/j.eng.2022.04.002
12. Yu, Y., Gong, M., Dong, C., and Xu, X., Thin-film deposition techniques in surface and interface engineering of solid-state lithium batteries, *Next Nanotechnol.*, 2023, vol. 3–4, article # 100028. https://doi.org/10.1016/j.nxnano.2023.100028
13. Machín, A., Morant, C., and Márquez, F., Advancements and Challenges in Solid-State Battery Technology: An In-Depth Review of Solid Electrolytes and Anode Innovations, *Batteries*, 2023, vol. 10, article # 29. https://doi.org/10.3390/batteries10010029
14. Jetybayeva, A., Aaron, D.S., Belharouak, I., and Mench, M.M., Critical review on recently developed lithium and non-lithium anode-based solid-state lithium-ion batteries, *J. Power Sources*, 2023, vol. 566, article # 232914. https://doi.org/10.1016/j.jpowsour.2023.232914
15. Wu, D., Chen, L., Li, H., and Wu, F., Solid-state lithium batteries-from fundamental research to industrial progress, *Prog. Mater. Sci.*, 2023, vol. 139, article # 101182. https://doi.org/10.1016/j.pmatsci.2023.101182
16. Shalaby, M.S., Alziyadi, M.O., Gamal, H., and Hamdy, S., Solid-state lithium-ion battery: The key components enhance the performance and efficiency of anode, cathode, and solid electrolytes, *J. Alloys Comp.*, 2023, vol. 969, article # 172318. https://doi.org/10.1016/j.jallcom.2023.172318
17. Bates, J.B., Dudney, N.J., Gruzalski, G.R., Zuhr, R.A., Choudhury, A., Luck, C.F., and Robertson, J.D., Electrical properties of amorphous lithium electrolyte thin films, *Solid State Ionics*, 1992, vol. 53–56, p. 647. https://doi.org/10.1016/0167–2738(92)90442-R
18. Bates, J.B., Dudney, N.J., Gruzalski, G.R., Zuhr, R.A., Choudhury, A., Luck, C.F., and Robertson, J.D., Fabrication and characterization of amorphous lithium electrolyte thin films and rechargeable thin-film batteries, *J. Power Sources,* 1993, vol. 43/44, p. 103. https://doi.org/10.1016/0378–7753(93)80106-Y
19. Bates, J.B., Dudney, N.J., Lubben, D.C., Gruzalski, G.R., Kwak, B.S., Yu, X., and Zuhr, R.A., Thin-film rechargeable lithium batteries, *J. Power Sources,* 1995, vol. 54, p. 58. https://doi.org/10.1016/0378–7753(94)02040-A
20. Wang, B., Bates, J.B., Hart, F.X., Sales, B.C., Zuhr, R.A., and Robertson, J.D., Characterization of Thin-Film Rechargeable Lithium Batteries with Lithium Cobalt Oxide Cathodes, *J. Electrochem. Soc.*, 1996, vol. 143, p. 3203. DOI 10.1149/1.1837188
21. Notten, P.H.L., Roozeboom, F., Niessen, R.A.H., and Baggetto, L., 3-D Integrated All-Solid-State Rechargeable Batteries, *Adv. Mater.*, 2007, vol. 19, p. 4564. DOI: 10.1002/adma.200702398
22. Ferrari, S., Loveridge, M., Beattie, S.D., Jahn, M., Dashwood, R.J., and Bhagat, R., Latest advances in the manufacturing of 3D rechargeable lithium microbatteries. *J. Power Sources*, 2015, vol. 286, p. 25. http://dx.doi.org/10.1016/j.jpowsour.2015.03.133
23. Long, J.W., Dunn, B., Rolison, D.R., and White, H.S., Three-dimensional battery architectures, *Chem. Rev.,* 2004, vol. 104, p. 4463. https://doi.org/10.1021/cr020740l
24. Edstrom, K., Brandell, D., Gustafsson, T., and Nyholm, L., Electrodeposition as a Tool for 3D Microbattery Fabrication, *Interface*, 2011, vol. 20, no. 2, p. 41. DOI 10.1149/2.F05112if [open access]
25. Roberts, M., Johns, P., Owen, J., Brandell, D., Edstrom, K., El Enany, G., Guery, C., Golodnitsky, D., Lacey, M., Lecoeur, C., Mazor, H., Peled, E., Perre, E., Shaijumon, M.M., Simon, P., and Taberna, P.-L., 3D lithium ion batteries – from fundamentals to fabrication, *J. Mater. Chem.*, 2011, vol. 21, p. 9876. DOI: 10.1039/c0jm04396f
26. Arthur, T.S., Bates, D.J., Cirigliano, N., Johnson, D.C., Malati, P., Mosby, J.M., Perre, E., Rawls, M.T., Prieto, A.L., and Dunn, B., Three-dimensional electrodes and battery architectures, *MRS Bull.*, 2011, vol. 36, p. 523. https://doi.org/10.1557/mrs.2011.156
27. Rolison, D.R., Long, J.W., Lytle, J.C., Fischer, A.E., Rhodes, C.P., McEvoy, T.M., Bourga, M.E., and Lubers, A.M., Multifunctional 3D nanoarchitectures for energy storage and conversion, *Chem. Soc. Rev.*, 2009, vol. 38, p. 226. https://doi.org/10.1039/B801151F
28. Zhang, F., Wei, M., Viswanathan, V.V., Swart, B., Shao, Y., Wu, G., and Zhou, C., 3D printing technologies for electrochemical energy storage, *Nano Energy*, 2017, vol. 40, p. 418. http://dx.doi.org/10.1016/j.nanoen.2017.08.037
29. Sun, K., Wei, T.-S., Ahn, B.Y., Seo, J.Y., Dillon, S.J., and Lewis, J.A., 3D Printing of Interdigitated Li-Ion Microbattery Architectures, *Adv. Mater.*, 2013, vol. 25, p. 4539. DOI: 10.1002/adma.201301036
30. Wei, M., Zhang, F., Wang, W., Alexandridis, P., Zhou, C., and Wu, G., 3D direct writing fabrication of electrodes for electrochemical storage devices, *J. Power Sources*, 2017, vol. 354, p. 134. http://dx.doi.org/10.1016/j.jpowsour.2017.04.042
31. Yang, Y., Jeong, S., Hu, L., Wu, H., Lee, S.W., and Cui, Y., Transparent Lithium-Ion Batteries, *Proc. Natl. Acad. Sci. U.S.A.,* 2011, vol. 108, p. 13013. www.pnas.org/cgi/doi/10.1073/pnas.1102873108
32. Oukassi, S., Baggetto, L., Dubarry, C., Le Van-Jodin, L., Poncet, S., and Salot, R., Transparent Thin Film Solid-State Lithium Ion Batteries, *ACS Appl. Mater. Interfaces*, 2019, vol. 11, p. 683. DOI: 10.1021/acsami.8b16364
33. Zhang, Z., Shao, Y., Lotsch, B., Hu, Y.S., Li, H., Janek, J., Nazar, L.F., Nan, C., Maier, J., Armand, M., and Chen, L., New horizons for inorganic solid state

ion conductors, *Energy Environ. Sci.*, 2018, vol. 11, p. 1945. DOI: 10.1039/c8ee01053f

34. Takada, K., Progress in solid electrolytes toward realizing solid-state lithium batteries, *J. Power Sources*, 2018, vol. 394, p. 74. https://doi.org/10.1016/j.jpowsour.2018.05.003
35. Campanella, D., Belanger, D., and Paolella, A., Beyond garnets, phosphates and phosphosulfides solid electrolytes: New ceramic perspectives for all solid lithium metal batteries, *J. Power Sources*, 2021, vol. 482, article # 228949. https://doi.org/10.1016/j.jpowsour.2020.228949
36. Thangadurai, V., Narayanan, S., and Pinzaru, D., Garnet-type solid-state fast Li ion conductors for Li batteries: critical review, *Chem. Soc. Rev.*, 2014, vol. 43, p. 4714. DOI: 10.1039/c4cs00020j
37. Guo, R., Zhang, K., Zhao, W., Hu, Z., Li, S., Zhong, Y., Yang, R., Wang, X., Wang, J., Wu, C., and Bai, Y., Interfacial Challenges and Strategies toward Practical Sulfide-Based Solid-State Lithium Batteries, *Energy Mater. Adv.*, 2023, vol. 4, article #0022. https://doi.org/10.34133/energymatadv.0022
38. Liu, D., Zhu, W., Feng, Z., Guerfi, A., Vijh, A., and Zaghib, K., Recent progress in sulfide-based solid electrolytes for Li-ion batteries, *Mat. Sci. Eng. B*, 2016, vol. 213, p. 169. http://dx.doi.org/10.1016/j.mseb.2016.03.005
39. Zhang, X., Wang, J., Hu, D., Du, W., Hou, C., Jiang, H., Wei, Y., Liu, X., Jiang, F., Sun, J., Yuan, H., and Huang, X., High-performance lithium metal batteries based on composite solid-state electrolytes with high ceramic content, *Energy Storage Mater.*, 2024, vol. 65, article # 103089. https://doi.org/10.1016/j.ensm.2023.103089
40. Zhang, Z., Wang, X., Li, X., Zhao, J., Liu, G., Yu, W., Dong, X., and Wang, J., Review on composite solid electrolytes for solid-state lithium-ion batteries, *Mater. Today Sustainability*, 2023, vol. 21, article # 100316. https://doi.org/10.1016/j.mtsust.2023.100316
41. Devaraj, L., Thummalapalli, S.V., Fonseca, N., Nazir, H., Song, K., and Kannan, A.M., Comprehending garnet solid electrolytes and interfaces in all-solid lithium-ion batteries, *Mater. Today Sustainability*, 2024, vol. 25, article # 100614. https://doi.org/10.1016/j.mtsust.2023.100614
42. Han, Y., Chen, Y., Huang, Y., Zhang, M., Li, Z., and Wang, Y., Recent progress on garnet-type oxide electrolytes for all-solid-state lithium-ion batteries, *Ceram. Int.*, 2023, vol. 49, p. 29375. https://doi.org/10.1016/j.ceramint.2023.06.153
43. Joo, K.H., Sohn, H.J., Vinatier, P., Pecquenard, B., and Levasseur, A., Lithium Ion Conducting Lithium Sulfur Oxynitride Thin Film, *Electrochem. Solid State Lett.,* 2004, vol. 7, p. A256. DOI: 10.1149/1.1769317
44. Jones, S.D., Akridge, J.R., and Shokoohi, F.K., Thin film rechargeable Li batteries, *Solid State Ionics*, 1994, vol. 69, p. 357. https://doi.org/10.1016/0167–2738(94)90423–5
45. Ujiie, S., Hayashi, A., and Tatsumisago, M., Preparation and ionic conductivity of (100-x)($0.8Li_2S_{0.2}P_2S_5$)·xLiI glass–ceramic electrolytes, *J. Solid State Electrochem.*, 2013, vol. 17, p. 675. https://doi.org/10.1007/s10008–012–1900–7
46. Jung, W.D., Kim, J., Choi, S., Kim, S., Jeon, M., Jung, H., Chung, K.Y., Lee, J., Kim, B., Lee, J., and Kim, H., Superionic Halogen-Rich Li-Argyrodites Using In Situ Nanocrystal Nucleation and Rapid Crystal Growth, *Nano Lett.*, 2020, vol. 20, p. 2303. https://doi.org/10.1021/acs.nanolett.9b04597
47. Zhang, Z., Wu, L., Zhou, D., Weng, W., and Yao, X., Flexible Sulfide Electrolyte Thin Membrane with Ultrahigh Ionic Conductivity for All-Solid-State Lithium Batteries, *Nano Lett.*, 2021, vol. 21, p. 5233. https://doi.org/10.1021/acs.nanolett.1c01344
48. Fu, J., Superionic conductivity of glass-ceramics in the system Li_2O–Al_2O_3–TiO_2–P_2O_5, *Solid State Ionics*, 1997, vol. 96, p. 195. https://doi.org/10.1016/S0167–2738(97)00018–0
49. Mizuno, F., Hayashi, A., Tadanaga, K., and Tatsumisago, M., New, Highly Ion-Conductive Crystals Precipitated from Li_2S–P_2S_5 Glasses, *Adv. Mater.*, 2005, vol. 17, p. 918. DOI:10.1002/adma.200401286
50. Tatsumisago, M., Glassy materials based on Li_2S for all-solid-state lithium secondary batteries, *Solid State Ionics*, 2004, vol. 175, p. 13. https://doi.org/10.1016/j.ssi.2004.09.012
51. Seino, Y., Ota, T., Takada, K., Hayashi, A., and Tatsumisago, M., A sulphide lithium super ion conductor is superior to liquid ion conductors for use in rechargeable batteries, *Energy Environ. Sci.*, 2014, vol. 7, p. 627. DOI: 10.1039/c3ee41655k
52. Stramare, S., Thangadurai, V., and Weppner, W., Lithium Lanthanum Titanates: A Review, *Chem. Mater.*, 2003, vol. 15, p. 3974. https://doi.org/10.1021/cm0300516
53. Bohnke, O., The fast lithium-ion conducting oxides $Li_{3x}La_{2/3-x}TiO_3$ from fundamentals to application, *Solid State Ionics*, 2008, vol. 179, p.9. DOI: 10.1016/j.ssi.2007.12.022
54. Kanno, R. and Murayama, M., Lithium Ionic Conductor Thio-LISICON: The Li_2S–GeS_2–P_2S_5 System, *J. Electrochem. Soc.*, 2001, vol. 148, p. A742. DOI 10.1149/1.1379028
55. Takada, K., Inada, T., Kajiyama, A., Sasaki, H., Kondo, S., Watanabe, M., Murayama, M., and Kanno, R., Solid-state lithium battery with graphite anode, *Solid State Ionics*, 2003, vol. 158, p. 269. https://doi.org/10.1016/S0167–2738(02)00823–8
56. Kamaya, N., Homma, K., Yamakawa, Y., Hirayama, M., Kanno, R., Yonemura, M., Kamiyama, T., Kato, Y., Hama, S., Kawamoto, K., and Matsui, A., A lithium superionic conductor, *Nat. Mater.*, 2011, vol. 10, p. 682. DOI: 10.1038/NMAT3066

57. Murugan, R., Weppner, W., Schmid-Beurmann, P., and Thangadurai, V., Structure and lithium ion conductivity of bismuth containing lithium garnets $Li_5La_3Bi_2O_{12}$ and $Li_6SrLa_2Bi_2O_{12}$, *Mater. Sci. Eng. B.,* 2007, vol. 143, p. 14. https://doi.org/10.1016/j.mseb.2007.07.009

58. Ohta, S., Kobayashi, T., and Asaoka, T., High lithium ionic conductivity in the garnet type oxide $Li_{7-X}La_3(Zr_{2-X}, Nb_X)O_{12}$, *J. Power Sources*, 2011, vol. 196, p. 3342. https://doi.org/10.1016/j.jpowsour.2010.11.089

59. El Shinawi, H. and Janek, J., Stabilization of cubic lithium-stuffed garnets of the type ''$Li_7La_3Zr_2O_{12}$'' by addition of gallium, *J. Power Sources*, 2013, vol. 225, p. 13. https://doi.org/10.1016/j.jpowsour.2012.09.111

60. Allen, J.L., Wolfenstine, J., Rangasamy, E., and Sakamoto, J., Effect of substitution (Ta, Al, Ga) on the conductivity of $Li_7La_3Zr_2O_{12}$, *J. Power Sources*, 2012, vol. 206, p. 315. https://doi.org/10.1016/j.jpowsour.2012.01.131

61. Shen, Y., Zhang, Y., Han, S., Wang, J., Peng, Z., and Chen L., Unlocking the Energy Capabilities of Lithium Metal Electrode with Solid-State Electrolytes, *Joule*, 2018, vol. 2, p. 1674. https://doi.org/10.1016/j.joule.2018.06.021

62. Dudney, N., Thin film micro-batteries, *Interface*, 2008, no. 3, p. 44. DOI: 10.1149/2.F04083IF

63. Neudecker, B.J., Dudney, N.J., and Bates, J.B., "Lithium-Free" Thin-Film Battery with in situ Plated Li Anode, *J. Electrochem. Soc.*, 2000, vol. 147, p. 517. DOI: 10.1149/1.1393226

64. Baggetto, L., Niessen, R.A.H., and Notten, P.H.L., On the activation and charge transfer kinetics of evaporated silicon electrode/electrolyte interfaces, *Electrochim. Acta*, 2009, vol. 54, p. 5937. DOI:10.1016/j.electacta.2009.05.070

65. Phan, V.P., Pecquenard, B., and Le Cras, F., High-Performance All-Solid-State Cells Fabricated With Silicon Electrodes, *Adv. Funct. Mater.*, 2012, vol. 22, p. 2580. https://doi.org/10.1002/adfm.201200104

66. Sakabe, J., Ohta, N., Ohnishi, T., Mitsuishi, K., and Takada, K., Porous amorphous silicon film anodes for high-capacity and stable all-solid-state lithium batteries, *Commun. Chem.*, 2018, vol. 1, article # 24. https://doi.org/10.1038/s42004–018–0026-y

67. Miyazaki, R., Ohta, N., Ohnishi, T., Sakaguchi, I., and Takada, K., An amorphous Si film anode for all-solid-state lithium batteries, *J. Power Sources,* 2014, vol. 272, p. 541. http://dx.doi.org/10.1016/j.jpowsour.2014.08.109

68. Miyazaki, R., Ohta, N., Ohnishi, T., and Takada, K., Anode properties of silicon-rich amorphous silicon suboxide films in all-solid-state lithium batteries, *J. Power Sources,* 2016, vol. 329, p. 41. http://dx.doi.org/10.1016/j.jpowsour.2016.08.070

69. Ping, W., Yang, C., Bao, Y., Wang, C., Xie, H., Hitz, E., Cheng, J., Li, T., and Hu, L., A silicon anode for garnet-based all-solid-state batteries: Interfaces and nanomechanics, *Energy Storage Mater.*, 2019, vol. 21, p. 246. https://doi.org/10.1016/j.ensm.2019.06.024

70. Cangaz, S., Hippauf, F., Reuter, F.S., Doerfler, S., Abendroth, T., Althues, H., and Kaskel, S., Enabling High-Energy Solid-State Batteries with Stable Anode Interphase by the Use of Columnar Silicon Anodes, *Adv. Energy Mater.*, 2020, vol. 10, article # 2001320. DOI: 10.1002/aenm.202001320

71. Tan, D.H.S., Chen, Y., Yang, H., Bao, W., Sreenarayanan, B., Doux, J., Li, W., Lu, B., Ham, S., Sayahpour, B., Scharf, J., Wu, E.A., Deysher, G., Han, H.E., Hah, H.J., Jeong, H., Lee, J.B., Chen, Z., and Meng, Y.S., Carbon-free high-loading silicon anodes enabled by sulfide solid electrolytes, *Science*, 2021, vol. 373, p.1494. DOI: 10.1126/science.abg7217

72. Okuno, R., Yamamoto, M., Terauchi, Y., and Takahashi, M., Stable cyclability of porous Si anode applied for sulfide-based all solid-state batteries, *ACS Appl. Energy Mater.*, 2019, vol. 2, p. 7005. DOI: 10.1021/acsaem.9b01517

73. Kato, A., Yamamoto, M., Sakuda, A., Hayashi, A., and Tatsumisago, M., Mechanical properties of $Li_2S–P_2S_5$ glasses with lithium halides and application in all-solid-state batteries, *ACS Appl. Energy Mater.*, 2018, vol. 1, p. 1002. DOI: 10.1021/acsaem.7b00140

74. Cervera, R.B., Suzuki, N., Ohnishi, T., Osada, M., Mitsuishi, K., Kambara, T., and Takada, K., High performance silicon-based anodes in solid-state lithium batteries, *Energy Environ. Sci.*, 2014, vol. 7, p. 662. https://doi.org/10.1039/c3ee43306d

75. Roginskaya, Yu.E., Kulova, T.L., Skundin, A.M., Bruk, M.A., Klochikhina, A.V., Kozlova, N.V., Kal'nov, V.A., and Loginov, B.A., The Structure and Properties of a New Type of Nanostructured Composite Si/C Electrodes for Lithium Ion Accumulators, *Russ. J. Phys. Chem. A*, 2008, vol. 82, p. 1655. DOI: 10.1134/S0036024408100063

76. Roginskaya, Yu.E., Kulova, T.L., Skundin, A.M., Bruk, M.A., Zhikharev, E.N., Kal'nov, V.A., and Loginov, B.A., New Type of the Nanostructured Composite Si/C Electrodes, *Russ. J. Electrochem.*, 2008, vol. 44, p. 1197. DOI: 10.1134/S1023193508110025

77. Li, W., Yang, R., Wang, X., Wang, T., Zheng, J., and Li, X.J., Intercalated Si/C films as the anode for Li-ion batteries with near theoretical stable capacity prepared by dual plasma deposition, *J. Power Sources*, 2013, vol. 221, p. 242. https://doi.org/10.1016/j.jpowsour.2012.08.042

78. Kim, J.-B., Lim, S.-H., and Lee, S.-M., Structural Change in Si Phase of Fe/Si Multilayer Thin-Film Anodes during Li Insertion/Extraction Reaction, *J. Electrochem. Soc.*, 2006, vol. 153, p. A455. DOI: 10.1149/1.2158567

79. Hwang, C.-M. and Park, J.-W., Electrochemical characterizations of multi-layer and composite silicon–germanium anodes for Li-ion batteries using magnetron

sputtering, *J. Power Sources,* 2011, vol. 196, p. 6772. https://doi.org/10.1016/j.jpowsour.2010.10.061

80. Demirkan, M.T., Trahey, L., and Karabacak, T., Cycling performance of density modulated multilayer silicon thin film anodes in Li-ion batteries, *J. Power Sources,* 2015, vol. 273, p. 52. https://doi.org/10.1016/j.jpowsour.2014.09.027
81. Demirkan, M.T., Yurukcu, M., Dursun, B., Demir-Cakan, R., and Karabacak, T., Evaluation of double-layer density modulated Si thin films as Li-ion battery anodes, *Mater. Res. Express*, 2017, vol. 4, article # 106405. https://doi.org/10.1088/2053–1591/aa8f88
82. Rudyi, A.S., Mironenko, A.A., Naumov, V.V., Skundin, A.M., Kulova, T.L., Fedorov, I.S., and Vasil'ev, S.V., A Solid-State Lithium-Ion Battery: Structure, Technology, and Characteristics, *Tech. Phys. Lett*., 2020, vol. 46, no. 3, p. 217. DOI: 10.1134/S1063785020030141
83. Kulova, T.L., Mazaletsky, L.A., Mironenko, A.A., Rudy, A.S., Skundin, A.M., Tortseva, Yu.S., and Fedorov, I.S., Experimental Study of the Influence of the Porosity of Thin-Film Silicon-Based Anodes on Their Charge-Discharge Characteristics, *Russ. Microelectron*., 2021, vol. 50, no. 1, p. 45. DOI: 10.1134/S1063739720060074
84. Rudy, A.S., Mironenko, A.A., Naumov, V.V., Fedorov, I.S., Skundin, A.M., and Tortseva, Yu.S., Thin-Film Solid State Lithium-Ion Batteries of the $LiCoO_2$/Lipon/Si@O@Al System, *Russ. Microelectron*., 2021, vol. 50, no. 5, p. 333. DOI: 10.1134/S106373972105005X
85. Kurbatov, S., Mironenko, A., Naumov, V., Skundin, A., and Rudy, A., Effect of the Etching Profile of a Si Substrate on the Capacitive Characteristics of Three-Dimensional Solid-State Lithium-Ion Batteries, *Batteries,* 2021, vol. 7, Article # 65. https://doi.org/10.3390/batteries7040065
86. Rudy, A.S., Kurbatov, S.V., Mironenko, A.A., Naumov, V.V., Skundin, A.M., and Egorova, Yu.S., Effect of Si-Based Anode Lithiation on Charging Characteristics of All-Solid-State Lithium-Ion Battery, *Batteries*, 2022, vol. 8, Article # 87. https://doi.org/10.3390/batteries8080087
87. Rudy, A.S., Skundin, A.M., Mironenko, A.A., and Naumov, V.V., Current Effect on the Performances of All-Solid-State Lithium-Ion Batteries – Peukert's Law, *Batteries,* 2023, vol. 9, article # 370. https://doi.org/10.3390/batteries9070370
88. Dunlap, N.A, Kim, S., Jeong, J.J., Oh, K.H., and Lee, S., Simple and inexpensive coal-tar-pitch derived Si-C anode composite for all solid-state Li-ion batteries, *Solid State Ionics*, 2018, vol. 324, p. 207. https://doi.org/10.1016/j.ssi.2018.07.013
89. Whiteley, J.M., Kim, J.W., Piper, D.M., and Se-Hee Lee, S., High-Capacity and Highly Reversible Silicon-Tin Hybrid Anode for Solid-State Lithium-Ion Batteries, *J. Electrochem. Soc.*, 2016, vol. 163, p. A251. DOI: 10.1149/2.0701602jes
90. Son, S.B., Kim, S.C., Kang, C.S., Yersak, T.A., Kim, Y.C., Lee, C.G., Moon, S.H., Cho, J.S., Moon, J.T., Oh, K.H., and Lee, S.H., A Highly Reversible Nano-Si Anode Enabled by Mechanical Confinement in an Electrochemically Activated $Li_xTi_4Ni_4Si_7$ Matrix, *Adv. Energy Mater.*, 2012, vol. 2, p. 1226. DOI: 10.1002/aenm.201200180
91. Yersak, T.A., Son, S.B., Cho, J.S., Suh, S.S., Kim, Y.U., Moon, J.T., Oh, K.H., and Lee, S.H., An All-Solid-State Li-Ion Battery with a Pre-Lithiated Si-Ti-Ni Alloy Anode, *J. Electrochem. Soc.*, 2013, vol. 160, p. A1497. DOI: 10.1149/2.086309jes
92. Yamamoto, M., Terauchi, Y., Sakuda, A., and Takahashi, M., Slurry mixing for fabricating silicon-composite electrodes in all-solid-state batteries with high areal capacity and cycling stability, *J. Power Sources*, 2018, vol. 402, p. 506. https://doi.org/10.1016/j.jpowsour.2018.09.070
93. Kim, D.H., Lee, H.A., Song, Y.B., Park, J.W., Lee, S., and Jung, Y.S., Sheet-type Li_6PS_5Cl-infiltrated Si anodes fabricated by solution process for all-solid-state lithium-ion batteries, *J. Power Sources*, 2019, vol. 426, p. 143. https://doi.org/10.1016/j.jpowsour.2019.04.028
94. Kanazawa, S., Baba, T., Yoneda, K., Mizuhata, M., and Kanno, I., Deposition and performance of all solid-state thin-film lithium-ion batteries composed of amorphous Si/LiPON/VO-LiPO multilayers, *Thin Solid Films*, 2020, vol. 697, article # 137840. https://doi.org/10.1016/j.tsf.2020.137840
95. Chai, L., Wang, X., Su, B., Li, X., and Xue, W., Insight into the decay mechanism of non-ultra-thin silicon film anode for lithium-ion batteries, *Electrochim. Acta*, 2023, vol. 448, article # 142112. https://doi.org/10.1016/j.electacta.2023.142112
96. Ohzuku, T., Ueda, A., and Yamamoto, N., Zero-Strain Insertion Material of $Li[Li_{1/3}Ti_{5/3}]O_4$ for Rechargeable Lithium Cells, *J. Electrochem. Soc.*, 1995, vol. 142, p. 1431. DOI: 10.1149/1.2048592
97. Minami, K., Hayashi, A., Ujiie, S., and Tatsumisago, M., Electrical and electrochemical properties of glass–ceramic electrolytes in the systems Li_2S–P_2S_5–P_2S_3 and Li_2S–P_2S_5–P_2O_5, *Solid State Ionics*, 2011, vol. 192, p. 122. DOI:10.1016/j.ssi.2010.06.018
98. Tatsumisago, M., and Hayashi, A., Superionic glasses and glass–ceramics in the Li_2S–P_2S_5 system for all-solid-state lithium secondary batteries, *Solid State Ionics*, 2012, vol. 225, p. 342. DOI: 10.1016/j.ssi.2012.03.013
99. Kato, Y., Hori, S., Saito, T., Suzuki, K., Hirayama, M., Mitsui, A., Yonemura, M., Iba, H., and Kanno, R., High-power all-solid-state batteries using sulfide superionic conductors, *Nano Energy*, 2016, vol. 1, article # 16030. DOI: 10.1038/NENERGY.2016.30
100. Song, S., Hong, S., Park, H.Y., Lim, Y.C., and Lee, K.C., Cycling-Driven Structural Changes

in a Thin-Film Lithium Battery on Flexible Substrate, *Electrochem. Solid-State Lett.*, 2009, vol. 12, p. A159. DOI: 10.1149/1.3139530

101. Yamamoto, T., Iwasaki, H., Suzuki, Y., Sakakura, M., Fujii, Y., Motoyama, M., and Iriyama, Y., A Li-free inverted-stack all-solid-state thin film battery using crystalline cathode material, *Electrochem. Commun.*, 2019, vol. 105, article # 106494. https://doi.org/10.1016/j.elecom.2019.106494
102. Koo, M., Park, K., Lee, S.H., Suh, M., Jeon, D.Y., Choi, J.W., Kang, K., and Lee, K.J., Bendable Inorganic Thin-Film Battery for Fully Flexible Electronic Systems, *Nano Lett.*, 2012, vol. 12, p. 4810. dx.doi.org/10.1021/nl302254v
103. Xiao, D., Tong, J., Feng, Y., Zhong, G., Li, W., and Yang, C., Improved performance of all-solid-state lithium batteries using LiPON electrolyte prepared with Li-rich sputtering target, *Solid State Ionics*, 2018, vol. 324, p. 202. https://doi.org/10.1016/j.ssi.2018.07.011
104. Haruyama, J., Sodeyama, K., Han, L., Takada, K., and Tateyama, Y., Space–Charge Layer Effect at Interface between Oxide Cathode and Sulfide Electrolyte in All-Solid-State Lithium-Ion Battery, *Chem. Mater.*, 2014, vol. 26, p. 4248. https://doi.org/10.1021/cm5016959
105. Haruyama, J., Sodeyama, K., and Tateyama, Y., Cation Mixing Properties toward Co Diffusion at the $LiCoO_2$ Cathode/Sulfide Electrolyte Interface in a Solid-State Battery, *ACS Appl. Mater. Interfaces,* 2017, vol. 9, p. 286. DOI: 10.1021/acsami.6b08435
106. Sakuda, A., Hayashi, A., and Tatsumisago, M., Interfacial Observation between $LiCoO_2$ Electrode and Li_2S-P_2S_5 Solid Electrolytes of All-Solid-State Lithium Secondary Batteries Using Transmission Electron Microscopy, *Chem. Mater.*, 2010, vol. 22, p. 949. DOI: 10.1021/cm901819c
107. Woo, J.H., Trevey, J.E., Cavanagh, A.S., Choi, Y.S., Kim, S.C., George, S.M., Oh, K.H., and Lee, S., Nanoscale Interface Modification of $LiCoO_2$ by Al_2O_3 Atomic Layer Deposition for Solid-State Li Batteries, *J. Electrochem. Soc.*, 2012, vol. 159, p. A1120. DOI: 10.1149/2.085207jes
108. Ohta, N., Takada, K., Sakaguchi, I., Zhang, L., Ma, R., Fukuda, K., Osada, M., and Sasaki, T., $LiNbO_3$-coated $LiCoO_2$ as cathode material for all solid-state lithium secondary batteries, *Electrochem. Commun.*, 2007, vol. 9, p. 1486. DOI: 10.1016/j.elecom.2007.02.008
109. Ohta, N., Takada, K., Zhang, L., Ma, R., Osada, M., and Sasaki, T., Enhancement of the High-Rate Capability of Solid-State Lithium Batteries by Nanoscale Interfacial Modification, *Adv. Mater.*, 2006, vol. 18, p. 2226. DOI: 10.1002/adma.200502604
110. Kato, T., Hamanaka, T., Yamamoto, K., Hirayama, T., Sagane, F., Motoyama, M., and Iriyama, Y., *In-situ* $Li_7La_3Zr_2O_{12}/LiCoO_2$ interface modification for advanced all-solid-state battery, *J. Power Sources*, 2014, vol. 260, p. 292. http://dx.doi.org/10.1016/j.jpowsour.2014.02.102
111. Ohta, S., Kobayashi, T., Seki, J., and Asaoka, T., Electrochemical performance of an all-solid-state lithium ion battery with garnet-type oxide electrolyte, *J. Power Sources*, 2012, vol. 202, p. 332. DOI: 10.1016/j.jpowsour.2011.10.064
112. Kotobuki, M., Suzuki, Y., Munakata, H., Kanamura, K., Sato, Y., Yamamoto, K., and Yoshida, T., Fabrication of Three-Dimensional Battery Using Ceramic Electrolyte with Honeycomb Structure by Sol–Gel Process, *J. Electrochem. Soc.*, 2010, vol. 157, p. A493. DOI: 10.1149/1.3308459
113. Li, C., Zhang, B., and Fu, Z., Physical and electrochemical characterization of amorphous lithium lanthanum titanate solid electrolyte thin-film fabricated by e-beam evaporation, *Thin Solid Films*, 2006, vol. 515, p. 1886. DOI: 10.1016/j.tsf.2006.07.026
114. Kotobuki, M., Suzuki, Y., Munakata, H., Kanamura, K., Sato, Y., Yamamoto, K., and Yoshida, T., Compatibility of $LiCoO_2$ and $LiMn_2O_4$ cathode materials for $Li_{0.55}La_{0.35}TiO_3$ electrolyte to fabricate all-solid-state lithium battery, *J. Power Sources*, 2010, vol. 195, p. 5784. DOI: 10.1016/j.jpowsour.2010.03.004
115. Visbal, H., Aihara, Y., Ito, S., Watanabe, T., Park, Y., and Doo, S., The effect of diamond-like carbon coating on $LiNi_{0.8}Co_{0.15}Al_{0.05}O_2$ particles for all solid-state lithium-ion batteries based on $Li_2SeP_2S_5$ glass-ceramics, *J. Power Sources*, 2016, vol. 314, p. 85. http://dx.doi.org/10.1016/j.jpowsour.2016.02.088
116. Seino, Y., Ota, T., and Takada, K., High rate capabilities of all-solid-state lithium secondary batteries using $Li_4Ti_5O_{12}$-coated $LiNi_{0.8}Co_{0.15}Al_{0.05}O_2$ and a sulfide-based solid electrolyte, *J. Power Sources*, 2011, vol. 196, p. 6488. DOI: 10.1016/j.jpowsour.2011.03.090
117. Sakuda, A., Takeuchi, T., and Kobayashi, H., Electrode morphology in all-solid-state lithium secondary batteries consisting of $LiNi_{1/3}Co_{1/3}Mn_{1/3}O_2$ and Li_2S-P_2S_5 solid electrolytes, *Solid State Ionics*, 2016, vol. 285, p. 112. http://dx.doi.org/10.1016/j.ssi.2015.09.010
118. Kitsche, D., Tang, Y., Ma, Y., Goonetilleke, D., Sann, J., Walther, F., Bianchini, M., Janek, J., and Brezesinski, T., High Performance All-Solid-State Batteries with a Ni-Rich NCM Cathode Coated by Atomic Layer Deposition and Lithium Thiophosphate Solid Electrolyte, *ACS Appl. Energy Mater.*, 2021, vol. 4, p. 7338. https://doi.org/10.1021/acsaem.1c01487
119. Ding, J., Sun, Q., and Fu, Z., Layered $Li(Ni_{1/4}Co_{1/2}Mn_{1/3})\ O_2$ as Cathode Material for All-Solid-State Thin-Film Rechargeable Lithium-Ion Batteries, *Electrochem. Solid State Lett.*, 2010, vol. 13, p. A105. DOI: 10.1149/1.3432254
120. Neudecker, B.J., Zuhr, R.A., Robertson, J.D., and Bates, J.B., Lithium Manganese Nickel Oxides $Li_x(Mn_yNi_{1-y})_{2-x}O_2$. II. Electrochemical Studies on Thin-Film Batteries, *J. Electrochem. Soc.*, 1998, vol. 145, p. 4160. DOI: 10.1149/1.1838930

121. Hoshina, K., Yoshima, K., Kotobuki, M., and Kanamura, K., Fabrication of $LiNi_{0.5}Mn_{1.5}O_4$ thin film cathode by PVP sol–gel process and its application of all-solid-state lithium ion batteries using $Li_{1+x}Al_xTi_{2-x}(PO_4)_3$ solid electrolyte, *Solid State Ionics*, 2012, vol. 209–210, p. 30. DOI: 10.1016/j.ssi.2011.12.018

122. Lethien, C., Zegaoui, M., Roussel, P., Tilmant, P., Rolland, N., and Rolland, P.A., Micro-patterning of LiPON and lithium iron phosphate material deposited onto silicon nanopillars array for lithium ion solid state 3D micro-battery, *Microelectron. Eng.*, 2011, vol. 88, p. 3172. DOI: 10.1016/j.mee.2011.06.022

123. Dobbelaere, T., Mattelaer, F., Dendooven, J., Vereecken, P., and Detavernier, C., Plasma-Enhanced Atomic Layer Deposition of Iron Phosphate as a Positive Electrode for 3D Lithium-Ion Microbatteries, *Chem. Mater.*, 2016, vol. 28, p. 3435. DOI: 10.1021/acs.chemmater.6b00853

124. Aboulaich, A., Bouchet, R., Delaizir, G., Seznec, V., Tortet, L., Morcrette, M., Rozier, P., Tarascon, J.-M., Viallet, V., and Dollé, D., A New Approach to Develop Safe All-Inorganic Monolithic Li-Ion Batteries, *Adv. Energy Mater.*, 2011, vol. 1, p. 179. DOI: 10.1002/aenm.201000050

125. Kobayashi, E., Plashnitsa, L.S., Doi, T., Okada, S., and Yamaki, J., Electrochemical properties of Li symmetric solid-state cell with NASICON-type solid electrolyte and electrodes, *Electrochem. Commun.*, 2010, vol. 12, p. 894. DOI: 10.1016/j.elecom.2010.04.014

126. Huang, F., Fu, Z.W., Chu, Y.Q., Liu, W.Y., and Qin, Q.Z., Characterization of Composite 0.5Ag: V_2O_5 Thin-Film Electrodes for Lithium-Ion Rocking Chair and All-Solid-State Batteries, *Electrochem. Solid State Lett.*, 2004, vol. 7, p. A180. DOI: 10.1149/1.1736591

127. Jeon, E.J., Shin, Y.W., Nam, S.C., Cho, W.I., and Yoon, Y.S., Characterization of All-Solid-State Thin-Film Batteries with V_2O_5 Thin-Film Cathodes Using *Ex Situ* and *In Situ* Processes, *J. Electrochem. Soc.*, 2001, vol. 148, p. A318. DOI: 10.1149/1.1354609

128. Navone, C., Baddour-Hadjean, R., Pereira-Ramos, J.P., and Salot, R., Sputtered Crystalline V_2O_5 Thin Films for All-Solid-State Lithium Micro-batteries, *J. Electrochem. Soc.*, 2009, vol. 156, p. A763. DOI: 10.1149/1.3170922

129. Matsumura, T., Nakano, K., Kanno, R., Hirano, A., Imanishi, N., and Takeda, Y., Nickel sulfides as a cathode for all-solid-state ceramic lithium batteries, *J. Power Sources*, 2007, vol. 174, p. 632. DOI: 10.1016/j.jpowsour.2007.06.168

130. Aso, K., Sakuda, A., Hayashi, A., and Tatsumisago, M., All-Solid-State Lithium Secondary Batteries Using NiS-Carbon Fiber Composite Electrodes Coated with $Li_2S–P_2S_5$ Solid Electrolytes by Pulsed Laser Deposition, *ACS Appl. Mater. Interfaces*, 2013, vol. 5, p. 686. dx.doi.org/10.1021/am302164e

131. Jones, S.D., and Akridge, J.R., Development and performance of a rechargeable thin-film state microbattery, *J. Power Sources*, 1995, vol. 54, p. 63. https://doi.org/10.1016/0378–7753(94)02041-Z

132. Chen, M., Yin, X., Reddy, M.V., and Adams, S., All-solid-state $MoS_2/Li_6PS_5Br/In–Li$ batteries as a novel type of Li/S battery, *J. Mater. Chem. A*, 2015, vol. 3, p. 10698. DOI: 10.1039/c5ta02372f

133. Mauger, A., Julien, C.M., Paolella, A., Armand, M., and Zaghib, K., Building Better Batteries in the Solid State: A Review, *Materials*, 2019, vol. 12, article # 3892. DOI: 10.3390/ma12233892

134. Singer, C., Schnell, J., and Reinhart, G., Scalable Processing Routes for the Production of All-Solid-State Batteries – Modeling Interdependencies of Product and Process, *Energy Technol.*, 2021, vol. 9, article # 2000665. https://doi.org/10.1002/ente.202000665

135. Xiao, Y., Wang, Y., Bo, S., Kim, J.C., Miara, L.J., and Ceder, G., Understanding interface stability in solid-state batteries, *Nat. Rev. Mater.*, 2020, vol. 5, p. 105. https://doi.org/10.1038/s41578–019–0157–5

136. Fan, L., He, H., and Nan, C., Tailoring inorganic–polymer composites for the mass production of solid-state batteries, *Nat. Rev. Mater.*, 2021, vol. 6, p. 1003. https://doi.org/10.1038/s41578–021–00320–0

137. Banerjee, A., Wang, X., Fang, C., Wu, E.A., and Meng, Y.S., Interfaces and Interphases in All-Solid-State Batteries with Inorganic Solid Electrolytes, *Chem. Rev.*, 2020, vol. 120, p. 6878. https://doi.org/10.1021/acs.chemrev.0c00101

RUSSIAN JOURNAL OF ELECTROCHEMISTRY, 2025, Vol. 61, No. 1, pp. 52–62

OXYGEN-ION AND PROTON TRANSPORT IN Y^{3+}-DOPED HEXAGONAL PEROVSKITE $BA_7IN_6AL_2O_{19}$[1]

© 2025 I. E. Animitsa*, R. D. Andreev, D. V. Korona, A. R. Gilev, S. S. Nokhrin

Ural Federal University named after the First President of Russia B. N. Yeltsin, Yekaterinburg, Russia

**e-mail: Irina.animitsa@urfu.ru*

Received: July 16, 2024

Revised: September 19, 2024

Accepted: September 27, 2024

Abstract. In this work, the thermal and electrical properties of the Y^{3+}-doped $Ba_7In_{5.9}Y_{0.1}Al_2O_{19}$ phase, characterized by a hexagonal perovskite structure (a = 5.935(7) Å, c = 37.736(8) Å), were studied. It has been established that the phase is capable of incorporating protons and exhibiting proton conductivity. The introduction of an isovalent dopant, yttrium, led to an increase in the concentration of protons (up to the limiting values of $Ba_7In_{5.9}Y_{0.1}Al_2O_{19}\cdot 0.55H_2O$), as a result of an increase in the unit cell volume and, accordingly, the free space for the placement of OH^- groups in an oxygen-deficient block containing coordination-unsaturated polyhedra [BaO_9]. Isovalent doping led to an increase in the oxygen-ion conductivity, which is due to an increase in interatomic distances and a decrease in the migration activation energy. In a humid atmosphere ($pH_2O = 1.92\cdot 10^{-2}$ atm), the $Ba_7In_{5.9}Y_{0.1}Al_2O_{19}$ phase exhibited higher values of proton conductivity compared to the matrix compound $Ba_7In_6Al_2O_{19}$ and below 500 °C it was characterized by dominant proton transport both in air and in a wide range of pO_2 (10^{-18}–0.21 atm).

Keywords: *hexagonal perovskite, hydration, oxygen-ion conductivity, proton conductivity, ion transport numbers*

DOI: 10.31857/S04248570250103e2

INTRODUCTION

Research on high-temperature proton conductivity in oxide systems has been ongoing for more than 40 years, starting with the first works of H. Iwahara made on ABO_3 perovskites [1–4]. The possibility of proton defects in these compounds is due to the presence of oxygen vacancies, which are determined by the introduction of an acceptor dopant. When processed in an atmosphere containing water vapor, proton defects are formed in the structure of such compounds, which causes proton conductivity:

$$V_o^{\bullet\bullet} + H_2O_{gas} + O_o^{\times} \Leftrightarrow 2(OH)_o^{\bullet}, \qquad (1)$$

where $V_o^{\bullet\bullet}$ is the oxygen vacancy, $(OH)_O^{\bullet}$ is the hydroxyl group in the oxygen position, and $O_o^{\times}$ is the oxygen atom in the oxygen position. The possibility of using such materials as an electrolyte for medium-temperature fuel cells (the most promising among known electrochemical generators due to high efficiency, the absence of precious metals in their design, as well as minimal requirements for the composition of hydrogen-containing gas) stimulated intensive research of perovskites as high-temperature protonics [5–8]. The main direction in the development of such electrolytes is multi-cationic doping or modification of basic oxide compounds in order to: 1) reduce the temperature at which the electrolyte has sufficient ionic conductivity, 2) reduce the sintering temperature of the electrolyte material powders to a gas-dense state, 3) increase the mechanical strength of the electrolyte ceramics, 4) improve thermomechanical properties, in particular, suppress phase transitions and change the coefficient of thermal expansion (CTE) to achieve its proximity to the CTE of other components of electrochemical devices, 5) increase the chemical resistance of the electrolyte in relation to interaction with the gaseous medium and with other components of electrochemical devices, 6) reduce cost [9, 10].

Later, other structural types based on complex oxides were discovered, for which the process of proton incorporation occurs without the introduction of an acceptor dopant. For example, since 2019, phases based on $BaLaInO_4$, $SrLaInO_4$, $BaNdInO_4$, $BaNdScO_4$ and $BaLaInO_4$ [11–20] with the Ruddlesden-Popper structure have been intensively studied as representatives of a new class of proton conductors [14]. For such structures, the strategy for optimizing their proton-conducting properties is based on changing

[1] Based on the materials of the report at the 17th International Meeting "Fundamental and applied problems of solid state ionics", Chernogolovka, June 16–23, 2024.

the size of the rock salt block, since during hydration it is possible to increase the coordination number of the cation standing in the rock salt block with the participation of OH groups in its coordination.

For a more complex structural type, hexagonal perovskite-like compounds built on a block principle from fragments of various structural types, high-temperature proton transport was also discovered in the 1920s, and super proton conduction can be realized for such phases over a wide temperature range. For example, the phase of the composition $Ba_5Er_2Al_2ZrO_{13}$ exhibited proton conductivity of ~10^{-3} ohms^{-1}×cm^{-1} at 300 °C [21]. Structural analogues with different natures of the M^{3+}-cation with the general formula $Ba_5M_2Al_2ZrO_{13}$ (M=Gd-Lu, Y, Sc) are described in [22]. The structure of such phases can be represented as a result of the fusion of oxygen-deficient $Ba_2M^{3+}AlO_5$ and $BaZrO_3$ perovskite blocks [22]. The conductivity of the phases $Ba_5M_2Al_2ZrO_{13}$ (M=Dy, Er, Tm, Yb, and Lu) was measured in [21]. It was shown that in the temperature range of 400–800 °C in humid air, the differences in conductivities reach one order of magnitude, depending on the nature of the M^{3+}-cation. The conductivity increased in the range Lu<Tm<Dy<Yb≈Er. However, no analysis of the effect of the nature of REE on ion transport processes was carried out.

The interest in such phases is also caused by their high chemical resistance to atmospheres containing CO_2. For example, it was reported that a compound with a hexagonal $Ba_5Er_2Al_2SnO_{13}$ structure maintained phase stability after prolonged heat treatment at 600 °C in a carbon dioxide atmosphere [23].

For such structures, the process of proton incorporation (i.e., OH groups) is ensured by the presence of coordination-unsaturated Ba^{2+} polyhedra in the oxygen-deficient *h′*-layers, which have the shape of a nine-sided [BaO_9]. In such hexagonal *h′*-layers, aluminum tetrahedra connect through the vertex, forming the Al_2O_7 grouping, while oxygen-deficient BaO_2 layers (is the unoccupied oxygen position) are formed, alternating with oxygen-complete BaO_3 layers. Accordingly, coordination-unsaturated Ba^{2+} polyhedra are able to increase the coordination number with the participation of OH groups in their coordination.

Within the framework of quasi-chemical formalism, the process of dissociative dissolution of water vapor in the structure of hexagonal perovskites, by analogy with other complex oxides containing structural oxygen vacancies, can be described as follows:

$$(V_O^s)^\times + O_o^\times + H_2O \Leftrightarrow (OH)_o^\bullet + (OH)_i, \quad (2)$$

where $(V_O^s)^\times$ is the structural oxygen vacancy, $O_o^\times$ is the oxygen atom in the regular position, $(OH)_O^\bullet$ is the hydroxyl group in the oxygen position, and $(OH)_i$ is the hydroxyl group in place of the structural oxygen vacancy. Oxygen-ion and proton transport in hexagonal perovskite of the composition $Ba_5In_2Al_2ZrO_{13}$ was studied in more detail [24–27]. When studying the effect of various types of substitutions on ionic (O2-, H^+) transport, it was shown that for such structures, acceptor doping is not an effective strategy for significantly increasing ionic conductivity, compared with classical ABO_3 perovskites. At the same time, the isovalent doping method, which makes it possible to modify geometric characteristics, leads to an increase in ionic conductivity.

In addition to the compounds with the coherent fusion structure described above, high-temperature proton transport has recently been discovered in hexagonal perovskite $Ba_7In_6Al_2O_{19}$ [28]. The structure of this phase is also based on the block principle of fragments of various structural types, it can be represented as coalescence along the axis from two blocks Ba_2InAlO_5 and one block $Ba_3In_4O_9$. The $Ba_7In_6Al_2O_{19}$ phase was characterized by higher values of ionic (O^{2-}, H^+) conductivities than $Ba_5In_2Al_2ZrO_{13}$. However, there is no information in the literature about the possible types of substitutions in this phase and their effect on transport properties. In addition, it is of interest to compare the isovalent substitution method for two phases $Ba_7In_6Al_2O_{19}$ and $Ba_5In_2Al_2ZrO_{13}$, characterized by the coalescence of identical Ba_2InAlO_5 blocks (oxygen-deficient block), but differing in $Ba_3In_4O_9$ blocks (cation-deficient perovskite) and $BaZrO_3$ (complete perovskite).

For this purpose, in this work, the synthesis of the Y^{3+}-doped phase of the composition $Ba_7In_{5.9}Y_{0.1}Al_2O_{19}$ was carried out, its conductivity was studied as a function of temperature and pO_2 in atmospheres of different humidity, and the ability to hydrate was proved by thermogravimetry. The data obtained were compared with the Y^{3+}-doped phase of $Ba_5In_2Al_2ZrO_{13}$ [24–27].

EXPERIMENTAL PART

Samples of the compositions $Ba_7In_6Al_2O_{19}$ and $Ba_7In_{5.9}Y_{0.1}Al_2O_{19}$ were obtained by solid-phase synthesis from pre-dried $BaCO_3$ (operating hours 7–4), Al_2O_3 (operating hours 12–3), In_2O_3 (operating hours 12–3). The synthesis was carried out in air according to the scheme: 800 °C, 24 h.; 1000 °C, 24 h.; 1100 °C, 72 h., after each stage, grinding was carried out in an agate mortar in an ethyl alcohol medium.

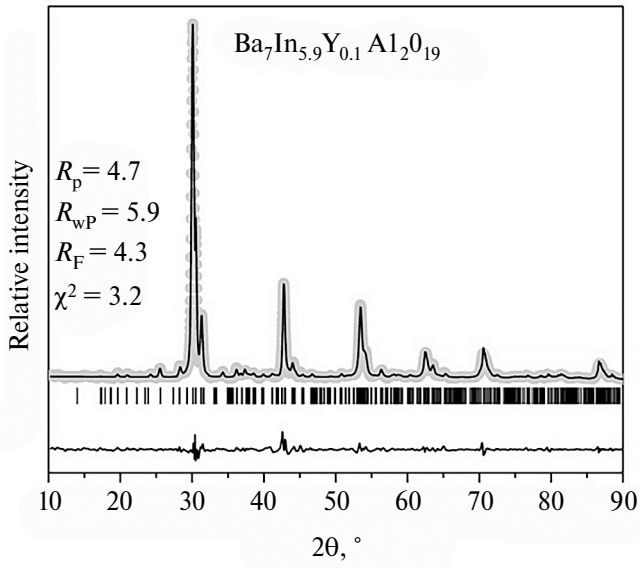

Fig. 1. Experimental, calculated, and differential radiographs, as well as the angular positions of the reflexes of the $Ba_7In_{5.9}Y_{0.1}Al_2O_{19}$ sample.

To measure the electrical properties, the samples were prepared in the form of tablets, sintering was carried out at a temperature of 1300 °C for 48 hours. The values of the relative density of the ρ_{rel} of the obtained ceramic samples were determined as the ratio of the geometric density to the X-ray density. For the studied phases, they were: ρ_{rel} = 82.7% for $Ba_7In_6Al_2O_{19}$ and ρ_{rel} = 81.6% for $Ba_7In_{5,9}Y_{0,1}Al_2O_{19}$. The palladium-silver electrodes were fired at a temperature of 900 °C for 3 hours.

X-ray analysis was performed on an ARL EQUINOX 3000 diffractometer (ThermoFisherScientific, USA) in CuK_α radiation at a tube voltage of 40 kV and a current of 40 mA. The imaging was carried out in the range of 2θ = 10°–90° with a step of 0.024° and an exposure of 1 s per point. The lattice parameters were calculated using the FullProf program.

The surface morphology of the powder samples and the local chemical composition were studied using a VEGA3 scanning electron microscope (SEM) (Tescan, Czech Republic) with an X-ray energy dispersion microanalyzer AztecLiveStandardUltimMax 40 (Oxford Instruments, Great Britain). The detection limit at normal energies (5–20 kV) was ~0.5 at.%, the concentration measurement error was ± 2%. The survey was carried out at a voltage of 20 kV in secondary and back-reflected electrons.

Hydrated sample forms were prepared for thermogravimetric (TG) measurements. The samples were previously calcined at a temperature of 1100 °C in a dry nitrogen atmosphere in order to remove possible carbonation products. The calcined samples were then slowly cooled in an atmosphere of moist nitrogen ($pH_2O = 1.92 \cdot 10^{-2}$ atm) to 200 °C. Nitrogen humidity was set according to the procedure described below for measuring electrical conductivity. Thus, the lower hydration temperature provided conditions that excluded the appearance of adsorption moisture in the sample. Next, thermogravimetric analysis of the hydrated samples was performed on TG STA 409 PC thermal balance (Netzsch, Germany). The measurements were carried out in the temperature range of 25–1000 °C with a heating rate of 10 °/min in an argon atmosphere.

The study of electrical conductivity was carried out by the electrochemical impedance method in the frequency range 10^2–3×10^6 Hz using the Elins Z-3000X impedance parameter meter (Elins LLC, Russia). All electrochemical measurements were performed under equilibrium conditions with T, pH_2O, and pO_2. The volumetric resistance was calculated using Zview software fitting. The values of the electrical conductivity of the samples σ were calculated according to the following formula:

$$\sigma = \frac{l}{SR_{vol}}, \quad (3)$$

where l is the height of the sample, S is the surface area of the sample. The values of the volume resistance R_{vol} were determined from the impedance spectroscopy data. The values of the activation energy E_a and the pre-exponential multiplier A were calculated using the Frenkel equation:

$$\sigma T = A \exp(\frac{-E_a}{kT}), \quad (4)$$

where A is the pre-exponential multiplier, k is the Boltzmann constant, and T is the absolute temperature.

The study of electrical conductivity with varying pO_2 was carried out in the oxygen partial pressure range of 10^{-18}–0.21 atm. The oxygen pressure was set and monitored using an "oxygen pump" and an oxygen partial pressure sensor made from a stabilized solid electrolyte based on ZrO_2. The oxygen partial pressure values were monitored by the Zirconia-M regulator (Research Technologies LLC, Russia).

The electrical conductivity of the studied phases was studied in atmospheres of different humidity. A moist atmosphere was obtained by bubbling gas at room temperature sequentially through distilled water and a saturated solution of potassium bromide KBr ($pH_2O = 1.92 \times 10^{-2}$ atm). The dry atmosphere was set by gas circulation through powdered phosphorus oxide P_2O_5 ($pH_2O = 3.5 \times 10^{-5}$ atm). In addition, to prevent possible carbonation of ceramics, preliminary removal of CO_2

Table 1. Values of parameters, volume and free volume of unit cells for phases $Ba_7In_6Al_2O_{19}$ and $Ba_7In_{5.9}Y_{0.1}Al_2O_{19}$

Phase	a, Å	c, Å	V, Å^3	$V_{св}$, Å^3
$Ba_7In_6Al_2O_{19}$	5.921(2)	37.717(4)	1145.2(3)	481.3(6)
$Ba_7In_{5.9}Y_{0.1}Al_2O_{19}$	5.935(7)	37.736(8)	1151.4(4)	487.3(9)

carbon dioxide from the air was carried out, for a wet atmosphere using a 20% NaOH solution, for a dry atmosphere using the Ascarite reagent. The humidity of the gases was controlled by a HIH-4000 gas humidity sensor (Honeywell, USA) of a capacitive type, which allows measurements of relative humidity from 0 to 100%. In addition to the sensor element, an electrical circuit is located on the sensor substrate, providing signal conversion, amplification and linearization. The sensor output is a function of voltage, ambient temperature, and humidity. The sensor was directly connected to the microcontroller to process the linear voltage signal.

RESULTS AND DISCUSSION

Phase analysis and morphological assessment

According to X-ray phase analysis, the $Ba_7In_6Al_2O_{19}$ matrix compound and the $Ba_7In_{5.9}Y_{0.1}Al_2O_{19}$ phase were obtained as single-phase and were characterized by a hexagonal structure (spatial group $P6_3/mmc$). Fig. 1 shows an example of X-ray data processing by the Rietveld method of full-profile analysis for a sample of the composition $Ba_7In_{5.9}Y_{0.1}Al_2O_{19}$.

When yttrium was introduced, the parameters of unit cells, volume, and free volume increased, due to the large value of the ionic radius of yttrium ($r_{Y^{3+}}$ = 0.90 Å) compared with indium ($r_{In^{3+}}$=0.80 Å) [29]. Table 1 shows the corresponding parameter values.

SEM images of the chipped surface of the ceramic and powder sample $Ba_7In_{5.9}Y_{0.1}Al_2O_{19}$ obtained in secondary electrons are shown in Fig. 2*a* and 2*b*, respectively. For the powder sample (Fig. 2*b*), small rounded crystallites with sizes of 2–5 μm were observed, partially agglomerated into larger irregularly shaped grains, the sizes of which averaged 10–12 μm. The crystalline grains of both the initial compound and the studied yttrium-substituted phase had approximately the same size and shape. Thus, the introduction of yttrium into the initial matrix did not affect the size and shape of the crystallites. No crystalline grains corresponding to any impurity phases were found in the images of all the samples studied. The chipped surface of the ceramic sample is represented by irregularly shaped fused grains, with individual pores visible (Fig. 2*a*). The cationic composition of the obtained samples was determined by the analysis of energy-dispersive X-ray spectroscopy (EDX)

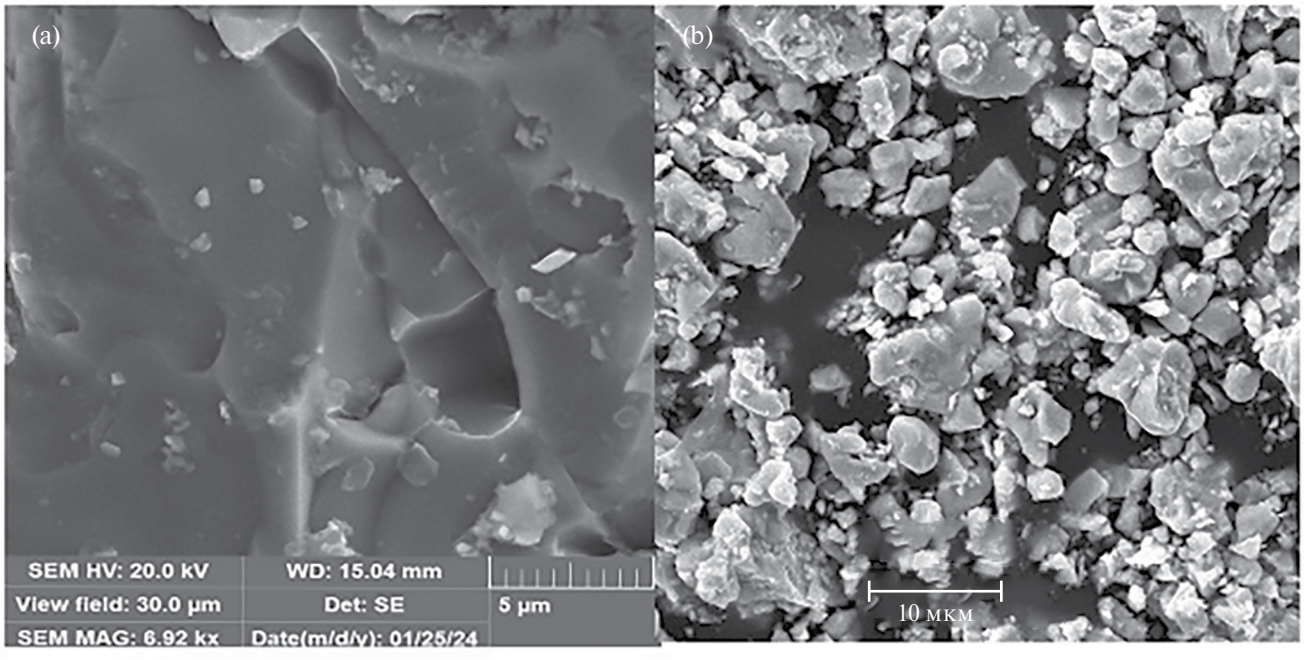

Fig. 2. SEM images of the surface of the chipped ceramic (a) and powder (b) samples $Ba_7In_{5.9}Y_{0.1}Al_2O_{19}$.

Table 2. Elemental analysis data based on the results of EDX studies for ceramic samples of the composition $Ba_7In_6Al_2O_{19}$ and $Ba_7In_{5.9}Y_{0.1}Al_2O_{19}$

Phase	at.% (theoretical)				at.% (experimental)			
	Ba	In	Y	Al	Ba	In	Y	Al
$Ba_7In_6Al_2O_{19}$	46.7	40.0	0.0	13.3	45.8	38.6	0	15.6
$Ba_7In_{5.9}Y_{0.1}Al_2O_{19}$	46.7	39.3	0.7	13.3	45.5	38.0	0.7	15.8

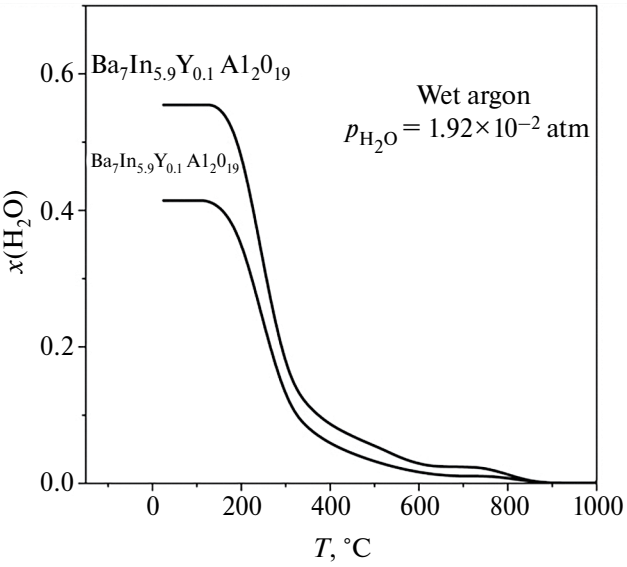

Fig. 3. TG curves of hydrated samples $Ba_7In_6Al_2O_{19}{\cdot}xH_2O$ and $Ba_7In_{5.9}Y_{0.1}Al_2O_{19}{\cdot}xH_2O$.

on the chips of ceramic samples. The experimentally obtained values are consistent with the theoretical ones, the difference in the values of the cation content did not exceed 2–2.5%, which makes it possible to conclude that the elemental composition was preserved for all the phases obtained (Table 2).

Thermal properties

Fig. 3 shows the results of thermal analysis of the hydrated phases of the compositions $Ba_7In_6Al_2O_{19}{\cdot}xH_2O$ and $Ba_7In_{5.9}Y_{0.1}Al_2O_{19}{\cdot}xH_2O$. The results are presented as moles of water (degree of hydration xH_2O) per formula unit. A similar type of TG curves was observed for both phases: mass changes occurred in the temperature range of 200–950 °C, while the main mass change occurred in the temperature range of 200–400 °C, and mass stabilization of the samples was observed above 950 °C.

The experimentally obtained values of the degree of hydration of the Y-doped phase (0.55 mol H_2O) were higher than for the matrix phase $Ba_7In_6Al_2O_{19}$ (0.41 mol H_2O). Since the isovalent doping method was used in the work, the increase in the degree of hydration is not associated with any additional disordering, but is caused by a change in the geometric characteristics of the unit cell. This behavior during hydration is due to the specifics of the structure of the phases under study, namely, the presence of oxygen-deficient BaO_2 layers in the hexagonal *h'* -block, respectively, an increase in the size of this block during doping makes it possible to incorporate large concentrations of OH groups.

It can be concluded that for block-type structures containing coordination-unsaturated polyhedra of large-sized cations, the strategy of increasing the size of such blocks is favorable for accommodating more OH groups coordinating these cations. Similar trends, such as an increase in the degree of hydration with an increase in the geometric parameters of the unit cell (or the volume of the unit cell), were observed for hydrated phases with the Ruddlesden–Popper $BaLaInO_4$ structure [30], and for hexagonal perovskites $Ba_5In_2Al_2ZrO_{13}$ [25–27].

Electrical properties

Fig. 4 shows examples of the evolution of impedance hodographs in Nyquist coordinates with temperature variation in dry (Fig. 4*a*) and humid (Fig. 4*b*) air.

As can be seen, the general appearance of the impedance spectra was similar – a semicircle emanating from the origin was observed in the region of the main frequencies under study, and an asymmetry of its right side was observed in the region of lower frequencies, which is the result of overlap with the second relaxation process. The capacity values obtained for the first semicircle were 10^{-12}–10^{-11} F, which corresponds to the volume contribution for the second, 10^{-10}–10^{-9}F, which corresponds to the contribution of grain boundaries. Therefore, the processing in the ZView program was carried out in accordance with the equivalent scheme shown in Fig. 4*b*. A small part of the third semicircle was observed in the low frequency region, which is typical for electrode processes. Further in the text, the volume resistance values obtained by extrapolating the corresponding semicircle to the abscissa axis (processing in ZView) will be discussed.

The electrical conductivity of all samples was studied over a wide range of oxygen partial pressures to determine the contributions of partial conductivities. Fig. 5 shows typical dependences. As can be seen,

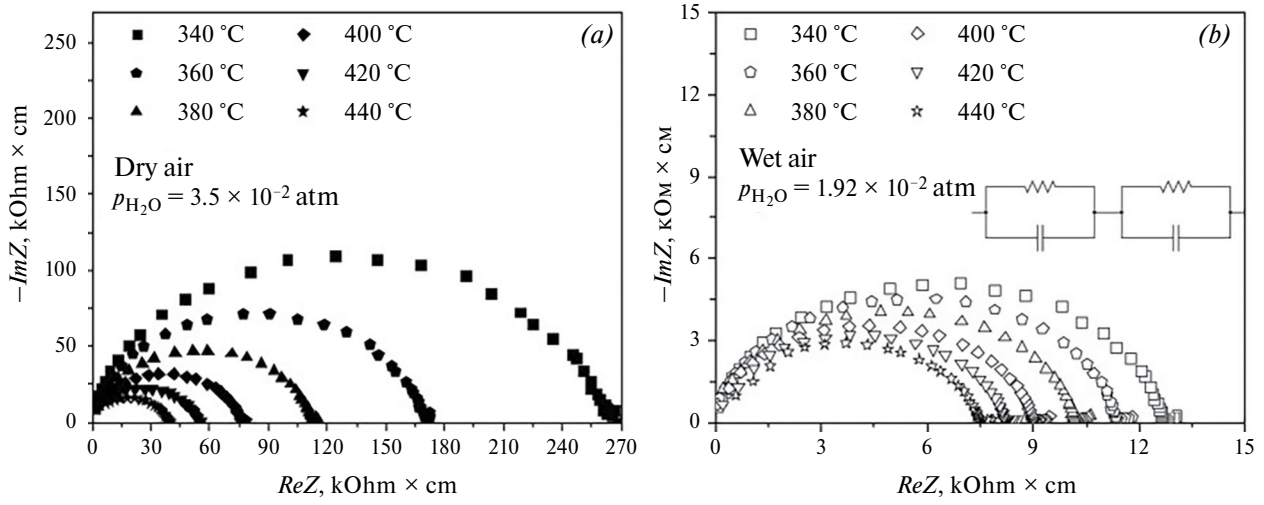

Fig. 4. Evolutions of impedance hodographs with temperature variation in dry (a) and moist (b) air for $Ba_7In_{5.9}Y_{0.1}Al_2O_{19}$.

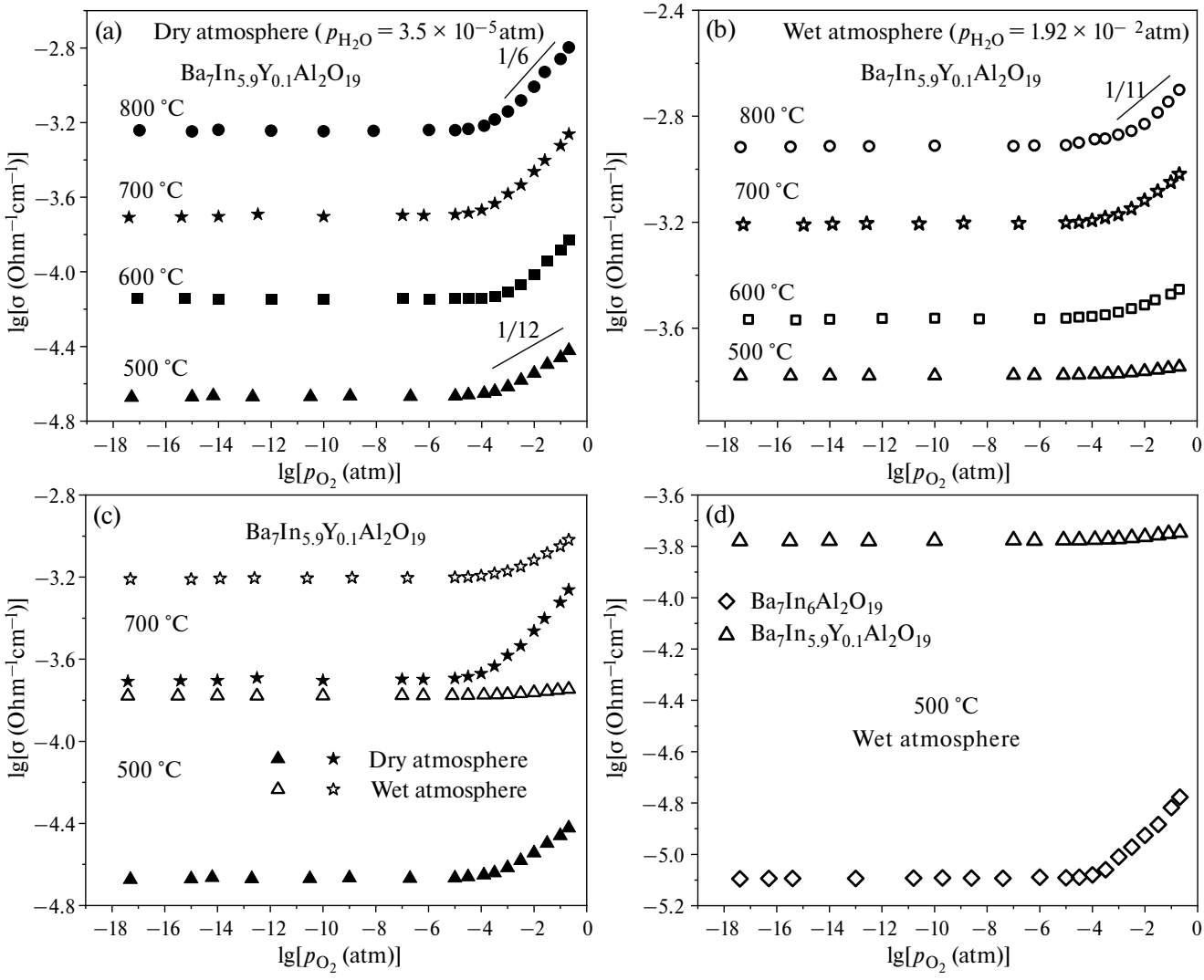

Fig. 5. Dependences of electrical conductivity on the partial pressure of oxygen of the $Ba_7In_{5.9}Y_{0.1}Al_2O_{19}$ phase in dry ($pH_2O = 3.5 \cdot 10^{-5}$ atm) (*a*) and wet ($pH_2O = 1.92 \cdot 10^{-2}$ atm) (*b*) atmospheres, as well as comparison of isotherms in dry and wet atmospheres (*c*) and comparison of with an undoped phase of $Ba_7In_6Al_2O_{19}$ at 500 °C (*d*).

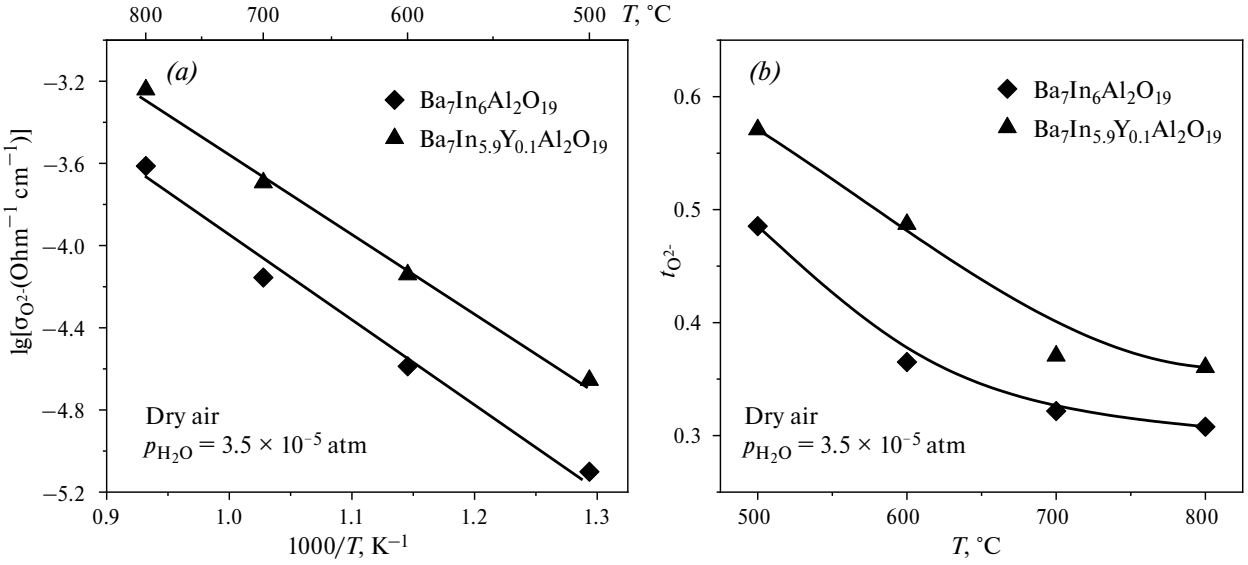

Fig. 6. Temperature dependences of oxygen-ion conductivity (*a*) and oxygen-ion transfer numbers (*b*) for $Ba_7In_6Al_2O_{19}$ and $Ba_7In_{5.9}Y_{0.1}Al_2O_{19}$ in dry air atmosphere ($pH_2O = 3.5\times10^{-5}$ atm).

the conductivity (Fig. 5*a*) in a wide range of partial pressures of oxygen pO_2 (10^{-18}–10^{-5} atm) remains constant – this is an electrolytic region where atomic defects are dominant. Taking into account the crystallochemical features of the $Ba_7In_6Al_2O_{19}$ structure (the presence of oxygen-deficient layers), the mechanism of oxygen-ion conductivity can be represented as an exchange of lattice oxygen and oxygen vacancies. At the same time, oxygen vacancies in such structures are nodes of the crystal lattice that are not occupied by atoms, i.e., a structural defect. Therefore, from a quasi-chemical point of view, this process can be described as follows:

$$O_O^{\times} + (V_O^s)^{\times} \leftrightarrow V_O^{\bullet\bullet} + O_i'', \qquad (5)$$

where $(V_O^S)^{\times}$ is the structural oxygen vacancy, $V_O^{\bullet\bullet}$ is the oxygen vacancy formed in place of the departed oxygen, $O_O^{\times}$ is oxygen in the oxygen position, O_i'' is the oxygen ion in the structural oxygen vacancy.

With an increase in the partial pressure of oxygen ($pO_2 > 10^{-5}$atm), the electrical conductivity begins to increase, which indicates the appearance of a contribution of hole conductivity:

$$(V_O^S)^{\times} + 1/2O_2 \leftrightarrow O_i'' + 2h^{\bullet}. \qquad (6)$$

Accordingly, total conductivity can be represented as the sum of the ionic conductivity, independent of pO_2, and the hole conductivity, for which the slope is $d\lg\sigma_h/d\lg pO_2 = 1/4$:

$$\sigma_{tot} = \sigma_{ion} + \sigma_h = \sigma_{ion} + KpO_2^{1/4}, \qquad (7)$$

where σ_{tot}, σ_{ion}, and σ_h are, respectively, the total, ionic, and hole conductivities, and K is a constant.

It should be noted that the general form of the $\lg\sigma_{tot}$–$\lg pO_2$ dependences for the studied phases had similar features: for dry atmosphere in the region of high partial pressures of oxygen pO_2, the positive slope of the total conductivity decreased with the decreasing temperature, which indicates an increase in the contribution of ionic conductivity. Thus, the values of oxygen-ion conductivity $\sigma_{O^{2-}}$ (conductivity in the plateau region) were obtained from the experimental $\lg\sigma$-$\lg pO_2$ data and the ion transfer numbers were calculated as $t_{O^2} = \sigma_{O^{2-}}/\sigma_{tot}$.

Fig. 6 shows the temperature dependences of the oxygen-ion conductivity of the studied phases. All dependences in the Arrhenius coordinates were characterized by a linear form. The calculated values of the activation energy E_a of oxygen-ion conductivity and the pre-exponential multiplier A in accordance with equation (4) are shown in Table 3.

As can be seen, the values of oxygen-ion conductivity increased for the yttrium-doped phase. At the same time, the activation energy decreased and the pre-exponential multiplier increased, both factors being favorable in terms of increasing oxygen-ion conductivity. The observed trends may be due to an increase in the volume (as well as the free volume) of the unit cell as a result

Table 3. Values of the activation energy of oxygen-ion conductivity and the pre-exponential multiplier for the phases of the composition $Ba_7In_6Al_2O_{19}$ and $Ba_7In_{5.9}Y_{0.1}Al_2O_{19}$

Phase	E_a, Ev	A, $Ohm^{-1}S^{-1}K$
$Ba_7In_6Al_2O_{19}$	0.85±0.01	2711±321
$Ba_7In_{5.9}Y_{0.1}Al_2O_{19}$	0.79±0.01	4374±518

of the substitution of indium for yttrium that is larger in size. As the geometric parameters increased, the values of the ion jump length increased, which was confirmed by an increase in the values of the pre-exponential multiplier. This fact is due to the proportionality of the pre-exponential factor A to the square of the jump length, in accordance with the formula

$$A = Gq^2a^2\nu_o/k, \quad (8)$$

where G is the geometric multiplier, q is the charge, a is the ion jump length, ν_o is the jump frequency, and k is the Boltzmann constant [8]. Accordingly, an increase in the lattice parameters will correlate with an increase in the jump length. Also the data in Table 3 demonstrates the often experimentally observed relationship between the activation energy and the pre-exponential multiplier. With an increase in the lattice parameters (respectively, the interatomic distances), the interaction forces of ions weaken, and their migration requires less energy, respectively, the migration energy of oxygen ions decreases and, as a result, the conductivity increases [31]. Indeed, the activation energy of oxygen-ion transfer determined from temperature dependences, which directly reflects the migration energy, decreases with the increasing lattice parameters (Tables 1, 3).

A parameter such as the free volume of a unit cell, introduced in [32] as a volume not occupied by atoms, allows us to estimate the free space for atomic migration, and its increase with the introduction of yttrium is also a favorable factor in increasing ionic conductivity.

The oxygen-ion transfer numbers (Fig. 6*b*) reflect the trends discussed above: doping led to an increase in oxygen-ion transfer numbers, with decreasing temperature the proportion of oxygen-ion transfer increased, and below 500 °C ion transport dominated.

A comparison of the oxygen-ion conductivities of the studied phase with hexagonal perovskite $Ba_5In_{1.9}Y_{0.1}Al_2ZrO_{13}$, described earlier in [24, 26], is shown in Fig. 7. As can be seen, the studied phase of $Ba_7In_{5.9}Y_{0.1}Al_2O_{19}$ exhibits more significant values of oxygen-ion conductivity than $Ba_5In_{1.9}Y_{0.1}Al_2ZrO_{13}$, which demonstrates the effect of cation deficiency in $Ba_7In_{5.9}Y_{0.1}Al_2O_{19}$, which, accordingly, is accompanied by large values of free migration volume, contributing to facilitated ion transport.

A similar set of studies was conducted for the humid air atmosphere ($pH_2O=1.92\times10^{-2}$ atm). The presence of oxygen vacancies in the structure of the phases $Ba_7In_6Al_2O_{19}$ and $Ba_7In_{5.9}Y_{0.1}Al_2O_{19}$ causes the appearance of proton defects in the interaction of samples with the water-containing gas phase and, as a result, the appearance of proton conductivity. Fig. 5*b* demonstrates the most typical behavior

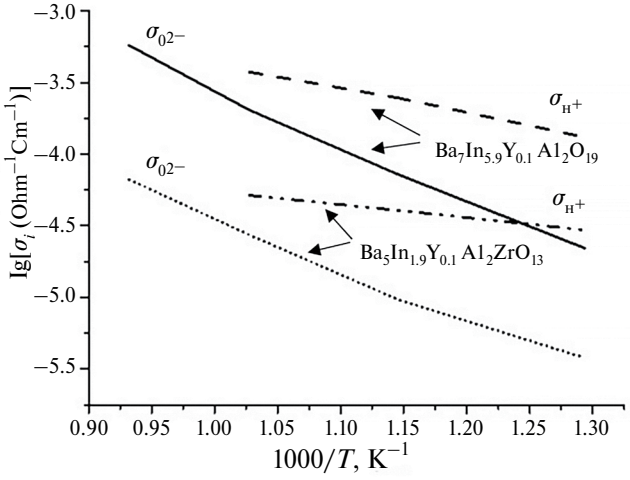

Fig. 7. Temperature dependences of the proton and oxygen-ion conductivities $Ba_7In_{5.9}Y_{0.1}Al_2O_{19}$ and $Ba_5In_{1.9}Y_{0.1}Al_2ZrO_{13}$.

of the conductivity of proton conductors with a change in atmospheric humidity. The following general patterns can be distinguished due to the introduction of water into the structure and the appearance of the proton component of conductivity:

— in a humid atmosphere, the total electrical conductivity increased compared to the values obtained in dry conditions (most significantly at temperatures below 600 °C), Fig. 5*c*;

— with a decrease in temperature, the area of the plateau of the $lg\sigma_{tot}-lgpO_2$ dependences expanded, the slope in the $pO_2 \geqslant 10^{-4}$ atm region became more shallow (Fig. 5*b*), as a result of an increase in the ionic conductivity contribution; below 500 °C in the entire studied area, the pO_2Y^{3+}-doped sample showed the dominant ion transport, Fig. 5*d*.

From the point of view of the quasi-chemical approach, the process of interaction of water vapor with structural oxygen vacancies (as an alternative to equation (2)) can be represented, in particular, as follows:

$$H_2O + 2O_O^{\times} + (V_O^S)^{\times} \rightarrow 2OH_O^{\bullet} + O_i^{''}. \quad (9)$$

According to this equation, the oxygen of the water molecule is embedded in the structural oxygen vacancy $(V_O^S)^{\times}$, protons are localized on regular oxygen nodes, forming the group $OH_O^{\bullet}$. Since the structural vacancy is considered as a neutral defect, i.e., it is identical to the free interstitial position, the additional oxygen ion embedded in such a position has the same effective charge as the interstitial oxygen ion $O_i^{''}$.

The value of proton conductivity was estimated from the experimental $lg\sigma$-$lgpO_2$ data on the difference in the values of ionic conductivity in wet and dry atmospheres. The temperature dependences of the proton electrical conductivities

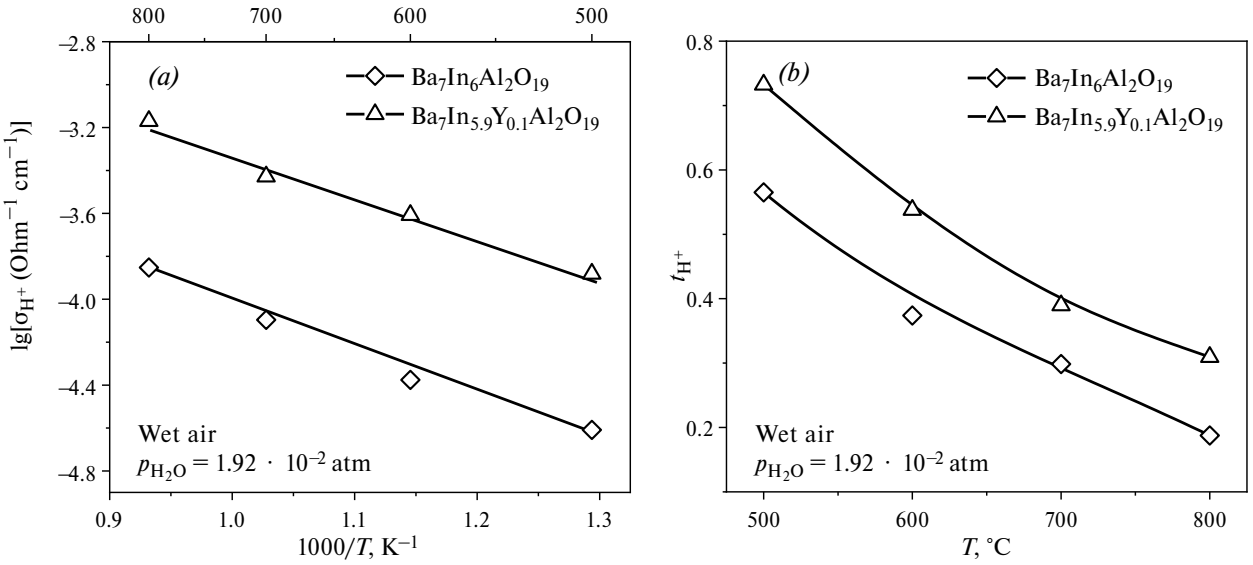

Fig. 8. Temperature dependences of proton conductivity and proton transfer numbers for phases $Ba_7In_6Al_2O_{19}$ and $Ba_7In_{5.9}Y_{0.1}Al_2O_{19}$.

are shown in Fig. 8 for the phases $Ba_7In_6Al_2O_{19}$ and $Ba_7In_{5.9}Y_{0.1}Al_2O_{19}$. Throughout the studied temperature range, an increase in proton conductivity values was observed for the yttrium-doped phase, while the activation energy values decreased to 0.40 eV compared with 0.47 eV for the undoped phase. The increase in proton conductivity for the yttrium-doped phase may be the result of higher proton concentrations, which is confirmed by TG studies. The temperature dependences of the proton transfer numbers $Ba_7In_{5.9}Y_{0.1}Al_2O_{19}$ (Fig. 8*b*) confirm the dominant proton transport below 500 °C.

A comparison of the temperature dependences of the proton conductivities of the two Y-doped phases $Ba_7In_{5.9}Y_{0.1}Al_2O_{19}$ and $Ba_5In_{1.9}Y_{0.1}Al_2ZrO_{13}$ is shown in Fig. 7. It can be seen that for both oxygen-ion conductivity and proton conductivity, higher values were observed for the $Ba_7In_{5.9}Y_{0.1}Al_2O_{19}$ phase. That is, we can state the influence of the dynamics of the oxygen sublattice on proton transport. The symbatic behavior of oxygen-ion and proton conductivities, demonstrating the effect of the state of the oxygen sublattice on the formation of proton conductivity, was previously described for acceptor-doped perovskites and confirmed for numerous compounds. Obviously, such general patterns are typical for various structural types of proton-conducting complex oxides.

Thus, it can be concluded that the strategy of doping hexagonal perovskite $Ba_7In_6Al_2O_{19}$ with yttrium is promising, as it allows increasing proton conductivity. Further study of the effect of doping on the transport properties of $Ba_7In_6Al_2O_{19}$ may be related to studies of a wide concentration range of Y^{3+} dopant, which can optimize proton transport to a greater extent, and also to the study of concentration dependences.

CONCLUSION

Hexagonal perovskite $Ba_7In_{5.9}Y_{0.1}Al_2O_{19}$ was obtained by solid-phase synthesis. The introduction of yttrium into the indium sublattice led to an increase in the unit cell parameters (a = 5.935(7) Å, c = 37.736(8) Å) compared with the undoped $Ba_7In_6Al_2O_{19}$ phase (a = 5.921(2) Å, c = 37.717(4) Å). Isovalent doping led to an increase in the degree of hydration to x=0.55 mol H_2O (compared with 0.41 mol H_2O for the undoped phase), as a result of an increase in lattice parameters and the possibility of incorporating large concentrations of OH groups into oxygen-deficient blocks. The increase in interatomic distances also contributed to an increase in oxygen-ion transport. The $Ba_7In_{5.9}Y_{0.1}Al_2O_{19}$ phase is capable of proton conduction in atmospheres with high partial pressures of water vapor ($pH_2O = 1.92 \cdot 10^{-2}$ atm), proton transfer became dominant below 500 °C.

The ionic (O^{2-}, H^+) conductivities of the studied phase $Ba_7In_{5.9}Y_{0.1}Al_2O_{19}$ and hexagonal perovskite $Ba_5In_{1.9}Y_{0.1}Al_2ZrO_{13}$, which does not contain barium vacancies, are compared. It has been established that cationic deficiency contributes to facilitated ion transport as a result of a greater free migration volume.

FUNDING

The work was supported by the Russian Science Foundation and the Government of the Sverdlovsk Region No. 24–13–20026, https://rscf.ru/project/24-13-20026/.

CONFLICT OF INTEREST

The authors declare that they have no conflict of interest.

REFERENCES

1. Takahashi, T. and Iwahara, H., Solid-state ionics: Protonic conduction in perovskite-type oxide solid solution, *Rev. Chem. Mineral*, 1980, vol. 17, no. 4, p. 243.
2. Iwahara, H., Esaka, T., Uchida, H., and Maeda, N., Proton conduction in sintered oxides and its application to steam electrolysis for hydrogen production, *Solid State Ionics,* 1981, vol. 3, no. 4, p. 359.
3. Uchida, H., Maeda, N., and Iwahara, H., Steam concentration cell using a high temperature type proton conductive solid electrolyte, *J. Appl. Chem.*, 1982, vol. 12, p. 645.
4. Iwahara, H., Uchida, H., and Maeda, N., High temperature fuel and steam electrolysis cells using proton conductive solid electrolytes, *J. Power Sources*, 1982, vol. 7, no. 3, p. 293.
5. Danilov, N., Lyagaeva, J., Vdovin, G., and Medvedev, D., Multifactor performance analysis of reversible solid oxide cells based on proton-conducting electrolytes, *Appl. Energy* 2019, vol. 237, p. 924.
6. Tarutin, A., Kasyanova, A., Lyagaeva, J., Vdovin, G., and Medvedev, D., Towards high-performance tubular-type protonic ceramic electrolysis cells with all-Ni-based functional electrodes, *J. Energy Chem.*, 2020, vol. 40, p. 65.
7. Medvedev, D.A., Current drawbacks of proton–conducting ceramic materials: How to overcome them for real electrochemical purposes, *Curr. Opin. Green Sustain. Chem.*, 2021, vol. 32, p. 100549.
8. Yaroslavtsev, A.B., Solid electrolytes: main prospects of research and development, *Russ. Chem. Rev.*, 2016, vol. 85, no. 11, p. 1255.
9. Kochetova, N., Animitsa, I., Medvedev, D., Demin, A., and Tsiakaras, P., Recent activity in the development of proton-conducting oxides for high-temperature applications, *RSC Adv.*, 2016, vol. 6, p. 73222.
10. Hyodo, J., Tsujikawa, K., Shiga, M., Okuyama, Y., and Yamazaki, Y., Accelerated discovery of proton-conducting perovskite oxide by capturing physicochemical fundamentals of hydration, *ACS Energy Lett.*, 2021, vol. 6, no. 8, p. 2985.
11. Zhou, Y., Shiraiwa, M., Nagao, M., Fujii, K., Tanaka, I., Yashima, M., Baque, L., Basbus, J., Mogni, L., and Skinner, S., Protonic conduction in the $BaNdInO_4$ structure achieved by acceptor doping, *Chem. Mater.*, 2021, vol. 33, p. 2139.
12. Shiraiwa, M., Kido, T., Fujii, K., and Yashima, M., High-temperature proton conductors based on the (110) layered perovskite $BaNdScO_4$, *J. Mat. Chem.* A, 2021, vol. 9, p. 8607.
13. Troncoso, L., Arce, M.D., Fernandez-Diaz, M.T., Mogni, L.V., and Alonso, J.A., Water insertion and combined interstitial-vacancy oxygen conduction in the layered perovskites $La_{1.2}Sr_{0.8-x}Ba_xInO_{4+d}$, *New J. Chem.*, 2019, vol. 43, p. 6087.
14. Tarasova, N., Animitsa, I., Galisheva, A., and Korona, D., Incorporation and conduction of protons in Ca, Sr, Ba-doped $BaLaInO_4$ with Ruddlesden-Popper Structure, *Materials*, 2019, vol. 12, p. 1668.
15. Tarasova, N., Animitsa, I., Galisheva, A., and Pryakhina, V., Protonic transport in the new phases $BaLaIn_{0.9}M_{0.1}O_{4.05}$ (M=Ti, Zr) with Ruddlesden-Popper structure, *Solid State Sci.*, 2020, vol. 101, p. 106121.
16. Tarasova, N., Animitsa, I., and Galisheva, A., Electrical properties of new protonic conductors $Ba_{1+x}La_{1-x}InO_{4-0.5x}$ with Ruddlesden-Popper structure, *J. Solid State Electrochem.*, 2020, vol. 24, p. 1497.
17. Tarasova, N., Galisheva, A., and Animitsa, I., Improvement of oxygen-ionic and protonic conductivity of $BaLaInO_4$ through Ti doping, *Ionics*, 2020, vol. 26, p. 5075.
18. Tarasova, N., Galisheva, A., and Animitsa, I., Ba^{2+}/Ti^{4+}- co-doped layered perovskite $BaLaInO_4$: the structure and ionic (O^{2-}, H^+) conductivity, *Intern. J. Hydrogen Energy,* 2021, vol. 46, p. 16868.
19. Tarasova, N., Galisheva, A., Animitsa, I., and Korona, D., Hydration and the state of oxygen–hydrogen groups in the complex oxide $BaLaIn0_{.9}Nb_{0.1}O_{4.1}$ with the Ruddlesden–Popper structure, *Russ. J. Phys. Chem. A*, 2020, vol. 94, p. 818.
20. Tarasova, N., Galisheva, A., Animitsa, I., and Dmitrieva, A., The Effect of donor doping on the ionic (O^{2-}, H^+) transport in novel complex oxides $BaLaIn_{1-x}Nb_xO_{4+x}$ with the Ruddlesden–Popper structure, *Russ. J. Electrochem.*, 2021, vol. 57, p. 962.
21. Murakami, T., Hester, J., and Yashima, M., High proton conductivity in $Ba_5Er_2Al_2ZrO_{13}$, a hexagonal perovskite-related oxide with intrinsically oxygen-deficient layers, *J. Am. Chem. Soc.*, 2020, vol. 142, p. 11653.
22. Shpanchenko, R.V., Abakumov, A.M., Antipov, E.V., Nistor, L., Van Tendeloo, G., and Amelinckx, S., Structural study of the new complex oxides $Ba_{5-y}Sr_yR_{2-x}Al_2Zr_{1+x}O_{13+x/2}$ (R = Gd-Lu, Y, Sc), *J. Solid State Chem.*, 1995, vol. 118, p. 180.
23. Matsuzaki, K., Saito, K., Ikeda, Y., Nambu, Y., and Yashima, M., High Proton Conduction in the Octahedral Layers of Fully Hydrated Hexagonal Perovskite-Related Oxides, *J. Amer. Chem. Soc.,* 2024, vol. 146, p. 18544.
24. Andreev, R., Korona, D., Anokhina, I., and Animitsa, I., Proton and oxygen-ion conductivities of hexagonal perovskite $Ba_5In_2Al_2ZrO_{13}$, *Materials*, 2022, vol. 15, no. 11, p. 3944.
25. Andreev, R.D., Anokhina, I.A., Korona, D.V., Gilev, A.R., and Animitsa, I.E., Transport properties

of In^{3+}- and Y^{3+}-doped hexagonal perovskite $Ba_5In_2Al_2ZrO_{13}$, *Russ. J. Electrochem.*, 2023, vol. 59, p. 190.

26. Andreev, R.D., and Animitsa, I.E., Protonic transport in the novel complex oxide $Ba_5Y_{0.5}In_{1.5}Al_2ZrO_{13}$, *Ionics,* 2023, vol. 29, no. 11, p. 4647.
27. Andreev, R.D., Korona, D.V., Vlasov, M.I., and Animitsa, I.E., Protonic ceramics $Ba_5In_{2-x}Y_xAl_2ZrO_{13}$ with the perovskite-related hexagonal structure for solid oxide fuel cells: synthesis, optical band gap and transport properties, *Ceramics International*, 2024. https://doi.org/10.1016/j.ceramint.2024.04.227
28. Andreev, R., and Animitsa I., Transport properties of intergrowth structures $Ba_5In_2Al_2ZrO_{13}$ and $Ba_7In_6Al_2O_{19}$, *Appl. Sci.*, 2023, vol. 13, no. 6, p. 3978.
29. Shannon, R., Revised effective ionic radii and systematic studies of interatomic distances in halides and chalcogenides, *Acta Crystallogr. Sect. A Cryst. Phys. Diffr. Theor. Gen. Crystallogr.*, 1976, vol. 32, p. 751.
30. Tarasova, N., and Animitsa, I., Materials $A^{II}LnInO_4$ with Ruddlesden–Popper structure for electrochemical applications: relationship between ion (oxygen-ion, proton) conductivity, water uptake, and structural changes, *Materials*, 2022, vol. 15, no. 1, p. 114.
31. Chebotin, V.N., and Perfilev, M.V., *Electrochemistry of solid electrolytes* (in Russian), Moscow: Khimiya, 1978. 313 p.
32. Sammells, A.F., Kendall, K.R., Navas, C., Thomas, J.K., Loye, H.C., Amsif, M., and Hayashi, H., Structural consideration on the ionic conductivity of perovskite-type oxides, *Solid State Ionics*, 1999, vol. 122, p. 1.

RUSSIAN JOURNAL OF ELECTROCHEMISTRY, 2025, Vol. 61, No. 1, pp. 63–70

INFLUENCE OF METALLOPHILIC INTERACTIONS ON PHYSICOCHEMICAL PROPERTIES OF ION-CONDUCTING GLASS SYSTEM (1-x)(0.27Sb_2Se_3–0.73$GeSe_2$) -$x$$Ag_2Se$[1]

© 2025 V. V. Tomaev [a, b, *], Yu. S. Tveryanovich [b, **], S. S. Lunkov [b], S. A. Zaitseva [a, b]

[a] Saint Petersburg Institute of Technology (Technical University), Saint Petersburg, Russia

[b] Saint Petersburg State University, Saint Petersburg, Russia

*e-mail: tvaza@mail.ru

**e-mail: tys@bk.ru

Received: July 01, 2024
Revised: October 08, 2024
Accepted: October 30, 2024

Abstract: The influence of silver selenide concentration on plasticity, microhardness and softening temperature interrelationship, energy of metal atoms in chalcogenide glass system (1-x)(0.27Sb_2Se_3–0.73$GeSe_2$)-$x$$Ag_2Se$ is presented. Particular attention is paid to a multiple increase in plasticity with an increase in silver selenide content in chalcogenide glass. The observed effects are associated with the formation of metallophilic interactions of silver-silver. The studies are supplemented with the results of impedancemetry, due to the fact that metallophilic interactions in chalcogenide glass can actively influence not only the glass transition temperature, but also many other important properties, including the mechanism of electronic and ion conductivity.

Keywords: *chalcogenide glass, silver selenide, ionic conductivity, plasticity, metallophilic bonds Ag-Ag, glass mesh*

DOI: 10.31857/S04248570250104e2

INTRODUCTION

Flexible electronics are predicted to revolutionize the electronics industry of the 21st century, so it is not surprising that this area is currently developing very intensively [1–3]. Such rapid changes are facilitated not only by the convenience of using flexible devices in technology, but also by the possibility of placing various sensors based on them directly on controlled mobile objects, for example, on the human body or clothing [4, 5]. In practice, all components of flexible electronic devices, including functional components, must withstand repeated mechanical deformations in order to ensure structural and functional integrity, including at above room temperatures [6–8].

It should be noted that most of the known inorganic semiconductors are brittle at room temperature [9–11], and are poorly suited for flexible electronics purposes. Therefore, the discovery of the plasticity of the Ag_2S semiconductor at room temperature [12–14] is a breakthrough in solving this long-standing dilemma between mechanical deformability and electrical characteristics and may open up wide opportunities for more intensive development of flexible electronics [15–17].

Semiconductor materials that are currently used in flexible electronics can be divided into three main groups: inorganic nanocrystalline [18–20], inorganic amorphous [21–23] and organic [24–26]. The group of inorganic nanocrystalline semiconductor materials has relatively high stability of functional properties, but low flexibility and plasticity. Organic semiconductors are quite plastic, but their properties degrade relatively quickly. Inorganic amorphous semiconductors, represented mainly by amorphous silicon, occupy an intermediate position in this series, but their electronic properties are not well-regulated. A separate group of promising materials used in flexible electronics could be plastic glasslike materials [27–29], which however as a rule, are characterized by high brittleness, which causes their low resistance to mechanical stress and temperature fluctuations [30].

Nevertheless, chalcogenide glasses with a high silver content have been found not only to have significant ionic conductivity over silver, but also, as previously shown [31–33], to exhibit increased plasticity compared to other chalcogenide glasses. The latter is related to the ability of silver atoms to form non-directional metallophilic bonds at high concentrations in the glass mesh.

On the other hand, it is known that glasses have a number of advantages compared to crystals:

[1] Based on the materials of the report at the 17th International Meeting "Fundamental and applied problems of solid state ionics", Chernogolovka, June 16–23, 2024.

their properties change smoothly with changes in composition, ionic conductivity is higher than that of a crystal of the same composition. As disordered systems they are less susceptible to impurities, modern glass technologies make it possible to manufacture products of almost any shape, etc. [34, 35].

Nevertheless, it is known that plastic crystalline inorganic semiconductors based on Ag_2S, Ag_2Se, and Ag_2Te [36–38], which relate to solid electrolytes and are currently being intensively studied for these purposes, are one of the materials in demand for creating flexible sensors.

Summarizing the above, we can assume that glass capable of including at least 20 mol% silver chalcogenide in their composition without loss of glass-forming ability, may be promising materials used in flexible electronics. These observations may lead to an interest in Ag_2Se-based glass.

In [32], the glass transition temperature of chalcogenide glasses with ionic conductivity was analyzed depending on the content of silver chalcogenides. Here, the peculiarities of the change in the glass transition temperature of a silver chalcogenide-based material are explained by the coexistence of covalent silver–chalcogen (Ag–Ch) bonds and metallophilic silver-silver (Ag–Ag) bonds. When assessing the degree of constraint of a chalcogenide glass grid, it is traditionally assumed that the number of bonds formed by each atom coincides with its degree of oxidation. However, the analysis showed that a large number of studied chalcogenide glass-forming systems containing silver demonstrate a common relationship, which allows us to conclude that the silver bonding coefficient in chalcogenide glass significantly exceeds its formal degree of oxidation, since silver forms metallophilic bonds in addition to covalent ones.

Expecting that metallophilic interactions affect not only the glass transition temperature, but also many other important properties of these glasses, including ionic conductivity, the authors measured the conductivity as a function of the concentration of silver selenide in the glass of the $(1\text{-}x)(0{,}27Sb_2Se_3–0{,}73GeSe_2)\text{-}xAg_2Se$ system.

The choice of this system for research was determined by the following considerations.

The authors of [39], examining glass of the $Ag_2Se–Sb_2Se_3–GeSe$ system, convincingly confirmed the assumption of high silver coordination in chalcogenide glass, leading to a corresponding change in the properties of the glass, in particular the softening temperature T_g. According to these data, the replacement of Sb_2Se_3 with Ag_2Se leads to a significant increase in T_g.

Considering that the introduction of Ag_2Se into the glass of the $Sb_2Se_3–GeSe_2$ system leads to a significant increase in plasticity [32], the authors of this article paid increased attention to the study of this system.

In addition, the concept of the existence of metallophilic bonds in chalcogenide glass is new and therefore needs comprehensive consideration and additional justification.

According to our data [33] obtained for glass of the $Ag_2Se\text{-}As_2Se_3(Sb_2Se_3)\text{-}GeSe_2$ system, T_g does not decrease even when trivalent metal selenides are replaced by Ag_2Se.

Considering in more detail the data we obtained in [33], it can be assumed that $GeSe_2$, as a compound containing a metal with a maximum coordination number in the glass-forming system under study, will mainly determine the value of T_g. It was also concluded that Ag_2Se in the composition of the studied glasses has the same effect on the value of T_g as the trivalent metal selenides As and Sb. This is consistent with the conclusion of the authors [40] that the average atomic coordination in glasslike nanodomains of the Ag_2Se composition is close to 2.4.

In [31], the dependence of the plasticity of the $(1\text{-}x)(0.27Sb_2Se_3–0.73GeSe_2)\text{-}xAg_2Se$ system glass synthesized by us on the Ag_2Se concentration calculated using the Milman ratio [41] is presented. The observed increase in plasticity can contribute to a significant improvement in functional properties, in particular, improved resistance to temperature fluctuations and good prospects for use in flexible electronics.

Thus, based on the presented brief overview of glass, the authors selected the $(1\text{-}x)(0.27Sb_2Se_3–0.73GeSe_2)\text{-}xAg_2Se$ system for research, which exhibits high plasticity and is promising for use in flexible electronics.

The purpose of this work is to develop the concept of metallophilic interactions of silver atoms in chalcogenide glass, to study their effect on the energy of interatomic interactions by the XPS method and on ion transport, according to impedance spectroscopy. These results are discussed in conjunction with experimental results on the softening temperature and plasticity of glasses.

MATERIALS AND METHODS

Synthesis of glass (GS). Chalcogenide glass was synthesized from simple substances and contained the following amounts of the main component: Sb (99.995%), Se (99.997%), Ag (99.990%) and Ge (99.999%) according to the procedure presented in [42]. The following sample compositions were synthesized with the appropriate numbering: (0) $x = 0.00$; (1) $x =$

0.05; (2) $x = 0.10$; (3) $x = 0.15$; (4) $x = 0.20$; (5) $x = 0.25$; (6) $x = 0.30$; (7) $x = 0.35$; and (8) $x = 0.40$; (9) $x = 0.45$. For each case, the components of the appropriate composition were placed in quartz ampoules, which were then pumped out to a pressure of 10^{-4} mm Hg and sealed. This ensured the consistency of the glass composition during the manufacturing process. For all compositions, synthesis was carried out in a muffle furnace at a temperature of 900 °C for 3 hours with constant stirring. In order to increase the cooling rate, ampoules were placed in ice water immediately after synthesis. All the research methods used, with the exception of impedance spectroscopy, do not impose special requirements to the shape of the samples. The samples for impedance spectroscopy were annealed and then processed to obtain plane-parallel plates with a thickness of 3 mm.

X-ray structure analysis (XRD). X-ray phase analysis of all synthesized glasses was performed using the method presented in [42] using an ARL X'TRA diffractometer in the θ—2θ scanning mode (CuKα radiation, λ = 1.541 Å) in the angle range 2θ = 20°—60°, with a scanning step of 0.04° and an exposure time of 2 s per point. This technique, despite the controversial opinion regarding its usefulness for studying the structure of glass, has long been in the field of view of researchers [43, 44].

Differential scanning calorimetry (DSC). A high-sensitivity Netzsch DSC 204 F1 Phoenix differential scanning calorimeter with a μ-sensor was used to measure the T_g value of the glass [45]. The concept of the measuring chamber is based on homogeneous heating of the disk μ-sensor in order to obtain a stable and reproducible baseline, and an efficient cooling system. The glass of the studied compositions was pre-crushed in an agate mortar and placed in an aluminum crucible. The analysis was carried out in the temperature range 30–350 °C, and the heating rate was 10 degrees/min.

Together with high temperature accuracy, the μ-sensor provides a high level of sensitivity, which was previously unattainable in calorimetry.

X-ray photoelectron spectroscopy (XPS). The method of photoelectron spectroscopy based on the phenomenon of the photoeffect is a modern method for studying filled electronic states in a solid and is able to provide additional information about the properties of the studied glass [46].

To measure the glass of the studied compositions using the XPS method, the analytical module of photoelectron spectroscopy of the Nanolab platform and the Thermo Fisher Scientific Escalab 250Xi integrated photoelectronic and scanning Auger electron spectrometer were used.

Impedance spectroscopy (IS). The glass of the studied compositions was measured by impedance spectroscopy using an Elins Z-1000P impedance meter (Elins LLC, Russia) in a two-contact cell with reversible Ag electrodes in the frequency range of 1–106 Hz [47]. The glass samples in the form of a cube with a side size of 3 mm were carefully polished. A silver paste was applied to the opposite faces of all the glass items as a reversible electrode. All measured impedance hodographs were processed using a special ZView program and the Origin graphics software package from OriginLab Corporation. The resistance of the sample was determined based on the data obtained and electrical conductivity was calculated.

RESULTS AND THEIR DISCUSSION

The introduction of monovalent metal compounds into chalcogenide glass leads to a decrease in the average number of bonds per atom. This reduces the degree of constraint of the glass grid. The result is a rapid decrease in T_g. When the concentration of Ag_2Se increases to 20 mol there is a possibility that silver atoms will form not only covalent bonds with selenium, but also metallophilic interactions with each other. This leads to a significant slowdown in the decrease in T_g. The result is that glass containing 40 mol.% Ag_2Se has T_g=200 °C. This is more than the softening temperature that such classical chalcogenide glass as As_2S_3 and As_2Se_3 has.

Synthesis of glass. All synthesized glass samples had a black color and a typical conchoidal fracture.

X-ray phase analysis. According to the results of X-ray phase analysis of all synthesized glass, diffractogram systems contain exceptionally wide amorphous peaks (halos) characteristic of glasslike materials, which confirms the absence of crystalline inclusions. The exception is the 9th sample, which contains, according to the XRD data, crystalline inclusions.

Differential scanning calorimetry (DSC). Fig. 1 shows the measured DSC curve of a glass sample having a composition of x=0.30. The glass softening effect is characterized by a good resolution, which makes it possible (as shown in Fig. 1) to analyze the concentration dependences of not only the glass softening temperature (T_g) itself.

Fig. 2 shows the dependence of the glass transition temperature on the concentration of Ag_2Se according to DSC data. The T_g value of Ag_2Se-free glass is 280 °C and is in satisfactory agreement with the literature data [48].

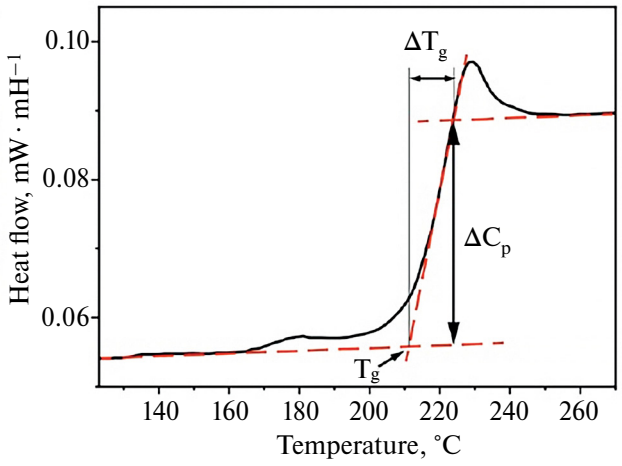

Fig. 1. DSC curve of a glass sample with x=0.30, showing how to determine the values of T_g, ΔC_p and ΔT_g based on the graph.

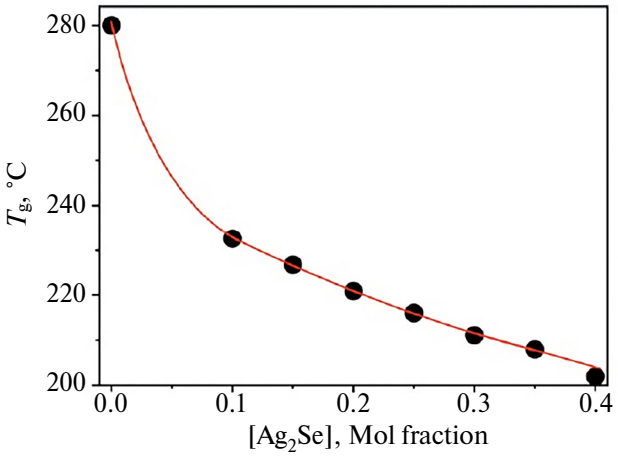

Fig. 2. Dependence of the glass transition temperature, determined by the DSC method for the glass of the studied system, on the concentration of Ag_2Se.

Photoelectron spectroscopy. The XPS of all elements (with the exception of Ag spectra) consists of several lines. Therefore, after deconvolution of the spectrum, the concentration dependence of the weighted average binding energy of the entire spectrum for each element was calculated using the formula:

$$E_s = \frac{\sum_i E_i \cdot A_i}{\sum_i A_i},$$

where E_i is the position of the maximum of the i–th band of the spectrum; A_i is its integral relative intensity.

The obtained dependences of the binding energy (E_S) of each element included in the glass on the concentration of Ag_2Se are shown in Fig. 3.

According to the presented results, the following assumptions can be made.

The Sb binding energy (Fig. 3*a*) is practically independent of the glass composition. The binding energy of the remaining elements (Fig. 3*b*–3*d*) increases with the increasing silver content. The ratio of concentrations of antimony and germanium selenides does not change. Therefore, it can be assumed that the changes are associated with an increase in the content of Ag_2Se.

XRF did not detect crystalline inclusions in glasses with $x \leqslant 0.4$. At x=0.45, crystalline inclusions of the compound Ag_8GeSe_6 appear. Therefore, it can be assumed that the growth of E_s for Ag, Ge, and Se is the result of the formation of triple structural units of the specified compound in the glass grid. However, the $GeSe_2$ content in glass with x=0 is high (73 mol.%). Therefore, for the first Ag_2Se additives, there are no difficulties in forming the structural units of the Ag_8GeSe_6 compound and E_s^{Ag} should not depend on the composition. On the other hand, E_s^{Ge} should grow linearly with an increase in the Ag_2Se content. The observed changes in E_s for Ag, Ge, and Se have a zero derivative at low Ag_2Se concentrations. This means that the effect is described by a power-law dependence on the content of Ag_2Se with a degree index of at least 2. Metallophilic Ag-Ag interactions satisfy this requirement.

Thus, E_s^{Ag} increases with the increasing silver content due to metallophilic Ag-Ag interactions. According to the induction mechanism, this growth extends to the elements located in the first and second coordination spheres of silver. These elements include selenium and germanium. Antimony is not one of them, since structural units of compounds based on Ag, Ge, and Se, which do not include Sb, are formed in glass. This compound is released into an independent crystalline phase during crystallization of alloys as a result of exceeding the critical content of Ag_2Se.

Impedance spectroscopy. The measured dependences of the imaginary part of the impedance Z" on the real Z' have a typical form for solid electrolytes (Fig. 4).

Based on this, the obtained experimental values of resistivity were attributed to ionic conductivity.

According to the results of impedance spectroscopy, the dependence of resistivity on the Ag_2Se content in glass (x) was found. According to the equations proposed to describe the transport of singly charged cations in chalcogenide glasses [49, 50]: $\lg R \sim -\sqrt[3]{M}$ (where R is the resistivity, M is the atomic fraction of the singly charged cation). The experimental data plotted in these coordinates shown in Fig. 5 demonstrate the observance of this relationship.

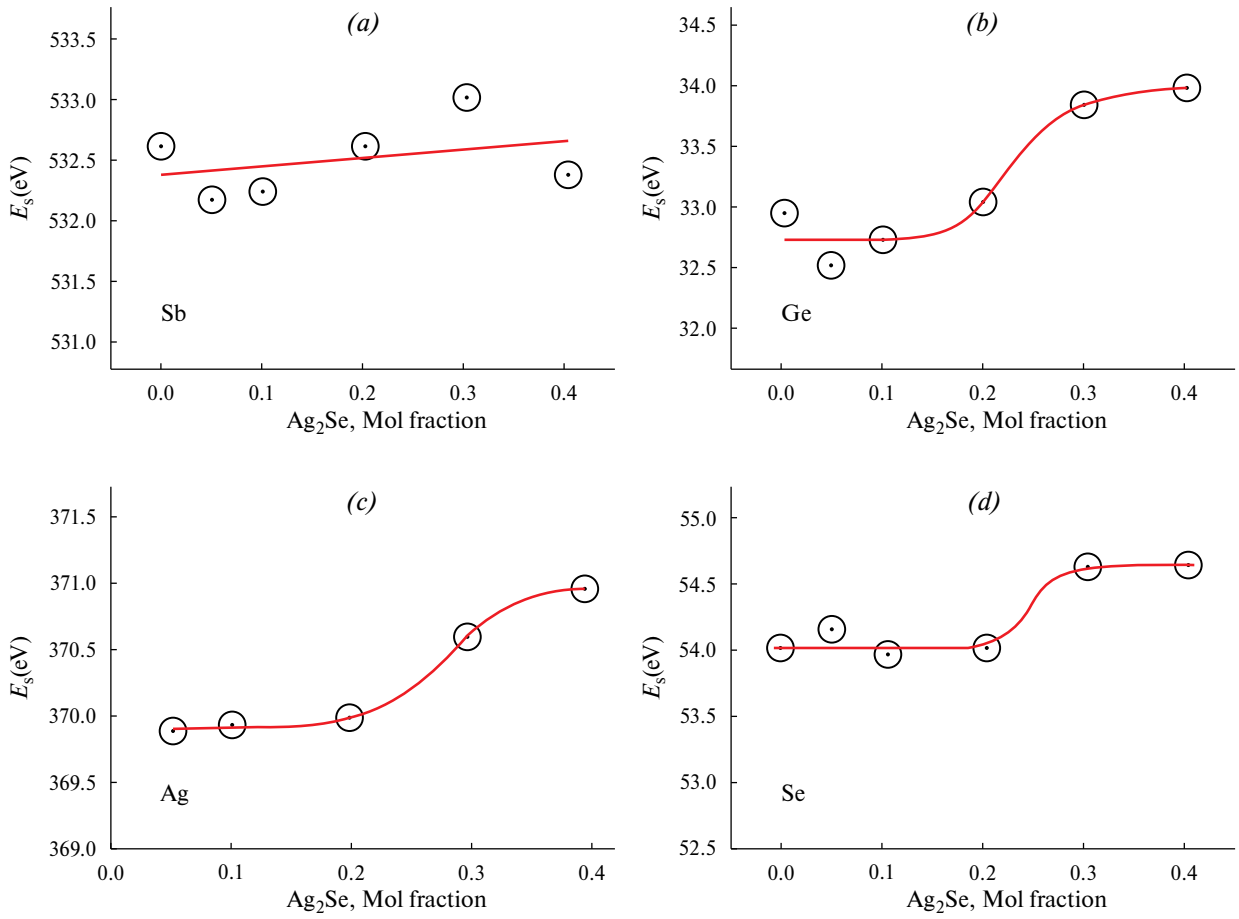

Fig. 3. Dependence of the weighted average binding energy of each element in the glass of the (1-*x*)($0.27Sb_2Se_3$–$0.73GeSe_2$)-*x*Ag_2Se system on the concentration of Ag_2Se.

Moreover, extrapolation of the found dependence to the silver concentration corresponding to the Ag_2Se composition gives a resistivity value of 54 ohms cm. Considering that we are not talking about a crystalline compound of the specified composition, but about hypothetical glass, this resistivity value can be considered reasonable.

The obtained impedance hodographs are semicircles, the center of which is located below the axis of the abscissa. The reason for this, as is known, is the fluctuation spread of the values of the characteristic time τ describing the corresponding hodograph (the inverse of the voltage frequency corresponding to the maximum value of the imaginary part of the hodograph). The wider the τ spread, the lower the center of the circle of the hodograph is located. The fluctuating nature is characteristic of the glasslike state.

Fluctuations τ can be compared to the fluctuation of potential barriers overcome by cations during their migration. The magnitude of these frozen fluctuations is determined by the glass formation temperature (T_g). For the studied glasses with x varying from 0.2 to 0.4, the deviation of T_g from its average value in this concentration range is ± 2%. This allows us to consider the fluctuation in the height of potential barriers as a constant value. The height of potential barriers itself, depending on the concentration of Ag_2Se, varies significantly, leading to a considerable change in the logarithm of resistivity. From this it can be concluded that the relative role of τ fluctuations will increase with an increase in the concentration of Ag_2Se and a decrease in R.

The parameter that numerically characterizes the displacement of the center of the circle (and, accordingly, the fluctuation τ), regardless of the resistivity value, is the tangent of the angle (tgα) formed by the abscissa and the radius of the circle drawn to the point of its intersection with the abscissa.

Fig. 6 shows the dependence of the logarithm tgα on the logarithm of resistivity.

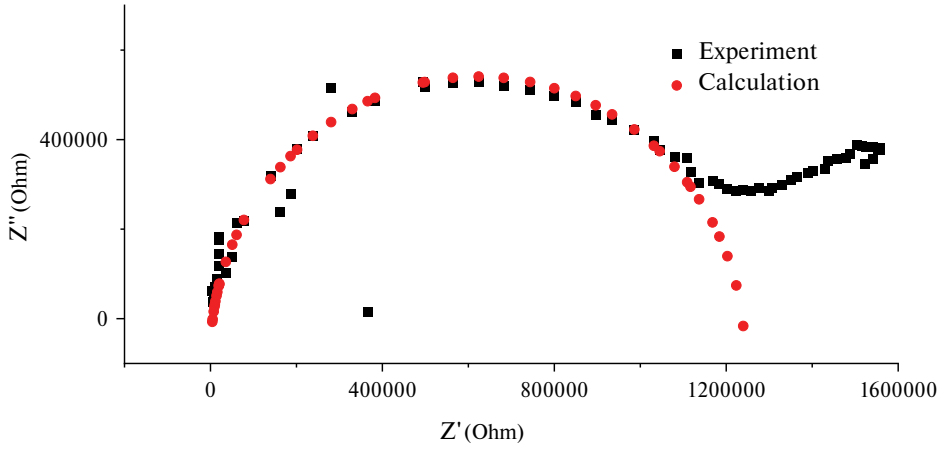

Fig. 4. Dependence of the imaginary part of the impedance on the real one for glass with x=0.4. Black dots are experimental data; red dots are the result of approximation.

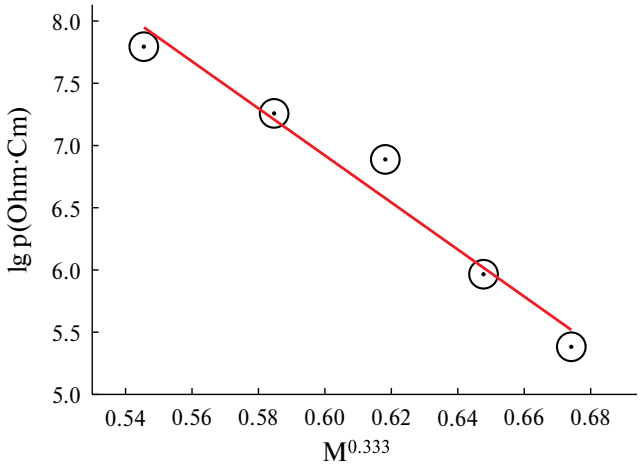

Fig. 5. Dependence of the logarithm of the resistivity of the glass of the (1-x)(0,27Sb_2Se_3–0,73$GeSe_2$)-$x$$Ag_2Se$ system on the cubic root of the atomic fraction of silver.

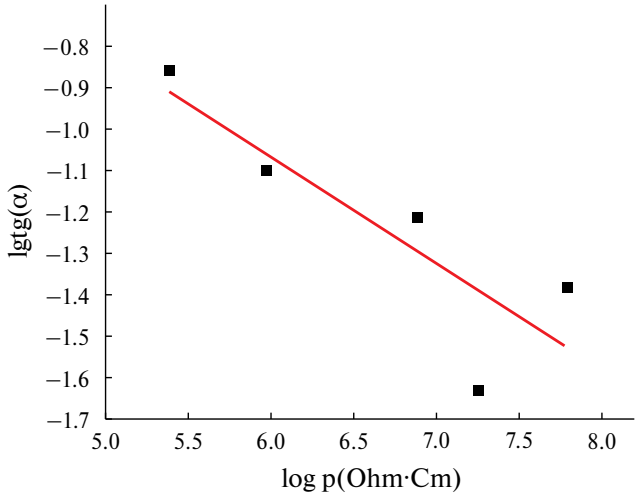

Fig. 6. Dependence of the logarithm tgα on the logarithm of the resistivity of the glass of the (1-x)(0,27Sb_2Se_3–0,73$GeSe_2$)-$x$$Ag_2Se$ system.

As expected, the increase in the resistivity of glass is accompanied by a decrease in the role of the fluctuation spread of the characteristic times of the hodographs.

CONCLUSION

The experimental results obtained and, in particular, the threshold character of the increase in the binding energy of Ge, Se, and Ag with an increase in the content of the latter confirm the formation of metallophilic Ag-Ag bonds in the glass of the (1-x)(0,27Sb_2Se_3–0,73$GeSe_2$)-$x$$Ag_2Se$ system at an Ag_2Se concentration above 20 mol.%. However, it was not possible to detect any features in the behavior of the concentration dependence of ion conductivity. Apparently, this is due to the following circumstances. Ag_2Se, chalcogenide glasses in general, including the glasses of the studied system, are formed by covalent metal-chalcogen chemical bonds with an ionic content of less than 10%. Due to this, there is no strong Coulomb repulsion between silver atoms, which makes it possible for them to converge and form a metallophilic interaction. For ion transfer, the Ag atom must acquire an electric charge, which will lead to the decay of the metallophilic interaction. Thus, the metallophilic interaction has no effect on the movement of Ag ions. However, its contribution to the process of transition of silver atoms from a covalently bonded state with a minimum effective charge to a state with an integer charge involved in ion transport cannot be excluded.

ACKNOWLEDGMENTS

The work was supported by the Russian Science Foundation, grant No. 24-23-00140.

Measurements of the properties of materials were carried out in the Scientific Park of St. Petersburg State University (Interdisciplinary Resource Center in the field of Nanotechnology, Resource Center: X-ray diffraction research methods, Resource Center: thermogravimetric and calorimetric research methods, Resource Center: physical methods of surface research, Resource Center: diagnostics of functional materials for medicine, pharmacology and nanoelectronics) and the engineering center of the St. Petersburg Institute of Technology (Technical University).

CONFLICT OF INTERESTS

The authors declare that they have no conflict of interest.

REFERENCES

1. Chen, K., Pan, J., Yin, W., Ma, C., and Wan, L., Flexible electronics based on one-dimensional inorganic semiconductor nanowires and two-dimensional transition metal dichalcogenides, *Chinese Chem. Letters*, 2023, vol. 34, 108226, 16 p.
2. Chen, H., Wei, T.-R., Zhao, K., Qiu, P., Chen, L., He, J., and Shi, X., Room-temperature plastic inorganic semiconductors for flexible and deformable electronics, *InfoMat*, 2021, vol. 3, p. 22.
3. Li, H., Cao, Y., Wang, Z., and Feng, X., Flexible and stretchable inorganic optoelectronics, *Optical Mater. Express*, 2019, vol. 9, no. 10, p. 4024.
4. Gao, W., Ota, H., Kiriya, D., Takei, K., and Javey, A., Flexible Electronics toward Wearable Sensing, *Acc. Chem. Res.*, 2019, vol. 52, p. 523.
5. Hu, J., Dun, G., Geng, X., Chen, J., Wu, X., and Ren, T.-L., Recent progress in flexible micro-pressure sensors for wearable health monitoring, *Nanoscale Adv.*, 2023, vol. 5, p. 3131.
6. Kim, J., Lee, J., Son, D., Choi, M.K., and Kim, D.H., Deformable devices with integrated functional nanomaterials for wearable electronics, *Nano Convergence*, 2016, vol. 3, no. 4, p. 13.
7. Vu, C.C., Kim, S.J., and Kim, J., Flexible wearable sensors – an update in view of touch-sensing, *Sci. and Technol. Adv. Mater.*, 2021, vol. 22, no. 1, p. 26.
8. Amani, A.M., Tayebi, L., Abbasi, M., Vaez, A., Kamyab, H., Chelliapan, S., and Vafa, E., The Need for Smart Materials in an Expanding Smart World: MXene-Based Wearable Electronics and Their Advantageous Applications, *ACS Omega*, 2024, vol. 9, no. 3, p. 3123.
9. Pisula, W., Inorganic Semiconductors in Electronic Applications, *Electron. Mater.*, 2023, vol. 4, p. 136.
10. Wang, S., Sun, M., and Hung, N.T., Advanced Inorganic Semiconductor Materials, *Inorganics*, 2024, vol. 12, p. 81.
11. Sun, Y., and Rogers, J.A., Inorganic Semiconductors for Flexible Electronics, *Adv. Mater.*, 2007, vol. 19, p. 1897.
12. Shi, X., Chen, H., Hao, F., Liu, R., Wang, T., Qiu, P., Burkhardt, U., Grin, Y., and Chen, L., Room-temperature ductile inorganic semiconductor, *Nature Mater*, 2018, vol. 17, p. 421.
13. Liang J., Wang T., Qiu P., Yang S., Ming C., Chen H., Song Q., Zhao K., Wei T.-R., Ren D., Sun Y.-Y., Shi X., He J., Chen L., Flexible thermoelectrics: from silver chalcogenides to full-inorganic devices, *Energy & Environmental Sci.*, 2019, vol. 17, no. 8, p. 9.
14. Min, Zhu, Xiao-Lei, Shi, Hao, Wu, Qingfeng, Liu, and Zhi-Gang, Chen, Advances in Ag_2S-based thermoelectrics for wearable electronics: Progress and perspective, *Chem. Engineering J.*, 2023, vol. 475, p. 146194.
15. Sadovnikov, S.I., Kostenko, M.G., Gusev, A.I., and Lukoyanov, A.V., Low-Temperature Predicted Structures of Ag_2S (Silver Sulfide), *Nanomaterials*, 2023, vol. 13, p. 2638.
16. Ge, B., Li, R., Zhu, M., Yu, Y., and Zhou, C., Deformation Mechanisms of Inorganic Thermoelectric Materials with Plasticity, *Adv. Energy Sustainability Res.*, 2024, vol. 5, p. 2300197.
17. Zhu, Y., Liang, J.-S., Shi, X., and Zhang, Z., Full-Inorganic Flexible Ag_2S Memristor with Interface Resistance–Switching for Energy-Efficient Computing, *ACS Appl. Mater. Interfaces*, 2022, vol. 14, p. 43482.
18. Wong, W.S. and Salleo, A., eds. Flexible Electronics: Materials and Applications William S. Wong and Alberto Salleo, eds. Springer 2009, 462 p.
19. Kim, D.-H., Lu, N., Ghaffari, R., and Rogers, J.A., Inorganic semiconductor nanomaterials for flexible and stretchable bio-integrated electronics, *NPG Asia Materials*, 2012, vol. 4, p. 9.
20. Wang, C., Cheng, R., Liao, L., and Duan, X., High performance thin film electronics based on inorganic nanostructures and composites, *Nano Today*, 2013, vol. 8, p. 514.
21. Jang, H.-J., Lee, K.J., Jo, K.-W., Katz, H.E., Cho, W.-J., and Shin, Y.-B., Top-down Fabrication and Enhanced Active Area Electronic Characteristics of Amorphous Oxide Nanoribbons for Flexible Electronics, *Scientific Reports*, 2017, vol. 7, p. 5728.
22. Martinez, R.V., Flexible Electronics: Fabrication and Ubiquitous Integration, *Micromachines*, 2018, vol. 9, p. 605.
23. Gupta, S., Navaraj, W.T., Lorenzelli, L., and Dahiya, R., Ultra-thin chips for high-performance flexible electronics, *npj Flex Electronics*, 2018, vol. 8, p. 17.

24. Li, L., Han, L., Hu, H., and Zhang, R., A review on polymers and their composites for flexible electronics, *Mater. Adv.*, 2023, vol. 4, p. 726.
25. Ling, H., Liu, S., Zheng, Z., and Yan, F., Organic Flexible Electronics, *Small Methods*, 2018, vol. 2, p. 1800070.
26. Liu, H., Liu, D., Yang, J., Gao, H., and Wu, Y., Flexible Electronics Based on Organic Semiconductors: from Patterned Assembly to Integrated Applications, *Small*, 2023, vol. 19, p. 2206938.
27. *Patent* US 2016/0002103 A1. Chemically Toughened Flexible Ultrathin Glass. Inventor: Xi Wang, Feng He, Jose Zimmer. Pub. No.: US 2016/0002103 A1. Pub. Date: Jan. 7, 2016. 2016–01–07. Publ. US20160002103A1. CO3C5/00 (2006.01).
28. Langgemach, W., Baumann, A., Ehrhardt, M., Preußner, T., and Rädlein, E., The strength of uncoated and coated ultra-thin flexible glass under cyclic, *AIMS Mater. Sci.*, 2024, vol. 11, no. 2, p. 343.
29. Garner, S., Glaesemann, S., and Li, X., Ultra-slim flexible glass for roll-to-roll electronic device fabrication, *Appl. Phys. A*, 2014, August. DOI: 10.1007/s00339–014–8468–2
30. Yan, J., Zhou, T., Masuda, J., and Kuriyagawa, T., Modeling high-temperature glass molding process by coupling heat transfer and viscous deformation analysis, *Precision Engineering*, 2009, vol. 33, p. 150.
31. Tveryanovich, Y.S., Fazletdinov, T.R., Tverjanovich, A.S., Fadin, Y.A., and Nikolskii, A.B., Features of Chemical Interactions in Silver Chalcogenides Responsible for Their High Plasticity, *Russ. J. Gen. Chem.*, 2020, vol. 90, no. 11, p. 2203.
32. Tveryanovich, Yu.S., Fazletdinov, T.R., Tverjanovich, A.S., Pankin, D.V., Smirnov, E.V., Tolochko, O.V., Panov, M.S., Churbanov, M.F., Skripachev, I.V., and Shevelko, M.M., Increasing the Plasticity of Chalcogenide Glasses in the System Ag_2Se–Sb_2Se_3–$GeSe_2$, *Chem. Mater.*, 2022, vol. 34, no. 6, p. 2743.
33. Tveryanovich, Yu. S., Fazletdinov, T.R., and Tomaev, V.V., *Russ. J. Electrochem.*, 2023, vol. 59, no. 8, p. 567.
34. Borisova, Z., *Glassy Semiconductors*, Springer US, 1981, 506 p.
35. Tveryanovich, Yu. S., Some ideas in chemistry and physics of chalcogenide glass, p. 147–157. *International year of glass in Russia*. Scientific conference proceedings, 2022, – ISBN: AIIR. 190 p.
36. Yang, D., Shi, X.-L., Li, M., Nisar, M., Mansoor, A., Chen, S., Chen, Y., Li, F., Ma, H., Liang, G.X., Zhang, X., Liu, W., Fan, P., Zheng, Z., and Chen, Z.-G., Flexible power generators by Ag_2Se thin films with record-high thermoelectric performance, *Nature Commun.*, 2024, vol. 1, no. 5, p. 923.
37. Yang, Q., Yang, S., Qiu, P., Peng, L., Wei, T.-R., Zhang, Z., Shi, X., and Chen, L., Flexible thermoelectrics based on ductile semiconductors, *Science*, 2022, vol. 377, no. 8, p. 854.
38. Evarestov, R.A, Panin, A.I, and Tverjanovich, Y.S., Argentophillic interactions in argentum chalcogenides: First principles calculations and topological analysis of electron density, *J. Comput. Chem.*, 2021, vol. 42, no. 4, p. 242.
39. Vassilev, V.S., Boycheva, S.V., and Ivanova, Z.G., Glass formation and physicochemical properties of the $GeSe_2$–Sb_2Se_3–Ag_2Se(ZnSe) systems, *J. Mater. Sci. Letters*, 1998, vol. 17, p. 2007.
40. Olekseyuk, I.D., Kogut, Yu.M., Parasyuk, O.V., Piskach, L.V., Gorgut, G.P., Kus'ko, O.P., Pekhnyo, V.I., and Volkov, S.V., Glass-formation in the Ag_2Se–Zn(Cd, Hg)Se–$GeSe_2$ systems, *Chem. Met. Alloys*, 2009, vol. 2, p. 146.
41. Milman, Y.V., Galanov, B.A., and Chugunova, S.I., Plasticity characteristic obtained through hardness measurement, *Acta Metallurgica et Materialia*, 1993, vol. 41, no. 9, p. 2523.
42. Tveryanovich, Y.S., Fokina, S.V., Borisov, E.N., and Tomaev, V.V., Preparation of films of vitreous solid electrolyte $(GeSe_2)_{30}(Sb_2Se_3)_{30}(AgI)_{40}$ using laser ablation method, *Glass Phys Chem.*, 2015, vol. 41, p. 440.
43. Tomaev, V.V., Tveryanovich, Yu. S., Balmakov, M.D., Zvereva, I.A., and Missyul, A.B., Ionic Conductovity of Ionic Conductivity of $(As_2Ss_3)_{1-x}(AgHal)_x$ (Hal = I, Br) Nanocomposites Glass Physics and Chemistry, *Glass Phys. Chem.*, 2010, vol. 36, no. 4, p. 455.
44. Kitaigorodskii, A.I., Glass structure and methods of its investigation by means of X-ray structural analysis, *UFN*, 1938, vol. 19, no. 2, p. 201.
45. http://www.netzsch-thermal-analysis.com/.
46. Briggs, D., *Surface analysis by the methods of Ohm and X-ray photoelectronic spectroscopy.* M.: Mir, 1984, 140 p.
47. Astafiev, E.A. and Shkerin, S.H., Instruments for impedance measurement: the relationship of price-quality-functionality, International Scientific Journal for Alternative Energy and Ecology, 2008, vol. 58, p. 150.
48. Olivier, M., Tchahame, J.C., Němec, P., Chauvet, M., Besse, V., Cassagne, C., Boudebs, G., Renversez, G., Boidin, R., Baudet, E., and Nazabal, V., Structure, Nonlinear Properties, and Photosensitivity of $(GeSe_2)_{100-x}(Sb_2Se_3)_x$ Glasses, *Opt. Mater. Express*, 2014, vol. 4, p. 525.
49. Tveryanovich, Yu. S., Aleksandrov, V.V., Murin, I.V., and Nedoshovenko, E.G., Glass-forming ability and cationic transport in gallium containing chalcogenide glasses, *J. Non-Cryst. Sol.*, 1999, vol. 256–257, p. 237.
50. Bychkov, E.A., Tveryanovich, Yu.S., and Vlasov, Yu.G., Ion Conductivity and Sensors. In *Semiconductors and Semimetals*, 2004, V. 80, "Semiconducting Chalcogenide Glasses III", p. 103–168.

RUSSIAN JOURNAL OF ELECTROCHEMISTRY, 2025, Vol. 61, No. 1, pp. 71–79

CONSOLIDATION OF Al AND Ta-SUBSTITUTED $Li_7La_3Zr_2O_{12}$ POWDERS WITH LITHIUM–ION CONDUCTIVITY BY SPARK PLASMA SINTERING [1]

© 2025 G. B. Kunshina[a, *], I. V. Bocharova[a], A. A. Belov[b], O. O. Shichalin[b], E. K. Papynov[b]

[a]Tananaev Institute of Chemistry, Subdivision of the Federal Research Centre "Kola Science Centre of the Russian Academy of Sciences", Apatity, Russia

[b]Far Eastern Federal University, Vladivostok, Russia

[*]e-mail: g.kunshina@ksc.ru

Received: July 02, 2024
Revised: October 18, 2024
Accepted: October 28, 2024

Abstract. Monophase powders of cubic modification with nominal composition $Li_{6.4}Al_{0.2}La_3Zr_2O_{12}$ (Al-LLZO) and $Li_{6.52}Al_{0.08}La_3Zr_{1.75}Ta_{0.25}O_{12}$ (Ta-LLZ) were synthesized. Dense (~97–98%) ceramic samples of solid electrolyte with increased stability in air were obtained from these powders by spark plasma sintering. High Li-ion conductivity parameters ($4–6\times10^{-4}$ S/cm) meeting to the world standard have been achieved.

Keywords: *solid electrolyte, lithium lanthanum zirconate, spark plazma sintering, cubic modification ionic conductivity*

DOI: 10.31857/S04248570250105e4

INTRODUCTION

In the last decade, inorganic solid electrolytes with high Li^+ ion conductivity have been intensively studied in order to use them as membranes, composite electrodes, and electrolytes in solid-state electrochemical devices [1, 2]. Solid electrolytes have a number of advantages over liquid and polymer materials, as they are characterized by high mechanical strength, chemical and thermal stability. The use of solid electrolytes can significantly increase the safety of lithium-ion batteries (LIB) [3]. Substituted lithium titanophosphates and germanophosphates with the NASICON structure, solid solutions based on lithium-lanthanum titanates with the perovskite structure, and representatives of a new family of lithium-conducting solid electrolytes with the garnet structure of the composition $Li_{7-3x}Al_xLa_3Zr_2O_{12}$ are considered promising in terms of ion conductivity and stability [4].

The structure of $Li_7La_3Zr_2O_{12}$ garnet has two crystal modifications: tetragonal and cubic. Tetragonal $Li_7La_3Zr_2O_{12}$ contains a fully ordered Li^+ distribution and crystallizes in the $I41/acd$ space group. Cubic $Li_7La_3Zr_2O_{12}$ crystallizes in the $Ia\bar{3}d$ space group and exhibits a disordered distribution of lithium ions and vacancies caused by lithium deficiency. The lithium-ion conductivity of the tetragonal modification is two orders of magnitude lower than that of the cubic one. The cubic modification can be stabilized by partial cationic substitution, for which the solid electrolyte $Li_7La_3Zr_2O_{12}$ is doped with ions Al^{3+}, Ga^{3+}, Nb^{5+}, Ta^{5+}, etc. The largest number of studies are devoted to the partial replacement of Li^+ with Al^{3+}, which is an inexpensive alloying additive and can also be inadvertently introduced into the garnet structure during annealing in corundum crucibles. However, the Al^{3+} ion blocks lithium positions, which leads to a decrease in Li^+ concentration and a slowdown in Li^+ diffusion (unlike Ta^{5+}, which is used to replace Zr^{4+} to avoid a decrease in Li+ content).

We synthesized powders of Al-substituted $Li_7La_3Zr_2O_{12}$ **(Al-LLZO)** of cubic modification by melting the charge followed by solid-phase annealing, which consists in the interaction of charge components consisting of low-melting crystallohydrates $ZrO(NO_3)_2{\cdot}2H_2O$, $La(NO_3)_3{\cdot}6H_2O$ and $Al(NO_3)_3{\cdot}9H_2O$ [5–7]. The powders were pressed into tablets without binding components in a mold with a diameter of 12 mm with a force of 100 MPa and sintered in air at a temperature of 1100–1150° C in a program-controlled MIMP-3 muffle under a mother powder of the same composition. For further practical use, it is necessary to obtain samples with maximum density from these powders. As noted in these papers, it was not possible to obtain dense

[1] Based on the materials of the report at the 17th International Meeting "Fundamental and applied problems of solid state ionics", Chernogolovka, June 16–23, 2024.

Table 1. Modes of solid-phase sintering of Al-LLZO tablets

I stage (heating rate, 10 degr./min.)		II stage (heating rate 2 degr./min)			Total heat treatment time, h	ρ,%
t, °C	Heating time, min	t, °C	Heating time, min	Hold, h		
20–1100	110	1100–1150	25	4	6	75
				6	8	76–78
20–1050	105	1050–1100	25	8	10	72
		1050–1150	50	6	8.5	79
		1050–1150	50	8	10.5	76–77
20–1000	100	1000–1100	50	8	10.5	74–79
				12	14.5	76–77
20–1200	180	1200		7	10	80
20–900	90	900–1150	125	8	11.5	74
		900–1200	150	8	12	73–74

samples using the classical method of high-temperature 2-stage sintering with prolonged exposure (Table 1).

The maximum density did not exceed 80% (even with the use of preliminary mechanical activation of powders on the AGO-2C centrifugal planetary mill). At the same time, only dense Al-LLZO ceramics increase the overall ionic conductivity and prevent lithium dendrites from penetrating through the pores during cycling, which can lead to a short circuit or destruction of the sample [8, 9]. In addition, Al-LLZO ceramic samples with low density are unstable when stored in air under normal conditions [10–13]. In this regard, it is necessary to obtain samples with maximum density.

To increase the density of solid electrolytes by solid-phase sintering, various sintering additives (Li_2CO_3, Li_3PO_4, $LiBO_2$, LiOH, LiCl, LiF, $Li_2B_4O_7$) are used, which contribute to the compaction of samples, improve the microstructure, which leads to a decrease in grain boundary resistance and an increase in ionic conductivity [14]. However, sintering additives partially induce the formation of small amounts of amorphous phases in the grain boundary regions. The formation of secondary phases limits the ionic conductivity of the material [15].

An innovative spark plasma sintering (**SPS**) method, which consists in high-speed consolidation of dispersed materials of various chemical and fractional compositions due to electrical pulse heating during mechanical compression, may be promising for obtaining solid electrolytes with maximum density [16, 17]. The absence of sintering additives and plasticizers, as well as the short cycle time of single-stage sintering (minutes) to achieve maximum material density (up to 100% of the theoretical) are the advantages of the SPS method over traditional sintering technologies. Despite the fact that the SPS method is a high-tech approach in a new generation of ceramic synthesis and is a global trend in the creation of modern ceramic materials for functional purposes, it is rarely used to consolidate solid electrolytes [18–22].

We have demonstrated the positive experience of using the IPS method to obtain a solid electrolyte with a NASICON structure of composition $Li_{1.3}Al_{0.3}Ti_{1.7}(PO_4)_3$ in [23]. From powders $Li_{1.3}Al_{0.3}Ti_{1.7}(PO_4)_3$ (LATP) with a narrow granulometric composition, high-density lithium-conductive ceramics (~97–98%) were obtained by SPS method under optimal technological conditions (sintering temperature 900 °C, molding pressure 50 MPa, sintering duration 5 min). There was no change in the phase composition of the LATP samples during the SPS process. The use of the SPS method made it possible to significantly reduce the consolidation time, reduce the sintering temperature, and achieve an increase in the density and ionic conductivity of LATP ceramics. The maximum ionic conductivity (σ total = 2.9×10^{-4} S/cm and σ bulk = 1.6×10^{-3} S/cm) is achieved for single-phase LATP samples in combination with the maximum density (97–98%). This is significantly higher than the results presented by the authors [24].

The purpose of this work was to develop a method for obtaining dense samples of Al- and Ta-doped solid electrolyte $Li_7La_3Zr_2O_{12}$ with high ionic conductivity by the SPS method for use in new-generation lithium batteries (fully solid-state, lithium-sulfur and lithium-air batteries).

Table 2. Modes of preparation of initial powders of cubic modification Al-LLZO and Ta-LLZO and subsequent consolidation by SPS method

	I stage			II stage			III stage				SPS				
	t, °C	τ, h	XRF	t, °C	τ, h	XRF	MA	t, °C	τ, h	XRF	t, °C	τ, min	XRF	ρ, g/cm^3	σ, S/cm
Al-LLZO	900	4	t-LLZO, c-LLZO	–			–				1000	10	t-LLZO, c-LLZO	89–90%	$1\cdot10^{-5}$
	900	4	t-LLZO, c-LLZO	1000	4	t-LLZO, c-LLZO	4x1 min	1000	4	c-LLZO	1000	10	c-LLZO	4.9 (96%)	$4\cdot10^{-4}$
Ta-LLZO	900	4	t-LLZO, c-LLZO, La_2O_3, ZrO_2, Ta_2O_5	1000	4	t-LLZO, c-LLZO	–	1100	6	c-LLZO	1100	15	c-LLZO	5.18 (98%)	$6\cdot10^{-4}$

EXPERIMENTAL PART

Preparation of Al-LLZO and Ta-LLZO powders

Monophase powders of Al-substituted solid electrolyte $Li_7La_3Zr_2O_{12}$ of nominal composition $Li_{6.4}Al_{0.2}La_3Zr_2O_{12}$ (Al-LLZO) were prepared as described in [5]. Mechanical activation (**MA**) after powder annealing at 900 °C for 4 hours was carried out in an AGO-2C planetary mill in a 4x1 min mode with a centrifugal factor of 20 g in drums, the inner surface of which is made of zirconium dioxide, using balls of the same material [25]. The balls: load mass ratio is 20:1. In order to ensure the macro uniformity of the powders, the mill was switched off every 1 min and the contents of the drums were mixed with a spatula. Next, the mechanically activated powder was calcined at a temperature of 1000 °C (heating rate of 10 degrees /min) for 4 hours.

Monophase powders of Ta-substituted solid electrolyte Li7La3Zr2O12 of nominal composition $Li_{6.52}Al_{0.08}La_3Zr_{1.75}Ta_{0.25}O_{12}$ **(Ta-LLZO)** were prepared as described in [26]. Since substitution with Ta ions ensures the transition of the tetragonal modification to a cubic one under milder conditions than when substituting with Al ions, mechanical activation of Ta-LLZO powders was not performed. The authors [27] conducted all experiments to study the chemical and thermal stability of Ta-LLZO after SPS using commercial $Li_{6.4}La_3Zr_{1.4}Ta_{0.6}O_{12}$ [28].

Consolidation of Al-LLZO and Ta-LLZO powders by SPS method

The consolidation of the prepared Al-LLZO and Ta-LLZO powders by the SPS method was carried out at the Spark Plasma Sintering System SPS-515S installation (Dr. Sinter·LAB™, Japan) according to the scheme: 1.5 g of LLZO powder was placed in a graphite mold (working diameter 1.25 mm), pressed (pressure 20.7 MPa), then the blank was placed in a vacuum chamber (10^{-5} atm) and sintered. Graphite foil with a thickness of 200 microns was used to prevent the consolidated powder from baking to the mold and plungers, as well as for unhindered extraction of the resulting sample. SPS consolidation of LLZO powders was carried out at a pressure of 50 MPa with a heating rate of 50 °C/min in the range of 900–1100 °C with exposure for 5–15 minutes.

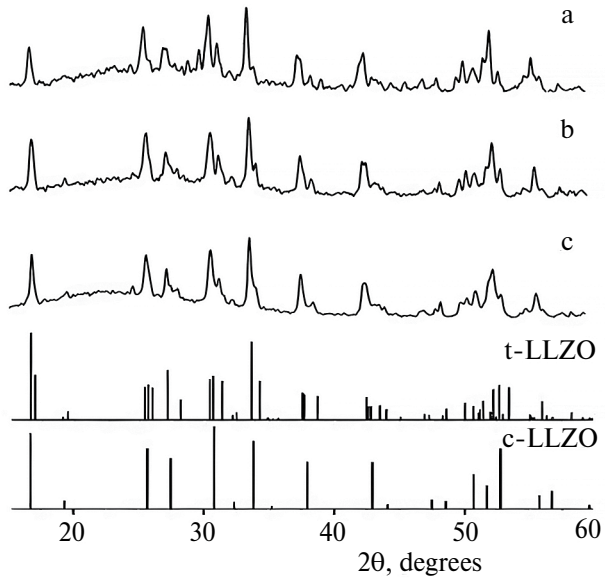

Fig. 1. Diffractograms of Al-LLZO powder after solid-phase annealing at 900 °C (a) and 1100 °C (b) and after SPS at 1000 °C for 10 min (c).

The synthesized solid electrolytes Al-LLZO and Ta-LLZO were characterized by X-ray phase analysis (**XRF**), energy dispersive X-ray spectroscopy (**EDX**), and impedance spectroscopy. Phase analysis was performed using an XRD-6000 and Rigaku MiniFlex-600 diffractometer, CuKα radiation, scattering angle range $2\theta = 10–70^o$. Data processing by the Rietveld method (refinement of lattice parameters)

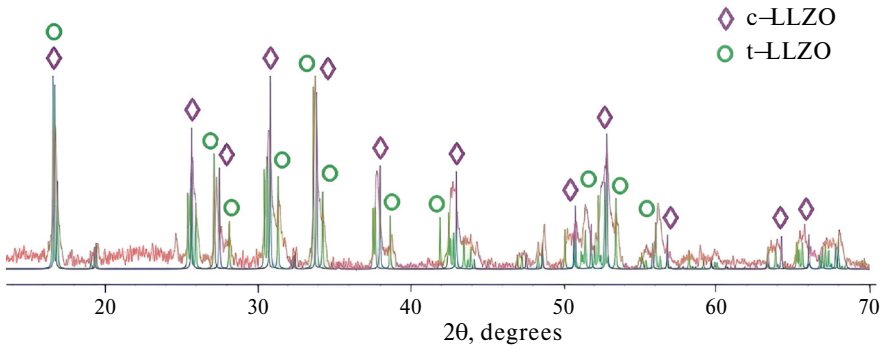

Fig. 2. Diffractograms of Al-LLZO powder after SPS at 1000 °C for 10 min.

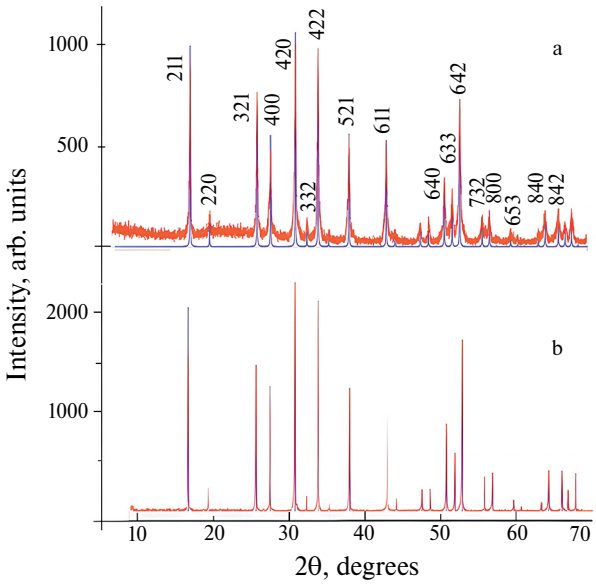

Fig. 3. Diffractograms of mechanically activated Al-LLZO powder of cubic modification (a) after annealing at 1000 °C and (b) subjected to SPS.

was performed using the smartLAB Studio II software within the Rigaku MiniFlex-600 diffractometer. The international database ICDD PDF-4 was used to decipher diffractograms.

The density of the samples was determined by hydrostatic weighing (on an LV-210A electronic scale with an accuracy of 0.001 g) using CCl_4 as an immersion liquid. The theoretical (radiographic) density for Al-LLZO was 5.1 g/cm^3 (ICDD 01–080–7219), and for Ta-LLZO it was 5.26 g/cm^3 (ICDD 04–023–7624).

Ion conductivity (σ) was studied by electrochemical impedance spectroscopy [29] with an AC signal amplitude of 0.1 V using a Z-2000 impedance meter (Elins). The measurements were carried out using a two-electrode circuit in a shielded cell of a clamping structure with graphite electrodes. The frequency range of measurements was 10^2–2×10^6 Hz. The specific ionic conductivity (σ_{total}) was calculated taking into account the geometric dimensions according to the formula:

$$\sigma_{total} = \frac{4h}{R\pi d^2}, \quad (1)$$

where R is the resistance of the tablet, determined based on the analysis of the impedance spectrum, h and d are the height and diameter of the tablet, respectively.

The electronic conductivity was determined by potentiostatic chronoamperometry (**PCA**), recording the current density as a function of time after switching on the polarizing potential [9] using a P-8 potentiostat (Elins, Russia). The value of the electronic conductivity of Ta-LLZO was calculated using the formula:

$$\sigma_e = \frac{I_{st}h}{US}, \quad (2)$$

where I_{st} is the stabilization current, U is the applied DC voltage, and h and S are the height and cross-sectional area of the tablet, respectively.

RESULTS AND DISCUSSION

According to the results of XRF, it was established (Fig. 1*a*), that after the 1st stage of Al-LLZO synthesis, as a result of annealing at 900 °C for 4 hours, a product with a garnet structure containing no initial unreacted substances and non-conductive impurity phases (La_2O_3, ZrO_2, $La_2Zr_2O_7$) was formed. The samples are well-crystallized powders of individual Al-LLZO in the form of a mixture of 2 modifications: tetragonal (ICDD PDF 01–080–6140) and cubic (ICDD PDF 01–080–7219) in commensurate quantities. An increase in temperature (up to 1100 °C) and the duration of powder annealing (up to 6 hours) did not provide a pure cubic modification of Al-LLZO, and a mixture of tetragonal and cubic modifications was also present on the X-ray image (Fig. 1*b*).

Initially, Al-LLZO powders obtained after annealing at 900 °C were used for SPS consolidation. According

Table 3. Al-LLZO lattice parameters determined by the Rietveld method

Sample	$a = b = c$, Å	Rp,%	Rwp,%	χ^2	V, Å^3
Al-LLZO	12.9735	10.57	13.47	2.1449	2185
Al-LLZO after SPS	12.96052	3.04	4.13	2.1934	2177
Al-LLZO [30]	12.96529	2.895	4.105	2.099	2179

to the XRF data, at various SPS modes (sintering temperature 900–1000 °C, molding pressure 50 MPa, sintering duration 5–10 min), Al-LLZO tablets were also obtained as a mixture of 2 modifications (Fig. 2). In this regard, the ionic conductivity measured by electrochemical impedance spectroscopy was insignificant (it was at the level of 1×10^{-5} S/cm). Apparently, the short-term SPS process does not ensure the complete transformation of the low-conducting tetragonal modification of Al-LLZO into a cubic one. When using the tetragonal modification, the authors [21] needed additional heat treatment for 12 hours at 1175 °C of LLZO samples subjected to SPS, since the total ionic conductivity of LLZO samples after SPS was only 7×10^{-6} S/cm.

Many researchers have encountered the problem of the formation of a non-conductive impurity phase $La_2Zr_2O_7$ after the consolidation of the solid electrolyte LLZO by the SPS method [18–22]. In this regard, the data obtained in a recent paper [22] seem contradictory, where the authors claim a high ionic conductivity with a cubic modification of LLZO in the sample at the level of 84% and a non-conducting impurity phase $La_2Zr_2O_7$ at the level of 13%. Obviously, for the SPS method, powders of a purely cubic modification must be synthesized as the initial LLZO powder, as the authors [19] do, who ground the initial $LiOH\cdot H_2O$, La_2O_3, ZrO_2 and Ta_2O_5 in a ball mill with isopropyl alcohol for 12 hours. After drying, the powder was calcined at 900 °C for 6 hours, then crushed, dried under the same conditions, and heated at 1100 °C for 12 hours in the 2nd stage. The powder was then re-ground, pressed into tablets, and sintered at 1130 and 1230 °C for 36 hours to obtain a cubic structure electrolyte [19]. The listed processing operations are lengthy, labor-intensive and energy-consuming.

We have optimized the transition from tetragonal modification to cubic modification using mechanical activation. As a result of MA, the dispersion and reactivity of the powders increases and the tetragonal modification of Al-LLZO is completely transformed into a cubic one after annealing at 1000 °C (Fig. 3*a*).

Subsequent SPS consolidation of Al-LLZO and Ta-LLZO powders of purely cubic modification (obtained according to Table 2) led to the formation of tablets with a density of ~96–98% of the theoretical. At the same time, the structure of the cubic modification

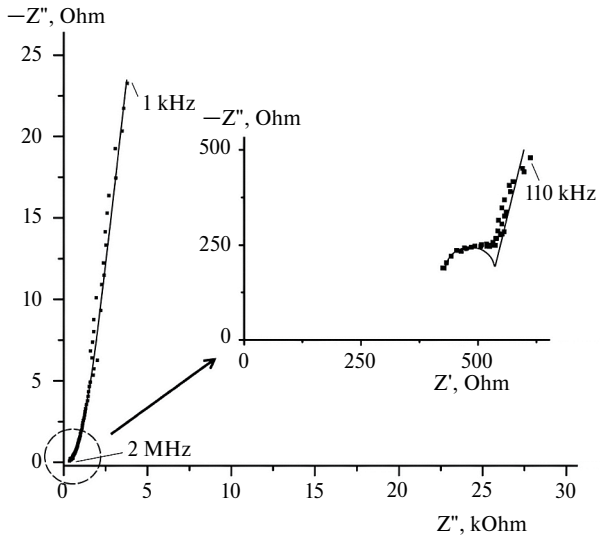

Fig. 4. The spectrum of the Ta-LLZO electrochemical impedance after SPS in the range of 10^3–10^6 Hz. The insert has a high-frequency section (10^5–10^6 Hz).

($Ia\bar{3}d$ space group) was preserved and the peak intensity increased significantly, which indicates an increase in the crystallinity of the samples after SPS (Fig. 3*b*). It should be emphasized that it was not possible to obtain samples of the specified density using the multi-stage classical solid-phase sintering of powders with prolonged exposure, especially for Ta-LLZO [26].

For monophase Al-LLZO powders obtained after annealing at 1000°C, as well as Al-LLZO samples subjected to SPS, Rietveld analysis was performed. The lattice parameters of cubic Al-LLZO were calculated by the method of full-profile analysis of WPPF (Whole Powder Pattern Fitting) radiographs. The R-factor criteria were the values of the profile R-factors Rp and Rwp, calculated using standard formulas (Table 3). The values of the WPPF parameters, commonly used to assess the quality of profile fitting, confirm the good quality of the results obtained. The WPPF refinement showed that the structure of the samples corresponds to the cubic phase with the $Ia\bar{3}d$ space group.

Fig. 4 shows the spectrum of the electrochemical impedance of a Ta-LLZO tablet subjected to SPS. The impedance hodographs of the Ta-LLZO and Al-LLZO samples constructed on the complex plane $Z''=f(Z')$ are identical and consistent with the results

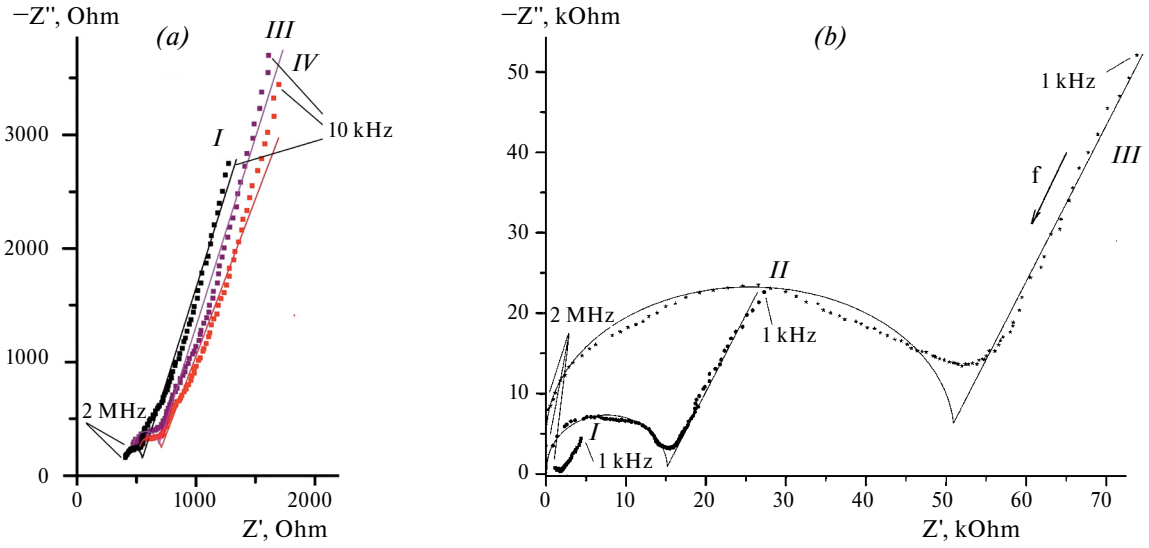

Fig. 5. Impedance hodographs of Ta-LLZO samples after SPS (*a*) and after solid-phase sintering (*b*). *I* – measured immediately after synthesis, *II* – after 10 days, *III* – after 1 month, *IV* – after 2 months of storage in air.

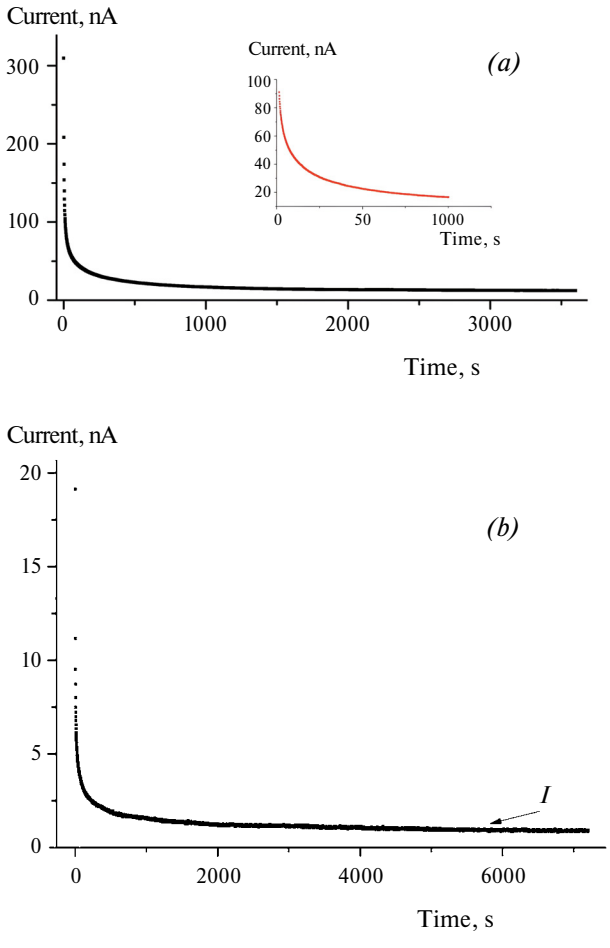

Fig. 6. Chronoamperometric curves for Ta-LLZO after solid-phase sintering (a) and after SPS (b).

of the authors [20, 31–33], who conclude that the impedance of the grain boundaries is negligible compared to the impedance of the grains, probably due to almost complete absence of grain-boundary resistance. The conductivity value was calculated by extrapolating the high-frequency section of the hodograph onto the active resistance axis. The value of the specific total ionic conductivity (σ_{total}) of Ta-LLZO tablets at 20 °C, calculated by formula (1), was 6×10^{-4} S/cm and 6 times higher than the value measured on Ta-LLZO tablets with a low density (69%), previously obtained by solid-phase sintering [26]. The value of the total ionic conductivity of Al-LLZO tablets at room temperature was 4×10^{-4} S/cm, which corresponds to the maximum values given by most researchers [34] and is twice higher than the value of the ionic conductivity of Al-LLZO tablets with a density of 75–85%, obtained earlier by solid-phase sintering [6–7]. This confirms the conclusion that the main factors influencing the ionic conductivity of Al-LLZO and Ta-LLZO are the absence of impurity phases, highly conductive cubic modification, and maximum sample density [35].

As noted [5], LLZO samples are unstable when stored in air under normal conditions due to the formation of nonconducting phases: Li_2CO_3 (on the surface of the tablets) and $La_2Zr_2O_7$ (in volume) due to reaction with H_2O and CO_2. The kinetics of hydration and carbonation of Ta-LLZO powders has recently been studied in [36]. It has been established that the rate of the hydration and carbonation reactions strongly depends on the particle size and, consequently, on the surface area. For Al-LLZO tablets with a porosity of 17%, it was found that spontaneous

cracking and a decrease in ionic conductivity by 3 orders of magnitude occur after three weeks of storage [13]. The process of Li_2CO_3 formation is reversible, since upon repeated annealing of the LLZO tablet at a temperature of 900°C, the conductivity value practically returned to the initial result [5].

A distinctive feature of the Al-LLZO and Ta-LLZO tablets consolidated by the SPS method (density ~96–98%) is increased air stability. As follows from Fig. 5*a*, the ionic conductivity of Ta-LLZO samples remained almost unchanged after long-term storage under normal conditions (for 2 months). For comparison, as a result of storage of Ta-LLZO tablets (with a density of 68–70%) after solid-phase sintering for one month, the ionic conductivity decreased by 2 orders of magnitude and amounted to 3×10^{-6} S/cm (Fig. 5*b*). Achieving good storage stability is an important prerequisite for the practical use of solid electrolytes with a garnet structure.

The ideal solid electrolyte should be a purely ionic conductor, since electronic conductivity causes an electrical leak or short circuit in the LIB. High electronic conductivity may be responsible for the formation of dendrites in solid electrolytes [9]. A critical requirement for solid electrolytes is considered to be high ionic conductivity $>10^{-4}$ S/cm. Low electronic conductivity should be another criterion for solid electrolytes regarding their practical use [9]. The electronic conductivity of Ta-LLZO was evaluated by the PCA method [37]. A constant voltage of 1 V from the potentiostat was applied to a symmetrical cell C/Ta-LLZO/C with blocking graphite electrodes. The steady-state current was set for 1–2 hours. The polarization chronoamperometric curves of Ta-LLZO obtained by solid-phase sintering and the SPS method are shown in Fig. 6.

The chronoamperometric curves are identical and the value of the electronic conductivity is almost the same, since the electronic conductivity depends less on the density of the sample, but is determined mainly by the deviation from stoichiometry and the presence of uncontrolled impurities in the solid electrolyte. The value of the electronic conductivity σ_e Ta-LLZO did not exceed 10^{-9} S/cm, which is 5 orders of magnitude lower than the value of the ionic conductivity. The ratio between the ionic and electronic conductivity of Ta-LLZO meets the requirements for materials for the development of solid-state devices based on them.

CONCLUSION

The possibility of obtaining high-density ceramics (~97–98%) by spark plasma sintering (SPS) from powders of cubic modification of solid electrolytes Al-LLZO and Ta-LLZO with a garnet structure under optimal processing conditions (sintering temperature 1000–1100 °C, molding pressure 50 MPa, sintering duration 10–15 min) is shown. The SPS process is an effective technology for compaction of cubic modification of Al- and Ta-substituted $Li_7La_3Zr_2O_{12}$.

It has been established that during the SPS process there is no change in the phase composition of the Al-LLZO and Ta-LLZO samples and the formation of nonconducting impurity phases.

Total ionic conductivity ($\sigma_{total} = 4–6\times10^{-4}$ S/cm) and electron conductivity (at the level of 10^{-9} S/cm) are achieved for single-phase LLZO samples free of impurity phases (La_2O_3, ZrO_2, $La_2Zr_2O_7$) with a maximum density (97–98%). The characteristics of Al-LLZO and Ta-LLZO ceramics consolidated by the SPS method correspond to the characteristics of the products of leading companies in the field of commercialization of solid electrolytes [28].

FUNDING

The work was carried out within the framework of the state assignment of the Ministry of Science and Higher Education of the Russian Federation, topic FMEZ-2022–0015 and topic FZNS-2023–0003 (regarding the synthesis of ceramics using the SPS technology).

CONFLICT OF INTEREST

The authors declare that they have no conflict of interest.

REFERENCES

1. Yaroslavtsev, A.B., Solid electrolytes: main prospects of research and development, *Russ. Chem. Rev.*, 2016, vol. 85, no. 11, p. 1255. DOI: 10.1070/RCR4634
2. Zhao, J., Wang, X., Wei, T., Zhang, Z., Liu, G., Yu, W., Dong, X., and Wang, J., Current challenges and perspectives of garnet-based solid-state electrolytes, *J. Energy Storage*, 2023, vol. 68, 107693. https://doi.org/10.1016/j.est.2023.107693
3. Han, Y., Chen, Y., Huang, Y., Zhang, M., Li, Z., and Wang, Y., Recent progress on garnet-type oxide electrolytes for all-solid-state lithium-ion batteries, *Ceram. Int.,* 2023, vol. 49, p. 29375. https://doi.org/10.1016/j.ceramint.2023.06.153
4. Kundu, S., Kraytsberg, A., and Ein-Eli, Y., Recent development in the field of ceramics solid-state electrolytes: I–oxide ceramic solid-state electrolytes, *J. Solid State Electrochem.*, 2022, vol. 26, p. 1809.
5. Kunshina, G.B., Ivanenko, V.I., and Bocharova, I.V., Synthesis and Study of Conductivity of Al-Substituted $Li_7La_3Zr_2O_{12}$, *Russ. J. Electrochem.*, 2019, vol. 55, p. 558. DOI: 10.1134/S1023193519060132

6. Kunshina, G.B., Bocharova, I.V., and Shcherbina, O.B., Electrical Conductivity and Mechanical Properties of $Li_{7-3x}Al_xLa_3Zr_2O_{12}$ Solid Electrolyte, *Inorg. Mater.,* 2022, vol. 58, no. 2, p. 147. DOI: 10.1134/S0020168522020091
7. Kunshina, G.B., and Bocharova, I.V., Specific Features of the Formation of Cubic Al-substituted $Li_7La_3Zr_2O_{12}$, *Russ. J. Appl. Chem.*, 2022, vol. 95, no. 6, p. 789. DOI: 10.1134/S1070427222060039
8. Druzhinin, K.V., Shevelin, P.Yu., and Il'ina, E.A., Cycling Performance at $Li_7La_3Zr_2O_{12}$ |Li Interface, *Russ. J. Appl. Chem.,* 2018, vol. 91, p. 63. https://doi.org/10.1134/S107042721801010X
9. Han, F., Westover, A.S., Yue, J., Fan, X., Wang, F., Chi, M., Leonard, D.N., Dudney, N.J., Wang, H., and Wang, C., High electronic conductivity as the origin of lithium dendrite formation within solid electrolytes, *Nature Energy*, 2019, vol. 4, p. 187.
10. Cheng, L., Wu, C.H., Jarry, A., Chen, W., Ye, Y., Zhu, J., Kostecki, R., Persson, K., Guo, J., Salmeron, M., Chen, G., and Doeff, M., Interrelationships among Grain Size, Surface Composition, Air Stability, and Interfacial Resistance of Al-Substituted $Li_7La_3Zr_2O_{12}$ Solid Electrolytes, *ACS Appl. Mater. & Interfaces,* 2015, vol. 7(32), p. 17649.
11. Sharafi, A., Yu, S., Naguib, M., Lee, M., Ma, C., Meyer, H.M., Nanda, J., Chi, M., Siegel, D.J., and Sakamoto, J., Impact of air exposure and surface chemistry on Li-$Li_7La_3Zr_2O_{12}$ interfacial resistance, *J. Mater. Chem. A.,* 2017, vol. 5, p. 13475.
12. Xia, W., Xu, B., Duan, H., Tang, X., Guo, Y., Kang, H., Li, H., and Liu, H., Reaction mechanisms of lithium garnet pellets in ambient air: The effect of humidity and CO_2, *J. Amer. Ceram. Soc.,* 2017, vol. 100, issue 7, p. 2832.
13. Kobi, S., and Mukhopadhyay, A., Structural (in) stability and spontaneous cracking of Li-La-zirconate cubic garnet upon exposure to ambient atmosphere, *J. Eur. Ceram. Soc.,* 2018, vol. 38, p. 4707.
14. Waetzig, K., Heubner, C., and Kusnezoff, M., Reduced Sintering Temperatures of Li^+ Conductive $Li_{1.3}Al_{0.3}Ti_{1.7}(PO_4)_3$ Ceramics, *Crystals,* 2020, vol. 10, p. 408. DOI: 10.3390/cryst10050408
15. Vinnichenko, M., Waetzig, K., Aurich, A., Baumgaertner, C., Herrmann, M., Ho, C.W., Kusnezoff M., and Lee, C.W., Li-Ion Conductive $Li_{1.3}Al_{0.3}Ti_{1.7}(PO_4)_3$ (LATP) Solid Electrolyte Prepared by Cold Sintering Process with Various Sintering Additives, *Nanomaterials*, 2022, vol. 12, p. 3178. https://doi.org/10.3390/nano12183178
16. Shichalin, O.O., Belov, A.A., Zavyalov, A.P., Papynov, E.K., Azon, S.A., Fedorets, A.N., Buravlev, I.Yu, Balanov, M.I., Tananaev, I.G., Qian, Zhang, Yun, Shi, Mingjun, Niu, Wentao, Liu, and Portnyagin, A.S., Reaction synthesis of $SrTiO_3$ mineral-like ceramics for strontium-90 immobilization via additional in-situ synchrotron studies, *Ceram. Int.,* 2022, vol. 48, iss. 14, p. 19597. https://doi.org/10.1016/j.ceramint.2022.03.068
17. Papynov, E.K., Shichalin, O.O., Buravlev, I.Yu., Belov, A.A., Portnyagin, A.S., Fedorets, A.N., Azarova, Yu.A., Tananaev, I.G., and Sergienko, V.I., Spark plasma sintering-reactive synthesis of $SrWO_4$ ceramic matrices for ^{90}Sr immobilization, *Vacuum*, 2020, vol. 180, p. 109628.
18. Kotobuki, M. and Koishi, M., High conductive Al-free Y-doped $Li_7La_3Zr_2O_{12}$ prepared by spark plasma sintering, *J. Alloys Compd.*, 2020, vol. 826, p. 154213.
19. Baek, S.-W., Lee, J.-M., Young Kim, T., Song, M.-S., and Park, Y., Garnet related lithium ion conductor processed by spark plasma sintering for all solid state batteries, *J. Power Sources*, 2014, vol. 249, p. 197. http://dx.doi.org/10.1016/j.jpowsour.2013.10.089
20. Yamada, H., Ito, T., and Basappa, R.H., Sintering Mechanisms of High-Performance Garnet-type Solid Electrolyte Densified by Spark Plasma Sintering, *Electrochim. Acta*, 2016, vol. 222, p. 648. http://dx.doi.org/10.1016/j.electacta.2016.11.020
21. Xue, J., Zhang, K., Chen, D., Zeng, J., and Luo, B., Spark plasma sintering plus heat-treatment of Ta-doped $Li_7La_3Zr_2O_{12}$ solid electrolyte and its ionic conductivity, *Mater. Res. Express*, 2020, vol. 7, p. 025518. https://doi.org/10.1088/2053–1591/ab7618
22. Abdulai, M., Dermenci, K.B., and Turan, S., SPS sintering and characterization of $Li_7La_3Zr_2O_{12}$ solid electrolytes, *MRS Energy Sustain.*, 2023, vol. 10, p. 94. https://doi.org/10.1557/s43581–022–00055–7
23. Kunshina, G.B., Shichalin, O.O., Belov, A.A., Papynov, E.K., Bocharova, I.V., and Shcherbina, O.B., Properties of $Li_{1.3}Al_{0.3}Ti_{1.7}(PO_4)_3$ Lithium-Conducting Ceramics Synthesized by Spark Plasma Sintering, *Russ. J. Electrochem.*, 2023, vol. 59, p. 173. DOI: 10.1134/S1023193523030060
24. Tezuka, T., Inagaki, Y., Kodama, S., Takeda, H., and Yanase, I., Spark plasma sintering and ionic conductivity of $Li_{1.3}Al_{0.3}Ti_{1.7}(PO_4)_3$ fine particles synthesized by glass crystallization, *Powder Technology,* 2023, vol. 429, p. 118870. https://doi.org/10.1016/j.powtec.2023.118870
25. Kunshina, G.B., Bocharova, I.V., and Kalinkin, A.M., Optimization of LLZO solid electrolyte transition from tetragonal modification into cubic one using mechanical activation, *Inorg. Mater.,* 2024, vol. 60, no.1, pp. 111-119
26. Bocharova, I.V., Kunshina, G.B., and Efremov, V.V., Synthesis and Study of Electrochemical Characteristics of Ta-doped Solid Electrolyte $Li_7La_3Zr_2O_{12}$, *Tr. Kolsk. nauchn. tsentra RAN. Ser. Tekh. nauki*, (in Russian), 2023, vol. 14, no 3, p. 54.
27. Charrad, G., Pradeilles, S., Taberna, P.-L., Simon, P., and Rozier, P., Investigation of Chemical and Thermal Stability of $Li_{7-x}La_3Zr_{2-x}Ta_xO_{12}$ Garnet Type Solid-State Electrolyte to Assemble Self-

Standing Li-based All Solid-State Battery, *Energy Technol.,* 2023, vol. 11, 2300234.

28. https://www.msesupplies.com
29. Irvin, J.T.S., Sinclair, D.C., and West, A.R., Electroceramics: Characterization by Impedance Spectroscopy, *Adv. Mater.,* 1990, vol. 2, no. 3, p. 132.
30. Xue, W., Yang, Y., Yang, Q., Liu, Y., Wang, L., Chen, C., and Cheng, R., The effect of sintering process on lithium ionic conductivity of $Li_{6.4}Al_{0.2}La_3Zr_2O_{12}$ garnet produced by solid-state synthesis, *RSC Adv.,* 2018, vol. 8, p. 13083. DOI: 10.1039/c8ra01329b
31. Kotobuki, M., Munakata, H., Kanamura, K., Sato, Y., and Yoshida, T., Compatibility of $Li_7La_3Zr_2O_{12}$ Solid Electrolyte to All-Solid-State Battery Using Li Metal Anode, *J. Electrochem. Soc.,* 2010, vol. 157 (10), A1076. DOI: 10.1149/1.3474232
32. Zhang, Y., Chen, F., Tu, R., Shen, Q., and Zhang, L., Field assisted sintering of dense Al-substituted cubic phase $Li_7La_3Zr_2O_{12}$ solid electrolytes, *J. Power Sources*, 2014, vol. 268, p. 960.
33. Dong, Z., Xu, C., Wu, Y., Tang, W., Song, S., Yao, J., Huang, Z., Wen, Z., Lu, L., and Hu, N., Dual Substitution and Spark Plasma Sintering to Improve Ionic Conductivity of Garnet $Li_7La_3Zr_2O_{12}$, *Nanomaterials,* 2019, vol. 9, p. 721. DOI: 10.3390/nano9050721
34. Salimkhani, H., Yurum, A., and Gursel, S.A., A glance at the influence of different dopant elements on $Li_7La_3Zr_2O_{12}$ garnets, *Ionics,* 2021, vol. 27, p. 3673. https://doi.org/10.1007/s11581−021−04152−4
35. Zhu, Y., Zhang, J., Li, W., Zeng, Y., Wang, W., Yin, Z., Hao, B., Meng, Q., Xue, Y., Yang, J., and Li, S., Enhanced Li^+ conductivity of $Li_7La_3Zr_2O_{12}$ by increasing lattice entropy and atomic redistribution via Spark Plasma Sintering, *J. Alloys Compd.*, 2023, vol. 967, p. 171666.
36. Hoinkis, N., Schuhmacher, J., Leukel, S., Loho, C., Roters, A., Richter, F.H., and Janek, J., Particle Size-Dependent Degradation Kinetics of Garnet-Type $Li_{6.5}La_3Zr_{1.5}Ta_{0.5}O_{12}$ Solid Electrolyte Powders in Ambient Air, *J. Phys. Chem. C.,* 2023, vol. 127 (17), p. 8320. https://doi.org/10.1021/acs.jpcc.3c01027
37. Yi, M., Liu, T., Wang, X., Li, J., Wang, C., and Mo, Y., High densification and Li-ion conductivity of Al-free $Li_{7-x}La_3Zr_{2-x}Ta_xO_{12}$ garnet solid electrolyte prepared by using ultrafine powders, *Ceram. Int.*, 2019, vol. 45, p. 786. https://doi.org/10.1016/j.ceramint.2018.09.245

RUSSIAN JOURNAL OF ELECTROCHEMISTRY, 2025, Vol. 61, No. 1, pp. 80–89

INHIBITORY PROTECTION OF LOW CARBON STEEL IN A FLOW OF PHOSPHORIC ACID SOLUTION CONTAINING IRON(III) PHOSPHATE

© 2025 Ya. G. Avdeev[a,*], A. V. Panova[a], T. E. Andreeva[a]

[a]Frumkin Institute of Physical Chemistry and Electrochemistry Russian Academy of Sciences, Moscow, Russia

*e-mail: avdeevavdeev@mail.ru

Received: September 03, 2024
Revised: September 16, 2024
Accepted: September 24, 2024

Abstract. The corrosion of low carbon steel in a flow of H_3PO_4 solutions containing $FePO_4$, including media with additives of mixture of corrosion inhibitors consisting of a 3-substituted derivative of 1,2,4-triazole (IFKhAN-92) and KNCS, was studied. In the discussed medium, partial reactions of anodic ionization of iron, cathodic reduction of H^+ and Fe(III) cations are realized on steel. The first two reactions are characterized by kinetic control, and the last one is diffusion-controlled. The accelerating effect of $FePO_4$ on steel corrosion in a H_3PO_4 solution is mainly due to the reduction of Fe(III). In inhibited acid, the accelerating effect of Fe(III) cations affects all partial reactions of steel. Despite such an accelerating effect, the mixtures of IFKhAN-92 and KNCS retain a high inhibitory effect on the electrode reactions of steel, which is an important result. The data on corrosion of low carbon steel in the flow of the studied media, obtained from the mass loss of metal samples, are in satisfactory agreement with the results of the study of partial electrode reactions. The accelerating effect of $FePO_4$ on steel corrosion in the flow of H_3PO_4 solutions, including in the presence of inhibitors, is noted. In these media, steel corrosion is determined by the convective factor, which is typical of processes with diffusion control. Mixtures of inhibitors IFKhAN-92 + KNCS provide significant slowdown of steel corrosion in the flow of H_3PO_4 solution containing $FePO_4$, which is the result of its effective slowdown of all partial electrode reactions of the metal.

Keywords: *convection, diffusion kinetics, diffusion coefficient, acid corrosion, low carbon steel, phosphoric acid, iron (III) phosphate, corrosion inhibitors*

DOI: 10.31857/S04248570250106e2

INTRODUCTION

Phosphoric acid solutions are promising industrial media for cleaning the surfaces of products and processing equipment made of low carbon steels from thermal scale, rust and mineral deposits, which often include phases of Fe(III) oxides and oxyhydroxide. The relatively high dissolution rate of iron oxide phases (FeO, Fe_3O_4, Fe_2O_3) in these media is their important advantage compared to hydrochloric and sulfuric acid solutions traditionally used for acid purification of steels [1–3]. During operation, H_3PO_4 solutions, primarily due to their interaction with the surface phases of Fe(III) oxides and oxyhydroxide, accumulate Fe(III) phosphates. Phosphate Fe(III) is insoluble in water. The solubility of Fe(III) phosphate in H_3PO_4 solutions is the result of its chemical interaction with acid, leading to the formation of a mixture of acid phosphates of complex composition [4]. In the future, such systems will be formally considered as an H_3PO_4 solution containing $FePO_4$.

The accumulation of soluble Fe(III) salts in the media under consideration significantly increases their oxidizing ability, increases the aggressiveness of solutions against steel structures [5], and makes the use of corrosion inhibitors (**CIs**) ineffective in such solutions [6]. A specific feature of corrosion of steels in acid solutions containing Fe(III) salts is their sensitivity to the hydrodynamic parameter of the medium. In acid solutions, including inhibited media, corrosion of steel increases with an increase in the flow rate of the medium [7].

The practical significance of the presented research is determined by the need to create efficient low carbon steels in acid solutions for the needs of modern production [8]. At the same time, it is important to imagine how the developed CIs will protect steel in the flow of a corrosive medium when Fe(III) salts accumulate in it.

To understand the processes occurring in low carbon steel systems, H_3PO_4 solution containing $FePO_4$, it is important to analyze the influence of convection conditions of an aggressive environment both at individual stages and on the corrosion of steel as a whole. The effect of CI on the kinetic parameters

of the system should be determined. The assessment of the influence of hydrodynamic parameters of acid solutions containing Fe(III) salts on steel corrosion is important not only theoretically, which makes it possible to identify the diffusion stages of the corrosion process and determine their kinetic parameters, but also in practice, since the industrial operation of these media is often carried out under conditions of liquid flow or is accompanied by significant natural convection as a result of the release on the metal surface of hydrogen gas formed due to the metal's reaction with acid.

We studied a mixture of IFKhAN-92 (3-substituted 1,2,4-triazole) and KNCS as corrosion inhibitors for steel in an H_3PO_4 solution containing $FePO_4$. It was shown [9] that a mixture of 5 mM IFKhAN-92 + 0.5 mM KNCS effectively protects low carbon steels in static solutions of H_3PO_4. The protective effect of this CI is based on its ability to form a polymolecular layer from a solution of H_3PO_4 on the surface of steel, consisting of a polymer complex formed by Fe(II) cations, molecules of 3-substituted 1,2,4-triazole and rhodanide anions [10].

Corrosion of low carbon steels in solutions of mineral acids (so-called "non-oxidants") is described in a simplified form by the total reaction

$$2\,H^+ + Fe = Fe^{2+} + H_2, \quad (1)$$

which is the result of the predominant course of partial reactions [11, 12]: cathodic hydrogen release

$$2\,H^+ + 2\,e = H_2 \quad (2)$$

and anodic dissolution of iron

$$Fe - 2\,e = Fe^{2+}. \quad (3)$$

The features of the reaction mechanism (2) realized on the surface of steels in acid solutions are discussed in [11–13]. The mechanisms of reaction (3) were studied by Heusler [11], Bockris [14], Kolotyrkin and Florianovich [15], and Reshetnikov [16]. Kolotyrkin and Florianovich showed [15] that the dissolution of iron in phosphate solutions is carried out with the participation of OH^- and $H_2PO_4^-$, while the participation of $H_2PO_4^-$ ions in the anodic process is observed only at pH > 4. Later, Reshetnikov [16], when studying solutions with a higher total content of phosphate anions, showed the participation of $H_2PO_4^-$ in the anodic reaction on steels at lower pH values.

We have shown [5] that in H_3PO_4 solutions containing Fe(III) phosphate, corrosion of low carbon steels occurs through three independent partial reactions: anodic ionization of iron (3), cathodic release of hydrogen (2), and reduction of Fe(III) cations:

$$Fe^{3+} + e = Fe^{2+}. \quad (4)$$

In solutions with a high content of H_3PO_4, partial reactions (2) and (3) are carried out with kinetic control, and reaction (4) with diffusion control.

In our study, it seems appropriate to study the possibility of slowing down the partial reactions of steel (2)—(4) in H_3PO_4 solutions containing Fe(III) phosphate with IFKhAN-92 + KNCS mixed additives. We assume that the effective inhibition of reactions (2)—(4) by the studied mixed CIs should ensure a significant slowdown in steel corrosion not only in static but also in dynamic H_3PO_4 solutions containing Fe(III) phosphate.

EXPERIMENTAL PART

H_3PO_4 ("chemically pure" grade) and distilled water were used to prepare the solutions. H_3PO_4 solutions containing Fe(III) phosphate were obtained by the reaction of $Fe(OH)_3$ precipitated by NaOH ("chemically pure" grade) from a solution of $FeCl_3$ with an excess of H_3PO_4. To prepare a solution of Fe(III) chloride, $FeCl_3 \cdot 6H_2O$ ("pure" grade) was used. The inhibitor IFKhAN-92, which is a 3-substituted 1,2,4-triazole, and KNCS ("chemically pure" grade) were studied as corrosion inhibitors.

Electrochemical measurements of low carbon steel St3 (composition, in wt.%: C 0.14–0.22; P 0.04; Si 0.15–0.33; Mn 0.40–0.65; S 0.05; Cr 0.3; Ni 0.3; N 0.008; Cu 0.3; As 0.08; Fe the rest) was carried out on a rotating disk electrode (n = 460 rpm) in a solution of 2 M H_3PO_4 at t = 25 °C. The potential of the steel was measured relative to a silver chloride electrode filled with a saturated KCl solution. The steel electrode was cleaned with sandpaper (M20) and degreased with acetone. The polarization curves (**PC**) were taken using an EL-02.061 potentiostat at a polarization rate of 0.0005 V/s for the working electrode. Before applying polarization, the electrode was kept in the test solution for 30 minutes to establish the E_{cor} free corrosion potential, and then the curves of the anodic and cathodic polarization of the steel were taken. After removing them, the dependence of the cathode current, maintaining E = –0.30 V, on the speed of rotation of the electrode (n = 0, 460, 780, 1090 and 1400 rpm) was studied. In the case of steel corrosion in H_3PO_4 solutions containing Fe(III) salts, the cathode process includes reaction (2). The nature of its flow may depend on the pressure of hydrogen gas in the system. To obtain stable results of electrochemical measurements, the removal of dissolved oxygen from the studied media was carried out by deaeration with gaseous hydrogen. This made it possible to carry out electrochemical measurements at a constant pressure of hydrogen gas in the system. The solutions were deaerated for 30 minutes before

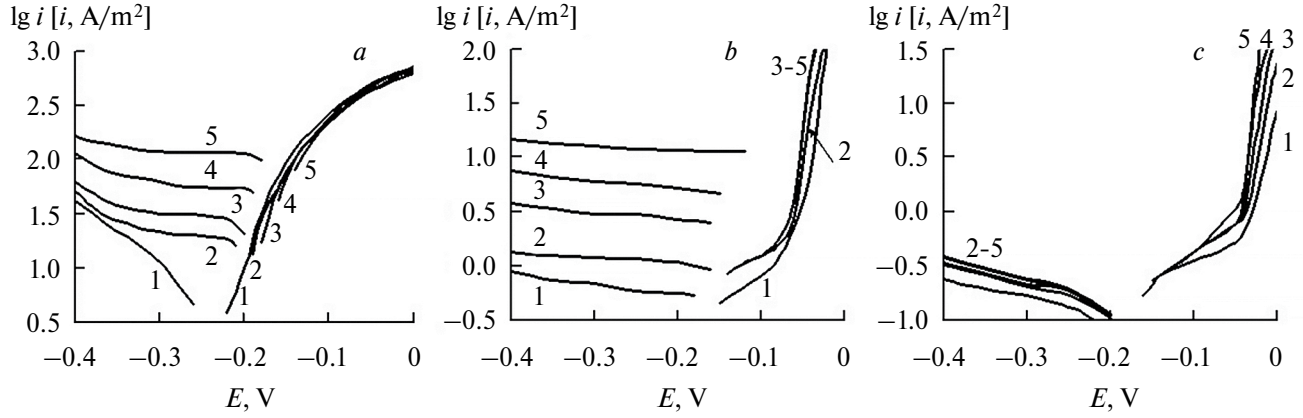

Fig. 1. Polarization curves of St3 steel in 2 M M H_3PO_4 (*a*) with additions of 0.5 mM IFKhAN-92 + 0.5 mM KNCS (*b*) and 5 mM IFKhAN-92 + 0.5 mM KNCS (*c*) containing $FePO_4$, M: *1*–0; *2*–0.01; *3*–0.02; *4*–0.05; *5*–0.10. The value of $n = 460$ rpm; $t = 25$ °C.

the start of the studies. Hydrogen was obtained in an electrolyzer from a solution of NaOH. The average gas supply rate was 1 mL/s. During the electrochemical measurements, the transmission of hydrogen directly through the acid solution was stopped.

The lowest of the discussed values, 460 rpm, was chosen as the base rotation speed of the steel disc electrode during electrochemical studies. At such a rotational frequency, the densities of kinetic and diffusion currents characterizing the cathode reaction occurring on the electrode under experimental conditions are the closest. This situation allows us to hope for a more correct assessment of the effect of Fe(III) phosphate additives on the partial cathode reactions of steel.

The effect of inhibitors on electrode processes was assessed by the values of the cathode inhibition coefficient.

$$\gamma_c = i_{c,0}\, i_{c,in}^{-1} \quad (5)$$

and anodic reactions:

$$\gamma_a = i_{a,0}\, i_{a,in}^{-1}, \quad (6)$$

where $i_{c,0}$ and $i_{a,0}$ are the densities of the cathode and anode currents in the background solution, $i_{c,in}$ and $i_{a,in}$ are the densities of the cathode and anode currents in the solution with the additive under study at potentials of –0.30 and –0.10 V, respectively. When calculating the values of γ_c and γ_a, a solution containing only Fe(III) cations of the appropriate concentration as additives was taken as the background solution.

The values of the electrode potentials are given according to the standard hydrogen scale.

The corrosion rate of steel 08PS (composition, in wt.%: C 0.08; Mn 0.5; Si 0.11; P 0.035; S 0.04; Cr 0.1; Ni 0.25; Cu 0.25; As 0.08; Fe the rest) in 2 M H_3PO_4 at a temperature of 20±2 °C was determined by the mass loss of samples (⩾ 5 per point) measuring 50 mm × 20 mm × 0.5 mm, based on the calculation of 50 mL of acid solution per sample:

$$k = \Delta m\, S^{-1}\, \tau^{-1}, \quad (7)$$

In this case, Δm is the change in the mass of the sample, g; S is the sample area, m^2; τ is the duration of corrosion tests, 1 hour; the duration of experiments is 2 hours. The studies were performed in both static and dynamic corrosive environments at the rotation speed of the magnetic stirrer w = 250, 420, 750 and 1080 rpm. Before the experiment, the samples were cleaned on an abrasive wheel (ISO 9001, grain size 60) and degreased with acetone.

The effectiveness of the inhibitors was assessed by the values of the inhibition coefficients

$$\gamma = k_0\, k_{in}^{-1}, \quad (8)$$

where k_0 and k_{in} are the corrosion rate of 08PS steel in the background solution and in the solution with the additive under study. When calculating the values of γ, a solution containing only Fe(III) cations of the appropriate concentration was taken as the background solution.

The effect of the presence of dissolved Fe(III) salt in the acid, at the same flow rate of the solution, and the nature of the flow of the corrosive medium, at a constant content of Fe(III), on the corrosion rate of steel was estimated by the increments of corrosion losses

$$\Delta k_{Fe(III)} = k_{Fe(III)} - k_0, \quad (9)$$

$$\Delta k_{dyn} = k_{dyn} - k_{st} \quad (10)$$

and the coefficient of corrosion acceleration

$$\gamma_{Fe(III)}^{-1} = k_{Fe(III)}\, k_0^{-1}, \quad (11)$$

Table 1. Values of corrosion potentials (E_{cor}) of St3 steel, Tafel slopes of polarization curves (b_c and b_a), cathode and anode current densities (i_c and i_a), deceleration coefficients of cathode and anode reactions (γ_c and γ_a) obtained at $E = -0.30$ and -0.10 V, respectively. The values of E are given in V, i in A/m^2, $n = 460$ rpm; $t = 25$ °C

$C_{Fe(III)}$, M	E_{cor}	b_c	i_c	γ_c	b_a	i_a	γ_a
2 M H_3PO_4							
0	-0.23	0.125	11.5	-	0.06	262	-
0.01	-0.20	i_{lim}*	21.5	-	0.06	236	-
0.02	-0.19	i_{lim}	31.5	-	0.06	227	-
0.05	-0.18	i_{lim}	63.1	-	0.06	226	-
0.10	-0.17	i_{lim}	119	-	0.06	215	-
2 M H_3PO_4 + 0.5 mM IFKhAN-92 + 0.5 mM KNCS							
0	-0.16	i_{lim}	0.69	16.7	i_{lim}**	0.81	323
0.01	-0.15	i_{lim}	1.2	17.9	i_{lim}**	1.2	197
0.02	-0.15	i_{lim}	3.0	10.5	i_{lim}**	1.2	189
0.05	-0.13	i_{lim}	6.0	10.5	i_{lim}**	1.2	188
0.10	-0.12	i_{lim}	12.6	9.4	i_{lim}**	1.2	179
2 M H_3PO_4 + 5 mM IFKhAN-92 + 0.5 mM KNCS							
0	-0.17	i_{lim}	0.16	71,8	i_{lim}**	0.35	749
0.01	-0.16	i_{lim}	0.20	108	i_{lim}**	0.42	562
0.02	-0.16	i_{lim}	0.22	143	i_{lim}**	0.42	540
0.05	-0.16	i_{lim}	0.23	274	i_{lim}**	0.42	538
0.10	-0.16	i_{lim}	0.24	496	i_{lim}**	0.42	512

* i_{lim} – limiting current.
** The value refers to the first linear section of the anode PC.

$$\gamma_{dyn}^{-1} = k_{dyn} k_{st}^{-1}, \quad (12)$$

where $k_{Fe(III)}$ and k_0 are the corrosion rates of 08PS steel in an acid solution in the presence and absence of Fe(III) salts, and k_{dyn} and k_{st} are the corrosion rates of steel in dynamic and static media.

The measurements were carried out on instruments of the Center for Collective Use of Physical Methods of the Frumkin Institute of Physical Chemistry and Electrochemistry of the Russian Academy of Sciences (CCPM IPCE RAS).

RESULTS AND DISCUSSION

Important information about the features of the mechanism of steel corrosion in acid solutions containing Fe(III) salt can be obtained by studying the kinetics of electrode reactions of metal by voltammetry [15]. In 2 M H_3PO_4, the polarization curve shape of low carbon steel is characteristic of corrosion occurring in the range of its active dissolution potentials (Fig. 1, Table 1). In this medium, the slope of the cathode PC of steel (b_c) is close to the theoretically predictable value of 0.120 V for iron, but the slope of the anode PC of metal (b_a) is higher than the theoretical value 0.035 V [16]. The increase in the b_a steel slope was the result of the formation of a sludge layer on its surface, which was visually observed. The presence of $FePO_4$ acid in the solution shifts the potential of free corrosion of steel (E_{cor}) to more positive values, which is the result of the dissolution of this additive in the cathodic reaction. Fe(III) cations have practically no effect on the anodic process, but there is a positive order in the cathodic reaction in their concentration. The initial section of the cathode PCs is characterized by a limiting current (i_{lim}). On the contrary, the slope of the anode PC corresponds to the background dependence.

The presence of $FePO_4$ additives in the H_3PO_4 solution practically does not affect the nature of the anode reaction, which proceeds in accordance with equation (3) both in the absence and in the presence of Fe(III) phosphate. The nature of the cathode PC indicates the participation of Fe(III) in the cathode reaction. In concentrated acid solutions

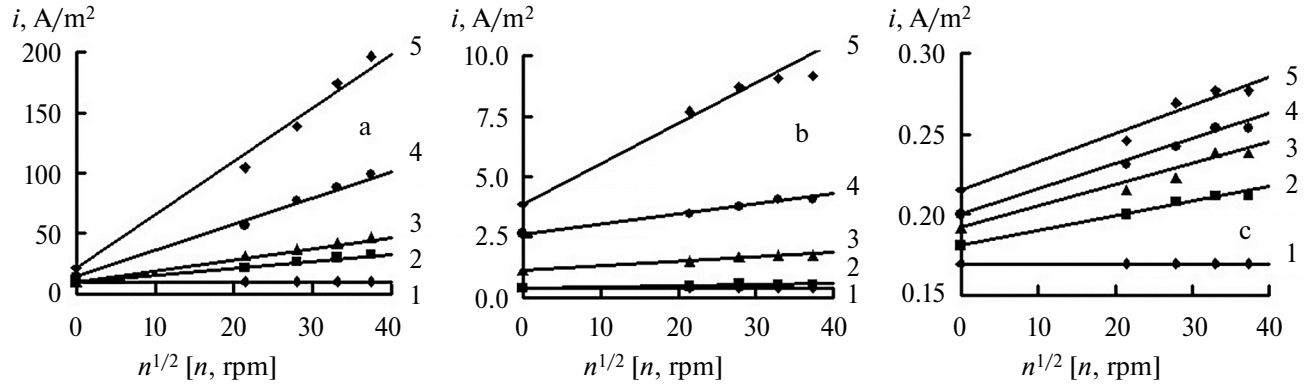

Fig. 2. Dependence of the cathode current density on the rotation frequency of a steel disc in 2 M H_3PO_4 (a) with 0.5 mM IFKhAN-92 + 0.5 mM KNCS (b) and 5 mM IFKHAN-92 + 0.5 mM KNCS (c) containing $FePO_4$, M: *1*–0; *2*–0.01; *3*–*0.*02; *4*–0.05; *5*–0.10. $E = -0.30$ V, $t = 25$ °C.

(pH < 2), the cathode reaction corresponding to equation (2) proceeds in the kinetic control region [18], which is confirmed by the nature of the cathode reaction. In the presence of Fe(III) phosphate, they are complicated by the limiting current, which indicates a change in the mechanism of the cathode reaction. The observed limiting current may be due to diffusion limitations associated with the delivery of oxidizing agents H^+ and Fe^{3+} present in the acid solution to the steel surface. Since the concentration of H^+ is more than an order of magnitude higher than $C_{Fe(III)}$, the limiting current is more likely to be the result of diffusion restrictions on the delivery of Fe(III) cations to the steel surface. To confirm this assumption, it is necessary to investigate the effect of the electrolyte flow on the rate of the cathode reaction of steel, which is usually carried out using a disk electrode. By changing the frequency of its rotation, the mode of liquid flow near the metal surface is regulated [19, 20].

For the cathode process of steel, determined by reaction (2) occurring in the kinetic region and reaction (4) controlled by diffusion, the equation is applicable:

$$i_c = i_k + i_d, \quad (13)$$

where i_k and i_d are the densities of kinetic and diffusion currents. In the case of laminar fluid motion near the surface of a rotating metal disk, the value of i_d is directly proportional to the square root of the rotational speed of the disk electrode (n), and therefore expression (13) is as follows:

$$i_c = i_k + fn^{1/2}. \quad (14)$$

In 2 M H_3PO_4 + $FePO_4$, the experimental dependence of i_c on $n^{1/2}$ has a linear form (Fig. 2, Table 2). However, in 2 M H_3PO_4, there is no response of the cathode current to a change in the rotation frequency of the steel disc, which indicates the kinetic nature of the reaction (2). In the presence of $FePO_4$, the kinetic component of the cathode current is the same as in its absence, which indicates the independence of reactions (2) and (4). In addition, it is clear that reaction (2) occurs in the kinetic region, and reaction (4) in the diffusion region.

The diffusion current caused by the reduction of Fe(III) on a steel cathode during laminar fluid flow is described by equation [18]:

$$i_d = 0.62zFC^*D^{2/3}\eta^{-1/6}n^{1/2}. \quad (15)$$

Here C^* is the concentration of Fe(III) in the depth of the solution, η is the kinematic viscosity of the liquid (0.011 cm^2/s [21]), and n is the angular velocity of rotation of the steel disc. Using equation (15), it is possible to calculate $D_{Fe(III)}$ in 2 M H_3PO_4 (Table 2). The obtained value of $D_{Fe(III)}$ has good convergence with the data obtained by cyclic voltammetry of a Pt electrode in 2 M H_3PO_4 containing $FePO_4$ and given in [5].

In background solutions of H_3PO_4 containing $FePO_4$, reactions (2) and (4) occur independently on steel. In further discussing the results related to the inhibition of steel corrosion in such environments, we will proceed from the assumption that both of these partial cathode processes are also implemented independently.

The introduction of 0.5 mM IFKhAN-92 + 0.5 mM KNCS and, especially, 5 mM IFKhAN-92 + 0.5 mM KNCS additives into 2 M H_3PO_4 significantly affects the parameters of the electrode reactions of St3 steel (Fig. 1, Table 1). In the presence of these CIs, both electrode reactions of St3 steel are inhibited, and the values of the E_{cor} value are shifted to the region of positive potentials in comparison with the background medium by 0.07 and 0.06 V, respectively, which indicates that these mixtures predominantly slow down the anode reaction of the metal. In media containing CIs, the slope of the cathode PC, compared with the background

2 M H_3PO_4, is increased to the limiting current. Anode PCs have two linear sections. The first section adjacent to E_{cor} is characterized by a limiting diffusion current due to the effective inhibition of the anode reaction by the protective film of the inhibitor. At higher potentials, a region of metal anodic activation is observed, characterized by a significant increase in current [22, 23]. It is primarily associated with partial desorption from the surface of the inhibitor steel. In such media, there is no response of the cathode current to the rotation frequency of the steel disc electrode (Fig. 2, Table. 2), and the cathode process, as in 2 M H_3PO_4 in the absence of $FePO_4$, should be due to reaction (2), which is realized with kinetic control. In inhibited media, especially in the presence of 5 mM IFKhAN-92 + 0.5 mM KNCS, i_k values are lower than in the background environment.

The presence of $FePO_4$ in a corrosive environment worsens the inhibition of the anode and, especially, cathode reactions of steel by mixed CIs, and this effect for the cathode reaction increases with an increase in the content of Fe(III) in the solution (Fig. 1, Table 1). There is a response of the cathode current to the rotation frequency of the disk electrode (Fig. 2, Table 2). In such a system, the cathode current will consist of kinetic current, determined by the partial reaction (2), and diffusion current, caused by the partial reaction (4). An increase in the content of $FePO_4$ in the inhibited acid leads to an increase in both i_k and i_d values. It turns out that Fe(III) salts in the inhibited acid accelerate the cathodic reaction, participating in it not only as an additional depolarizer, but also reduce the inhibition of CI cathodic hydrogen release, which generally negatively affects the protection of steel. All other things being equal, in the presence of an additive of 5 mM IFKhAN-92 + 0.5 mM KNCS, the negative effect of $FePO_4$ on the inhibition of electrode reactions in steel is significantly less pronounced than in media inhibited by 0.5 mM IFKhAN-92 + 0.5 mM KNCS. Despite this, the values of the i_k and i_d parameters in the inhibited media are significantly lower than in similar background solutions. The result obtained allows us to hope for effective protection of low carbon steel with a mixture of IFKhAN-92 and KNCS in H_3PO_4 solutions containing $FePO_4$.

It should be understood how the presence of mixed CIs in an aggressive environment will affect the value of $D_{Fe(III)}$. The values of $D_{Fe(III)}$ observed in the inhibited 2 M H_3PO_4, especially in the presence of 5 mM IFKhAN-92 + 0.5 mM KNCS, are significantly lower than those typical for the background environment with the same parameters (Table 2). It should be clarified that, unlike 2 M H_3PO_4 containing $FePO_4$, in the inhibited media equation (15) allows us to calculate not the true values of $D_{Fe(III)}$, but the effective ones. The introduction of minor CI additives (no more than 5.5 mM) into the acid solution cannot significantly change the true value of $D_{Fe(III)}$ in it. We see another reason for this phenomenon: the inhibitor molecules, being adsorbed on the steel surface, form polymolecular protective layers. The composition and structure of polymolecular protective layers formed by a mixed inhibitor of IFKHAN-92 + KNCS are discussed in [10]. To recover, the Fe(III) cation must overcome the protective layer and reach the surface of the steel. The rate of such a process will be determined by the diffusion of Fe(III) cations in the protective layer formed by the CI. It is the values of $D_{Fe(III)}$ in the near-surface protective layer of the inhibitor that largely determine the values of effective $D_{Fe(III)}$ obtained by equation (15).

Table 2. Values of constants i_k and f in equation (14) at $E = -0.30$ V for the cathode reaction of a steel rotating disk electrode in 2 M H_3PO_4 containing $FePO_4$. Values of i_k in A/m^2, f in A rpm$^{-1/2}$ m^{-2}, $t = 25$ °C

$C_{Fe(III)}$, M	i_k	f	D, μm^2/s,
2 M H_3PO_4			
0	10.2	0	-
0.01	10.2	0.50	130±10
0.02	10.2	0.97	
0.05	10.2	2.34	
0.10	10.2	4.84	
2 M H_3PO_4 + 0.5 mM IFKhAN-92 + 0.5 mM KNCS			
0	0.38	0	-
0.01	0.38	0.0046	0.1
0.02	1.12	0.020	0.3
0.05	2.61	0.042	0.3
0.10	3.85	0.17	0.8
2 M H_3PO_4 + 5 mM IFKhAN-92 + 0.5 mM KNCS			
0	0.17	0	-
0.01	0.18	0.0010	Less than 0.01
0.02	0.19	0.0013	
0.05	0.20	0.0015	
0.10	0.22	0.0017	

Our identification of the kinetic parameters of the system under study allows us to predict the nature of corrosion of low carbon steel in it. Corrosion of steel in 2 M H_3PO_4 containing $FePO_4$ proceeds through stages characterized by both kinetic control and diffusion restrictions. Therefore, the nature of steel corrosion in such systems should

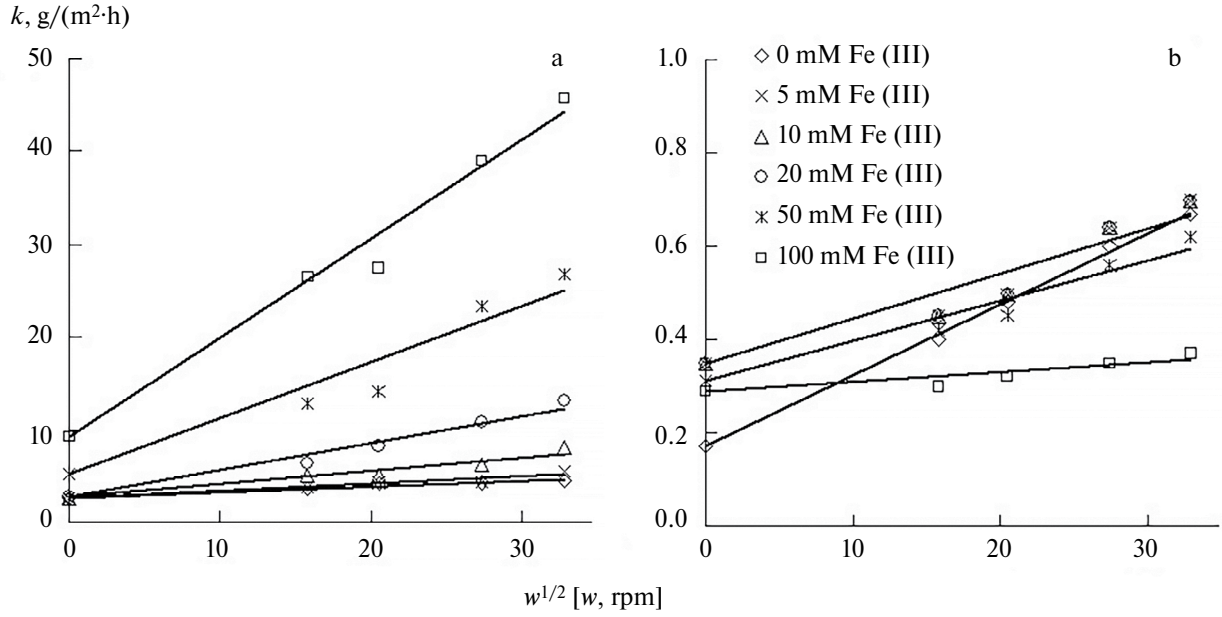

Fig. 3. Dependence of the corrosion rate of 08PS steel on the rotation speed of a propeller agitator in a corrosive environment at 20±2 °C in 2 M H_3PO_4 (a) with the addition of 5 mM IFKhAN-92 + 0.5 mM KNCS (b) containing $FePO_4$. The duration of the experiments is 2 hours.

Table 3. Values of constants k_{st} (g/(m² h)) and λ (g rpm$^{-1/2}$ m^{-2} h^{-1}) in equation (16) for corrosion of low carbon steel 08PS at t = 20±2 °C in a solution of 2 M H_3PO_4 containing $FePO_4$

$C_{Fe(III)}$, M	2 M H_3PO_4		2 M H_3PO_4 + 5 mM IFKhAN-92 + 0.5 mM KNCS	
	k_{st}	λ	k_{st}	λ
0	2.5	0.065	0,17	0,015
0.005	2.6	0.079	0,35	0,010
0.01	2.7	0.14	0,35	0,010
0.02	2.8	0.29	0,35	0,010
0.05	5.2	0.60	0,31	0,009
0.10	9.2	1.1	0,29	0,002

significantly depend on the nature of the convection of an aggressive medium. Effective protection of low carbon steel in 2 M H_3PO_4 containing $FePO_4$ with mixed CIs is to be expected, since they effectively slow down the partial electrode reactions of steel, including the reduction of Fe(III) cations. The higher the content of IFKhAN-92 in the mixed CI, the more significant its effect on the partial reactions of steel.

These assumptions were confirmed when studying the corrosion of low carbon steel 08PS in a stream of 2 M H_3PO_4 containing $FePO_4$ by the mass loss of metal samples (Fig. 3, Table 3). Both in the absence of mixed CI and in its presence, the corrosion of low carbon steel in 2 M H_3PO_4 containing $FePO_4$ increases with increasing $C_{Fe(III)}$. In almost all the media studied, the response of the corrosion process to the mixing rate of the corrosive medium is observed. The experimental dependence of the corrosion rate of low carbon steel on the rotational speed of a propeller agitator used to create forced convection of an aggressive medium can be described by the equation

$$k = k_{st} + \lambda w^{1/2}, \quad (16)$$

where k_{st} is the corrosion of low carbon steel in a static environment, w is the speed of rotation of the propeller agitator, λ is an empirical coefficient characterizing the intensity of the corrosion rate increment. Equation (16) formally corresponds to equation (14), which characterizes electrode reactions occurring with diffusion control. It should be noted that in 2 M H_3PO_4, both in the absence of CI and in their presence, there is a slight response of the corrosion process to an increase in the flow rate of the corrosive medium, which is explained by the presence of dissolved aerial oxygen in the media under consideration. Since the observed effect of oxygen is insignificant, we will not take it into account in our further discussions.

In media inhibited by 5 mM IFKhAN-92 + 0.5 mM KNCS, the values of k_{st} and λ are significantly lower than those observed in solutions without CI at all concentrations of $FePO_4$ (Table 3). Effective protection of low carbon steel in a flow of a corrosive medium containing $FePO_4$ occurs. A decrease in the content of substituted triazole in the IFKhAN-92 + 0.5 mM

KNCS mixture leads to a decrease in its protective effect (Fig. 4, Table 4). The residual protective effect is manifested even at $C_{IFKhAN-92} = 0.01$ mM.

Analysis of experimental data shows that an increase in the content of $FePO_4$ in a corrosive medium accelerates the corrosion of low carbon steel (Table 5). The most significant increase in $C_{Fe(III)}$ affects the rate of corrosion of steel in an environment that does not contain inhibitors. Also, in the presence of $FePO_4$ in an H_3PO_4 solution, corrosion of steel accelerates during the transition from a static to a dynamic medium. On the contrary, in inhibited media, the response of the corrosion rate to an increase in $C_{Fe(III)}$ and an acceleration of the flow of aggressive media is insignificant. The considered mixed CIs provide metal protection in the studied solutions in both static and dynamic environments (Table 6).

The result has important theoretical and practical significance. It has been shown that by using mixtures of substances capable of forming polymolecular protective layers on the metal surface as corrosion retardants, it is possible to provide effective protection of steels in the flow of an acid solution containing Fe(III) salts. For the first time, a mixed individual inhibitor, IFKhAN-92 + KNCS, capable of protecting steel in the flow of an H_3PO_4 solution containing Fe(III), has been proposed. In harsh conditions of aggressive medium flow (750 rpm) containing 0.1 M Fe(III), the addition of 5 mM IFKhAN-92 + 0.5 mM KNCS slows down the corrosion of low carbon steel by almost 110 times, providing $k = 0.35$ g/(m^2 h).

CONCLUSION

1. The corrosion of low carbon steel in a dynamic H_3PO_4 solution containing $FePO_4$ accelerates with an increase in the flow rate of the medium and an increase in the concentration of Fe(III) salt in it. The empirical dependence of the corrosion rate of steel on the intensity of the flow of the media under study, mixed by a propeller agitator, can be represented as a linear relationship:

$$k = k_{st} + \lambda w^{1/2},$$

where k_{st} is the rate of corrosion of steel in a static medium, w is the speed of rotation of the propeller agitator, and λ is the empirical coefficient.

2. Corrosion of low carbon steel in the flow of an H_3PO_4 solution containing $FePO_4$ is realized as a result of three partial reactions on the metal: anodic ionization of iron and cathodic reduction of protons and Fe(III) cations.

3. For the first time, the possibility of inhibitory protection of low carbon steel in the flow of an H_3PO_4 solution containing $FePO_4$ by additives of a mixture of IFKhAN-92 and KNCS has been shown. Mixed CIs provide a significant slowdown in steel corrosion in these environments. The reason for the high inhibitory effects of IFKhAN-92 and KNCS mixtures when protecting steel in the flow of an H_3PO_4 solution containing $FePO_4$ is their effective deceleration of partial electrode reactions of the metal: anodic ionization of iron and cathodic reduction of protons and Fe(III) cations.

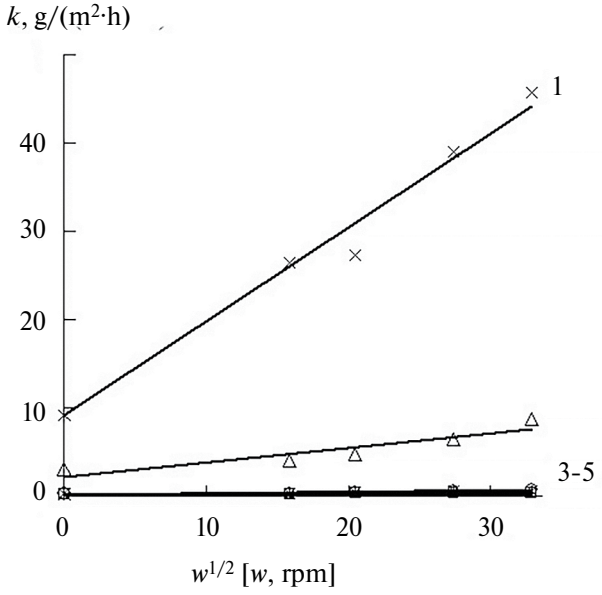

Fig. 4. Dependence of the corrosion rate of 08PS steel on the rotation speed of a propeller agitator in a corrosive environment at 20±2 °C in 2 M H_3PO_4 + 0.1 M $FePO_4$ (1) with additives 0.01 mM IFKhAN-92 + 0.5 mM KNCS (2), 0.1 mM IFKhAN-92 + 0.5 mM KNCS (3), 0.5 mM IFKhAN-92 + 0.5 mM KNCS (4), 5 mM IFKhAN-92 + 0.5 mM KNCS (5). The duration of the experiments was 2 hours.

Table 4. Values of constants k_{st} (g/(m^2 h)) and λ (g rpm$^{-1/2}$ m^{-2} h^{-1}) in equation (16) for corrosion of low carbon steel 08PS at t = 20±2 °C in a solution of 2 M H_3PO_4 containing 0.1 M $FePO_4$ + 0.5 mM KNCS

$C_{IFKhAN-92}$, mM	k_{st}	λ
0.01	3.0	0.13
0.1	0.34	0.010
0.5	0.30	0.008
5	0.29	0.002

FUNDING

This work was supported by the Ministry of Science and Higher Education of the Russian Federation.

Table 5. Corrosion rate (k), corrosion loss increment (Δk) and corrosion acceleration coefficient (γ^{-1}) of 08PS steel in 2 M H_3PO_4 solutions containing Fe(III). k and Δk in g/(m^2 h). The duration of the experiments was 2 hours, $t = 20\pm2$ °C

$C_{Fe(III)}$, M	Static medium			Dynamic medium (750 rpm)			Δk_{dyn}**	γ_{dyn}^{-1}**
	k	$\Delta k_{Fe(III)}$*	$\gamma_{Fe(III)}^{-1}$*	k	$\Delta k_{Fe(III)}$*	$\gamma_{Fe(III)}^{-1}$*		
2 M H_3PO_4								
0	2.5	-	-	4.2	-	-	1.7	1.7
0.005	2.6	0.1	1.0	4.4	0.2	1.0	1.8	1.7
0.01	2.6	0.1	1.0	6.2	2.0	1.5	3.6	2.4
0.02	2.8	0.3	1.1	11	6.6	2.6	8.0	3.9
0.05	5.2	2.7	2.1	23	19	5.5	18	4.4
0.10	9.2	6.7	3.7	39	30	9.3	30	4.2
2 M H_3PO_4 + 0.01 mM IFKhAN-92 + 0.5 mM KNCS								
0.10	3.0	-	-	6.5	-	-	3.5	2.2
2 M H_3PO_4 + 0.1 mM IFKhAN-92 + 0.5 mM KNCS								
0.10	0.34	-	-	0.62	-	-	0.28	1.8
2 M H_3PO_4 + 0.5 mM IFKhAN-92 + 0.5 mM KNCS								
0.10	0.30	-	-	0.56	-	-	0.26	1.9
2 M H_3PO_4 + 5 mM IFKhAN-92 + 0.5 mM KNCS								
0	0.17	-	-	0.60	-	-	0.43	3.5
0.005	0.35	0.18	2.1	0.64	0.04	1.1	0.29	1.8
0.01	0.35	0.18	2.1	0.64	0.04	1.1	0.29	1.8
0.02	0.35	0.18	2.1	0.64	0.04	1.1	0.29	1.8
0.05	0.31	0.14	1,8	0.56	-0.04	0.93	0.25	1.8
0.10	0.29	0.12	1,7	0.35	-0.29	0.58	0.06	1.2

* – Change in value as a result of the presence of Fe(III) in the solution at the same flow rate of the solution.
** – Change in value as a result of acceleration of the solution flow at a constant content of Fe(III) in it.

Table 6. Corrosion inhibition coefficients (γ) of 08PS steel in 2 M H_3PO_4 solutions containing Fe(III) with IFKhAN-92 + KNCS additives. The duration of the experiments was 2 hours, $t = 20\pm2$ °C

$C_{Fe(III)}$, M	Static medium	Dynamic medium (750 rpm)
5 mM IFKhAN-92 + 0.5 mM KNCS		
0	15	7.0
0.005	7.4	6.9
0.01	7.4	9.7
0.02	8.0	17
0.05	17	41
0.10	32	110
0.5 mM IFKhAN-92 + 0.5 mM KNCS		
0.10	30	70
0.1 mM IFKhAN-92 + 0.5 mM KNCS		
0.10	27	63
0.01 mM IFKhAN-92 + 0.5 mM KNCS		
0.10	3.1	6.0

CONFLICT OF INTEREST

The authors declare that they have no conflict of interest.

REFERENCES

1. Kuzin, A.V., Gorichev, I.G., Shelontsev, V.A., Kuzmenko, A.N., Plakhotnaia, O.N., and Ovsyannikova, L.V., The Role of a Complex Formation in the Dissolution of Iron Oxides in Orthophosphoric Acid, *Moscow Univ. Chem. Bull.,* 2021, vol. 76, no. 6, p. 398. DOI: 10.3103/S0027131421060055
2. Kuzin A. V., Gorichev I. G., Shelontsev, V.A., Eliseeva, E.A., and Mamankov, A.V., Dissolution of magnetite in orthophosphoric acid: study and modeling, *Russ. Metall.*, 2021, vol. 2021, p. 260. DOI: 10.1134/S0036029521030083
3. Kuzin, A.V., Gorichev, I.G., and Lainer, Y.A., Stimulating effect of phosphate ions on the dissolution kinetics of iron oxides in an acidic medium, *Russ. Metall.*, 2013, vol. 2013, p. 652. DOI: 10.1134/S0036029513090073
4. Prodan, I.E., Yeshchenko, L.S., and Pechkovsky, V.V., Study of the crystallization of iron phosphates in the system iron (III) – phosphoric acid – water, *Russ. J. Inorg. Chem.*, (in Russian), 1989, vol. 34, no. 7, p. 1860.
5. Avdeev, Ya.G., Panova, A.V., and Andreeva, T.E., Corrosion of Low-Carbon Steel in a Flow of Phosphoric Acid Solution Containing Iron (III) Phosphate, *Russ. J. Electrochem.*, 2023, vol. 59, p. 512. DOI: 10.1134/S1023193523070030
6. Avdeev, Ya.G., Panova, A.V., and Anfilov, K.L., Effect of Fe(III) salts on the protection of low carbon steel in sulfuric acid solutions by some corrosion inhibitors, *Int. J. Corros. Scale Inhib.*, 2024, vol. 13, no. 2, p. 1135. DOI: 10.17675/2305–6894–2024–13–2–26
7. Avdeev, Ya.G., and Andreeva, T.E., Mechanism of Steel Corrosion in Inhibited Acid Solutions Containing Iron (III) Salts, *Russ. J. Phys. Chem. A.,* 2022, vol. 96, no. 2, p. 423. DOI: 10.1134/S0036024422020030
8. Kuznetsov, Yu.I., Andreev, N.N., and Marshakov, A.I., Physicochemical Aspects of Metal Corrosion Inhibition, *Russ. J. Phys. Chem., A,* 2020, vol. 94, no. 3. p. 505. DOI: 10.1134/S0036024420030152
9. Avdeev, Ya.G., Tyurina, M.V., and Kuznetsov, Yu.I., Protection of low-carbon steel in phosphoric acid solutions by mixtures of a substituted triazole with sulfur-containing compounds, *Int. J. Corros. Scale Inhib.,* 2014, vol. 3, no. 4, p. 246. DOI: 10.17675/2305–6894–2014–3–4–246–253
10. Avdeev, Ya.G., Tyurina, M.V., Kuznetsov, Yu.I., Pronin, Yu.E., and Kazanskiy, L.P., Protection of low-carbon steel in phosphoric acid solutions with IFKhAN-92 inhibitor. Part 2, *Corros.: mater., prot.* (in Russian), 2013, no. 6, p. 17.
11. Kaesche, H., *Die Korrosion der Metalle. Physikalischchemische Prinzipien und Aktuelle Probleme* (in German), Springer, Berlin, 1979.
12. Pletnev, M.A. and Reshetnikov, S.M., Cooperative Effects in the Problem of Acid Corrosion of Metals, *Prot. Met.*, 2004, vol. 40, p. 460. DOI: 10.1023/B:PROM.0000043064.20548.e0
13. Antropov, L. I. *Theoretical Electrochemistry* (in Russian), Vysshaya Shkola, Moscow, 1965, p. 348–380.
14. Bockris, J.O'M., Drazic, D., and Despic, A.R., The electrode kinetics of the deposition and dissolution of iron, *Electrochim. Acta,* 1961, vol. 4, no. 2–4, p. 325. DOI: 10.1016/0013–4686(61)80026–1
15. Katrevich, A.N., Florianovich, G.M., and Kolotyrkin, Ya.M., Elucidation of the kinetic parameters of the reaction of active dissolution of iron in phosphate solutions, *Prot. Met.,* (in Russian), 1974, vol. 10, no. 4, p. 369.
16. Reshetnikov, S.M., and Makarova, L.L., Kinetics and mechanism of cathodic and anodic processes that determine acid corrosion of metals in the area of active dissolution, *Redox and adsorption processes on the surface of solid metals* (in Russian), Udmurt State University, Izhevsk, 1979, p. 25–49.
17. Reshetnikov, S.M., *Inhibitors of acid corrosion of metals*, (in Russian), Leningrad: Khimiya, 1986.
18. Pleskov, Yu.V., and Filinovskii, V. Yu., *The Rotating Disk Electrode,* Consultants Bureau, New York, 1976.
19. Du, C., Tan, Q., Yin, G., and Zhang, J., Rotating Disk Electrode Method, *In Rotating Electrode Methods and Oxygen Reduction Electrocatalysts,* Eds. W. Xing, G. Yin, J. Zhang, Elsevier B. V. 2014, p. 171–198. DOI: 10.1016/B978–0–444–63278–4.00005–7
20. Jia, Z., Yin, G., and Zhang, J., Rotating Ring-Disk Electrode Method, *In Rotating Electrode Methods and Oxygen Reduction Electrocatalysts,* Eds. W. Xing, G. Yin, J. Zhang, Elsevier B. V. 2014, p. 199–229. DOI: 10.1016/B978–0–444–63278–4.00006–9
21. Xing, W., Yin, M., Lv, Q., Hu, Y., Liu, C., and Zhang J., Oxygen solubility, diffusion coefficient, and solution viscosity, *In Rotating Electrode Methods and Oxygen Reduction Electrocatalysts,* Eds. W. Xing, G. Yin, J. Zhang, Elsevier B. V. 2014, p. 1–31. DOI: 10.1016/B978–0–444–63278–4.00001-X
22. Avdeev, Ya.G., About the nature of iron anodic activation in solutions of mineral acids, *Int. J. Corros. Scale Inhib.*, 2020, vol. 9, no. 4, p. 1375. DOI: 10.17675/2305–6894–2020–9–4–10
23. Pletnev, M.A., Effect of inhibitors on the desorption potentials in the anodic dissolution of iron in acid solutions – A review, *Int. J. Corros. Scale Inhib.*, 2020, vol. 9, no. 3, p. 842. DOI: 10.17675/2305–6894–2020–9–3–4

RUSSIAN JOURNAL OF ELECTROCHEMISTRY, 2025, Vol. 61, No. 1, pp. 90–95

ANODIC DISSOLUTION AND CORROSION OF Al IN KOH SOLUTIONS IN 90% ETHANOL CONTAINING ADDITIVES OF GALLIUM AND INDIUM COMPOUNDS. INHIBITORY EFFECT OF CITRIC ACID

© 2025 K. V. Rybalka*, L. A. Beketaeva

Frumkin Institute of Physical Chemistry and Electrochemistry, Russian Academy of Sciences, Moscow, Russia

**e-mail: mamaison2000@yandex.ru*

Received: October 14, 2024
Revised: November 01, 2024
Accepted: November 02, 2024

Abstract. The influence of addition of citric acid monohydrate on anodic dissolution and corrosion rate of aluminum in KOH solutions in 90% ethanol containing additives of gallium and indium compounds has been considered. It is shown that the introduction of citric acid monohydrate into the solution allows to reduce the magnitude of aluminum corrosion current without reducing the rate of its anodic dissolution. The inhibition efficiency of citric acid monohydrate when introduced into the solution at a concentration of $5 \cdot 10^{-4}$ M is 58%. The discharge galvanostatic curves in the above electrolyte show a discharge plateau up to a discharge current density of 16 mA/cm^2.

Keywords: *aluminum, KOH, ethanol, anodic dissolution, hydrogen release, corrosion current*

DOI: 10.31857/S04248570250107e6

INTRODUCTION

Aluminum, due to its high volumetric specific capacity (8.04 mA h/cm^3) and the value of the standard electrode potential (–1.66 V), is a promising anode material for creating energy-intensive current sources. These features of aluminum and its widespread occurrence in the Earth's crust have long attracted the attention of researchers working in the field of chemical power sources. An element with an aluminum anode in a solution of nitric acid as an electrolyte was proposed by Buff as early as 1897. The EMF of this current source is 1.377 V [1]. Later, various salt, acid, and alkaline water-based electrolytes were considered in the works on creating current sources with an aluminum anode [2–4].

A significant limitation of the use of aluminum as an anode in current sources with an aqueous electrolyte is due to the significant self-dissolution of aluminum caused by the active release of hydrogen. To overcome this complication, many researchers have switched to using non-aqueous electrolytes [5–9]. The electrochemical behavior of aluminum depends not only on the electrolyte used, but also on the pretreatment of its surface. The use of aluminum as an anode in non-aqueous electrolytes requires the use of labor-intensive pretreatment necessary to remove the oxide film on the electrode [7, 9]. This complicates the practical use of aluminum as an anode in current sources.

The use of alkaline water-alcohol solutions [10–16] makes it possible to overcome this complication, since the destruction of the insulating oxide layer on the electrode occurs directly upon contact of aluminum with the working electrolyte. The electrochemical activity of the aluminum electrode in these solutions depends on the water content in the electrolyte, increasing with increasing concentration [11, 12, 15]. Simultaneously with an increase in the activity of aluminum, an increase in the water content leads to an increase in the rate of its corrosion. A number of corrosion inhibitors used in aqueous solutions have also proved effective in aqueous alcohol electrolytes. In [13], the effect of Na_2SnO_3 on the anodic behavior of aluminum and the rate of its corrosion in a 4 M KOH solution in a mixed solvent methanol/water (volume ratio 4/1) was studied. The introduction of sodium stannate significantly slows down the corrosion of aluminum due to the deposition of tin on its surface. The authors of [13] found that with a significant increase in the concentration of sodium stannate in the electrolyte, the tin precipitate on the surface of the aluminum electrode cracks, leading to a decrease in the inhibitory effect of the stannate. The introduction of Na_2SnO_3 simultaneously improves the discharge characteristics of aluminum by inhibiting the formation of a dense deposit of reaction products on the electrode surface. This effect increases with increasing stannate concentration in the electrolyte. At a sodium stannate concentration of 10.0 mM/l,

galvanostatic curves with a discharge current density up to 20 mA/cm^2 demonstrate a discharge plateau. At the same current density, the discharge curves in solutions containing stannate are shifted towards negative potential values compared to the curves obtained in solutions without an inhibitor. In [17], a hybrid inhibitor was proposed for aluminum-air current sources, including sodium stannate and casein. The introduction of 0.05 M Na_2SnO_3 and 0.6 g/l casein into a 4 M NaOH solution reduces the rate of aluminum corrosion by an order of magnitude and increases the discharge capacity of the current source by 89.3%. The presence of ethylene glycol in the hybrid Na_2SnO_3/ ethylene glycol inhibitor [18] promotes a more uniform and dense deposition of tin on the surface of the aluminum electrode, which makes it possible to enhance the inhibitory effect of sodium stannate. At the same time, the discharge characteristics of the anode are improved. The best results are achieved by using 10% ethylene glycol (mass fraction) and 0.05 M Na_2SnO_3. In [18], a study of the corrosion behavior of the 1060 Al alloy in a 4 M aqueous NaOH solution showed that the use of the above hybrid inhibitor makes it possible to increase the use of the anode from 16% to 43%, and the specific energy density from 543 to 1577 Wh/kg. Zinc oxide is known to be an effective inhibitor of aluminum corrosion in alkaline electrolytes. The effectiveness of aluminum corrosion inhibition in KOH solutions depends on both the concentration of ZnO and the concentration of KOH [19]. The authors of [19] established that in KOH solutions saturated with zinc oxide, a dense zinc film forms on the aluminum surface, which has strong adhesion and maximum protective properties. The open-circuit potential of the aluminum electrode shifts towards positive values when ZnO is introduced. In a 55% KOH solution saturated with ZnO, this displacement is ~200 mV. With anodic polarization, the discrepancy between the polarization curves in a pure KOH solution and in the presence of ZnO additives decreases. The rate of aluminum corrosion in the above electrolyte decreases by 2 orders of magnitude compared to what is observed in the absence of ZnO additives.

A number of researchers have proposed hybrid inhibitors based on the combined use of zinc oxide and specially selected organic compounds. The effect of ZnO additives on the corrosion behavior of aluminum in a 4 KOH solution in a mixed methanol/water solvent (3/2 by volume ratio) was considered in [14]. The corrosion rate of aluminum in this solution (6.46 mA/cm^2) is significantly lower than in the corresponding 4 M aqueous KOH solution. The addition of ZnO to the electrolyte makes it possible to further reduce the rate of aluminum corrosion, and this effect can be enhanced by simultaneous administration of hydroxytryptamine into the solution. The introduction of 0.2 M ZnO and 1.0 ml/l hydroxytryptamine into the solution reduces the corrosion current of aluminum by 82 times, reducing it from 6.46 to 0.079 mA/cm^2. At the same time, the presence of zincate in the solution leads to a shift in the open-circuit potential of the aluminum electrode by 300 mV towards positive values. In [20], the effect of the combined use of zinc oxide and polyethylene glycol (**PEG**) on the electrochemical behavior and corrosion rate of aluminum in a 4 M KOH solution was considered. The authors [20] note that in the absence of PEG, the zinc precipitate on the aluminum surface has a loose, spongy structure and weak adhesion. In this case, it cannot be ensured that aluminum corrosion is inhibited for a long time. The introduction of PEG makes it possible to improve the characteristics of the zinc precipitate. The effectiveness of PEG depends on its concentration in the solution. The maximum effectiveness of this inhibitor is achieved by introducing 0.2 M ZnO and 2 mM PEG into the solution. The introduction of an inhibitor makes it possible to significantly reduce the rate of aluminum corrosion, at the same time, the conductivity of aluminum shifts by about +0.5 V. relative to that in the absence of an inhibitor. Accordingly, the discharge curves proceed at relatively low values of the electrode potential. The authors of [21] proposed a hybrid inhibitor including ZnO and α, ω-Bis (2-carboxymethyl) polyethylene glycol (PEG-diacid). The introduction of PEG-diacid affects the morphology of the zinc layer formed on the surface of aluminum, increasing its density and reducing porosity. The ZnO/PEG diacid inhibitor impedes the corrosion of aluminum in alkaline solutions by reducing the rate of the cathode reaction. Its use provides effective protection of the aluminum electrode from corrosion without affecting its discharge characteristics. During the discharge of the aluminum anode, the protective layer formed in the presence of an inhibitor is quickly removed from the surface of the aluminum anode, ensuring its effective discharge. Upon termination of the discharge, the protective layer of ZnO/PEG-diacid is restored, resuming protection of the anode from corrosion in the time intervals between discharges. The effectiveness of this inhibitor depends on both the amount of ZnO in the solution and the concentration of PEG-diacid. The optimal effect is achieved by introducing 5000 ppm PEG diacid and 16 g/l of ZnO into the solution.

The effect of calcium oxide and sodium and potassium citrate additives on the corrosion and anodic behavior of aluminum Al-2S in 4 M aqueous solutions of sodium and potassium hydroxide was studied in [22]. The authors of [22] suggest that aluminum in an alkaline

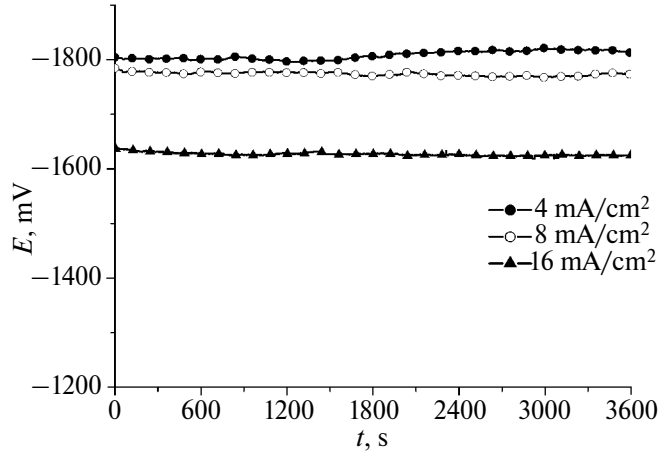

Fig. 1. Galvanostatic discharge curves on an Al electrode in a 2 M KOH solution in 90% ethanol containing 10^{-4} M Ga^{3+} and 10^{-3} M In^{3+} at various values of current density.

solution in the form of aluminate ions, interacting with Ca^{2+} ions, forms calcium aluminate, which precipitates as a thin film on the surface of aluminum, preventing its corrosion. At the same time, Al^{3+} ions, reacting with an excess of citrates, form aluminum citrate. Thus, calcium and aluminum citrates can also have an inhibitory effect on aluminum corrosion. It has been shown that the effectiveness of inhibition increases with increasing concentrations of both calcium oxide and sodium and potassium citrates. The inhibition efficiency in these solutions reaches 93%.

A study of the effect of calcium ions and tartrate ions on the behavior of aluminum in a 4 M aqueous KOH solution [23] showed that tartrate ions themselves have a slight inhibitory effect, but significantly enhance the inhibitory effect of calcium ions. The inhibition efficiency is 85%. The combined effect may be associated, according to the authors, with the formation of complexes leading to an increase in the solubility of $Ca(OH)^2$. In [24], the inhibitory effect of urea and thiourea on the corrosion behavior of the Al-Mg-In-Mn alloy in a 5 M aqueous KOH solution was investigated. It has been shown that the introduction of the above corrosion inhibitors into a solution in an amount of 25 mM makes it possible to reduce the corrosion current density of the alloy from 26 mA/cm^2 in a solution containing no inhibitors to 12.6 and 11.2 mA/cm^2 in the case of urea and thiourea additives, respectively. The effectiveness of the effect of urea and thiourea on the corrosion current grows with an increase in their concentration in solution.

Many of these inhibitors could not be used by us due to their low solubility in ethanol. Citric acid is one of the most effective corrosion inhibitors of aluminum and its alloys in an aqueous alkaline environment [25], however, it is highly soluble in both water and ethanol. These properties of citric acid led to its choice as an inhibitor in this work.

Earlier [15], we examined the effect of additives of gallium and indium compounds on the electrochemical activity of Al in a 2 KOH solution in 96% ethanol. It has been shown that the activating effect of gallium ions is most effective when their content in solution ranges from 10^{-5} to 10^{-4} M. Discharge galvanostatic curves in KOH solutions in 96% ethanol with additives of gallium and indium compounds at concentrations of 10^{-4} M and 10^{-3} M, respectively, make it possible to obtain a discharge plateau at current densities up to 4 mA/cm^2.

The purpose of this study is to search for the composition of an electrolyte based on a mixed aqueous-ethanol solvent that provides the maximum possible current of anodic dissolution of aluminum with a minimum current of its corrosion.

EXPERIMENTAL METHODS

Al electrodes were obtained from aluminum sheet of 99.999% purity. To carry out electrochemical measurements, smooth sheets 0.5 mm thick were cut into 5 x 10 mm rectangles with a tap for electrical contact. The surface of the Al electrode was treated with P 400 grit sandpaper and degreased with ethyl alcohol before measurement. All measurements were carried out in a 2 M KOH solution in 90% ethanol containing $Ga(NO_3)_3$ and $In(NO_3)_3$ additives. Electrolyte solutions were obtained using chemically pure reagents. 90% ethanol was used as a solvent.

The measurements were carried out in a small (15 cm^3) glass three-electrode cell. All measurements were carried out after preliminary exposure of the Al electrode in the working solution for 1 h. The reference electrode was a silver chloride electrode. The auxiliary electrode is made of platinum. Galvanostatic measurements at current densities of 4.8 and 16 mA/cm^2 were performed using an IPC2000 Pro potentiostat (EKONIKS, Russia). All measurements were performed at a temperature of 25 °C.

The traditional method of measuring the rate of gas release on aluminum in the working electrolyte was used. A small sample of the aluminum sheet used to make the electrodes was placed in a vessel with the test solution. The gas released on the aluminum sample was fed into an upside-down burette filled with water to measure the volume of released gas by the volume of displaced water. The volume of the released gas was brought to normal conditions by applying the ratio $V=V_m \cdot 273 \cdot (P-P_w)/(760 \cdot (273+t))$. Here V is the volume of gas brought to normal conditions, V_m is the measured volume of the released gas, P is atmospheric pressure, P_w is the partial pressure of water vapor under experimental conditions,

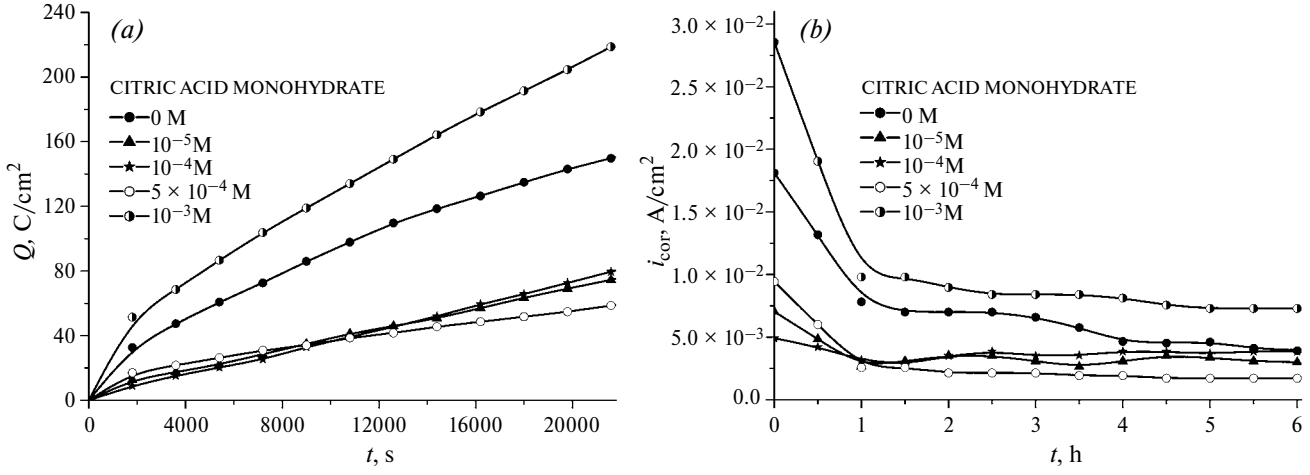

Fig. 2. Dependences: (a) of the amount of electricity spent on hydrogen release on Al, (b) of the current density of Al corrosion on the time it was in a 2 M KOH solution in 90% ethanol containing 10^{-4} M Ga^{3+} and 10^{-3} M In^{3+} and additives of citric acid monohydrate.

t is the temperature in °C. The amount of electricity (Q) spent on hydrogen reduction and the volume of hydrogen released, related to the surface unit of the aluminum sample under study, are related by the ratio $Q = 2FV/V_o$, where F is the Faraday number, V is the volume of released gas reduced to normal conditions, and V_o is the volume of one mole of gas under normal conditions. The density of the corrosion current caused by hydrogen release (i_{cor} = dQ/dt) can be easily determined by differentiating the dependence of Q on t, where t is the residence time of the aluminum sample in solution.

The effectiveness of the inhibitor (citric acid monohydrate) was determined by its effect on the rate of hydrogen release on aluminum. All measurements were carried out in a 2 M KOH solution in 90% ethanol containing additives $Ga(NO_3)_3$, $In(NO_3)_3$ and various concentrations of citric acid monohydrate.

RESULTS AND THEIR DISCUSSION

Fig. 1 shows chronopotentiograms of galvanostatic discharge obtained on an aluminum electrode in a 2 M KOH solution in 90% ethanol containing 10^{-4} M Ga^{3+} and 10^{-3} M In^{3+}.

The displacement of the electrode potential towards positive values from the steady-state value of the open circuit potential at an anode current density of 4 mA/cm^2 does not exceed 50 mV. The stability of the potential value of the Al electrode during the discharge process should be noted. An increase in the water content in a mixed aqueous-ethanol solution from 4 to 10% leads to a fourfold increase in the achievable value of the discharge current density compared to what was previously obtained in a similar electrolyte containing 96% ethanol [15]. Fig. 2*a* shows the curves of the dependence of the amount of electricity spent on the release of hydrogen on aluminum, determined by the volume of the released gas, on the residence time of the Al sample in a solution containing various concentrations of the inhibitor. By differentiating the dependence of the amount of electricity Q on time t, the dependences of the corrosion current of aluminum i_{cor} on the time it was in the solution are obtained (Fig. 2b). As follows from Fig. 2*b*, the addition of citric acid monohydrate, depending on its concentration in the solution, leads to both a decrease and an increase in the density of the corrosive current. Citric acid monohydrate has the maximum inhibitory effect at a concentration of $5\cdot10^{-4}$ M in solution.

With higher and lower concentrations of citric acid monohydrate, the density of the corrosive current increases.

The corrosion current of aluminum, as can be seen from the data shown in Fig. 2, depends on the time it is in solution. The effectiveness of the inhibitor was evaluated using a steady-state value of the corrosion current. The corrosion inhibition efficiency η was calculated using the ratio $\eta = [(i_{oc} - i_c) / i_{oc}] \cdot 100$, where i_{oc} and i_c are the corrosion currents in the absence of the inhibitor and when it is in solution, respectively. At a concentration of citric acid monohydrate $5\cdot10^{-4}$ M, the inhibition efficiency calculated after a six-hour exposure of the aluminum sample in solution is 58%. The steady-state value of the corrosion current density is 1.7 mA/cm^2.

Fig. 3 shows chronopotentiograms of galvanostatic discharge of Al in a 2 M KOH solution in 90% ethanol containing additives of 10^{-4} M Ga^{3+}, 10^{-3} M In^{3+} and $5\cdot10^{-4}$ M citric acid monohydrate. A comparison

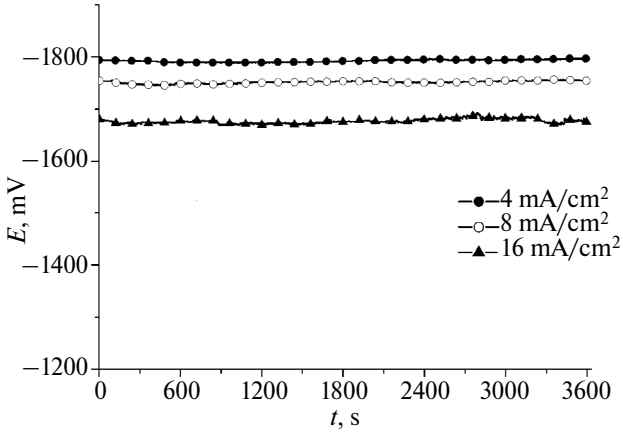

Fig. 3. Galvanostatic discharge curves on an Al electrode in a 2 M KOH solution in 90% ethanol containing 10^{-4} M Ga^{3+}, 10^{-3} M In^{3+} and $5\cdot10^{-4}$ M citric acid monohydrate at various current densities.

of the data shown in Fig. 1 and 3 shows that the introduction of citric acid monohydrate into the solution at a concentration of $5\cdot10^{-4}$ M does not impair the discharge characteristics of the aluminum electrode. Just as in the absence of an inhibitor, curves with a discharge current density of up to 16 mA/cm^2 demonstrate a stable discharge plateau.

CONCLUSION

1. An increase in the water content in a 2 M KOH solution in ethanol containing additives of gallium and indium compounds from 4 to 10% leads to a fourfold increase in the achievable value of the discharge current density.

2. Discharge galvanostatic curves in a 2 M KOH solution in 90% ethanol containing 10^{-4} M Ga^{3+} and 10^{-3} M In^{3-} at current densities up to 16 mA/cm^2 demonstrate a discharge plateau.

3. The introduction of citric acid monohydrate into the above solution at a concentration of $5\cdot10^{-4}$ M reduces the current density of aluminum corrosion to 1.7 mA/cm^2. The inhibition efficiency of citric acid monohydrate is 58%.

4. The introduction of citric acid monohydrate into the solution reduces the amount of aluminum corrosion current without reducing the rate of its anodic dissolution.

ACKNOWLEDGMENTS

The work was carried out with the support of the Ministry of Science and Higher Education of the Russian Federation. The topic of the State Assignment is "Physicochemistry and technology of electrochemical and bioenergy materials" No. 122011300058−3 No. FFZS-2022−0016.

CONFLICT OF INTEREST

The authors declare that they have no conflict of interest.

REFERENCES

1. Tommasi, D., *Traité des pilles électriques, piles hidro-électriques-accumulateurs, piles thermo-électriques et pyro-électriques*, Carré, G., Ed, Paris, 1889, p.185.
2. Despic, A., and Parkhutik, V.P., *Electrochemistry of Aluminum in Aqueous Solutions and Physics of its Anodic Oxide, in 'Modern Aspects of Electrochemistry*. Conway, B.E., Bockris, J.O'M., and White, R.E., Eds, New York: Plenum Press, 1991, vol. 20, p. 401.
3. Li, Q., and Bjerrum, N.J., Aluminum as anode for energy storage and conversion: a review, *J. Power Sources,* 2002, vol. 110, p. 1.
4. Skundin, A.M. and Osetrova, N.V., The use of aluminum in low-temperature current sources, *Electrochemical kinetics*, 2005, vol. 5, no. 1, p. 3.
5. Levitin, G., Tel-Vered, R., Yarnitzky, C., and Licht, S., Organic solvents for anodic aluminum electrochemistry, *Rev. Anal. Chem.,* 1999, vol. 18, p. 269.
6. Licht, S., Levitin, G., Yarnitzky, C., and Tel-Vered, R., Organic phase for aluminum batteries, *Electrochemical and solid-state letters*, 1999, vol. 2, no. 6, p. 262.
7. Licht, S., Tel-Vered, R., Levitin, G., and Yarnitzky, C., Solution activators of aluminum electrochemistry in organic media, *J. Electrochem.Soc.*, 2000, vol. 147, no. 2, p. 496.
8. Tel-Vered, R., Levitin, G., Yarnitzky, C., and Licht, S., Analytical determination of In activation of aluminum anodes in the organic phase, *Rev. Anal. Chem.,* 1999, vol. 18, no. 5, p. 249.
9. Licht, S., Levitin, G., Tel-Vered, R., and Yarnitzky, C., The effect of water on the anodic dissolution of aluminum in non-aqueous electrolytes, *Electrochem. Commun.*, 2000, vol. 2, p. 329.
10. Gontmakher, N.M., Grigoriev, V.P., Nechaeva, O.N., Berkman, E.A., Guterman, V.E., and Petrova, G.M., Dissolution of aluminum and Al-Mg-Hg alloys in organic and aqueous-organic solvents, *Soviet Electrochemistry,* 1984, vol. 20, p. 76.
11. Shao, H.B., Wang, J.M., Wang, X.Y., Zhang, J.Q., and Cao, C.N., Anodic dissolution of aluminum in KOH ethanol solutions, *Electrochem. Commun.,* 2004, vol. 6, p. 6.
12. Wang, J.B., Wang, J.M., Shao, H.B., Zhang, J.Q., and Cao, C.N., The corrosion and electrochemical behaviour of pure aluminium in alkaline methanol solutions, *J. Appl. Electrochem.*, 2007, vol.37, p. 753.
13. Chang, X., Wang, J., Shao, H., Wang, J., Zeng, X., Zhang, J., and Cao, C., Corrosion and anodic behaviors of pure aluminum in a novel alkaline electrolyte, *Acta Phys. -Chim. Sin.*, 2008, vol. 24(9), p. 1620.

14. Wang, J.B., Wang, J.M., Shao, H.B., Chang, X.T., Wang, L., Zhang, J.Q., and Cao, C.N., The corrosion and electrochemical behavior of pure aluminum in additive-containing alkaline methanol–water mixed solutions, *Mater. and Corr.,* 2009, vol. 60, no. 4, p. 269.

15. Rybalka, K.V., and Beketaeva, L.A., Effect of Ga^{3+} and In^{3+} Ions on the Anodic Dissolution of Aluminum in KOH Ethanol Solutions, *Russ. J. Electrochem.,* 2023, vol. 59, p. 162.

16. Rybalka, K.V., and Beketaeva, L.A., Anodic dissolution of Al in KOH solutions of in the mixed ethanol/acetonitrile solvent, *Russ. J. Electrochem.,* 2023, vol. 59, p. 1102.

17. Nie, Y., Gao, J., Wang, E., Jiang, L., An, L., and Wang, X., An effective hybrid organic/inorganic inhibitor for alkaline aluminum-air fuel cells, *Electrochim. Acta*, 2017, vol. 248, p. 478.

18. Ma, C., Hu, C., Xu, X., Song, Y., Shao, M., Lin, J., and Jiang, Z., Inhibition Effect and Mechanism of Na_2SnO_3-Ethylene Glycol Hybrid Additives on 1060 Aluminum in Alkaline Aluminum-Air Batteries, *Chem. Select,* 2021, vol. 6, p. 1804. doi.org/10.1002/slct.202004844

19. Faegh, E., Shrestha, S., Zhao, X., and Mustain, W.E., In-depth structural understanding of zinc oxide addition to alkaline electrolytes to protect aluminum against corrosion and gassing, *J. Appl. Electrochem.*, 2019, vol. 49, p. 895.

20. Wang, X.Y., Wang, J.M., Wang Q. L., Shao, H.B., and Zhang, J.Q., The effects of polyethylene glycol (PEG) as an electrolyte additive on the corrosion behavior and electrochemical performances of pure aluminum in an alkaline zincate solution, *Mater. and Corr.*, 2011, vol. 62, no. 12, p. 1149.

21. Gelman, D., Lasman, I., Elfimchev, S., Starosvetsky, D., and Ein-Eli, Y., Aluminum corrosion mitigation in alkaline electrolytes containing hybrid inorganic/organic inhibitor system for power sources applications, *J. Power Sources*, 2015, vol. 285, p. 100.

22. Sarangapani, K.B., Balaramachandran, V., Kapali, V., Venkatakrishna Iyer, S., and Potdar, G., Aluminium as the anode in primary alkaline batteries, *Surface Technol.*, 1985, vol. 26, p. 67.

23. Shao, H.B., Wang, J.M., Zhang, Z., and Cao, C.N., The cooperative effect of calcium ions and tartrate ions on the corrosion inhibition of pure aluminum in an alkaline solution, *Mater. Chem. and Phys.*, 2002, vol. 77, p. 305.

24. Moghadam, Z., Shabani-Nooshabadi, M., and Behpour, M., Electrochemical performance of aluminium alloy in strong alkaline media by urea and thiourea as inhibitor for aluminium-air batteries, *J. Molec. Liquids*, 2017, vol. 242, p. 971. DOI: 10.1016/j.molliq.2017.07.119

25. Wysocka, J., Cieslik, M., Krakowiak, S., and Ryl, J., Carboxylic acids as efficient corrosion inhibitors of aluminium alloys in alkaline media, *Electrochim. Acta*, 2018, vol. 289, p. 175.